



CHARACTERIZATION OF RESIDUAL STRESS IN  
MICROELECTROMECHANICAL SYSTEMS (MEMS) DEVICES USING  
RAMAN SPECTROSCOPY

DISSERTATION  
LaVern A. Starman  
Captain, USAF

AFIT/DS/ENG/02-01

DEPARTMENT OF THE AIR FORCE  
AIR UNIVERSITY

**AIR FORCE INSTITUTE OF TECHNOLOGY**

Wright-Patterson Air Force Base, Ohio

APPROVED FOR PUBLIC RELEASE; DISTRIBUTION UNLIMITED.

## Report Documentation Page

<b>Report Date</b> 26 Mar 02	<b>Report Type</b> Final	<b>Dates Covered (from... to)</b> Jun 00 - Mar 02
<b>Title and Subtitle</b> Characterization of Residual Stress in Microelectromechanical Systems (MEMS) Devices Using Raman Spectroscopy	<b>Contract Number</b>	
	<b>Grant Number</b>	
	<b>Program Element Number</b>	
<b>Author(s)</b> Capt La Vern A. Starman, USAF	<b>Project Number</b>	
	<b>Task Number</b>	
	<b>Work Unit Number</b>	
<b>Performing Organization Name(s) and Address(es)</b> Air Force Institute of Technology Graduate School of Engineering and Management (AFIT/EN) 2950 P Street, Bldg 640 WPAFB, OH 45433-7765	<b>Performing Organization Report Number</b> AFIT/DS/ENG/02-01	
<b>Sponsoring/Monitoring Agency Name(s) and Address(es)</b> AFRL/MLMR ATTN: Mr. John D. Busbee 2977 P Street Rm 215 WPAFB, OH 45433-7746 AFRL/MLPJ ATTN: Lt Col William D. Cowan 2977 P Street WPAFB OH 45433-7746	<b>Sponsor/Monitor's Acronym(s)</b>	
	<b>Sponsor/Monitor's Report Number(s)</b>	
<b>Distribution/Availability Statement</b> Approved for public release, distribution unlimited		
<b>Supplementary Notes</b> The original document contains color images.		
<b>Abstract</b> Due to the small scale of MEMS devices, the inherent residual stresses during the deposition processes can affect the functionality and reliability of the fabricated devices. Residual stress often causes device failure due to curling, buckling, or fracture. Currently, few techniques are available to measure the residual stress in MEMS devices. In this dissertation, Raman spectroscopy is used to measure and monitor the residual and induced stresses in MUMPs polysilicon MEMS devices. Raman spectroscopy was selected since it is nondestructive, fast, and provides potential in situ stress monitoring. Raman spectroscopy scans on unreleased and released MEMS fixed-fixed beams, cantilevers, and micromirror flexures were performed to obtain residual stress profiles. The profiles are compared to analytical models to assess the accuracy of Raman spectroscopy. I performed post-processing thermal anneals, phosphorous diffusions and phosphorous ion implantations to characterize the residual stress changes within MEMS devices. From post-processing experiments, the Raman residual stress profiles on MUMPs structures indicate a stress reduction by over 90%, which is verified with on-chip test structures. The reduced residual stress levels can improve the performance, reliability, and yield of the MEMS devices as they become smaller. In addition, I present the first Raman stress measurements in III-V MEMS		
<b>Subject Terms</b> Residual Stress, Raman Spectroscopy, MUMPs, MEMS, Polysilicon		

<b>Report Classification</b> unclassified	<b>Classification of this page</b> unclassified
<b>Classification of Abstract</b> unclassified	<b>Limitation of Abstract</b> UU
<b>Number of Pages</b> 297	

Research sponsored in part by the Air Force Research Laboratory, Air Force Materiel Command, USAF. The United States Government is authorized to reproduce and distribute reprints notwithstanding any copyright notation thereon. The views and conclusions contained in this dissertation are those of the author and should not be interpreted as necessarily representing the official policies or endorsements, either expressed or implied, of the Air Force Research Laboratory, Department of Defense, or the United States Government.

AFIT/DS/ENG/02-01

CHARACTERIZATION OF RESIDUAL STRESS IN  
MICROELECTROMECHANICAL SYSTEMS (MEMS) DEVICES  
USING RAMAN SPECTROSCOPY

DISSERTATION

Presented to the Faculty

School of Engineering and Management

Air Force Institute of Technology

Air University

Air Education and Training Command

In Partial Fulfillment of the Requirements for the  
Degree of Doctor of Philosophy in Electrical Engineering

LaVern A. Starman, B.S.E.E., M.S.E.E.

Captain, USAF

April 2002

APPROVED FOR PUBLIC RELEASE; DISTRIBUTION UNLIMITED.


CHARACTERIZATION OF RESIDUAL STRESS IN  
MICROELECTROMECHANICAL SYSTEMS (MEMS) DEVICES  
USING RAMAN SPECTROSCOPY

DISSERTATION


LaVern A. Starman, B.S.E.E., M.S.E.E.

Captain, USAF


Approved:

  
Lt Col James A. Lott, PhD, Committee Chairman  
Professor of Electrical Engineering

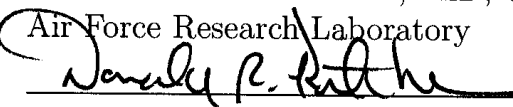
09 April 2002  
Date

  
Maher S. Amer, PhD, Committee Member  
Assistant Professor of Materials Science and Engineering


4-9-2002  
Date

  
Lt Col William D. Cowan, PhD, Committee Member  
Air Force Research Laboratory

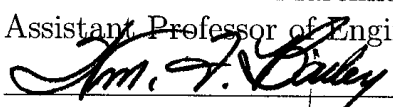
9 April 02  
Date

  
Col Donald R. Kitchen, PhD, Committee Member  
Head, Department of Electrical and Computer Engineering

9 April 02  
Date

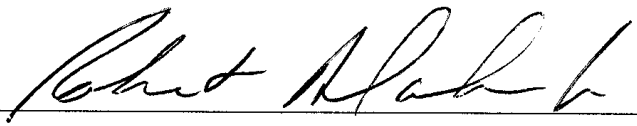
  
Lt Col Michael A. Marciniak, PhD, Committee Member  
Assistant Professor of Engineering Physics

9 Apr 02  
Date

  
William F. Bailey, PhD, Dean's Representative  
Associate Professor of Engineering Physics

9 Apr 2002  
Date

Accepted:

  
Robert A. Calico, Jr.  
Dean, Graduate School of Engineering and Management

24 May '02  
Date

## *Acknowledgements*

Without the constant love, support, prayers, and understanding of my wonderful wife and son, this dissertation research effort would not have been possible. Despite my many absences from home, both physically and mentally, my heart and thoughts were always with you. I would like to thank my Mom, as well as my Parents In-Law, for understanding the many months between visits and the constant love and support you provided my family in my absence. I would also like to thank our friends, Lynn, Ginge, Ryan, Leslie, Chris, Randy, and Dina who called or emailed us numerous times to lend their support. I truly appreciate all the support and prayers you provided.

I owe a huge debt of gratitude to my research advisor and committee chairman, Lt Col James Lott, who's persistence and guidance permitted my transfer into AFIT to pursue my doctoral degree. Although this was a relatively new research area, I appreciate your constant encouragement and leadership you provided to enable me to fulfill my research endeavors. I am also thankful to the other members of my research committee, Lt Col Bill Cowan for your constant support, encouragement and willingness to share your vast knowledge in the area of MEMS and MEMS research. Lt Col Mike Marciniak for your assistance with providing insight in many of the physics issues. I'd also like to thank Col Donald Kitchen for his enthusiasm and willingness to join my committee late in the research period. Finally, a very special thanks to Dr. Maher Amer for the continuous use of his Raman spectroscopy system. Without your generosity and sincere indebtedness, this research would not have been possible. I also appreciated your time spent addressing many of my Raman spectroscopy questions and concerns. Thanks also go to my Deans Representative, Dr. William Bailey, for serving on my committee.

I'd like to thank all the members of AFIT's Microgroup for your support and assistance throughout my research. A special thanks goes to Capt Eddie Ochoa for

his endless knowledge and support in answering my many programming questions, providing suggestions and lab assistance during my research.

I want to especially thank Dr. Tom Nelson, Mr. Bill Siskaninetz, and the entire MEMS group at AFRL for all your assistance, expertise and usage of the SND cleanroom. A special thanks goes to Dr. Becky Cortez for taking the time to perform the SEM imagery necessary for this research and Dr. Tom Nelson for performing the reflectivity measurements.

Most of the work in this dissertation would not have been possible without the credit card and procurement expertise of Mr. Charlie Powers. Technicians Rick Patton and Bill Trop were indispensable in providing assistance before, during, and after AFIT's laboratory move to minimize research delays.

I also must recognize several people outside AFIT for their contributions to my research. Mr. Dave Koester at Microelectronics Center of North Carolina was extremely forthcoming with details of the MUMPs® processes. Dr. Nelsimar Vandelli and others at CoventorWare for your endless knowledge and suggestions to improve FEM modelling of MEMS devices and Ralph Sinclair at Implant Sciences for your quick turnaround of all implants.

I appreciate the funding and support provided by Lt Col William Cowan and John Busbee from the Laser Laser Hardening and Materials Research branches of the Air Force Research Laboratory. I thank these organizations for their financial support.

Finally, I would like to dedicate this work to my father who passed away during my doctoral studies. I appreciate the time and memories we shared and for instilling the work ethics necessary for fulfillment of my doctoral degree. I know you would be proud of me. We miss and love you, May God Bless you.

- LaVern A. Starman

## *Table of Contents*

	Page
Acknowledgements . . . . .	iii
List of Figures . . . . .	x
List of Tables . . . . .	xviii
Abstract . . . . .	xix
I. Introduction . . . . .	1-1
1.1 Introduction . . . . .	1-1
1.2 Problem Statement and Approach . . . . .	1-2
1.3 MEMS Background . . . . .	1-3
1.4 Stress Characterization and Measurement Techniques . . . . .	1-4
1.5 Research Accomplishments . . . . .	1-8
1.6 Dissertation Organization . . . . .	1-10
Bibliography . . . . .	1-12
II. MEMS Modelling and Foundry Fabrication Processes . . . . .	2-1
2.1 Chapter Overview . . . . .	2-1
2.2 Multi-User MEMS Process (MUMPs®) . . . . .	2-2
2.2.1 MUMPs® Fabrication Process . . . . .	2-2
2.2.2 MUMPs® Buffered Oxide Etch. . . . .	2-4
2.3 Sandia Ultra-planar Multi-level MEMS Technology . . . . .	2-9
2.3.1 Fabrication Process . . . . .	2-9
2.4 Multi User Silicon Carbide (MUSiC) Process . . . . .	2-10
2.4.1 Fabrication Process . . . . .	2-11
2.5 <i>TSUPREM<sup>TM</sup></i> Modelling . . . . .	2-12
2.5.1 <i>TSUPREM<sup>TM</sup></i> Model of MUMPs® Fabrication Process . . . . .	2-14
2.6 MEMCAD FEM Modelling . . . . .	2-17
2.6.1 MEMCAD Elements . . . . .	2-18
2.6.2 MEMCAD Components . . . . .	2-18
2.6.3 MEMS Stress Modelling . . . . .	2-21
2.6.4 Poly1 Microbridge Simulation . . . . .	2-21
2.6.5 Micromirror Simulations . . . . .	2-23
2.6.6 Managed Simulations . . . . .	2-30
2.7 Summary of Chapter II . . . . .	2-32

	Page
Bibliography . . . . .	2-33
III. Raman Spectroscopy on MEMS Structures . . . . .	3-1
3.1 Introduction . . . . .	3-1
3.2 History of Raman Spectroscopy . . . . .	3-1
3.3 Raman Instrumentation . . . . .	3-2
3.3.1 Excitation Sources . . . . .	3-2
3.3.2 Sample Illumination . . . . .	3-2
3.3.3 Monochromator . . . . .	3-2
3.3.4 Detection . . . . .	3-3
3.4 Raman Signal Detection . . . . .	3-3
3.4.1 Cosmic Ray Events . . . . .	3-4
3.4.2 Fluorescence . . . . .	3-4
3.5 Phenomenon of Raman Effect . . . . .	3-5
3.6 Raman Spectrum . . . . .	3-6
3.6.1 Benefits of Raman Spectroscopy . . . . .	3-8
3.7 Raman Frequency Shift Calculation . . . . .	3-9
3.8 Stress Calculation . . . . .	3-12
3.8.1 Uniaxial Stress Calculation . . . . .	3-13
3.8.2 Biaxial Stress Calculation . . . . .	3-14
3.8.3 Phonon Deformation Potential Experimental De- termination . . . . .	3-14
3.8.4 Raman Penetration Depth Calculation . . . . .	3-17
3.9 Raman Spectroscopy Characterization . . . . .	3-19
3.9.1 Unstressed Silicon Characterization . . . . .	3-20
3.9.2 Laser Focusing . . . . .	3-21
3.9.3 Laser Stability . . . . .	3-22
3.9.4 Analytical Thermal Model . . . . .	3-24
3.9.5 Experimental Thermal Tests . . . . .	3-30
3.10 Summary of Chapter III . . . . .	3-36
Bibliography . . . . .	3-37
IV. Stress in MEMS Structures . . . . .	4-1
4.1 Chapter Overview . . . . .	4-1
4.2 Sources of Film Stress . . . . .	4-2
4.3 Residual Stress . . . . .	4-3
4.4 Background Raman Stress Profiles and Characterization . . . . .	4-4
4.4.1 Analytical Stress Model for a Fixed-Fixed Beam . . . . .	4-5
4.4.2 Fixed-Fixed Beams . . . . .	4-6

	Page
4.4.3 Analytical Stress Model for a Cantilever . . .	4-10
4.4.4 Cantilever . . . . .	4-11
4.4.5 SUMMIT Cantilevers . . . . .	4-12
4.4.6 Micromirror Flexure . . . . .	4-18
4.4.7 Induced Micromirror Stress Characterization .	4-18
4.4.8 Induced Stress on a Micromirror Flexure . . .	4-19
4.5 Residual Stress Measurement Techniques . . . . .	4-28
4.5.1 Beam Pull-in Measurement Technique . . . .	4-29
4.5.2 Wafer Curvature Measurement Technique . . .	4-31
4.5.3 Fixed Beam Measurement Technique . . . . .	4-34
4.5.4 Supercritical Carbon Dioxide ( $CO_2$ ) Drying .	4-37
4.6 Young's Modulus . . . . .	4-41
4.6.1 Resonator Measurement Technique . . . . .	4-42
4.6.2 Estimated Residual Stress Variation . . . . .	4-42
4.7 Summary of Chapter IV . . . . .	4-44
Bibliography . . . . .	4-48
V. Post-Fabrication Anneals on Polysilicon MEMS Structures . . .	5-1
5.1 Introduction . . . . .	5-1
5.2 Thermal Annealing . . . . .	5-1
5.3 <i>TSUPREM<sup>TM</sup></i> Anneal Modelling . . . . .	5-4
5.4 Oxidized vs. Unoxidized Stress Analysis . . . . .	5-5
5.5 $\mu$ Raman Spectroscopy Stress Analysis . . . . .	5-7
5.6 Micromechanical Stress Measurements . . . . .	5-12
5.7 Repeat Annealing . . . . .	5-21
5.8 Optical Characterization . . . . .	5-23
5.9 Summary of Chapter V . . . . .	5-25
Bibliography . . . . .	5-29
VI. Post-Fabrication Doping of MEMS Structures . . . . .	6-1
6.1 Introduction . . . . .	6-1
6.2 Doping Methods . . . . .	6-2
6.2.1 <i>TSUPREM<sup>TM</sup></i> Phosphorus Diffusion Model .	6-3
6.3 Phosphorous Diffusion Set-up and Experimentation . .	6-5
6.4 Diffusion Results and Analysis . . . . .	6-10
6.5 Ion Implant Doping . . . . .	6-17
6.6 Implant Modelling . . . . .	6-18

	Page
6.6.1 <i>TSUPREM<sup>TM</sup></i> Ion Implant Model . . . . .	6-18
6.6.2 Ion Beam Profile Code . . . . .	6-20
6.7 Implant Results and Analysis . . . . .	6-21
6.8 Residual Stress Profiles for Ion Implanted MEMS by $\mu$ Raman Spectroscopy . . . . .	6-24
6.9 Young's Modulus Measurements . . . . .	6-30
6.10 Analytical Residual Stress Measurements . . . . .	6-33
6.10.1 Residual Stress Calculation using Cantilever Deflection . . . . .	6-37
6.11 Optical Characterization . . . . .	6-39
6.12 Summary of Chapter VI . . . . .	6-42
Bibliography . . . . .	6-43
VII. $\mu$ Raman Spectroscopy Results and Analysis . . . . .	7-1
7.1 Introduction . . . . .	7-1
7.2 Stress Magnitudes . . . . .	7-1
7.3 Prediction Model . . . . .	7-3
7.3.1 Raw Data Analysis . . . . .	7-4
7.3.2 Buckling Beam Estimation . . . . .	7-7
7.4 Summary of Chapter VII . . . . .	7-10
Bibliography . . . . .	7-11
VIII. Raman Spectroscopy on III-V MEMS Structures . . . . .	8-1
8.1 Introduction . . . . .	8-1
8.2 Background . . . . .	8-1
8.3 III-V MEMS Fabrication . . . . .	8-4
8.4 Raman Residual Stress Characterization . . . . .	8-5
8.4.1 Oxidation of MEMS Structures . . . . .	8-8
8.4.2 Optical Characterization of Fabricated Micromirrors . . . . .	8-14
8.5 Summary of Chapter VIII . . . . .	8-15
Bibliography . . . . .	8-17
IX. Conclusions, Contributions, and Future Work . . . . .	9-1
9.1 Contributions and Significance . . . . .	9-1
9.2 Accomplishments . . . . .	9-1
9.3 Recommendations for Future Research . . . . .	9-3
9.4 Author's Publications . . . . .	9-5

	Page
Appendix A. . . . .	A-1
A.1 MEMS Release Procedure . . . . .	A-1
A.2 GaAs MEMS Fabrication and Release Procedure . . . .	A-3
A.3 Annealing Tube Preparation . . . . .	A-8
Appendix B. MEMS Test Chips . . . . .	B-1
B.1 Test Chips . . . . .	B-2
Appendix C. <i>TSUPREM<sup>TM</sup></i> Simulation of MUMPs <sup>®</sup> Fabrication .	C-1
C.1 <i>TSUPREM<sup>TM</sup></i> Input File for MUMPs <sup>®</sup> Poly 1 Fabrica- tion . . . . .	C-1
Appendix D. Vita . . . . .	D-1

## List of Figures

Figure		Page
1.1.	Polysilicon cantilevers curl due to residual stress. . . . .	1-4
1.2.	Residual stress effects on polysilicon micromirrors. Top image illustrates the curvature of a single micromirror surface. The bottom image is an interferometric microscope (IFM) image of an array of micromirrors illustrating the nonuniform curvature of the micromirror surfaces as illustrated by the fringe lines on the mirror surfaces. . . . .	1-5
1.3.	Figure a) Block diagram of a $\mu$ Raman spectroscopy system, (b) the Raman spectroscopy system at Wright State University	1-7
2.1.	Illustration of available layers in the MUMPs <sup>®</sup> Process . . .	2-2
2.2.	MUMPs <sup>®</sup> pre and post release images of a MEMS micromotor structure. (a) unreleased and (b) released. . . . .	2-5
2.3.	Schematic side-view of a Poly1 beam before and after the buffered oxide etch. (a) before the etch, and (b) after the etch . . . .	2-6
2.4.	SEM images of Poly2 fixed-fixed beams following the buffered etch. a) 1 $\mu m$ -wide, b) 1.5 $\mu m$ -wide, and c) 2 $\mu m$ -wide . . . .	2-7
2.5.	SEM image of buffered etch test array. . . . .	2-8
2.6.	Illustration of available layers in the <i>SUMMIT</i> <sup>TM</sup> process [6]	2-10
2.7.	Illustration of available layers in the MUSiC process [10] . .	2-11
2.8.	Illustration of the three step MUSiC release process [10] . . .	2-13
2.9.	<i>TSUPREM</i> <sup>TM</sup> diffusion profiles of the MUMPs <sup>®</sup> Poly1 structural layer at the completion of the MUMPs <sup>®</sup> run. Beam cross-sections for widths of 4 $\mu m$ , 10 $\mu m$ , and 20 $\mu m$ . Note lateral dimensions not to scale. . . . .	2-16
2.10.	<i>TSUPREM</i> <sup>TM</sup> diffusion profiles of the MUMPs <sup>®</sup> Poly2 structural layer at the completion of the MUMPs <sup>®</sup> run. Beam cross-sections for widths of 4 $\mu m$ , 10 $\mu m$ , and 20 $\mu m$ . Note lateral dimensions not to scale. . . . .	2-17
2.11.	Schematic Overview of MEMCAD [2] . . . . .	2-19
2.12.	Schematic of a 3D MEMS Poly1 micromirror. . . . .	2-20
2.13.	Micromirror conversion to enhance MEMCAD modelling . .	2-22
2.14.	MEMCAD 3D stress images for a Poly1 microbridge. . . . .	2-23
2.15.	MEMCAD 3D beam displacement vs. applied voltage for a Poly1 Microbridge. . . . .	2-24
2.16.	MEMCAD piston micromirror modelling exploiting device symmetry . . . . .	2-25

Figure		Page
2.17.	MEMCAD 3D stress images for a 200 $\mu m$ -square Poly1 micromirror with typical etch holes. . . . .	2-26
2.18.	MEMCAD 3D stress images for a 150 $\mu m$ -square Poly1 micromirror with modified etch holes. . . . .	2-27
2.19.	MEMCAD 3D displacement vs voltage images for a Poly1 micromirror. . . . .	2-28
2.20.	(a) MEMCAD images of two Poly1 micromirror designs illustrating localized induced stress magnitudes. (a) typical release etch holes, and (b) modified etch holes. . . . .	2-29
2.21.	x, y, and z-stress components obtained from MEMCAD for a micromirror flexure. (a) x-component, and (b) y and z-components. 2-30	
2.22.	MEMCAD 3D displacement in the x-direction for an enumerated Poly1 thermal actuator. Images are not to scale. . . . .	2-31
3.1.	Schematic of the excitation of a molecule resulting in a Raman spectrum . . . . .	3-7
3.2.	Raman Spectrum for bulk silicon using a 514.5 nm Argon ion laser excitation source. . . . .	3-9
3.3.	Example Raman spectral shift for a 2.5 $\mu m$ -thick polysilicon sample before and after annealing [15]. . . . .	3-10
3.4.	The four-point bending test fixture. (a) Top view and (b) Side view. . . . .	3-16
3.5.	Frequency shift of the hydrostatic component for an applied uniaxial stress applied along a 1.5 $\mu m$ -thick Poly2 cantilever with dimensions of 200 $\mu m$ -wide by approximately 4000 $\mu m$ -long. . . . .	3-18
3.6.	Laser stability stress curve for a 100 $\mu m$ -long by 10 $\mu m$ -wide released Poly1 fixed-fixed beam measured with the Raman spectroscopy system at WSU. . . . .	3-23
3.7.	Laser stability stress curve for a 100 $\mu m$ -long by 10 $\mu m$ -wide unreleased Poly2 fixed-fixed beam measured with the Raman spectroscopy system at WSU. . . . .	3-24
3.8.	Laser stability variations for a Poly2 fixed-fixed beam as measured with the Raman spectroscopy system at WSU. (Obtained over a one year period and consists of 87 Raman beam scans)	3-25
3.9.	Heat loss mechanisms for a polysilicon microbridge [9, 19]. . . . .	3-26
3.10.	Equivalent thermal test circuit for a fixed-fixed beam [9, 11]. . . . .	3-27
3.11.	Thermal stability test (5-minutes) for repeated Raman scans on a Poly2 fixed-fixed beam . . . . .	3-33
3.12.	Thermal stability test (5 hours) for repeated Raman scans on a Poly2 fixed-fixed beam. . . . .	3-34
3.13.	Thermal stability test on 370 $\mu m$ (unbuckled) and 380 $\mu m$ (buckled) Poly2 fixed-fixed beams . . . . .	3-35

Figure		Page
4.1.	Known causes of stress in crystalline silicon. [21] . . . . .	4-3
4.2.	Analytical stress model for a MEMS fixed-fixed beam [24]. . .	4-5
4.3.	Analytical stress profile of a fixed-fixed beam with a uniform load. . . . .	4-7
4.4.	Background residual stress profiles for a 100 $\mu m$ -long by 10 $\mu m$ -wide unreleased and released fixed-fixed beam. (a) Poly1 beam, (b) Poly2 beam and (c) Poly1-Poly2 stacked beam. . . . .	4-8
4.5.	Raman spectral images for a 100 $\mu m$ -long by 10 $\mu m$ -wide Poly1 fixed-fixed beam (a) Raman spectra map, (b) Raman camera image of defined area, (c) 2D Raman profile across the beam, and (d) Raman along the length of the beam. . . . .	4-9
4.6.	Analytical stress model for a MEMS cantilever [24]. . . . .	4-11
4.7.	Analytical stress profile of a cantilever with a uniform load. .	4-12
4.8.	Raman stress images for a 100 $\mu m$ -long by 10 $\mu m$ -wide Poly1 cantilever: (a) background residual stress profiles for unreleased and released cantilever; (b) Raman spectra map; (c) 2D Raman profile across the beam (y-direction); and (d) Raman along the length of the beam (x-direction) . . . . .	4-13
4.9.	Background residual stress profiles for an unreleased and released 100 $\mu m$ -long by 10 $\mu m$ -wide Poly2 cantilever made in MUMPs® run #43. . . . .	4-14
4.10.	(a) IFM image of the SUMMIT 120 $\mu m$ and 240 $\mu m$ -long cantilevers illustrating curvature. (b) Illustration of the deflected cantilevers showing the difference in the fringe line patterns on the cantilevers . . . . .	4-15
4.11.	Raman stress profiles measured on SUMMIT cantilevers. (a) 120 $\mu m$ -long cantilevers, (b) 240 $\mu m$ -long cantilever. . . . .	4-17
4.12.	Raman stress images for a 130 $\mu m$ -long by 13 $\mu m$ -wide Poly1 micromirror flexure (a) background residual stress profiles for unreleased and released flexure, (b) raman spectra map, (c) 2D Raman profile across the flexure (y-direction), and (d) Raman along the length of the flexure (x-direction). . . . .	4-19
4.13.	MUMPs® run #18 polysilicon piston micromirror designed with Poly1 flexures [6]. . . . .	4-20
4.14.	Mechanical beam model of a micromirror flexure . . . . .	4-21
4.15.	The residual stress distribution along the micromirror flexure shown in Figure 4.13. . . . .	4-22
4.16.	Schematic view of basic electrostatic piston micromirror [5].	4-23
4.17.	Interferometric microscope image of a set of micromirrors simultaneously in snap-down. Snap-down is observed by the multiple fringe lines on the micromirror surface and flexures. . . . .	4-24
4.18.	Induced stress profiles for a MEMS micromirror. (a) 3D stress map and (b) 2D stress map . . . . .	4-26

Figure		Page
4.19.	Induced stress profiles for a MEMS micromirror fitted with a third degree polynomial. (a) 3D stress map and (b) 2D stress map . . . . .	4-27
4.20.	MEMCAD FEM data extraction technique for a micromirror flexure at snap-down. . . . .	4-28
4.21.	FEM induced stress in the micromirror flexure shown in Figure 4.20 at snap-down . . . . .	4-29
4.22.	Y- and Z-stress components obtained from MEMCAD for the micromirror flexure shown in Figure 4.20 at snap-down. Figure (a) Y-Component and Figure (b) Z-Component . . . . .	4-30
4.23.	Schematic of MEMS Poly1 Microbridge for the “beam pull-in” measurement. . . . .	4-30
4.24.	Actuated MEMS Poly1 microbridge . . . . .	4-31
4.25.	Wafer curvature measuring illustration . . . . .	4-32
4.26.	Schematic of a MUMPs <sup>®</sup> Poly1 microbridge . . . . .	4-35
4.27.	Interferometric microscope (IFM) image of buckled MUMPs <sup>®</sup> Poly1 and Poly2 beams . . . . .	4-36
4.28.	SEM image of buckled Poly1 beams . . . . .	4-37
4.29.	Phases of $CO_2$ for various combinations of pressure and temperature with the regions used for release annotated, after [4, 18]. The release process begins at point 1, where liquid $CO_2$ displaces methanol. The pressure of the drying chamber is raised (point 2) to prevent the liquid from evaporating in the normal fashion when the temperature is raised (point 3). The $CO_2$ now exists in a supercritical state where it is both a liquid and a gas with no interface between the two. As the pressure is released the $CO_2$ becomes all vapor and escapes from the drying chamber (point 4). . . . .	4-39
4.30.	Poly1 comb drive resonator used to measure Young’s modulus	4-43
4.31.	Poly1 residual stress variations as a function of the buckling beam lengths. a) stress variations for buckling beam lengths of 100 $\mu m$ to 450 $\mu m$ , b) stress variations for buckling beam lengths of 450 $\mu m$ to 900 $\mu m$ . . . . .	4-46
4.32.	Poly2 residual stress variations as a function of the buckling beam lengths. a) stress variations for buckling beam lengths of 100 $\mu m$ to 450 $\mu m$ , b) stress variations for buckling beam lengths of 450 $\mu m$ to 900 $\mu m$ . . . . .	4-47
5.1.	Cross-section <i>TSUPREM<sup>TM</sup></i> simulations of the dopant density in oxidized and unoxidized Poly1 10 $\mu m$ -wide beams. Top-to-bottom anneal times (min): 0, 5, 10, 15, 20, 30, and 60-min. (a) with oxide cap, and (b) without the oxide cap. . . . .	5-5

Figure		Page
5.2.	Cross-section <i>TSUPREM<sup>TM</sup></i> simulations of the dopant density in oxidized and unoxidized Poly2 10 $\mu m$ -wide beams. Top-to-bottom anneal times (min): 0, 5, 10, 15, 20, 30, and 60-min. (a) with oxide cap, and (b) without oxide cap. . . . .	5-6
5.3.	SEM image of Poly1 microbridges used for residual stress characterization. . . . .	5-8
5.4.	$\mu$ Raman residual stress profiles for Poly1 10 $\mu m$ -wide oxidized and unoxidized beams (a) oxidized, (b) unoxidized. . . . .	5-9
5.5.	$\mu$ Raman residual stress profiles for Poly2 10 $\mu m$ -wide oxidized and unoxidized beams (a) oxidized, (b) unoxidized. . . . .	5-11
5.6.	IFM images of oxidized Poly1 and Poly2 buckling beam arrays following 1100 $^{\circ}C$ anneals and HF release. Buckling beam arrays illustrated include: a) foundry fabrication; b) post 30-min oxidation; (c) post-oxidation and 5-min 1100 $^{\circ}C$ anneal; d) post-oxidation and 15-min 1100 $^{\circ}C$ anneal; e) post-oxidation and 20-min 1100 $^{\circ}C$ anneal; f) post-oxidation plus 30-min 1100 $^{\circ}C$ anneal . . . . .	5-13
5.7.	IFM image of a Poly1 cantilever array used for residual stress characterization. . . . .	5-15
5.8.	Cantilever deflection obtained from an IFM for all 150 $\mu m$ -long by 10 $\mu m$ -wide oxidized Poly1 cantilevers. . . . .	5-17
5.9.	IFM images of unoxidized Poly1 and Poly2 buckling beam arrays following 1100 $^{\circ}C$ anneals and HF release. Anneal times illustrated include: a) 10-min, b) 20-min, c) 30-min, and d) 60-min. . . . .	5-19
5.10.	$\mu$ Raman residual stress profiles for Poly1 and Poly2 10 $\mu m$ -wide oxidized beams with repeated 1100 $^{\circ}C$ anneals (a) Poly1, (b) Poly2. . . . .	5-22
5.11.	IFM image of buckling beam array for a repeated anneal. . . . .	5-23
5.12.	IFM optical flatness profiles for a 200 $\mu m$ -square oxidized Poly1 micromirror prior to post-processing anneals at 1100 $^{\circ}C$ . . . . .	5-24
5.13.	IFM optical flatness deflection profiles for three 200 $\mu m$ by 200 $\mu m$ oxidized micromirrors following post-processing 1100 $^{\circ}C$ anneals. Top-image - oxidized mirror without 1100 $^{\circ}C$ anneal, Middle-Image - 5-min anneal, and Bottom-Image - 30-min anneal. . . . .	5-26
5.14.	IFM micromirror images illustrating surface curvature for a 200 $\mu m$ x 200 $\mu m$ oxidized micromirror. (a) oxidized with no anneal, and (b) oxidized with a 15-min 1100 $^{\circ}C$ anneal. . . . .	5-27
5.15.	IFM optical flatness profile for a 200 $\mu m$ x 200 $\mu m$ oxidized micromirror following a 15-min post-processing 1100 $^{\circ}C$ anneal. . . . .	5-28

Figure	Page
6.1. <i>TSUPREM<sup>TM</sup></i> diffusion profiles of a Poly1, 20 $\mu m$ -wide beam cross-section following a 90-min phosphorous diffusion. Dopant concentration illustrations of (a) MUMPs <sup>®</sup> as grown, (b) two-hour 950 $^{\circ}C$ activation anneal, (c) one hour, 1100 $^{\circ}C$ post-oxidation anneal . . . . .	6-4
6.2. <i>TSUPREM<sup>TM</sup></i> diffusion profiles of a Poly2, 20 $\mu m$ -wide beam cross-section following a 90-min phosphorous diffusion. Dopant concentration illustrations of (a) MUMPs <sup>®</sup> as grown, (b) two-hour 950 $^{\circ}C$ activation anneal, (c) one hour, 1100 $^{\circ}C$ post-oxidation anneal . . . . .	6-5
6.3. Images of polysilicon microbridges: (a) side-view of a Poly1 microbridge, (b) SEM image of microbridges with various widths.	6-6
6.4. Illustration of the phosphorus diffusion process. . . . .	6-8
6.5. Raw Raman stress data and accompanying fourth order polynomial curve fits of the raw stress data. . . . .	6-12
6.6. Residual stress profiles for 100 $\mu m$ -long by 10 $\mu m$ -wide Poly1 microbridges fabricated in the MUMPs <sup>®</sup> process. Phosphorous diffusion times are: (a) 45 min diffusion, (b) 90 min diffusion, and (c) 135 min diffusion. . . . .	6-13
6.7. Residual stress profiles for 100 $\mu m$ -long by 20 $\mu m$ -wide Poly2 microbridges fabricated in the MUMPs <sup>®</sup> process. Phosphorous diffusion time frames are: (a) 45-min diffusion, (b) 90-min diffusion, and (c) 135-min diffusion. . . . .	6-15
6.8. Residual stress profiles for all Poly1 100 $\mu m$ -long microbridges with varying widths following the 45-min diffusion and 1100 $^{\circ}C$ anneal. . . . .	6-16
6.9. Residual stress profiles for a series of Poly2 100 $\mu m$ -long microbridges with varying widths following the 45-min diffusion and 1100 $^{\circ}C$ anneal. . . . .	6-17
6.10. TSUPREM beam cross-section simulation of the 200 keV phosphorous implant (1E16 <i>ions/cm<sup>2</sup></i> dose) with associated post implant anneal times at 1100 $^{\circ}C$ for a Poly1 10 $\mu m$ -wide beam.	6-20
6.11. TSUPREM beam cross-section simulation of the 200 keV phosphorous ion implant (1E16 <i>ions/cm<sup>2</sup></i> dose) with associated post implant anneal times at 1100 $^{\circ}C$ for a Poly2 10 $\mu m$ -wide beam.	6-21
6.12. Gaussian profile for a 5E16 <i>ions/cm<sup>2</sup></i> , 200 keV phosphorous implant. . . . .	6-22
6.13. Poly1 residual stress profiles measured using $\mu$ Raman spectroscopy for 100 $\mu m$ -long by 10 $\mu m$ -wide unreleased beams following the 100 keV phosphorous implants and a 15-min 1100 $^{\circ}C$ anneal.	6-26
6.14. Poly2 residual stress profiles measured using $\mu$ Raman spectroscopy for 100 $\mu m$ -long by 10 $\mu m$ -wide unreleased beams following the phosphorous implants for doses as listed and implant energy of 200 keV, followed by a 15-min 1100 $^{\circ}C$ anneal. . . . .	6-27

Figure		Page
6.15.	Poly1 residual stress profiles measured using $\mu$ Raman spectroscopy for 100 $\mu m$ -long by 10 $\mu m$ -wide unreleased beams following the phosphorous implants at the doses listed for both the 100 keV (lighter line) and 200 keV (darker line) implant power levels followed by a 15-min anneal at 1100 $^{\circ}C$ . . . . .	6-28
6.16.	$\mu$ Raman residual stress profiles illustrating stress changes in Poly1 and Poly2 material layers during the post-processing of a 200 keV, 1E16 $ions/cm^2$ phosphorous ion implant. The $\mu$ Raman stress profiles illustrate: (a) Poly1 material layers, and (b) Poly2 material layer. . . . .	6-29
6.17.	$\mu$ Raman residual stress profiles illustrating stress uniformity in Poly1 beams following a 200 keV, 1E16 $ions/cm^2$ phosphorous ion implant. The $\mu$ Raman stress profiles illustrate: (a) Poly1 foundry stress profiles, and (b) Post implant and 15-min 1100 $^{\circ}C$ anneal. . . . .	6-31
6.18.	IFM image of Poly1 comb resonators: (a) image of foundry fabricated comb resonator, and (b) image following a 200 keV, 3E16 $ions/cm^2$ phosphorous implant and 15-min 1100 $^{\circ}C$ anneal. . . . .	6-32
6.19.	IFM images of Poly1 (top) and Poly2 (bottom) buckled beam arrays for various 200 keV phosphorous implants with an accompanying 15-min 1100 $^{\circ}C$ anneal. The arrays presented illustrate: (a) foundry fabricated arrays, (b) 5E15 $ions/cm^2$ implant (c) 1E16 $ions/cm^2$ implant, (d) 3E16 $ions/cm^2$ implant, (e) 5E16 $ions/cm^2$ implant, and (f) 1E17 $ions/cm^2$ implant. . . . .	6-34
6.20.	IFM images of buckled beam arrays representing changes in the residual stress for 200 keV phosphorous ion implants at doses of 5E15 $ions/cm^2$ and 1E16 $ions/cm^2$ and after a subsequent 5-min 1100 $^{\circ}C$ anneal. (a) 5E15 $ions/cm^2$ implant and oxidation (b) 5E15 $ions/cm^2$ implant, oxidation, and 5-min anneal (c) 1E16 $ions/cm^2$ implant and oxidation, and (d) 1E16 $ions/cm^2$ implant, oxidation, and 5-min anneal. . . . .	6-38
6.21.	IFM image illustrating optical flatness for a 150 $\mu m$ -square oxidized micromirror with various implant doses and 5-min 1100 $^{\circ}C$ anneal. . . . .	6-40
6.22.	IFM image of 200 keV, 1E16 $ions/cm^2$ phosphorous implant Poly1-Poly2 stacked micromirrors: Figure (a) implanted and oxidized, and (b) implant, oxidized and 15-min 1100 $^{\circ}C$ anneal. . . . .	6-41
7.1.	Unreleased and released $\mu$ Raman stress profiles for a 10 $\mu m$ -wide by 100 $\mu m$ -long Poly1 fixed-fixed beam. . . . .	7-2
7.2.	Comparison image of Poly1 $\mu$ Raman stress data to buckling beam stress data . . . . .	7-5
7.3.	Comparison image of Poly2 $\mu$ Raman stress data to buckling beam stress data . . . . .	7-6

Figure		Page
7.4.	Comparison image of Poly2 $\mu$ Raman stress to buckling beam stress data for the 1100 $^{\circ}C$ anneals and implants of 5E15 and 1E16 <i>ions/cm<sup>2</sup></i> . . . . .	7-7
7.5.	Buckling beam length prediction model for MUMPs <sup>®</sup> Poly1 (frequency shifts varies from 519 and 521 $cm^{-1}$ ). . . . .	7-9
7.6.	Modified buckling beam length prediction model for MUMPs <sup>®</sup> Poly1 (frequency shifts varies from 520.7 and 521 $cm^{-1}$ ). . .	7-10
8.1.	Residual film on the GaAs structural layer following the RIE etch . . . . .	8-5
8.2.	$\mu$ Raman spectrums for a (100) GaAs substrate. a) electronic grade GaAs wafer, b) UNM-1186 substrate . . . . .	8-7
8.3.	IFM image of a GaAs buckled beam array . . . . .	8-8
8.4.	IFM image of an oxidized GaAs micromirror anchor, and (b) Illustrates the oxidation characteristics of the bonding pad. . .	8-10
8.5.	IFM 3D image of the oxidized GaAs micromirror anchor. . .	8-11
8.6.	IFM images of bonding and micromirror cracks due to oxidation. a) 150 $\mu m$ -square anchor pad, b) 200 $\mu m$ by 150 $\mu m$ bonding pad . . . . .	8-12
8.7.	$\mu$ Raman residual stress images of GaAs 400 $\mu m$ -long by 16 $\mu m$ -wide fixed-fixed beam. . . . .	8-13
8.8.	IFM 3D image of the surface of an oxidized GaAs micromirror	8-15
C.1.	TSUPREM 3-D phosphorus doping profile for a 10 $\mu m$ -wide Poly2 linestructure. . . . .	C-9

# *List of Tables*

Table		Page
2.1.	MUMPs® Fabrication Process as Modelled in <i>TSUPREM</i> <sup>TM</sup> [4, 8] . . . . .	2-15
3.1.	Absorption coefficient ( $\alpha$ ) and penetration depth ( $d_p$ ) in crystalline silicon for various laser wavelengths ( $\lambda$ ) [25] . . . . .	3-19
3.2.	Material and Physical Parameters used in the Thermal Equations . . . . .	3-28
3.3.	Measured Raman Laser Power Levels for both Raman Systems.	3-32
4.1.	As Fabricated Compressive Residual Stress Comparisons. . .	4-34
5.1.	Oxidized buckled beam arrays residual stress values calculated from Figure 5.6 . . . . .	5-14
5.2.	Oxidized Poly1 cantilever residual stress values. . . . .	5-18
5.3.	Unoxidized buckling beam residual stress values from Figure 5.9	5-20
5.4.	Unoxidized Poly1 and Poly2 cantilever residual stress values.	5-20
6.1.	MUMPs® Post-Processing Phosphorus Diffusion as Modelled in <i>TSUPREM</i> <sup>TM</sup> . . . . .	6-3
6.2.	Resistivity values for 20 $\mu m$ wide Poly1 and Poly2 microbridges before the diffusion and again following both anneals (2-hours at 900 °C and 1-hour at 1100 °C) . . . . .	6-10
6.3.	MUMPs® Post-Processing Phosphorus Implant as Modelled in <i>TSUPREM</i> <sup>TM</sup> . . . . .	6-19
6.4.	Phosphorus Implant Parameters . . . . .	6-23
6.5.	Experimental phosphorous implant matrix. . . . .	6-24
6.6.	Measured resistivity values for 100 $\mu m$ -long by 10 $\mu m$ -wide Poly1 and Poly2 microbridges following a 200 keV phosphorous ion implant and a 15-min anneal at 1100°C. . . . .	6-25
6.7.	Buckled beam lengths and corresponding residual stress values from Figure 6.19 for a 15-min 1100 °C anneal. . . . .	6-35
6.8.	Poly1 and Poly2 150 $\mu m$ -long by 10 $\mu m$ -wide cantilever residual stress values for phosphorous ion implant doses of 5E15 and 1E16 <i>ions/cm</i> <sup>2</sup> . . . . .	6-39

## *Abstract*

Due to the unique structure and small scale of Micro-Electro-Mechanical Systems (MEMS), the inherent residual stresses during the deposition processes can have a profound affect on the functionality and reliability of the fabricated MEMS devices. Residual stress often causes device failure due to curling, buckling, or fracture. Typically, the material properties of thin films used in surface micromachining are not controlled during deposition. The residual stress, for example, tends to vary significantly for different deposition methods. Currently, few techniques are available to measure the residual stress in MEMS devices. In this dissertation research, I use  $\mu$ Raman spectroscopy to measure the residual and induced stresses in MUMPs<sup>®</sup> polysilicon and GaAs MEMS devices.  $\mu$ Raman spectroscopy was selected since it is nondestructive, fast, and provides the potential for *in situ* stress monitoring. I performed Raman spectroscopy line and mapping scans to obtain Raman residual stress profiles on unreleased and released MEMS fixed-fixed beams, cantilevers, and micromirror flexures. These profiles were compared to analytical models to assess the accuracy of the Raman stress profiles. Finite element residual and induced stress profiles are obtained from MEMCAD modeling software and used to assess the viability of  $\mu$ Raman spectroscopy as an *in situ* stress measurement technique. I performed several post-processing techniques to include thermal annealing, phosphorous diffusion, and phosphorous ion implantation to investigate methods to alter or control the residual stress within MEMS devices.  $\mu$ Raman spectroscopy is used to characterize and monitor the residual stress levels in the unreleased MEMS structures following each post-processing experiment to determine the magnitude of stress relaxation. Significant residual stress relaxation is observed in the Raman stress profiles and verified with on-chip test structures following the thermal anneals and doping. The MUMPs<sup>®</sup> foundry fabricated residual stress levels can be significantly reduced by

over 90% to stress levels less than 1 MPa following post-processing. The reduced residual stress levels can significantly improve device performance, reliability, and yield as MEMS devices become smaller. In addition to the polysilicon stress profiles, the first  $\mu$ Raman stress measurements in III-V MEMS is presented.

# Characterization of Residual Stress in Microelectromechanical Systems (MEMS) Devices using Raman Spectroscopy

## *I. Introduction*

### *1.1 Introduction*

Microelectromechanical systems (MEMS) systems are becoming an integral part of our everyday lives. MEMS are used in many applications from air bag triggers in automotive applications to adaptive optics for communications. MEMS are receiving significant interest in the Air Force for many different applications ranging from accelerometers used in inertial navigation systems for munitions and unmanned areal vehicles (UAV) to radio frequency (RF) microswitches for communications. MEMS are fabricated through either a surface or bulk micromachining process or a combination thereof. A MEMS fabrication process typically consists of a series of steps to include: material depositions, etches, and photolithography. Polysilicon is the most common material used for MEMS; however, other materials such as silicon carbide (SiC), gallium arsenide (GaAs), and amorphous silicon are becoming more popular since these materials have better optical and thermal capabilities. Since MEMS devices are built on the micrometer scale, residual stresses can play a major role in the successful use and reliability of the devices. In many MEMS devices with free standing structures, residual stress can physically warp the device to a degree that the free standing structure either curls upward or touches the substrate and is no longer useful. In micromirror arrays, residual stress gradients can destroy the flatness of the mirror surfaces making them unusable. However, if the residual stresses can be mapped, and eventually controlled during the manufacturing processes, the MEMS designer will no longer be forced to limit his/her design to account for the intrinsic manufacturing stresses.

Several different methods have been used to characterize stress in thin films of silicon to include the measurement of wafer curvature [6], membrane load deflection [12], and interferometric measurements of deflection and curvature [2]. X-ray diffraction techniques can also measure stress but are cumbersome and lack a high spatial resolution [2]. Micro-Raman ( $\mu$ Raman) spectroscopy is increasingly being used to measure stress in electronic silicon devices. This technique is nondestructive and accurate for most required stress measurements. Since it is an optical technique,  $\mu$ Raman spectroscopy shows promise as a minimally invasive *in situ* measurement technique that is useful for the manufacture of MEMS devices. It is also a useful tool for basic studies of stress of micrometer-scale crystalline or polycrystalline structures made from silicon or other semiconducting materials.

The dissertation problem statement and approach are detailed in Section 1.2. In Section 1.3, I provide a brief background and identify some causes of stress in MEMS. Stress characterization and an overview of  $\mu$ Raman spectroscopy are presented in Section 1.4. In Section 1.5, I summarize my research accomplishments and Section 1.6 provides the organization of this dissertation.

## 1.2 Problem Statement and Approach

The Committee on Advanced Materials and Fabrication Methods for Microelectromechanical Systems (MEMS) met in 1997 and reviewed all major advances and shortfalls in the area of MEMS research. Two of the shortfalls included the following: (1) The Integrated Circuit (IC) industry has an extensive body of knowledge concerning the behavior of silicon and related materials as they are scaled down in size. There is no comparable resource established for MEMS. (2) The electrical properties of polysilicon thin films are well known; however, not much is known about the micromechanical properties or the surface mechanics related to friction, wear, and stress-related failure [3]. The committee concluded that a thorough understanding of the micromechanical properties of the materials used in MEMS is not available

but should be vigorously investigated. The following quote from the committee's recommendation illustrates this concern [3]:

*"The characterization and testing of MEMS materials should be an area of major emphasis. Studies that address fundamental mechanical properties (e.g., Young's modulus, fatigue strength, residual stress, internal friction) and the engineering physics of long-term reliability, friction, and wear are vitally needed. It is important that these studies take into account fabrication processes, scaling, temperature, operational environment (i.e., vacuum, gaseous, or liquid), and size dependencies."*

In this dissertation, I investigate some of the deficiencies that currently exist in the design and fabrication of MEMS devices. These deficiencies include the measurement of Young's modulus and residual stress for polysilicon structural layers. The primary emphasis is the determination and verification of the residual stress that is inherently present during MEMS fabrication. The approach I pursue is to use available surface micromachining foundry processes for low cost fabrication of prototype MEMS test structures. I design and investigate these MEMS structures to assess and measure residual stress changes before, during, and after the application of post-processing techniques.  $\mu$ Raman spectroscopy is selected as the experimental technique to obtain the residual stress profiles from various MEMS structures (fixed-fixed beams, cantilevers, and micromirror flexures).

### 1.3 MEMS Background

Polysilicon films deposited by low pressure chemical vapor deposition (LPCVD) are the most widely used structural material in MEMS. Mechanical microstructures such as cantilevers, bridges, suspended structures, rotors, etc. are the basic sensing and actuating elements for MEMS. These elements can easily be fabricated using doped polysilicon as a structural material and silicon dioxide as a sacrificial material. The mechanical properties of the structural layers, in particular the stress and stress gradients, are very important for device performance. Residual stress often causes device failure due to curling, buckling, or fracture. Residual stress and stress

gradients are inherent in as-deposited, undoped polysilicon films for all deposition temperatures [7]. Stresses in films can result from mismatched lattice constants, thermal expansion coefficients between different materials, and the growth process [5]. The deposition and subsequent annealing parameters need to be tailored to achieve films with controllable residual stress and stress gradients. Post-deposition rapid thermal annealing (RTA) is a well known technique which can be used for obtaining nearly stress-free films [8]. Figure 1.1 illustrates the effects of residual stress on cantilever beams. Figure 1.2 shows the effects of residual stress on the optical surface of micromirrors. As seen in Figure 1.1 and 1.2, the inherent residual stress can have a profound effect on the functionality and reliability of thin films used for MEMS devices.

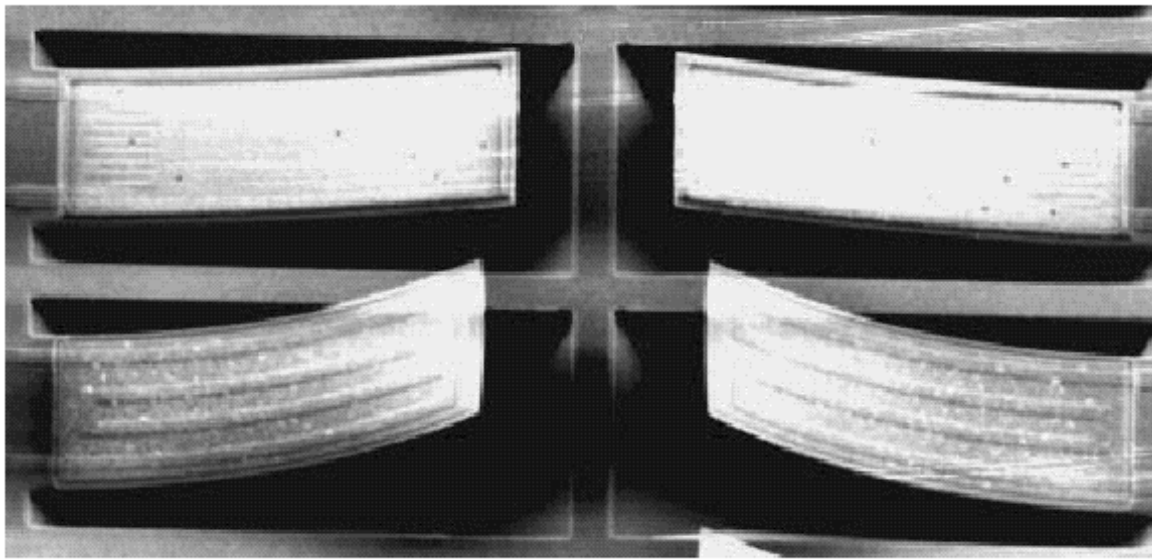


Figure 1.1: Polysilicon cantilevers curl due to residual stress.

#### *1.4 Stress Characterization and Measurement Techniques*

For the proper design and operation of MEMS devices, accurate control or estimation of the material properties of polysilicon deposited by LPCVD is critical. Current MEMS designers have little to no control of the fabrication processes. They must design MEMS devices to account for variations in the material characteristics

and fabrication tolerances. A nondestructive *in situ* measurement technique would enable precise control of the MEMS fabrication processes.

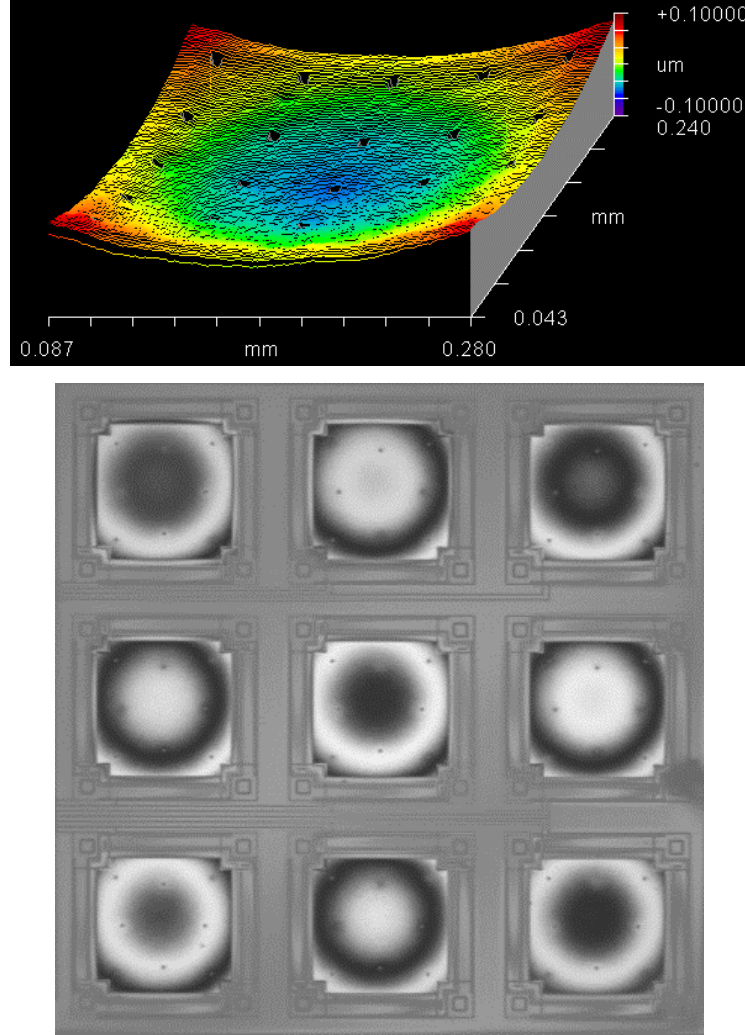


Figure 1.2: Residual stress effects on polysilicon micromirrors. Top image illustrates the curvature of a single micromirror surface. The bottom image is an interferometric microscope (IFM) image of an array of micromirrors illustrating the nonuniform curvature of the micromirror surfaces as illustrated by the fringe lines on the mirror surfaces.

During and after the processing of semiconductor devices, mechanical stresses develop in the different thin films and in the substrate. The problems associated with residual stresses become more acute with the increasing complexity and miniaturization of the devices. For this reason, a study of stress is very important. There

are a number of techniques that can be used to measure stress in thin films. However, they all have problems when applied to materials encountered in microelectronics. Either the resolution is limited, they are destructive, or the indirect measurement technique requires complex modeling of measured data. A measurement technique which has proven to be very valuable for the determination of local stress in thin film materials is  $\mu$ Raman spectroscopy [4, 11].

In  $\mu$ Raman spectroscopy, laser light is focused on the sample through a microscope. A laser beam irradiates the sample and the scattered light, which carries the Raman signals, is collected and directed into a spectrometer. The spectrometer measures the intensity of the Raman signal as a function of frequency. When the sample is unstressed, the spectrometer measures a reference spectrum. When the sample is placed in a stressed state, the Raman spectrum displays a shift in the frequency with respect to the reference spectrum. This frequency shift is a result of the residual or induced stress. Figure 1.3 shows a block diagram of a typical  $\mu$ Raman spectroscopy system and a picture of the Raman spectroscopy system at Wright State University.

Some factors which can influence the Raman peak frequency include instability of the laser and spectrometer, focusing changes of the laser on the sample [11], and heating of the sample by the focused laser beam. The frequency of the Raman peak is both stress and temperature sensitive. Until a few years ago, this technique was mostly applied in chemical studies as a complementary technique to infrared spectroscopy, giving information on the chemical composition and crystallinity of the sample [9]. However, since the first reports of Anastassakis [2] on the sensitivity of the Raman peak for mechanical stress, the technique has been increasingly used to study local mechanical stress in devices and structures used in microelectronics [10]. This technique has the advantage of being fast and nondestructive with micrometer spatial resolution [10]. In general, a Raman frequency higher than the stress-free frequency indicates compressive stress in the sample, while a Raman frequency lower

than the stress-free frequency indicates tensile stress. This is not always true, as nonzero stress tensor components influence the position of the Raman peak.

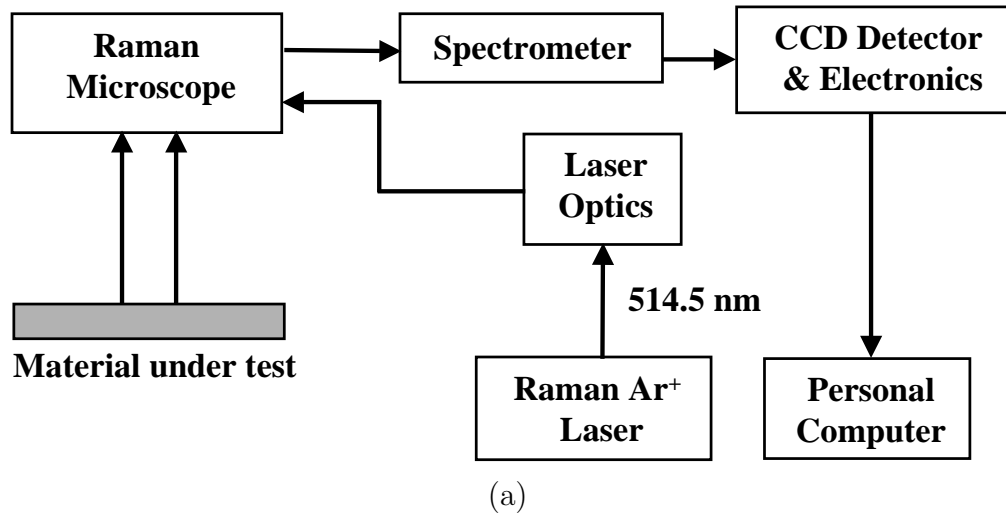


Figure 1.3: Figure a) Block diagram of a  $\mu$ Raman spectroscopy system, (b) the Raman spectroscopy system at Wright State University

In order to relate the measured Raman shift to the stress present in the sample, some prior knowledge of the stress distribution in the sample is necessary. When uniaxial, hydrostatic, or uniform biaxial stress is present in the system, calculations of the Raman shift as a function of this stress is a linear relation between the observed Raman shift and the stress. The penetration depth of the laser beam in the material, the spot size, and the relative intensity of the different Raman modes must be taken into account in order to correctly interpret the data [10]. Several analytical models to include a fixed-fixed beam thermal model and a fixed-fixed beam stress model are required to properly assess the stress profiles from Raman spectroscopy.

In this dissertation, I will focus on the assessment of the residual stress as measured by  $\mu$ Raman spectroscopy. I will evaluate the residual stress variations following post-processing techniques to include thermal anneals, phosphorous diffusion, and phosphorous implants. I will then compare the Raman stress values to analytical stress calculations as determined from on-chip buckling beam arrays and cantilever deflections. I was unable to perform Raman experimental tests using a different laser wavelength. The primary implication from this, is that all  $\mu$ Raman stress profiles will be obtained from a particular material depth determined by the laser wavelength. Currently both Raman systems employ a 514.5 nm argon laser which provides a Raman stress profile at a depth of approximately 700 nm in silicon and 50 nm in GaAs. The Raman system at WSU employs a second laser at a wavelength of 632 nm. Since the MEMS structures I am using are at most 3.5  $\mu m$ -thick, the 632 nm laser will penetrate completely through the MEMS structures, thus no usable stress data can be obtained.

### *1.5 Research Accomplishments*

The residual stress and stress gradients make it extremely difficult to accurately design a MEMS device and know that it will operate correctly. In this dissertation, I demonstrate a technique which can be used to measure the residual stress levels

in unreleased or released MEMS structures. For unwanted high residual stress levels in unreleased MEMS structures, I show that post-processing high temperature anneals or phosphorous doping can be used to enhance residual stress relaxation.  $\mu$ Raman spectroscopy is an essential technique used in this research to measure the level of inherent residual stress during foundry fabrication. I use this technique to measure Raman residual stress profiles during post-process annealing and/or doping experiments to illustrate control of the amount of stress relaxation.

In this dissertation, I also investigate the possibility of using  $\mu$ Raman spectroscopy as a technique for *in situ* residual stress monitoring during MEMS fabrication. The Raman characterization consisted of analytical and experimental tests involving laser and spectrometer stability, laser focusing, proper laser power level determination, and thermal characterization of the MEMS test structures. Following these characterization tests, I performed Raman line and mapping scans to obtain Raman residual stress profiles on unreleased and released MEMS fixed-fixed beams, cantilevers, and micromirror flexures. These profiles were compared to analytical models to assess the realization of the Raman profiles. Excellent correlation exists between the Raman and analytical stress profiles. In addition, several MEMS devices are modelled using the commercial MEMCAD [1] software to obtain finite element residual and induced stress profiles. These finite element model (FEM) stress curves are also used to assess the viability of  $\mu$ Raman spectroscopy as an *in situ* stress measurement technique.

In this research, several material parameters were determined, to include: Young's modulus for both available polysilicon (Poly1 and Poly2) structural layers, the localized residual stress values for both layers, and the phonon deformation potentials for both structural layers of the Multi-User MEMS Process (MUMPs®) foundry process. These parameters support my assessment and understanding of the residual stress profiles obtained via  $\mu$ Raman spectroscopy for the selected MEMS structures.

I performed several post-processing techniques to investigate methods to alter or control residual stress within MEMS devices. These post-processing techniques include thermal annealing, phosphorous diffusion, and phosphorous ion implants. I used  $\mu$ Raman spectroscopy to characterize and monitor the residual stress levels in the unreleased MEMS structures following each post-processing experiment to determine the magnitude of stress relaxation. I then released the MEMS die by selectively etching away the silicon dioxide layers. I then analytically calculated the remaining residual stress levels in the MEMS structures by using basic material data obtained from measurements on comb resonators and buckled beam arrays. I developed a model to predict the stress of thin film polysilicon layers. Through the experimental results and analytical calculations, I show that Raman spectroscopy is a viable method to estimate and monitor residual stress in MEMS. The potential control or engineering of the residual stress in MEMS structures can be made available through the combination of Raman spectroscopy to measure the residual stress levels and by performing one or more post-processing techniques.

From the results of my research, MEMS designers now have a new tool wherein they can design MEMS structures having an internal layer stress rather than designing the MEMS devices to compensate for stresses inherent in the fabrication process. This added control should increase device yield, reliability and functionality. But more importantly, the stress monitoring and control is essential as nano-MEMS structures become increasingly prevalent.

## 1.6 *Dissertation Organization*

The remainder of this dissertation is divided into 8 chapters. In Chapter II, I provide an overview of the MEMS foundry fabrication processes used to procure MEMS test devices for this research. Also, the modelling programs used to determine stress and dopant concentrations are described. In Chapter III, I discuss the experimental  $\mu$ Raman spectroscopy systems that I used for characterization techniques.

The causes of residual stress and stress gradients in thin film materials is presented in Chapter IV. Also in Chapter IV, I present foundry fabricated residual stress profiles obtained from my  $\mu$ Raman spectroscopy measurements. In Chapter V and VI, I present the results of the post-processing experiments to include anneals (Chapter V) and anneal/doping (Chapter VI) studies. In Chapter VIII, an introductory assessment of stress in III-V crystalline MEMS is presented. These are the first ever  $\mu$ Raman measurements of MEMS fixed-fixed beams fabricated in GaAs. Finally, I present my conclusions and recommendations for future research in Chapter IX.

## Bibliography

1. MEMCAD, May 1999. Microcosm Technologies Inc. Cambridge, MA 02142.
2. E. Anastassakis, A. Pinczuk, E. Burstein, F. H. Pollak, and M. Cardona. Effect of static uniaxial stress on the Raman spectrum of silicon. *Solid State Communications*, 8(2):133–138, 1970.
3. National Materials Advisory Board. Committee on Advanced Materials and Fabrication Methods for Microelectromechanical Systems, National Academy Press, Washington DC, 1997.
4. K. F. Dombrowski, I. De Wolf, and B. Dietrich. Stress measurements using ultraviolet micro-Raman spectroscopy. *Applied Physics Letters*, 75(16):2450–2451, October 1999.
5. G. Kaltsas, A. G. Nassiopoulou, M. Siakavellas, and E. Anastassakis. Stress effect on suspended polycrystalline silicon membranes fabricated by micromachining of porous silicon. *Sensors and Actuators A*, 68:429–434, 1998.
6. D. A. Koester, R. Mahadevan, B. Hardy, and K. W. Markus. MUMPs<sup>TM</sup> design handbook rev. 6, 2001. Cronos Integrated Microsystems, a JDS Uniphase Company, 3026 Cornwallis Rd., Research Triangle Park, NC 27709.
7. M. Siakavellas, E. Anastassakis, G. Kaltsas, and A. G. Nassiopoulos. Micro-Raman characterization of stress distribution within free standing mono- and poly-crystalline silicon membranes. *Microelectronic Engineering*, 41/42:469–472, 1998.
8. J. Singh, S. Chandra, and A. Chand. Strain studies in LPCVD polysilicon for surface micromachined devices. *Sensors and Actuators A*, 77:133–138, 1999.
9. I. De Wolf. Micro-Raman spectroscopy to study local mechanical stress in silicon integrated circuits. *Semiconductor Science Technology*, 11:139–154, 1996.
10. I. De Wolf and H. E. Maes. Stress measurements in silicon devices through Raman spectroscopy: Bridging the gap between theory and experiment. *Journal of Applied Physics*, 79(9):7148–7156, May 1996.
11. I. De Wolf and H. E. Maes. Mechanical stress measurements using micro-Raman spectroscopy. *Microsystem Technologies*, 5:13–17, 1998.
12. Q. Zou, Z. Li, and L. Liu. New methods for measuring mechanical properties of thin films in micromachining: beam pull-in (VPI) method and long beam deflection (LBD) method. *Sensors and Actuators A*, 48:137–143, 1995.

## II. MEMS Modelling and Foundry Fabrication Processes

### 2.1 Chapter Overview

In this research, I used MEMS die from two different polysilicon foundry fabrication processes. The foundry fabrication processes used are: 1) the Multi-User MEMS Process (MUMPs®) and 2) the Sandia Ultra-planar Multi-level MEMS Technology (*SUMMIT<sup>TM</sup>*) process. The MUMPs® foundry was selected to supply the silicon MEMS used in this research since this foundry provides a fast and predictable turn-around time and the cost is lower ( $\approx$  \$3k vs. \$10k) than MEMS made at the *SUMMIT<sup>TM</sup>* foundry. Therefore, most of the devices presented and investigated throughout this dissertation are MEMS structures fabricated in the MUMPs® process.

I use two separate modelling and simulation software packages called Coventorware (MEMCAD) and *TSUPREM<sup>TM</sup>*. These packages are used to model MEMS structures fabricated in the MUMPs® process to provide insight into both foundry fabrication characteristics and the post-processing techniques used for residual stress relaxation assessment. *TSUPREM<sup>TM</sup>* is a microelectronics fabrication simulation tool developed at Stanford University [1] and MEMCAD, developed by Microcosm, Inc. is a finite element method (FEM) modelling tool used to simulate MEMS structures [2].

In this chapter, I briefly address both the MUMPs® and *SUMMIT<sup>TM</sup>* foundry fabrication processes. In addition, both modelling and simulation packages are used to model several different MEMS devices. I use *TSUPREM<sup>TM</sup>* simulations to show peak dopant concentration locations within the MUMPs® structural layers. MEMCAD FEM models provide images illustrating residual and peak stress levels in MEMS devices.

## 2.2 Multi-User MEMS Process (MUMPs®)

The MUMPs® process was developed by the Microelectronics Center of North Carolina (MCNC), under a DARPA funded program. MUMPs® is a typical polysilicon surface micromachining process [3]. The process includes a nitride layer, a polysilicon ground (plane) layer, two structural polysilicon layers, two sacrificial phosphosilicate glass (PSG) oxide layers, and one metal layer used for electrical connections. Figure 2.1 is a cross sectional view showing the seven layers of the MUMPs® process.

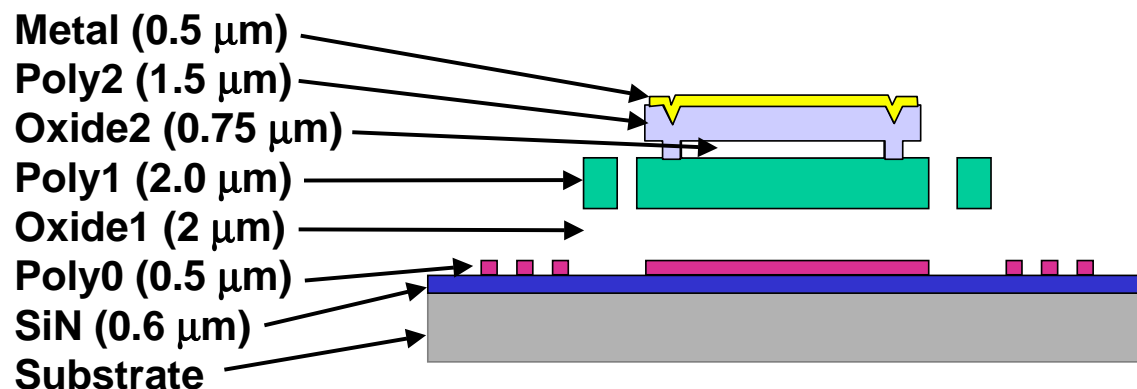


Figure 2.1: Illustration of available layers in the MUMPs® Process

**2.2.1 MUMPs® Fabrication Process.** The starting substrate for MUMPs® is a low resistivity ( $1\text{-}2\ \Omega\text{-cm}$ ) n-doped silicon wafer with a 100 crystal surface orientation [8]. Before any layers are deposited, the wafer surface is heavily doped with phosphorus (using  $\text{POCl}_3$ ) in a standard diffusion furnace. The highly doped surface helps reduce and prevent charge buildup during the operation of electrostatic devices. Phosphorus is an n-type dopant so no junction is formed but the heavy doping ( $\approx 10^{20}\text{ atoms/cm}^3$ ) is sufficient to have an effect on some silicon etchants [5].

The first surface layer deposited is a 600 nm-thick silicon nitride layer by low pressure chemical vapor deposition (LPCVD). The silicon nitride layer serves as an electrical isolation layer. Following the nitride deposition, a 0.5  $\mu\text{m}$ -thick LPCVD

polysilicon layer (Poly0) is deposited and patterned using standard photolithography techniques and reactive ion etching (RIE). The Poly0 layer is an unreleasable layer and is primarily used for wiring. Over the patterned Poly0 layer, a 2.0  $\mu m$ -thick PSG sacrificial layer (Oxide1) is deposited by LPCVD and annealed at 1050°C for 1-hour in argon. Two different photolithographic steps are applied to the Oxide1 layer. First, a DIMPLE mask is used to define and etch 0.75  $\mu m$  deep holes in the oxide. These holes are later filled during the Poly1 deposition and create dimples which serve to hold fully released polysilicon structures off the substrate. The dimples help reduce the surface contact area between the Poly1 and surface layers to help mitigate “stiction” effects. Dimples also provide a stop mechanism for fully deflected electrostatic devices to allow the devices to return to their rest position after the applied voltage is removed. The second photolithographic step provides anchor holes (ANCHOR1) entirely through the Oxide1 layer for attaching Poly1 structures to either the nitride or the Poly0 layers.

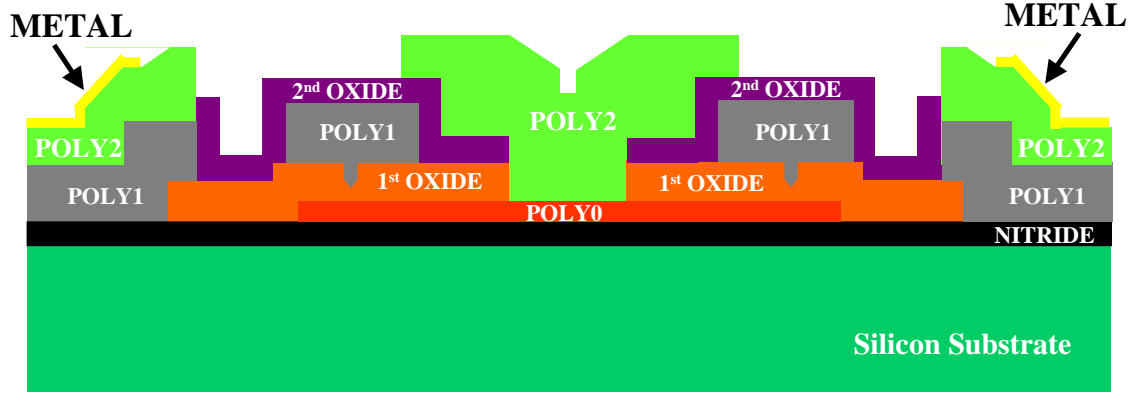
Following the ANCHOR1 patterning and RIE etching, the first structural layer is deposited by LPCVD. The entire wafer surface is blanketed with a 2.0  $\mu m$  thick polysilicon layer (Poly1). A 200 nm-thick layer of PSG is then deposited over the Poly1 layer and the wafer is annealed at 1050C for 1-hour. The anneal dopes the polysilicon (via diffusion) with phosphorus from the PSG layers surrounding the Poly1 structural layer. The anneal also reduces the intrinsic stress in the Poly1 layer. The Poly1 layer is then photolithographically patterned and selected Poly1 material is removed by RIE. After the patterning of Poly1, the wafer is blanketed with a 0.75  $\mu m$ -thick PSG sacrificial oxide layer (Oxide2) and annealed. Two separate photolithographic steps and etches are used to define holes in the Oxide2 layer. The Poly1-Poly2-Via (P1P2Via) etch provides etch holes between the two structural layers (Poly1 and Poly2). This provides a mechanical and electrical connection between the Poly1 and Poly2 layers. The anchoring of Poly2 structures to the nitride or Poly0 layers is accomplished using the ANCHOR2 etch. The ANCHOR2 etches

both Oxide1 and Oxide2 simultaneously; thus eliminating any misalignment between etched holes.

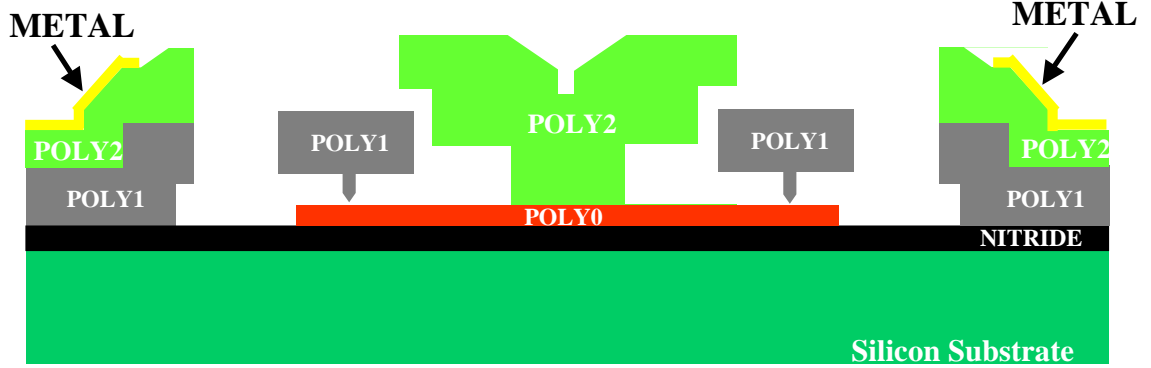
A second polysilicon structural layer (Poly2)  $1.5\ \mu\text{m}$ -thick is deposited and patterned in the same manner as the Poly1 layer. A 200 nm-thick layer of PSG is deposited over the Poly2 layer and the wafer is again annealed for one hour at  $1050\ ^\circ\text{C}$ . The high temperature ( $1050\ ^\circ\text{C}$ ) anneals are used to relieve stress and drive the phosphorus from the oxide layers into the polysilicon structural layers which also increases the conductivity of the polysilicon layers. The thin 200 nm-thick PSG layer is removed and a  $0.5\ \mu\text{m}$ -thick gold metallization layer with an  $\approx 100$  nm-thick chrome adhesion layer is deposited [8]. The metal layer provides for probing, bonding, and electrical routing. The metal is deposited and patterned using lift-off. Metal can be reliably deposited only on top of the Poly2 layer [3].

As discussed, the MUMPs<sup>®</sup> fabrication process is very similar to standard integrated circuit (IC) fabrication with the notable exceptions of layer thicknesses and the associated high temperature anneals. After fabrication, a release etch is used to remove the sacrificial oxide layers (Oxide1 and Oxide2) freeing the structural polysilicon layers (Poly1 and Poly2). The MUMPs<sup>®</sup> devices are generally shipped before the release etch and are covered with a protective layer of photoresist. The typical release etch is performed by immersing the die in a bath of room temperature 49% hydrofluoric acid (HF) for 2-3 minutes. This is followed by two rinses in methanol to remove the HF and reduce stiction followed by a rapid dry. See Appendix A for the complete MEMS release procedure with and without the use of a supercritical  $\text{CO}_2$  dryer. Figure 2.2 illustrates both an example pre and post-released MEMS device.

*2.2.2 MUMPs<sup>®</sup> Buffered Oxide Etch.* Midway through my research period, the MUMPs<sup>®</sup> foundry fabrication process was changed slightly following the metallization step. In an attempt to reduce “stringers” (small metal threads resulting from slight misalignment of lithographic masks, occasionally shorting neighboring



(a)



(b)

Figure 2.2: MUMPs® pre and post release images of a MEMS micromotor structure. (a) unreleased and (b) released.

contact pads), the foundry added a buffered oxide etch following metallization. The buffered oxide etch (BOE) consists of a 10:1 volume ratio of deionized water (DIW) and HF buffered with ammonia [7]. This wet etch undercuts the Poly2 structural layer by approximately 5,000-6,000 Å and the Poly1 structures by approximately 2,000-3,000 Å [8]. Figure 2.3 illustrates the effects on the Poly1 structural layer as a result of the buffered oxide etch. As illustrated in Figure 2.3, prior to etching with BOE, Poly1 structures were completely covered by the Oxide2 sacrificial layer. If not covered by metal, both the Poly1 and Poly2 structural layers are exposed following removal of the protective photoresist layer used for shipping. The exposed Poly1 is more susceptible to damage during any post-processing experiments. Additionally,

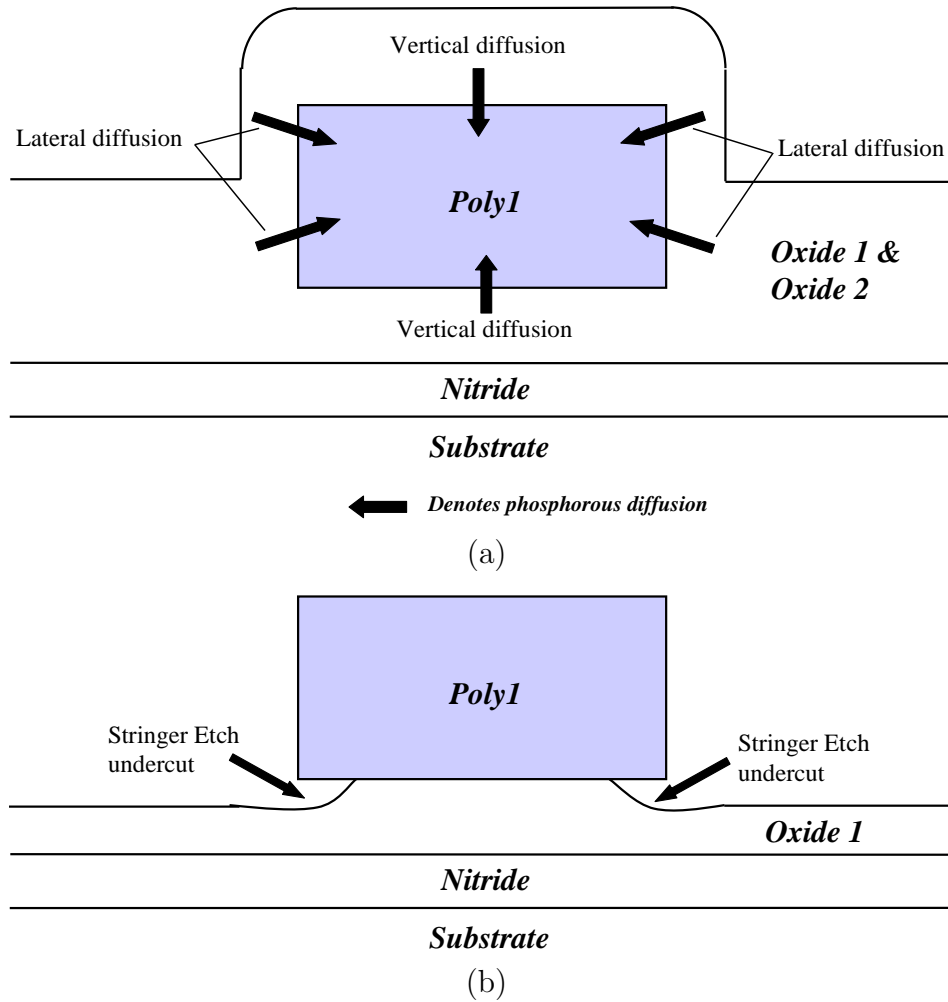


Figure 2.3: Schematic side-view of a Poly1 beam before and after the buffered oxide etch. (a) before the etch, and (b) after the etch

narrow and thus fragile polysilicon structures ( $< 2.0 \mu m$ -wide Poly2 and  $< 4.0 \mu m$ -wide Poly1-Poly2 stacked) may inadvertently be damaged before the post-processing can be performed. Following the BOE step, the die are covered with a protective photoresist layer and shipped to the customer. The foundry began performing the buffered oxide etch step with MUMPs<sup>®</sup> run #41 (14 Jan 01).

As can be observed in Figure 2.4, the buffered oxide etch essentially releases, removes, or severely damages Poly2 structures less than  $2 \mu m$ -wide (or  $< 4.0 \mu m$ -wide for Poly1-Poly2 stacked structures). Due to this added etch, the MUMPs<sup>®</sup>

design rules outlined in the MUMPs® handbook [3] need to be adhered to for small width structures using Poly2 or Poly1-Poly2 stacked structural layers. The minimum feature widths for Poly2 and Poly1-Poly2 stacked outlined in the MUMPs® design handbook are  $2\ \mu\text{m}$ -wide and  $4.0\ \mu\text{m}$ -wide respectively [8]. Poly1 structures of  $1\ \mu\text{m}$ -wide are possible but are usually damaged if released.

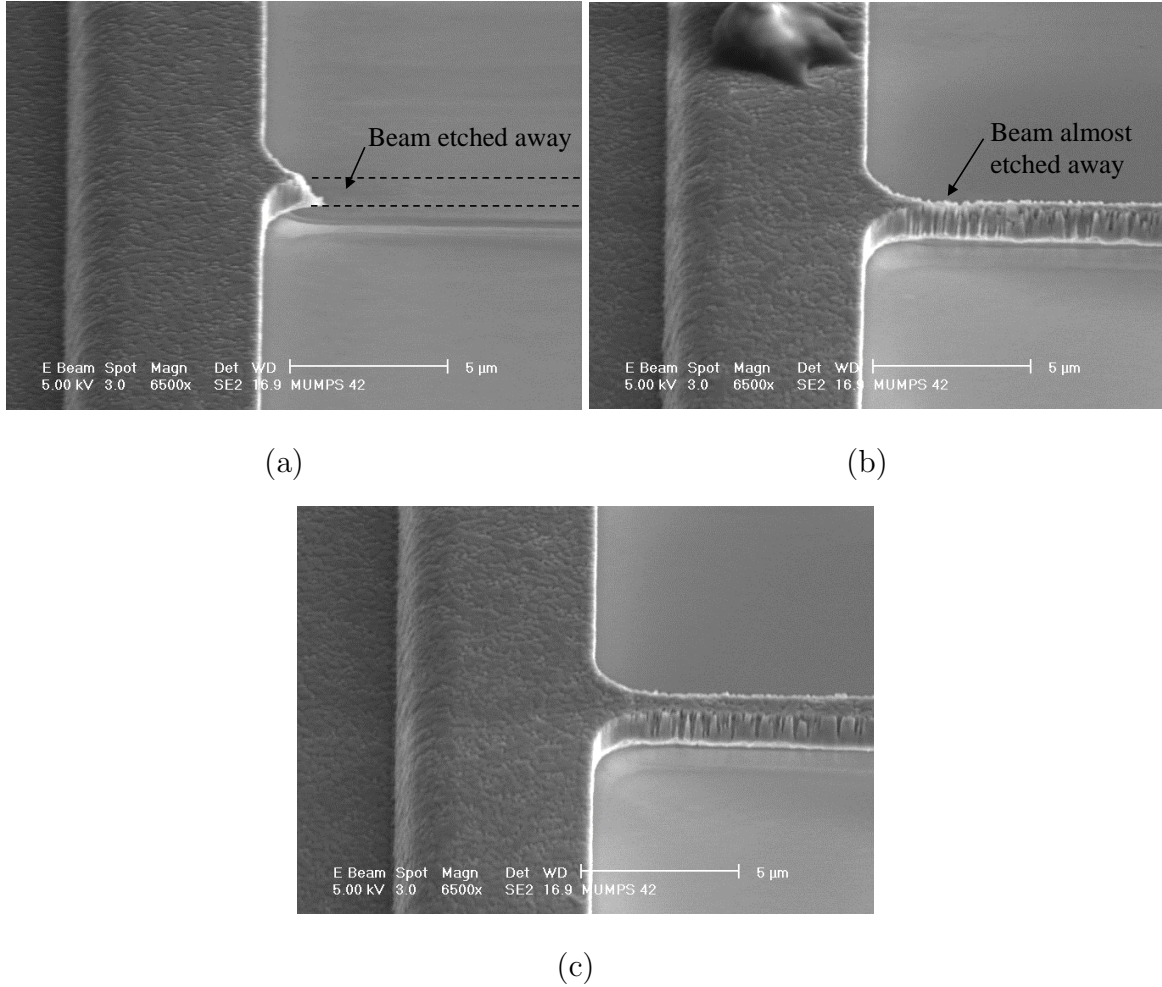


Figure 2.4: SEM images of Poly2 fixed-fixed beams following the buffered etch. a)  $1\ \mu\text{m}$ -wide, b)  $1.5\ \mu\text{m}$ -wide, and c)  $2\ \mu\text{m}$ -wide

A test array of Poly1, Poly2, and Poly1-Poly2 stacked fixed-fixed beams (see Figure 2.5) were used to assess the effects of the buffered oxide etch for all remaining MUMPs® runs (#43 to #45) that I used during my research period. The beam

widths for the structural layers in my test array include: Poly1 - less than  $4.0\text{ }\mu\text{m}$ -wide, Poly2 - less than  $6.0\text{ }\mu\text{m}$ -wide, and stacked Poly1-Poly2 - less than  $10.0\text{ }\mu\text{m}$ -wide. I monitored several die during my research period and most of the Poly2 beams that were less than  $2\text{ }\mu\text{m}$ -wide were missing or significantly damaged (due to the foundry's new BOE step). The stacked Poly1-Poly2 structural layer is the most susceptible to damage with the addition of the BOE etch. Structures with widths less than  $6\text{ }\mu\text{m}$ -wide are often found seriously damaged or completely removed following this etch.

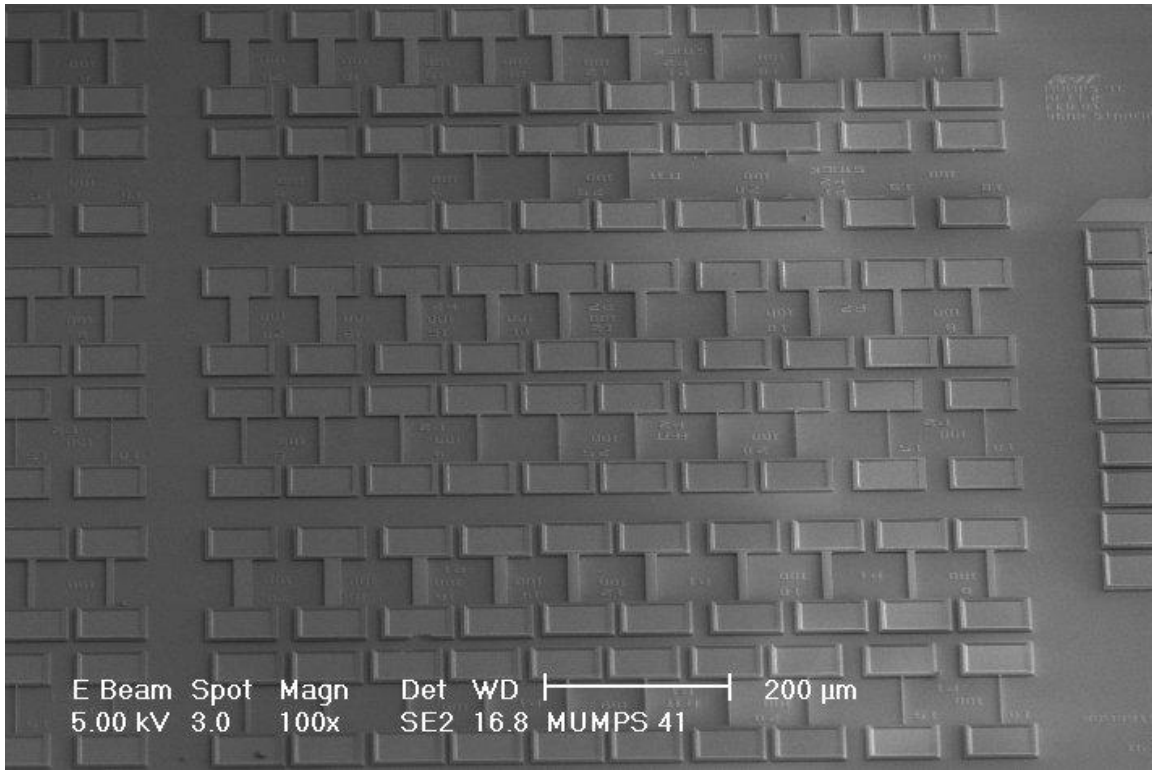


Figure 2.5: SEM image of buffered etch test array.

In addition, periodically dark black spots were noticed on the die following the protective photoresist removal. The spots may be due to silicon dust from the subdicing [7]. To alleviate or reduce the frequency of the black spots, I performed an aggressive agitation for the first few minutes in acetone on the die. Another possible cause is residual photoresist remaining following the acetone dip. To minimize this

possibility, I soaked the die in acetone for a minimum of 30 minutes. This is the same type of photoresist the MUMPs® foundry has been using since 1997 [7]. Following the above two procedures, the frequency of the black spots significantly reduced following the photoresist removal.

### 2.3 Sandia Ultra-planar Multi-level MEMS Technology

The Sandia Ultra-planar Multi-level MEMS Technology (*SUMMiT<sup>TM</sup>*) polysilicon surface micromachining process developed by Sandia National Laboratories [9] is similar in many respects to MUMPs®. The critical difference is the addition of a chemical mechanical polishing (CMP) step just prior to deposition of the third polysilicon (MMPOLY3) layer [5]. Another key difference is the method of phosphorous doping of the structural polysilicon layers. In the *SUMMiT<sup>TM</sup>* process, the structural polysilicon layers are doped as they are deposited. This method of doping creates a uniform doping concentration within the polysilicon layer. This combined with optimal annealing results in structural layers which are nearly stress free with minimal stress gradients.

*2.3.1 Fabrication Process.* Sandia's *SUMMiT<sup>TM</sup>* process begins with 6-inch n-doped  $< 100 >$ -oriented silicon wafers with a starting resistivity of  $2 - 20 \Omega - cm$ . A silicon dioxide (Oxide) layer  $0.6 \mu m$ -thick followed by a  $0.8 \mu m$ -thick silicon nitride layer make up the electrical isolation layers. The next layer is a non-releasable polysilicon (MMPOLY0) layer that is  $0.3 \mu m$ -thick and is used for ground planes and wiring. The first sacrificial oxide layer (SACOX1) is  $2 \mu m$ -thick. The next layer is MMPOLY1 and is  $1.0 \mu m$ -thick. The MMPOLY1 layer is followed by SACOX2, a thin  $0.5 \mu m$ -thick sacrificial oxide which is followed by a  $1.5 \mu m$ -thick polysilicon layer (MMPOLY2). The first releasable polysilicon layer (MMPOLY1), and second releasable polysilicon layer (MMPOLY2) can form a single polysilicon layer that is  $2.5 \mu m$ -thick [5]. The combination of the MMPOLY1 and MMPOLY2 structural layers is similar to the MUMPs® Poly1 layer. The next

layer is the third deposited sacrificial oxide layer (SACOX3) and is initially  $5.6\ \mu\text{m}$ -thick. Before the final polysilicon structural layer (MMPOLY3) is deposited onto the SACOX3 layer, the wafers are planarized by chemical mechanical polishing (CMP). The third deposited sacrificial oxide layer (SACOX3) is polished to a final thickness of approximately  $1.5$  to  $2\ \mu\text{m}$  above the highest polysilicon structure. After the patterning and etching of the planarized SACOX3, the final polysilicon structural layer (MMPOLY3,  $2.0\ \mu\text{m}$  thick) is deposited.

The sacrificial oxides used in the *SUMMiT<sup>TM</sup>* process are very hard (resistant to etching), and require a significantly longer hydrofluoric (HF) acid etch period (sometimes up to 1 hour) [5]. A noted difference in the *SUMMiT<sup>TM</sup>* process verses MUMPs® is the absence of metallization in the *SUMMiT<sup>TM</sup>* process. Thus, post foundry metallization if desired must be performed after the die are received. Figure 2.6 illustrates all the structural and sacrificial layers available in the *SUMMiT<sup>TM</sup>* fabrication process.

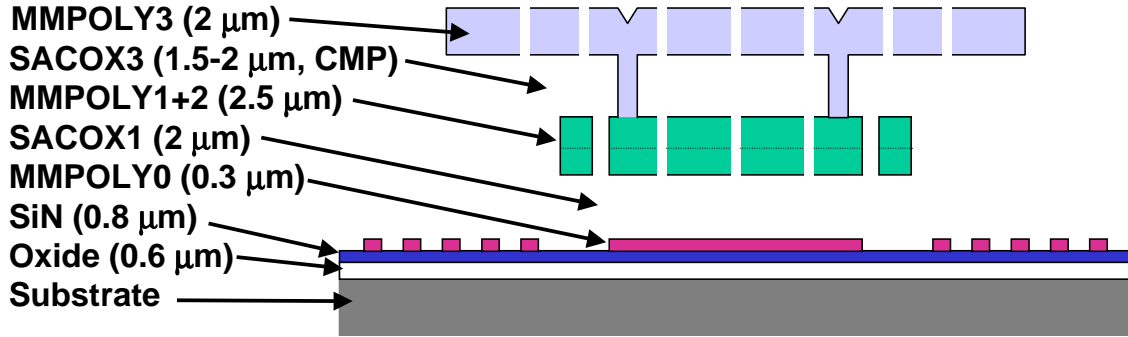


Figure 2.6: Illustration of available layers in the *SUMMiT<sup>TM</sup>* process [6]

#### 2.4 Multi User Silicon Carbide (MUSiC) Process

The Multi User Silicon Carbide (MUSiC) foundry fabrication process [10] is modeled after the MUMPs® process. In addition to employing polycrystalline silicon carbide as the structural material, the primary difference between the MUSiC and the MUMPs® processes is that the MUSiC process maintains a planar surface profile

up to the metal deposition through extensive use of CMP. Since the MEMS structures are constructed in a layer by layer process, the ANCHOR2 mask is not used in the MUSiC process. The first run of the MUSiC foundry was scheduled for Dec 01. I was invited to participate so I designed sets of buckled beam arrays for both structural layers (SiC-2 and SiC-3), cantilever arrays, several different micromirror designs, thermal actuators, and several different fixed-fixed beam test arrays to be used for possible UV  $\mu$ Raman spectroscopy. The MEMS designs I submitted are provided in Appendix B. The available layers in the MUSiC process is illustrated in Figure 2.7. I was not able to test my MUSiC devices prior to completing this dissertation.

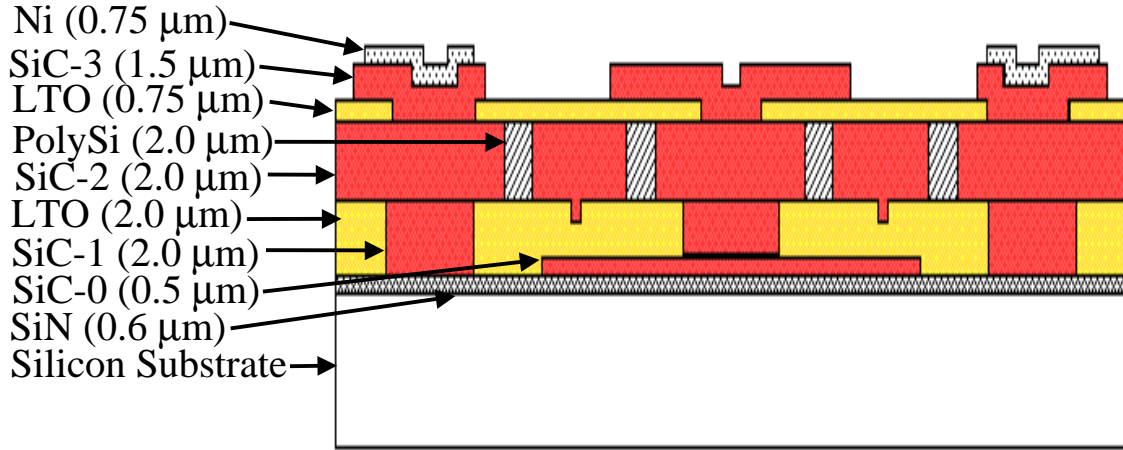


Figure 2.7: Illustration of available layers in the MUSiC process [10]

*2.4.1 Fabrication Process.* The starting substrate for the MUSiC process consists of a  $1-10 \Omega - cm$  resistivity, p-doped, silicon wafer. The first layer deposited is a 600 nm-thick layer of low-stress silicon nitride. The silicon nitride layer serves as an electrical isolation layer. Following the nitride deposition, a  $0.5 \mu m$ -thick layer of low temperature oxide (LTO) is deposited and patterned. A  $0.5 \mu m$ -thick layer of SiC film (SiC-0) is deposited on the first patterned LTO layer. The SiC-0 is then polished down to the first oxide surface. The patterning masks used for this layer are a combination of mask layer SiC0 and mask layer HOLE0. The SiC-0 layer is an

unreleasable layer and primarily used for wiring and actuation. Over the patterned SiC-0/LTO layer, a 2  $\mu m$ -thick layer of LTO is deposited and patterned. This is followed by the deposition of a 2  $\mu m$ -thick layer of SiC (SiC-1). The SiC-1 layer is again polished down to the second oxide surface. Mask ANCHOR1 provides anchor holes for attaching SiC-1 structures to either the nitride or SiC-0 layers. A DIMPLE mask is used to define and etch 0.75  $\mu m$ -deep holes in the LTO (using BOE). Following the ANCHOR1 and DIMPLE patterning and etching, a 2  $\mu m$ -thick polysilicon molding layer is deposited and patterned. This is followed by the deposition of a 2  $\mu m$ -thick layer of SiC (SiC-2). The SiC-2 layer is polished down to the polysilicon molding layer (this is the first structural layer). For this layer, the created holes and structural openings are filled with polysilicon. The mask for this layer consists of the combined mask layer SiC2 and mask layer HOLE2. Next, a 0.75  $\mu m$ -thick layer of LTO is deposited and patterned. Mask layer SiC2-SiC3-VIA defines the via connections through the oxide between the SiC2 and SiC3 layers. A 1.5  $\mu m$ -thick SiC layer (SiC-3) is then deposited and etched using RIE (this is the second structural layer). The masks used with the SiC-3 layer include mask layer SiC3 and mask layer HOLE3. The final layer is a 0.75  $\mu m$ -thick layer of nickel (Ni) for ohmic contact to the SiC. The masks used for patterning this layer consists of the combination of mask layer METAL and mask layer HOLEM. Finally, to release the structural devices, a three-step release process is required. First the top LTO layer is removed with HF. Second, the sacrificial polysilicon material is removed using KOH to gain access to the bottom LTO layer. Third, the underlying LTO is removed using HF. Figure 2.8 provides a series of layouts corresponding to the three step MUSiC release process.

## 2.5 *TSUPREM<sup>TM</sup> Modelling*

In the MUMPS<sup>®</sup> fabrication process, the doping of the polysilicon layers is accomplished through thermal diffusion of the phosphorus dopant from the PSG (oxide) layers to the surrounding polysilicon layers [8]. For structures with a large

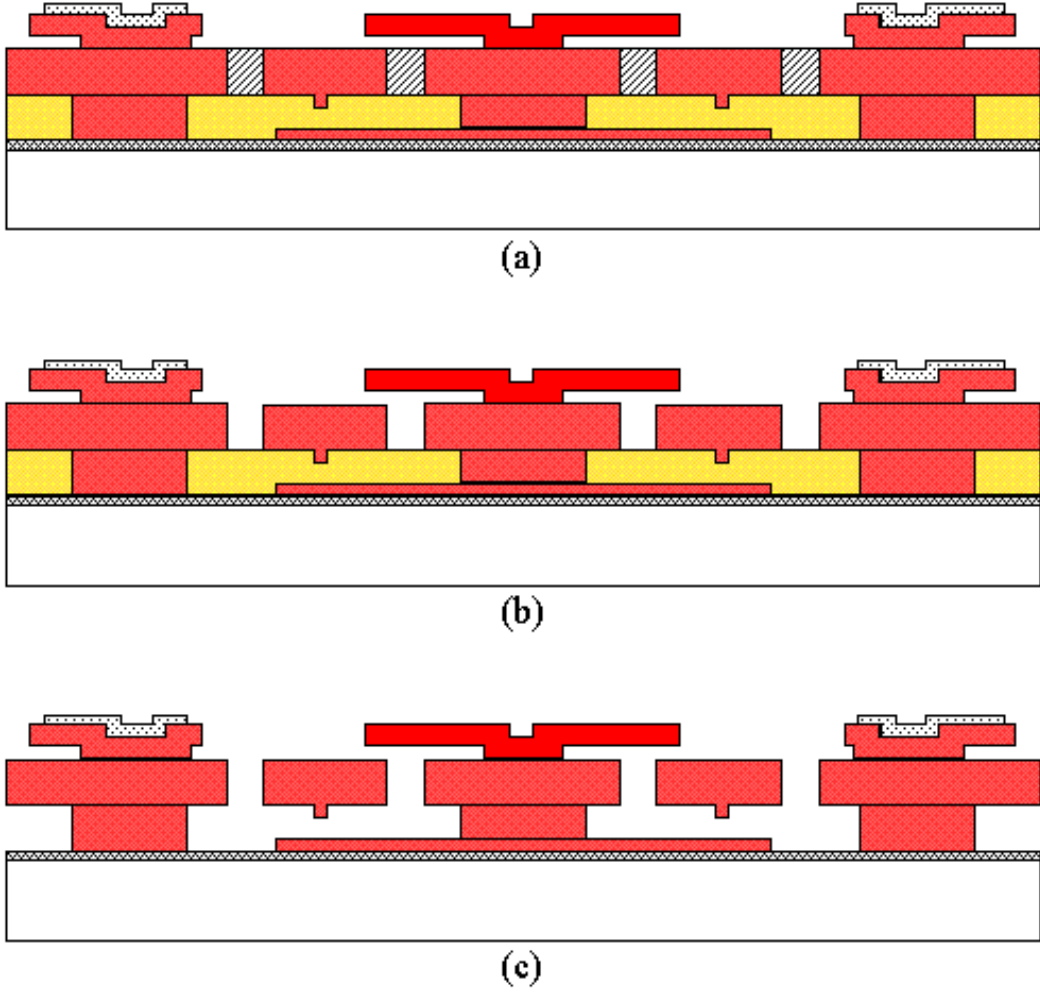


Figure 2.8: Illustration of the three step MUSiC release process [10]

width to thickness ratio  $w/t$ , the majority of the doping is achieved through the diffusion of the phosphorus dopant from the oxide layers directly above and below the polysilicon structural layer (vertical diffusion). However, for polysilicon structures for which the width is comparable to the thickness, the diffusion of phosphorus through the sidewalls (lateral diffusion) becomes significant and can impact the overall doping concentration. Figure 2.3-(a) illustrates the diffusion methods available to the Poly1 structural layer.

I used *TSUPREM<sup>TM</sup>* to model the MUMPs<sup>®</sup> fabrication process to illustrate this diffusion process and to identify peak dopant concentration levels within

the polysilicon structural layers. I also used *TSUPREM<sup>TM</sup>* to model the post-processing high temperature anneals, phosphorous diffusion, and phosphorous ion implants.

*2.5.1 TSUPREM<sup>TM</sup> Model of MUMPs<sup>®</sup> Fabrication Process.* To verify the lateral diffusion theory and overall doping concentrations, I used *TSUPREM<sup>TM</sup>* to model the MUMPs<sup>®</sup> fabrication process. I designed a series of microbridge test arrays of varying lengths and widths to gather quantitative  $\mu$ Raman stress data. These microbridges are analyzed using  $\mu$ Raman spectroscopy in Chapter V. With  $\mu$ Raman spectroscopy, I measure the differences in residual stress for the microbridges due to nonuniformities. I correlate the stress to the dopant concentration by modelling the phosphorous diffusion doping process of the microbridges.

The *TSUPREM<sup>TM</sup>* model of the MUMPs<sup>®</sup> fabrication process was based on the fabrication outline provided by JDS Uniphase [8] and by Butler [4]. An example *TSUPREM<sup>TM</sup>* input file is provided in Appendix C for further reference. Not all MUMPs<sup>®</sup> fabrication steps are modelled since my main goal is to investigate the phosphorus diffusion profile for both Poly1 and Poly2 structural layers as a function of the microbridge width (2-20  $\mu m$ -widths). Hence, only the processing steps which affect the phosphorus diffusion profile are included in the *TSUPREM<sup>TM</sup>* modelling. I add several additional steps to the MUMPs<sup>®</sup> fabrication process to provide insight into the post-processing techniques addressed in Chapter V and VI. Table 2.1 lists the steps in the MUMPs<sup>®</sup> as fabrication process as I modelled them using *TSUPREM<sup>TM</sup>*.

Figure 2.9 and 2.10 illustrate the phosphorous dopant concentration variations within the polysilicon structural layers for (from top-to-bottom) 4, 10, and 20  $\mu m$ -wide Poly1 and Poly2 beams as modelled in *TSUPREM<sup>TM</sup>*. The color legend in Figure 2.9 and 2.10 provide the magnitude of the phosphorous dopant concentration for a particular location in the beams. The *TSUPREM<sup>TM</sup>* simulations for Poly1

Table 2.1: MUMPs® Fabrication Process as Modelled in *TSUPREM<sup>TM</sup>* [4, 8]

Process Step	Thickness ( $\mu m$ )	Phosphorus Doping Conc. ( $cm^{-3}$ )	Temp ( $^{\circ}C$ )
1. P-doped silicon substrate	-	$1 \times 10^{21}$	-
2. Deposit Nitride	0.6	-	-
3. Deposit Poly0	0.5	-	-
4. Pattern Poly0 with RIE	-	-	-
5. Deposit Oxide1	2.0	$4.2 \times 10^{20}$	-
6. First Anneal (1 hour)	-	-	1050
7. Deposit Poly1	2.0	-	-
8. Deposit Oxide cap	0.2	$4.2 \times 10^{20}$	-
9. Second Anneal (1 hour)	-	-	1050
10. Pattern Poly1 with RIE	-	-	-
11. Deposit Oxide2	0.75	$4.2 \times 10^{20}$	-
12. Third Anneal (1 hour)	-	-	1050
13. Deposit Poly2	1.5	-	-
14. Deposit Oxide cap	0.2	$4.2 \times 10^{20}$	-
15. Fourth Anneal (1 hour)	-	-	1050
16. Pattern Poly2 with RIE	-	-	-

(Figure 2.9) demonstrate that lateral diffusion is a key contributor in obtaining a uniform doping concentration in small linewidth Poly1 structures. From Figure 2.9, one can identify the overall dopant uniformity and increased dopant concentration in the narrower  $4 \mu m$ -wide beam. For the  $20 \mu m$ -wide beam, the highest dopant concentration is near the outer edges of the beam indicating lateral phosphorus diffusion. As the beam width increases, the impact of lateral diffusion becomes less significant.

The *TSUPREM<sup>TM</sup>* simulation for the Poly2 beam shown in Figure 2.10 shows no lateral diffusion. This image illustrates that the dopant concentration is nonuniform throughout the beam structures and is independent of the beam width. In the MUMPs® fabrication process, Poly2 structures undergo a single anneal which adds to the observed nonuniformity of the phosphorus dopant in Figure 2.10.

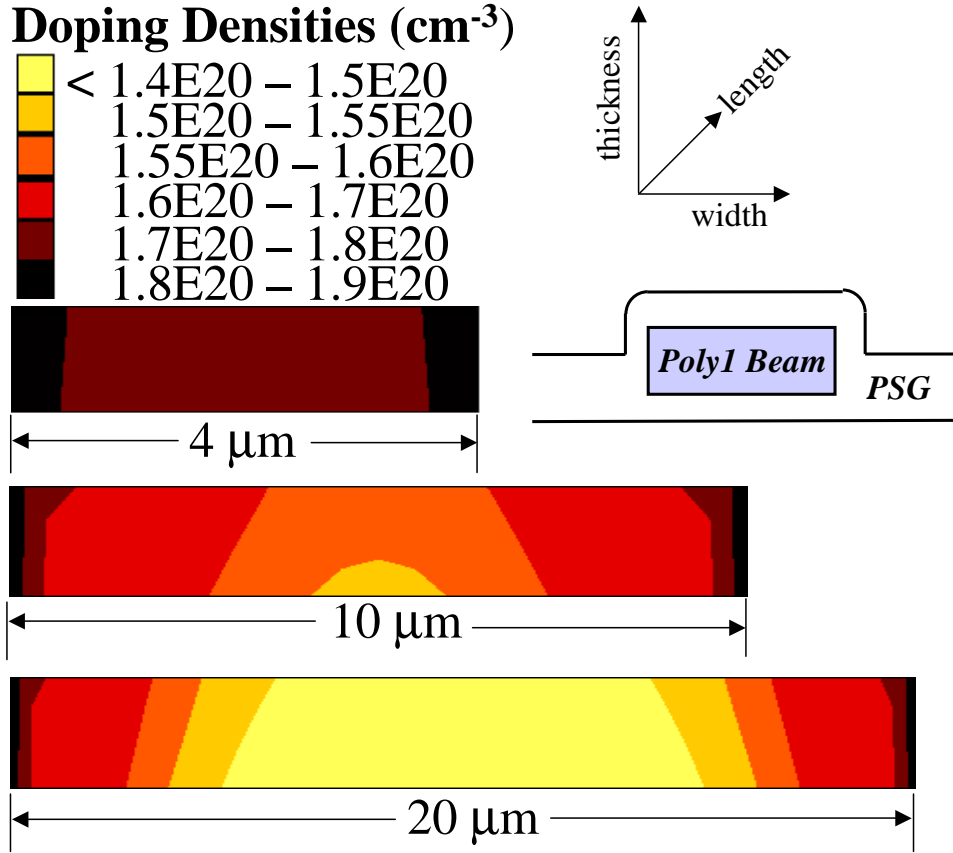


Figure 2.9: *TSUPREM<sup>TM</sup>* diffusion profiles of the MUMPs® Poly1 structural layer at the completion of the MUMPs® run. Beam cross-sections for widths of 4 μm, 10 μm, and 20 μm. Note lateral dimensions not to scale.

From Figure 2.9 and 2.10, a definite phosphorous nonuniformity in the dopant concentrations exist in both layers. This nonuniformity leads to increased stress gradients and higher residual stress levels. I provide additional *TSUPREM<sup>TM</sup>* modelling data and analysis in Chapter V and VI. I show that I can obtain an increased dopant uniformity and dopant concentration in the Poly1 and Poly2 structural layers by taking the as-grown MUMPs® die and performing additional high temperature anneals and dopant diffusion.

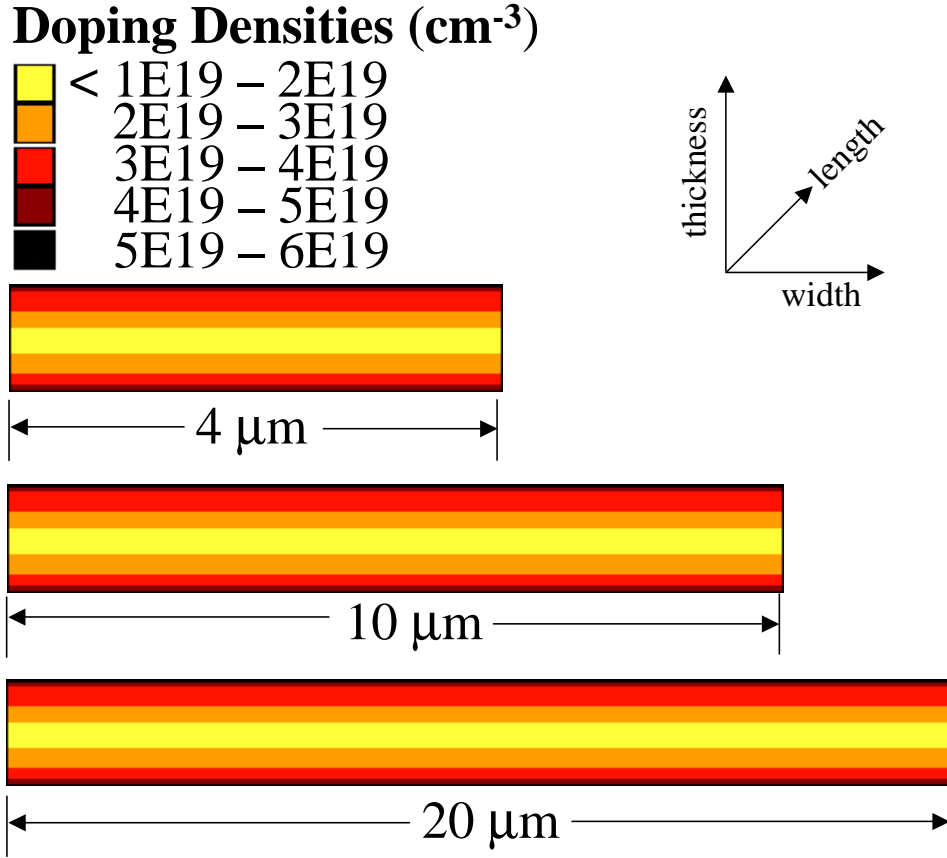


Figure 2.10: *TSUPREM<sup>TM</sup>* diffusion profiles of the MUMPs<sup>®</sup> Poly2 structural layer at the completion of the MUMPs<sup>®</sup> run. Beam cross-sections for widths of 4  $\mu\text{m}$ , 10  $\mu\text{m}$ , and 20  $\mu\text{m}$ . Note lateral dimensions not to scale.

## 2.6 MEMCAD FEM Modelling

I used the MEMCAD FEM software package [2] to characterize the stress in microbridges and micromirrors. MEMCAD provides 2D and 3D stress images. I compare this theoretical stress to the stress profiles I obtain using  $\mu$ Raman spectroscopy. In this section, I briefly address the primary elements which make up MEMCAD and present example stress and displacement results for several different MEMS structures including a microbridge, several different micromirrors, and a thermal actuator.

*2.6.1 MEMCAD Elements.* MEMCAD is an integrated suite of tools designed to help model MEMS designs. The tools enable one to design, specify, model, and create solutions for MEMS structures. The calculated results can be analyzed, graphed, and iterated to assist in completing the design process. Some of the available software processes used in MEMCAD include [2]:

- Catapult - generates a 2D layout of the MEMS design
- Process emulation - enables specific fabrication processes to be selected for simulation of the MEMS structures
- Autobuilder - generates a 3D solid model from the 2D masks
- Automesher - Performs the finite element meshing
- Solver Setup - electrical, mechanical, thermal, and/or fluidic solvers
- MemCap - Provides an electrostatic simulation to calculate all capacitance values between structural layers
- MemMech - Provides a mechanical simulation for initial results without electrostatic actuation
- CoSolve - Coupled electromechanical simulation - uses the electrostatic results from MemCap for the mechanical simulations

*2.6.2 MEMCAD Components.* Functionally, MEMCAD is divided into three major components which are illustrated in Figure 2.11. Each component is explained briefly in the next subsections.

*2.6.2.1 MEMS Designer.* MEMS designs can be created in a variety of ways. An integrated 2D layout editor (Catapult) supports comprehensive drawing and viewing for any design. Also, designs can be created with an independent layout tool (L-edit) and imported into MEMCAD in either CIF or GDSII format.

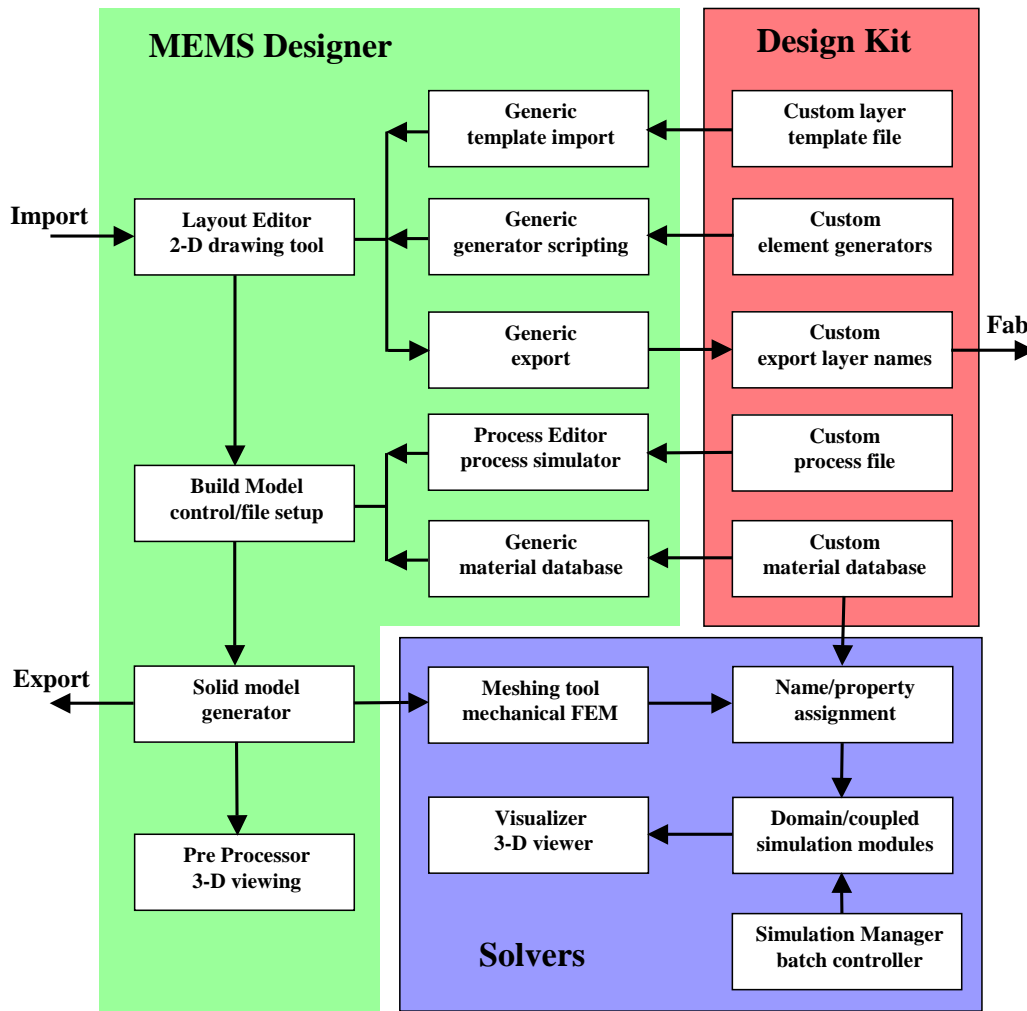


Figure 2.11: Schematic Overview of MEMCAD [2]

Once the mask layers are defined, the process editor creates a flow simulating the foundry process that will fabricate the MEMS design. Materials, mask dimensions, and etch profiles are entered into the process flow using a sequence of deposits and etch steps. Materials identified in the process flow are entered into the material property database, which stores the parameters needed to fully characterize the materials selected.

The completed mask/process description sequence is converted into a 3D model through AutoBuilder. An example of a 3D micromirror model as displayed in the visualizer is shown in Figure 2.12.

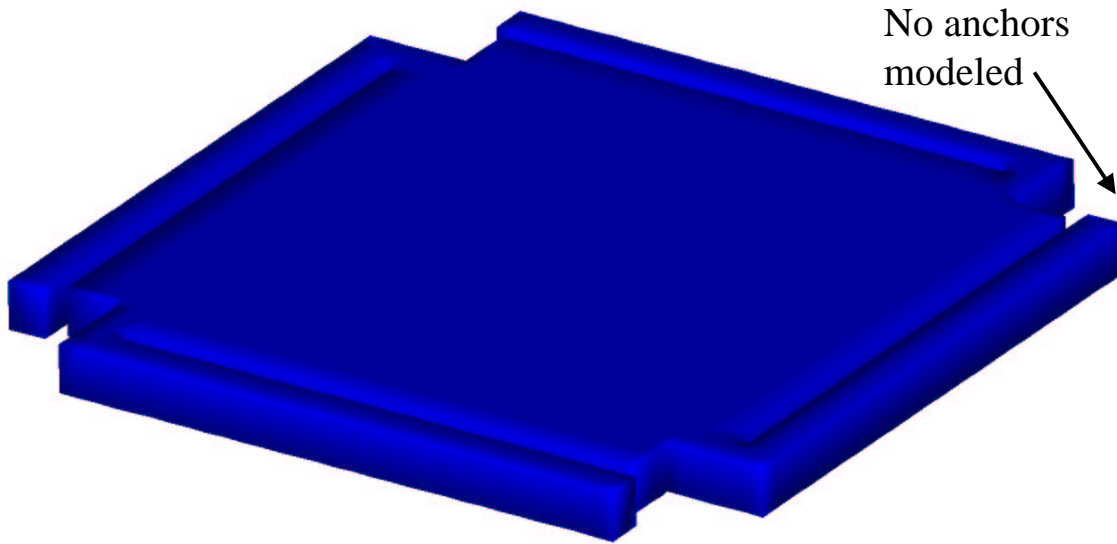


Figure 2.12: Schematic of a 3D MEMS Poly1 micromirror.

*2.6.2.2 Design Kit.* The design kit contains most of the functions used to generate the 2D model of the MEMS design. Since I used L-Edit to layout my MEMS designs, I used the design kit only to open the imported GDSII layout and convert it to a catapult file for MEMCAD analysis.

*2.6.2.3 Solvers.* This is by far the most important component in the MEMCAD software package. This component involves setting up boundary conditions and choosing one or more solvers to perform the desired analysis. AutoMesher is used for automatic partitioning and meshing of the solid model for finite element analysis. The solvers form the heart of MEMCAD and they include electrostatic, mechanical, thermal, fluidic, and coupled solution components. The MEMCAD solvers allow several different types of solutions to be computed. Some possible solutions include [2]:

- Capacitance and charge calculations
- Coupled electromechanical solutions
- Coupled electromechanical solutions with automatic pull-in analysis and hysteresis
- Solutions using full contact boundary conditions
- Solutions using applied stress gradients
- Thermal steady-state and thermal transient solutions
- Thermomechanical and thermoelectromechanical solutions

The completed solutions can be viewed using the MEMCAD Visualizer. The Visualizer maps a color-coded solution onto the rendered 3D model to allow users to view the different types of stresses, thermal variations, temperature gradients, pressures, current density, electrostatic fields, and mechanical deformations [2].

*2.6.3 MEMS Stress Modelling.* In an attempt to quantify the residual stress profiles obtained from  $\mu$ Raman spectroscopy, I used MEMCAD to obtain FEM stress profiles for comparison. The magnitude and curvature are compared for both methods to verify that proper stress profiles are observed.

Prior to MEMCAD analysis, the selected MEMS device is redrawn in L-edit to simplify the modelling. For example, in Figure 2.13, some parts of the micromirror design are not required in the FEM model (i.e. anchors, Poly0 under the flexures, dimples, etc.). These parts have negligible affects on the stress results. By splitting up the mirror into sections, I can finely mesh the parts of true interest (flexures) and coarsely mesh other parts (electrode and mirror surface). This helps me obtain smaller mesh counts which speeds up the simulation.

*2.6.4 Poly1 Microbridge Simulation.* I modelled several Poly1 and Poly2 electrostatically actuated microbridges to determine internal stresses and relative

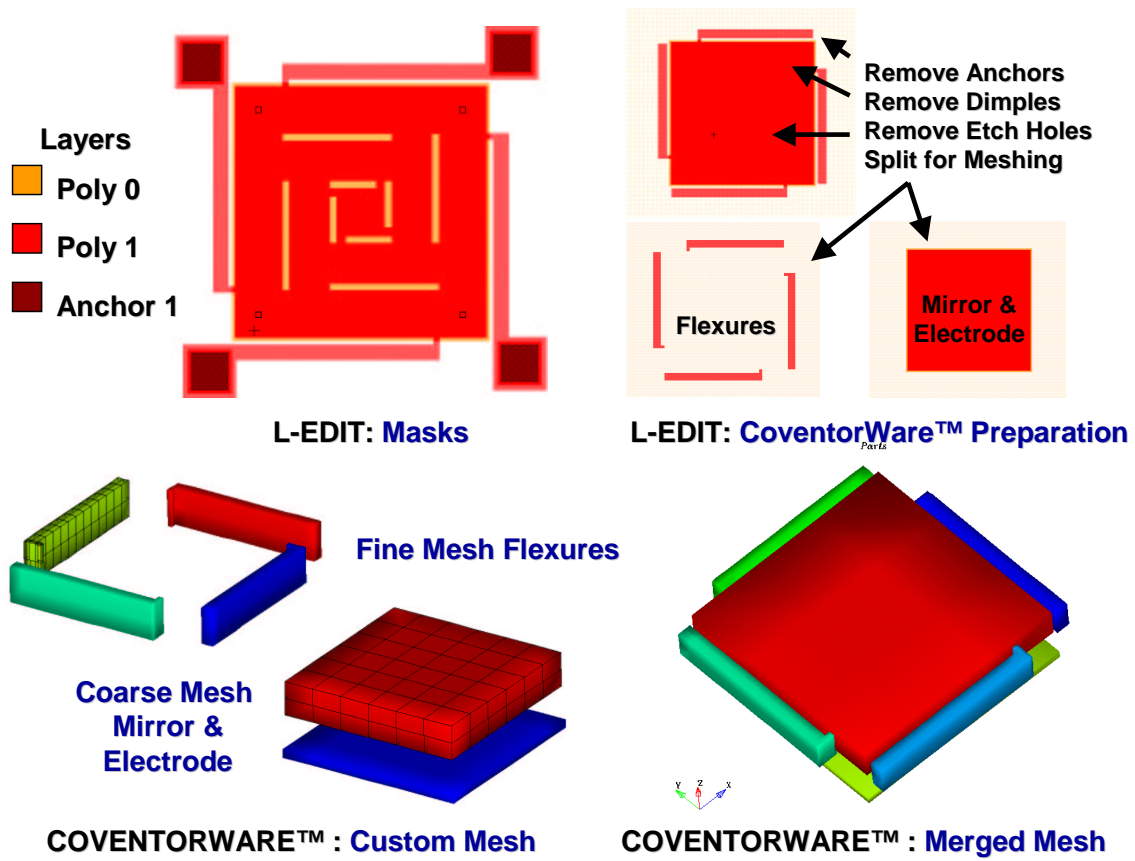


Figure 2.13: Micromirror conversion to enhance MEMCAD modelling

snap-down voltages. The  $40\text{ }\mu\text{m}$ -wide by  $100\text{ }\mu\text{m}$ -long electrode is located under the center of the bridge. The microbridge length and width are  $380\text{ }\mu\text{m}$ -long and  $20\text{ }\mu\text{m}$ -wide respectively. The stress images for this microbridge are illustrated in Figure 2.14, where each image represents a stress value for a specific applied voltage. The images represent stress with the following applied voltage: a) 0 V; b) 10 V; c) 20 V; d) 40 V; e) 50 V; and f) 56 V (snap-down). The MISES (MISES is equivalent to MPa) color stress scale located at the bottom of Figure 2.14 corresponds to the coloration of the beam images indicating the magnitude of the localized stress on the microbridge. At snap-down, the localized stress at the anchored ends and in the center of the microbridge is approximately -45 MPa.

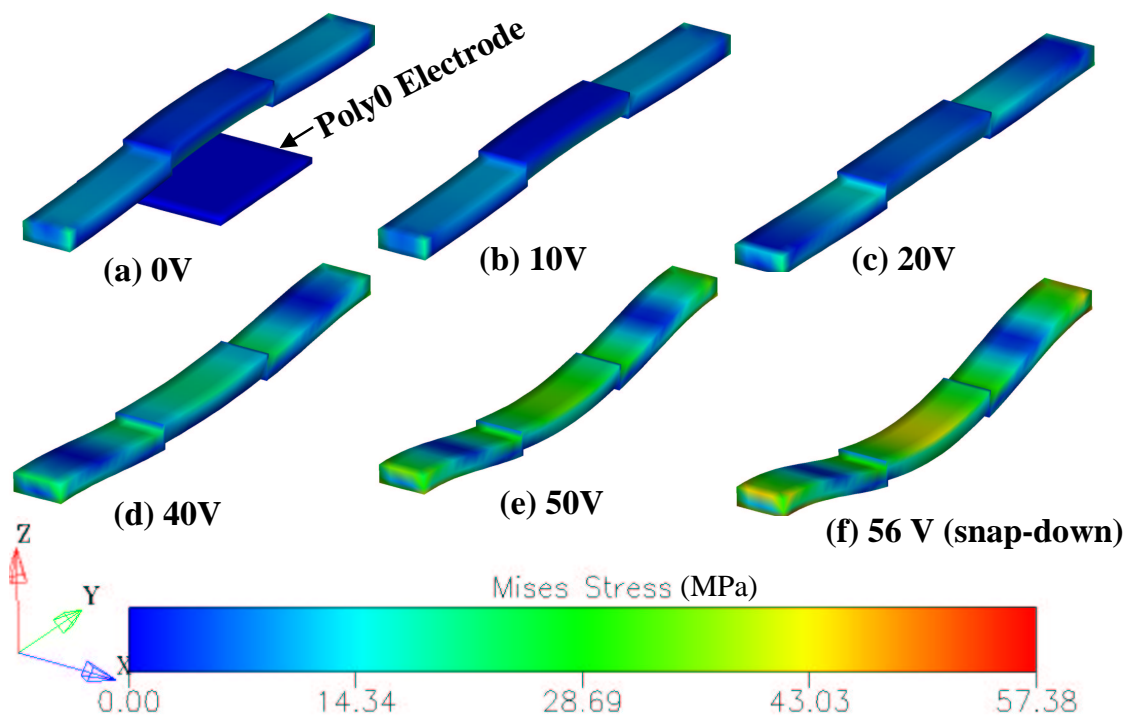


Figure 2.14: MEMCAD 3D stress images for a Poly1 microbridge.

The displacement verses applied voltage for a Poly1 microbridge is shown in Figure 2.15. The displacement images in Figure 2.15 correlate exactly to the voltage and stress values discussed previously in Figure 2.14. One should note the displacement at 56 V correlates well with the snap-down value of  $1/3$  the air gap ( $\approx 0.67 \mu\text{m}$ ).

The Poly2 microbridge is identical to the Poly1 microbridge with the exception of the beam thickness and distance from the Poly0 electrode. Nearly identical stress and displacement images are obtained with slight differences in snap-down and stress values. The appreciable differences include: Snap-down voltage is  $\approx 64 \text{ V}$ , and the maximum stress magnitude is approximately  $-75 \text{ MPa}$ .

*2.6.5 Micromirror Simulations .* I analyzed several different piston micromirrors to assess the impact of the micromirror design on the residual and induced stress curves. A key to modelling MEMS structures, especially micromirrors, is to

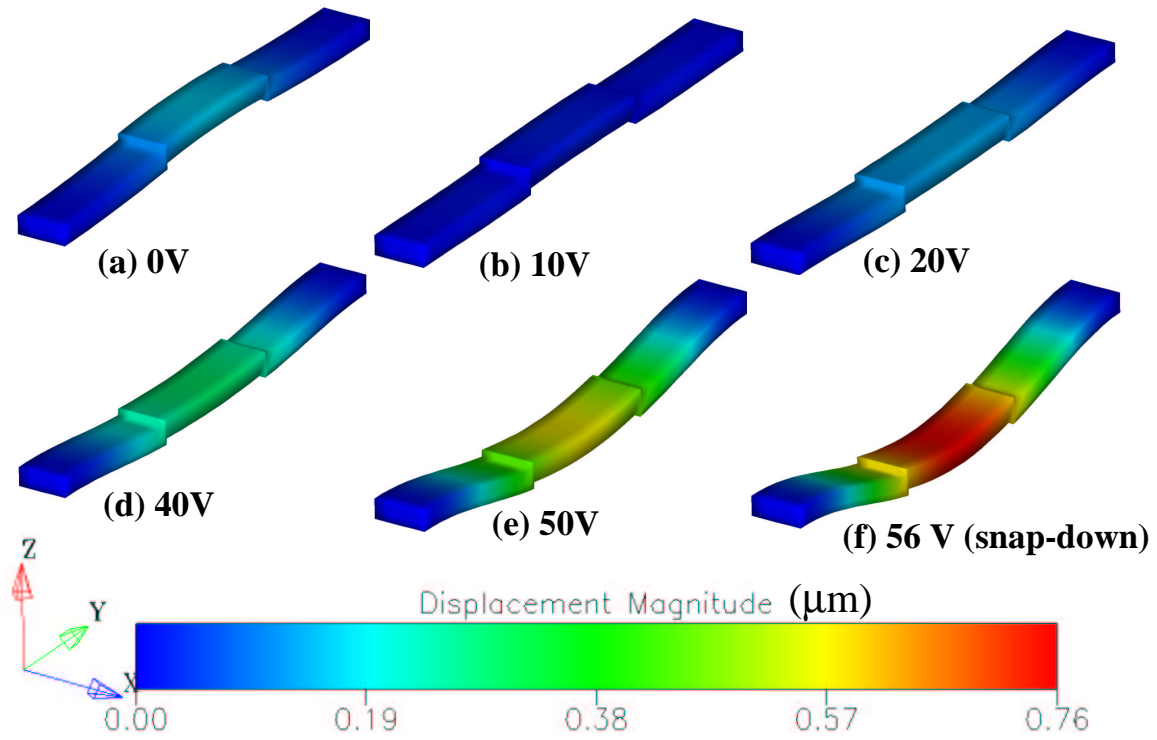


Figure 2.15: MEMCAD 3D beam displacement vs. applied voltage for a Poly1 Microbridge.

fully use the available symmetry of the device. In MEMCAD, the typical square piston micromirror can be modelled by considering only a quarter of the mirror as shown in Figure 2.16. The quarter size significantly reduces the number of mesh elements required to analyze the mirror. Moreover, it also enables the use of a finer x-y-z mesh on the flexure (e.g. mesh size of  $2 \times 2 \times 2 \mu m$ ) to obtain a more accurate stress profile. Alternatively, the mirror can be coarsely meshed (e.g.  $20 \times 20 \times 2 \mu m$ ) to reduce computation time but accuracy decreases. By using a quarter mirror as the modelled design, the accuracy of the model becomes nearly identical to the simple analytical calculation and correlates to the measured snap-down voltage of 13.5 V. The micromirror modeled is a  $200 \mu m$ -square Poly1 piston micromirror with flexures measuring  $13 \mu m$ -wide by  $125 \mu m$ -long.

The 3D stress images for a typical micromirror with etch holes (etch holes viewable in Figure 2.20a)) is shown in Figure 2.17. The associated snap-down for

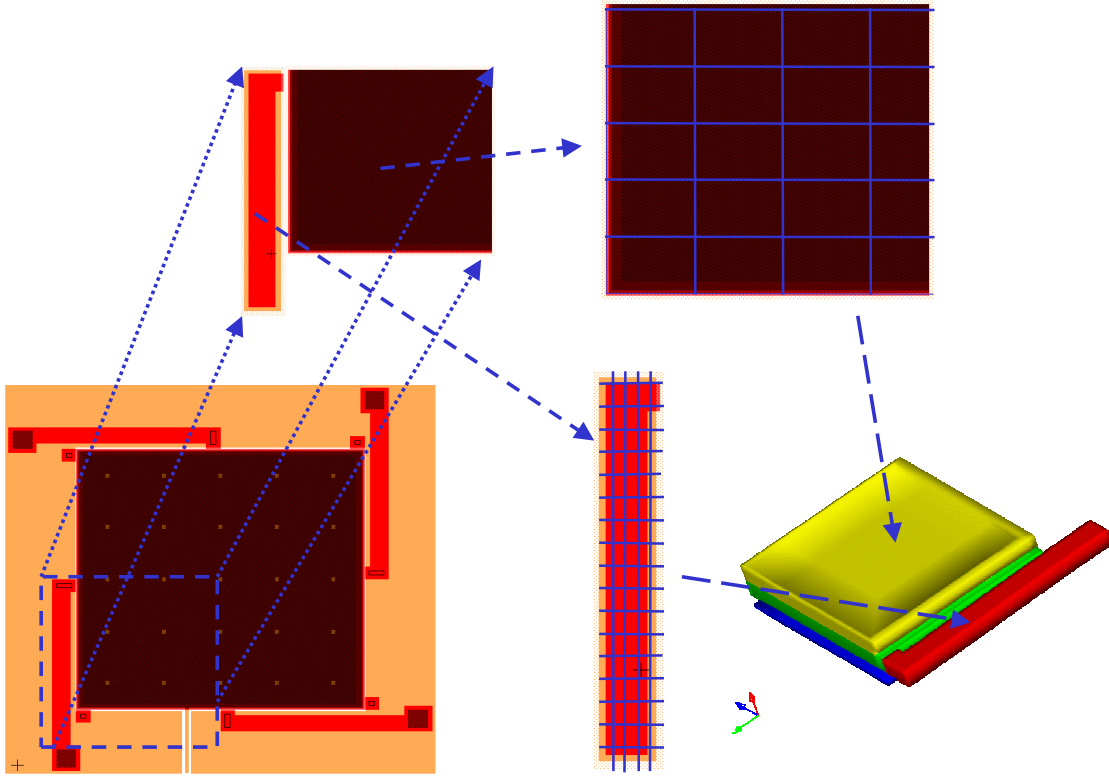


Figure 2.16: MEMCAD piston micromirror modelling exploiting device symmetry

this mirror as illustrated is approximately 14.2 V with a maximum peak induced stress value of  $\approx -16.63$  MPa at the anchors and mirror attachments. The individual images in Figure 2.17 each represent a stress value for an accompanying applied voltage as shown from 0 to 14.2 V. Since I analyzed the full micromirror, I increased the size of the x-y-z mesh elements in the flexures and mirror to be  $10 \times 10 \times 2 \mu m$  to reduce the number of elements.

With the emphasis in designing optically favorable micromirrors for optical applications, I designed and modelled the identical micromirror analyzed in Figure 2.17 with the exception of modified etch access holes. The micromirror with the modified etch access holes is shown in Figure 2.18 with several stress versus applied voltage images. The snap-down voltage for this micromirror remained at approximately 14.5 V and the induced stress in the micromirror flexures remained nearly the same.

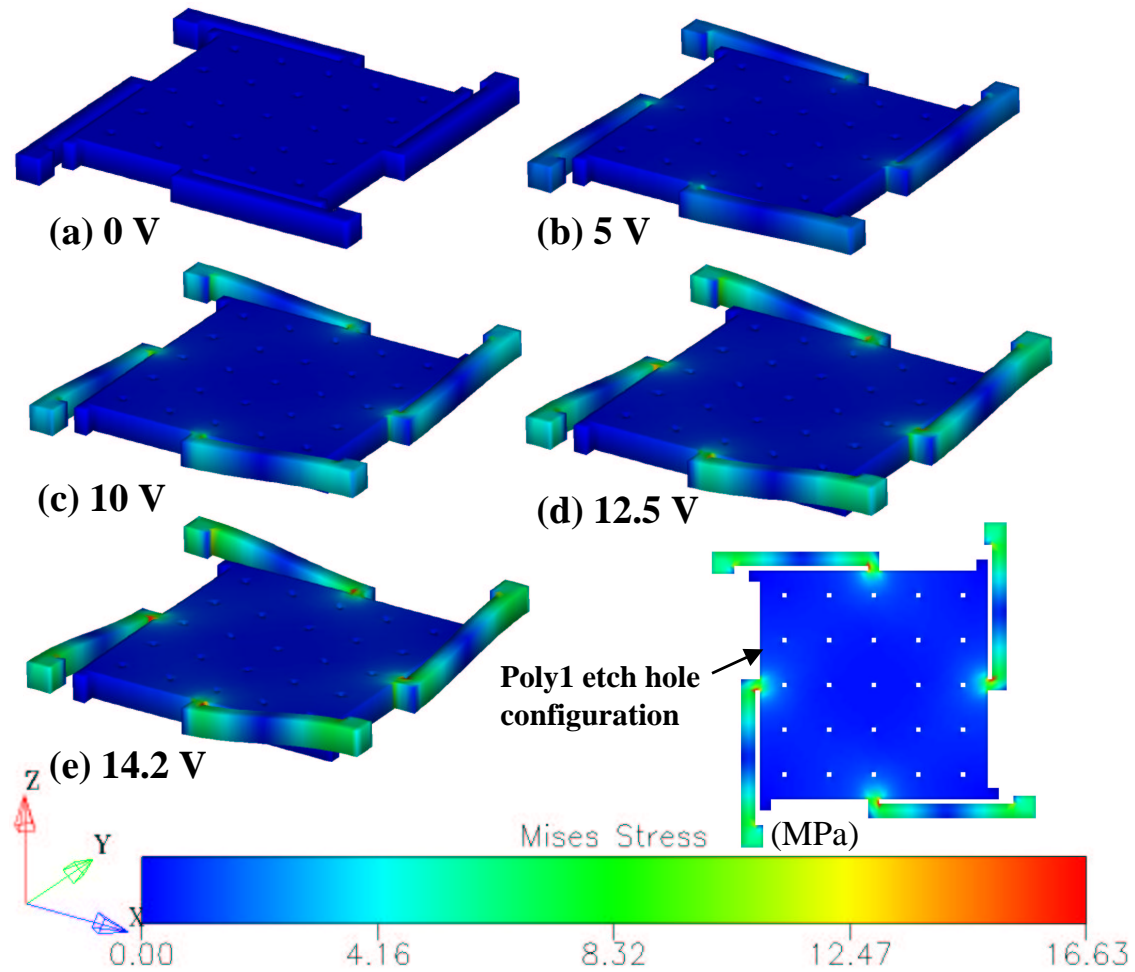


Figure 2.17: MEMCAD 3D stress images for a 200  $\mu\text{m}$ -square Poly1 micromirror with typical etch holes.

The only noticeable area of increased stress occurs at the flexure-to-mirror attachment where the localized stress increased by approximately -13 MPa. Although the stress increased at the flexure-to-mirror attachment, the stress did not propagate to the center mirror since the elongated etch holes channelled the stress away from the center of the micromirror.

The individual images in Figure 2.18 represent: a) foundry fabricated model with substrate; b) foundry fabricated model without substrate; c) 5 V; d) 10 V;

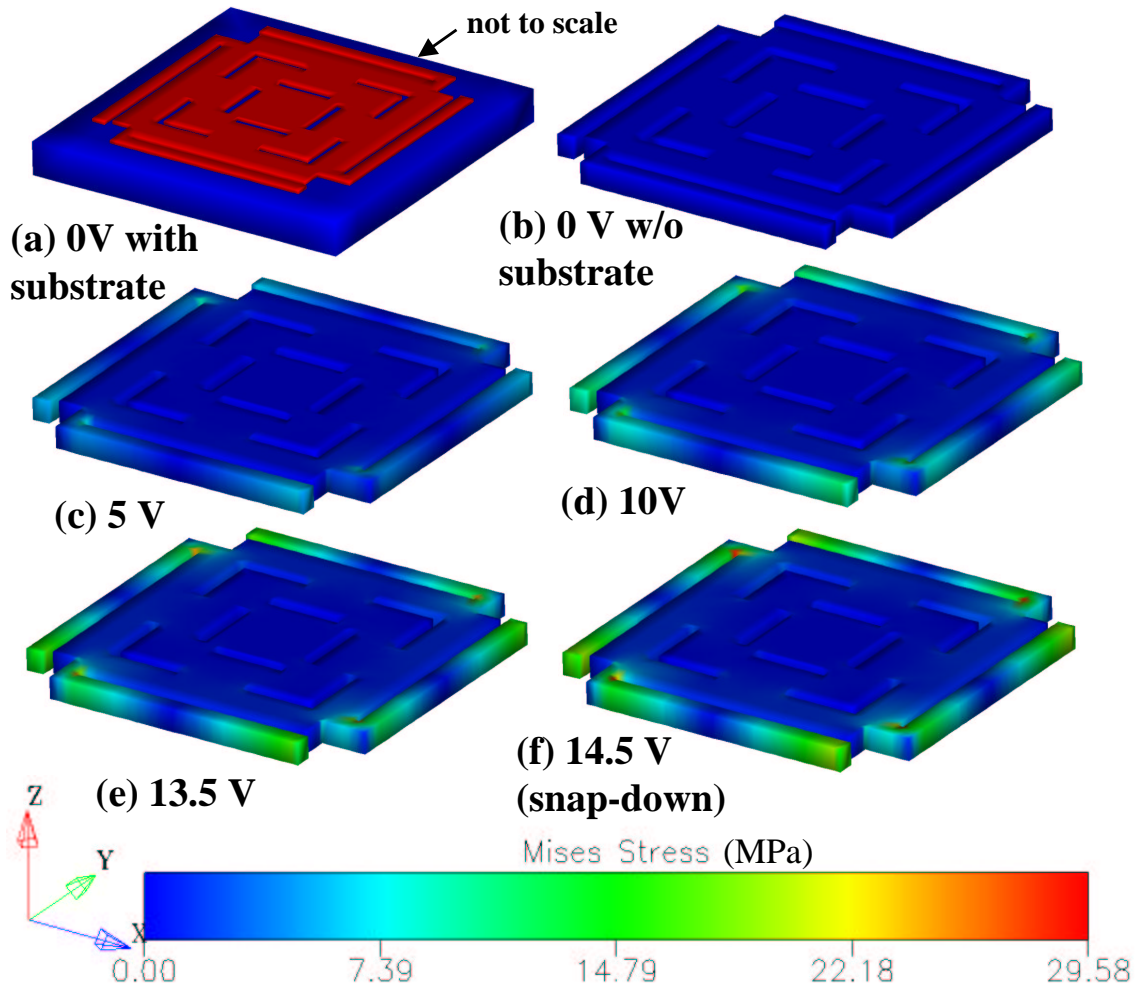


Figure 2.18: MEMCAD 3D stress images for a 150  $\mu\text{m}$ -square Poly1 micromirror with modified etch holes.

d) 13.5 V; and e) 14.5 V (snap-down). The meshed element size in the flexures and mirror were  $10 \times 10 \times 2 \mu\text{m}$ .

The displacement versus applied voltage for the modified Figure 2.18 micromirror is shown in Figure 2.19. Again the displacement images correspond to the applied voltages and induced stress levels as shown in Figure 2.18.

Figure 2.20 illustrates a comparison of two different MEMS micromirror designs to show stress variations on the micromirror surface. The stress in the center of the mirror is reduced in the modified micromirror as the L-shape etch holes iso-

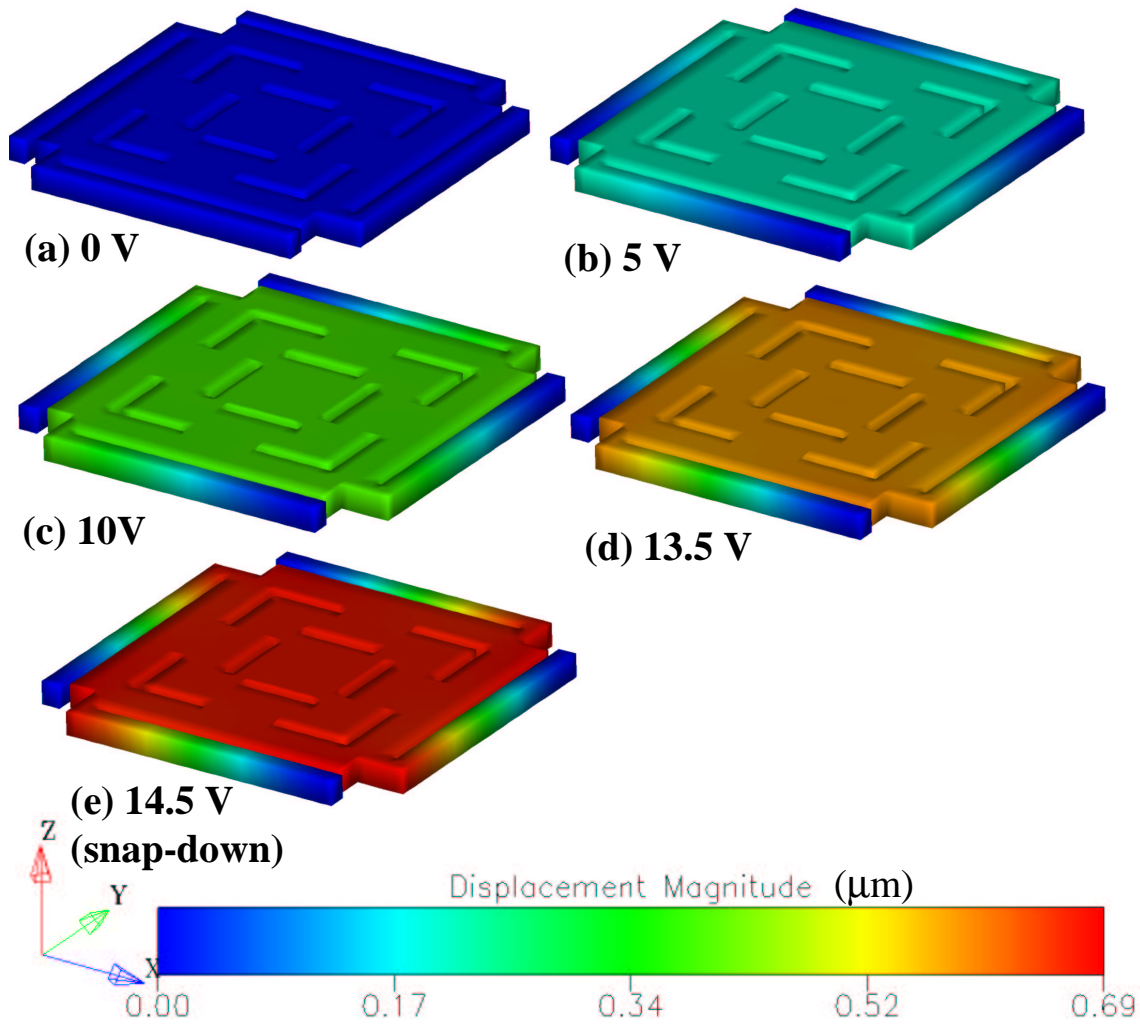


Figure 2.19: MEMCAD 3D displacement vs voltage images for a Poly1 micromirror.

late the center of the mirror plate from the flexure-mirror attachment points. This design provides the best stress reduction at the center of the micromirror. These micromirror designs were tentatively modeled for possible applications in MEMS tunable filters or lasers. As can be observed, the primary induced stress levels are highest at the flexure-mirror attachment. The modified etch hole design should increase the optical flatness of the micromirror due to isolation of the high stress level at the flexure-mirror attachment.

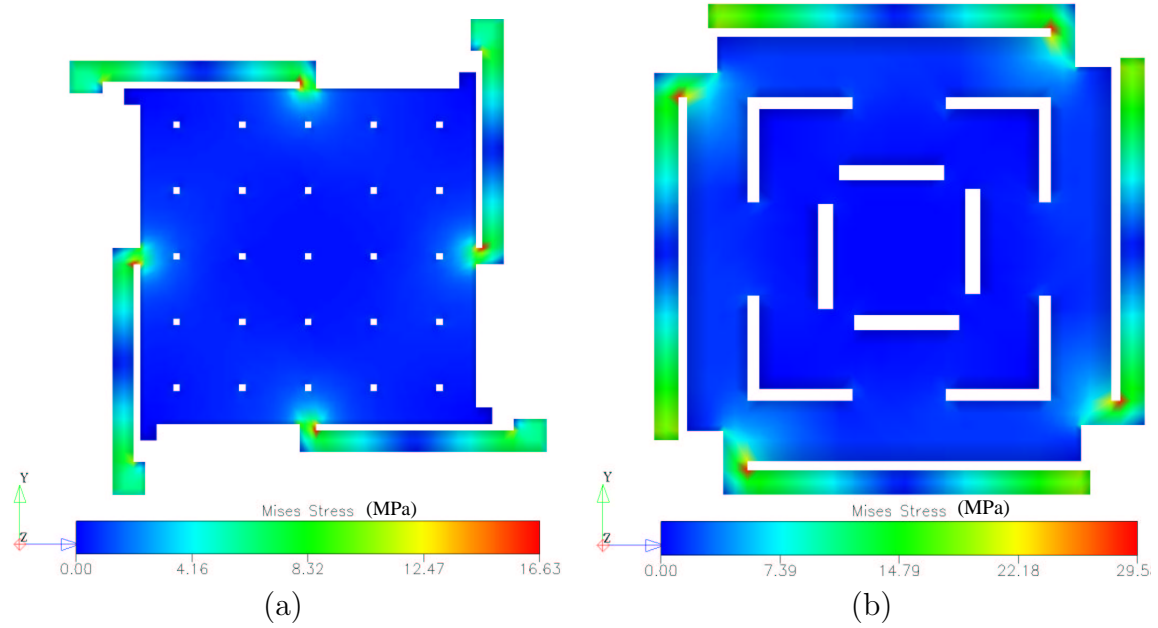


Figure 2.20: (a) MEMCAD images of two Poly1 micromirror designs illustrating localized induced stress magnitudes. (a) typical release etch holes, and (b) modified etch holes.

Prior to assessing the feasibility of using  $\mu$ Raman spectroscopy to measure residual stress in unreleased and released MEMS structures, I determine the stress in the MEMS structures as a function of length (x), width (y), and thickness (z). For this characterization, I modelled the micromirror flexure to determine the residual stress variation for beam type structures (micromirror flexures, fixed-fixed beams, and cantilevers). Figure 2.21 shows the calculated stress levels from MEMCAD for each stress direction (x, y, and z) on the flexure.

From Figure 2.21, the primary stress component lies along the length (x-direction) of the structure. The stress variation along the width and thickness of the flexure are negligible when compared to the x-component. Following further MEMCAD analysis on cantilevers and fixed-fixed beams, this held true for all beam type structures where the length is much greater than the width.

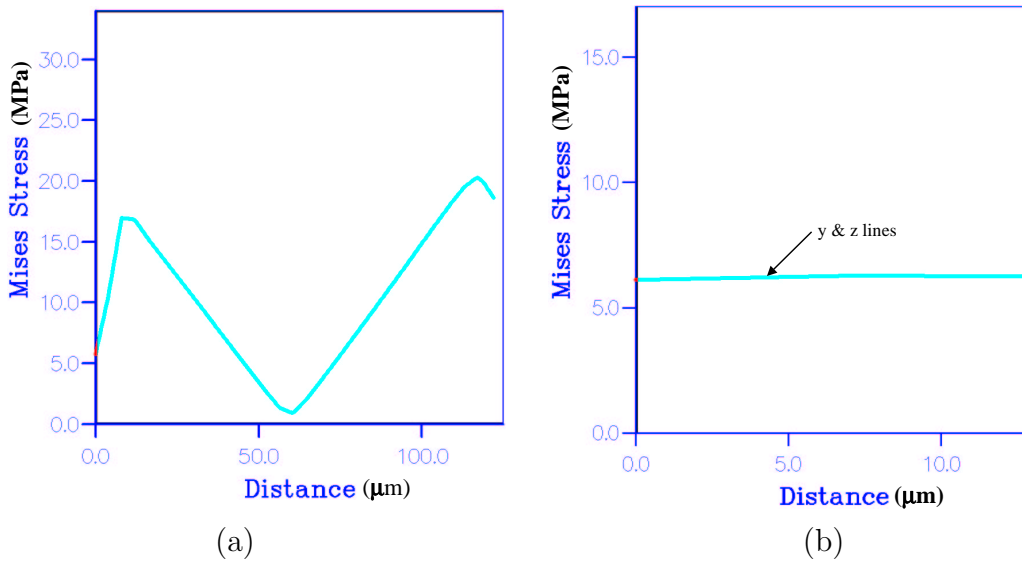


Figure 2.21: x, y, and z-stress components obtained from MEMCAD for a micromirror flexure. (a) x-component, and (b) y and z-components.

*2.6.6 Managed Simulations.* A unique component of MEMCAD that provides valuable analysis for MEMS designers is through the use of managed simulations. Once an analysis of a MEMS device has been completed, device parameters may be iterated to create a solution set for graphing or additional analysis. The simulation manager allows the creation of batch run iterations by defining one or more parameters to be varied during the simulation. Thus, a MEMS model can be run through a sequence of solver iterations using the simulation manager to vary model dimensions, material parameters, temperature or voltage values, or a variety of other boundary conditions without altering the base model. The completed solution set can be graphed or viewed in the visualizer as an animated sequence of events to clearly define trends and variations.

This type of modeling can be used to refine the device designs prior to device fabrication. This type of modeling can clearly aid in obtaining increased device yields, better design functionality, and proper device operation. The iterative modelling sequences could eliminate the need to design arrays of devices where lengths,

widths, or other device layout parameters are varied. Significant die space can be saved by eliminating or simply reducing the number of test structures used within these arrays. To illustrate the iterative technique, I analyzed a Poly1 thermal actuator where I performed the enumeration on the cold-arm of the actuator to obtain various deflection values with the same applied 5 volts. For each iteration, I lengthened the cold arm by  $50\ \mu\text{m}$ . Figure 2.22 shows the four enumerated Poly1 thermal actuators with a common displacement magnitude scale for all actuators. In Figure 2.22, the shortest thermal actuator ( $200\ \mu\text{m}$ -long) image is located in the upper left corner. This is followed by the image in the upper right, then lower left, and finally lower right. The maximum displacement in the x-direction of the smallest actuator is approximately  $7\ \mu\text{m}$  to the longest with a deflection of over  $23\ \mu\text{m}$ . From this simple model, several other enumerations could be performed to include widening of the hot and cold arms or a variation in the applied voltage to obtain voltage versus displacement profiles.

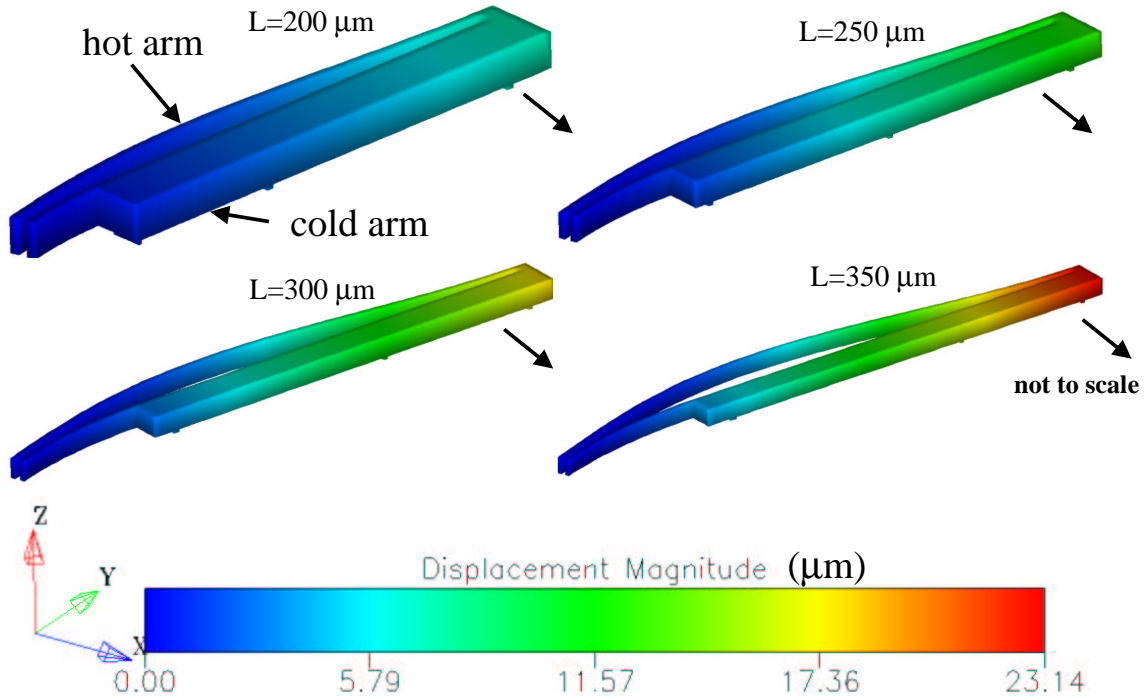


Figure 2.22: MEMCAD 3D displacement in the x-direction for an enumerated Poly1 thermal actuator. Images are not to scale.

## 2.7 Summary of Chapter II

In this chapter, I briefly addressed the two foundry fabrication processes used in this research and for completeness, I also gave an overview of the MUSiC foundry process for SiC MEMS. I addressed the buffered oxide etch now performed by the MUMPs® foundry to remove metal stringers. As a result of this etch, I decided to select slightly wider beam structures ( $> 6 \mu m$ ) for my subsequent  $\mu$ Raman spectroscopy analysis and post-processing experimentation. I modeled the MUMPs® fabrication process using *TSUPREM<sup>TM</sup>* and presented the results of my dopant concentration analysis. I conclude that dopant nonuniformity exists in both Poly1 and Poly2 (MUMPs®) structural layers that promotes an increase in residual stress and stress gradients. I also modeled several different MEMS structures using MEMCAD to assess the localized stress characteristics in various beams and flexures. Several micromirrors were modelled to assess stress propagation from the flexure-to-mirror attachment to the center of the micromirror. Finally, I performed a MEMCAD enumeration on a thermal actuator to demonstrate the added assurance the MEMS designer could employ prior to device fabrication through the use of a FEM modeling package.

## *Bibliography*

1. *TSUPREM-4 User's Manual*. 3950 Fabian Way, Palo Alto, CA 94303, December 1993. Technology Modeling Associates, Inc.
2. MEMCAD, May 1999. Microcosm Technologies Inc. Cambridge, MA 02142.
3. Cronos, MUMP<sup>®</sup>s run data. [www.memsrus.com/cronos/svcsdata45.html](http://www.memsrus.com/cronos/svcsdata45.html), 2001.
4. J. T. Butler. *Development and Packaging of Microsystems using Foundry Services*. PhD thesis, Air Force Institute of Technology (AETC), Wright-Patterson AFB OH, 1998. AFIT/DS/ENG/98-08.
5. W. D. Cowan. *Foundry Microfabrication of Deformable Mirrors for Adaptive Optics*. PhD thesis, Air Force Institute of Technology (AETC), Wright-Patterson AFB OH, 1998. AFIT/DS/ENG/98-07.
6. W. D. Cowan. Materials impacts on micro-opto-electro-mechanical systems. SPIE Conference Presentation, Sept 2000.
7. D. A. Koester, 2001. Personal Phone Communications, Cronos Integrated Microsystems Technical Processing Engineer.
8. D. A. Koester, R. Mahadevan, B. Hardy, and K. W. Markus. MUMP<sub>s</sub><sup>TM</sup> design handbook rev. 6, 2001. Cronos Integrated Microsystems, a JDS Uniphase Company, 3026 Cornwallis Rd., Research Triangle Park, NC 27709.
9. Sandia National Laboratory, 2002. Information available from the Sandia National Laboratory home page, url: <http://www.sandia.gov/mems/micromachine>.
10. Kevin C. Stark. Ninesigma music design rules, December 2001. 21945 Chagrin Blvd, Cleveland, OH 44122.

### *III. Raman Spectroscopy on MEMS Structures*

#### *3.1 Introduction*

Raman spectroscopy may be used as a non-contact method of measuring stresses at the surface of a crystalline structure. The Raman effect is observed as either the gain or loss of photon energy as a result of photon scattering from molecules or crystal lattices. It gives an indication of the lattice vibrational energy in a material in terms of frequency. As the material is strained, the energy state in the material is altered and thus the Raman frequency is different. The spatial resolution of Raman spectroscopy is on the order of one to a few micrometers [6, 27]. Thus this technique can be used to probe the local non-uniform stress distribution for various material layers. Presently, Raman spectroscopy is applied in structural chemistry, biochemistry, biology, medicine, solid-state applications, industrial applications, and materials science applications. This chapter includes a brief introduction to the history of Raman spectroscopy followed by descriptions of the instrumentation which makes up the Raman spectrometer. Raman detection improvements are addressed in addition to the Raman effect and Raman spectrum assessment. This is followed by the calculation of uniaxial and biaxial stress from the Raman spectrum. Several experimental and analytical tests are presented to characterize the Raman laser and spectrometer to include measurements of the phonon deformation potentials for MUMPs<sup>®</sup> polysilicon structural layers, laser stability, and thermal testing to identify possible heating from the focused laser beam.

#### *3.2 History of Raman Spectroscopy*

Sir C. V. Raman discovered what is now called Raman spectroscopy in the year 1928 [12]. He experimented with sunlight, a telescope, and his eyes which served as the detector. The instrumentation was crude initially but more sophisticated instrumentation was subsequently developed which included light quality holographic

gratings, improved detectors, and efficient computer treatment of the experimental data. With the introduction of Fourier transform methods, considerable improvements have been made in Raman spectroscopy. The elimination of fluorescence makes Raman spectroscopy a very popular analytical technique.

### 3.3 *Raman Instrumentation*

Five major components make up commercially available Raman spectrometers. The primary components include: an excitation source, which is generally a continuous wave (CW) laser; a sample illumination and scattered light collection system; a sample holder; a monochromator or spectrograph; and a detection system which consists of a detector, an amplifier, and an output device [12].

*3.3.1 Excitation Sources.* CW lasers such as Ar<sup>+</sup>, Kr<sup>+</sup> and He-Ne are commonly used for Raman spectroscopy. More recently pulsed lasers such as Nd:YAG, and diode lasers have been used for time-resolved and UV resonance Raman spectroscopy [12].

*3.3.2 Sample Illumination.* Since Raman scattering is inherently weak, the laser beam must be properly focused onto the sample, and the scattered radiation efficiently collected. The focusing of the laser beam onto the sample can be readily achieved because of the small diameter of the laser beam ( $\sim 1 \mu m$ ). Excitation and collection from the sample can be accomplished by using several optical configurations, such as the 90 and 180 degrees scattering geometries through polarization [12]. The 180 degrees scattering, or backscattering mode, is achieved by having the laser beam excitation source normal to the sample surface. The emitted phonons are then detected through the same optics as the laser beam excitation source.

*3.3.3 Monochromator.* A monochromator is an instrument that supplies light of one color or light within a narrow range of wavelengths. Filters (holo-

graphic notch) are used to block unwanted wavelengths and the 514.5 nm laser beam (Rayleigh scattering). The filters reduce the unwanted wavelengths by six orders-of-magnitude. In a single monochromator, extraneous light that bounces around the spectrometer may overlap the weak Raman scattered light. This is caused mainly by undiffracted light scattered from the face of the grating. Such stray light can be reduced considerably by arranging two spectrometers so that the output of one is purified by the second (double monochromator) [12]. A triple monochromator has even greater stray light rejection than a double monochromator and allows observation of Raman bands located very close to the Rayleigh line.

*3.3.4 Detection.* Since Raman signals are inherently weak, the problems involved with detection and amplification are severe. Most of the very early work was done by photographic detection using long exposure times. Furthermore, the time to develop plates and examine them with a microphotometer rendered Raman spectroscopy unfit as a routine technique. This situation has changed considerably since the development of strong laser sources and sensitive detection techniques. The charge-coupled device (CCD) has been increasingly used in recent years in Raman spectroscopy. A CCD is a device which has the form of a rectangular matrix with individual light sensitive elements. The elements convert an optical image into electrical signals or charge pulses. The output of each element can be extracted sequentially and stored for further processing. The charge pulse is stored as a number usually ranging from 0 (no light) to 65,535 (very intense light) [12]. A computer is used to reconstruct the original image by varying the light intensity for each pixel on the monitor in the proper order.

### *3.4 Raman Signal Detection*

If the Raman signal captured is weak and the signal-to-noise ratio (SNR) is poor, there are several options that can be employed to improve the quality of the data:

- Increasing the exposure time will allow the CCD array to register more Raman scattered light and will bring out the signal from the background noise. This method is recommended if the overall signal captured, including any background, is low. This method is not recommended if either the Raman peak or the background level are high. If this method is used in either of these instances, the CCD array may saturate, revealing no useful data at all.
- Accumulating the spectral data involves capturing identical spectra and co-adding them together off-chip in the personal computer (PC). This brings any weak Raman signals out of the background noise, and also reduces the noise level, when the signal is systematic and the noise is random.

These two options are often used in conjunction when attempting to improve signal detection quality. Two events which can affect the detection capabilities of the spectrometer include cosmic ray events and sample fluorescence.

*3.4.1 Cosmic Ray Events.* Cosmic Ray Events (CREs) often give rise to spurious peaks in the data that appear as very sharp emission lines. They are, however, totally random in both time of occurrence and position on the detector and can be correlated to high-energy particle passage through the CCD array causing generation of electrons, which the CCD interprets as part of the input signal [12]. However, immediate re-collection of the data should yield no such line at the same place. If a line is still apparent, it is potentially from spectral contamination (from room light, daylight, or a laser plasma line) or a detector fault (from a hot pixel with much higher noise than its neighbors) [12].

*3.4.2 Fluorescence.* High background noise in Raman spectroscopy is usually a result of sample fluorescence. Fluorescence is often intrinsic to the material of a sample and, therefore, unavoidably occurs as a result of using the laser to irradiate the sample. Fluorescence is typically not a problem with semiconductors but it depends on the the signal-to-noise ratio (SNR), sample cleaning, and preparation.

However, since fluorescence is often very much stronger than the Raman signal, it is necessary to minimize it in order to obtain the Raman signal. This can often be achieved by using the confocal mode to acquire data from the part of the sample most strongly irradiated by the laser [12]. However, if the signal from the fluorescence is too high, then the only way to avoid it is to change the excitation laser wavelength to a wavelength where the sample fluorescence is lower. By minimizing the fluorescence, an increased SNR can be achieved.

### 3.5 *Phenomenon of Raman Effect*

When a beam of monochromatic light is incident on a sample of material, some of the light is transmitted, some is absorbed, and some is scattered. Most of the scattered light has the same wavelength as the incident light. A small fraction of the scattered light, typically about one photon out of  $10^6$ , is inelastically scattered and shifted in wavelength by molecular vibrations and rotations of the molecules in the sample material [12]. The spectrum of this wavelength-shifted light is called a Raman spectrum. The intensity of Raman scattered light differs with direction. The angle between the direction of propagation of light and the Raman scattered light needs to be specified. Raman scattering is usually measured at 90 or 180 degrees from the direction of incident light.

The Raman spectrum obtained is unique for each material. When analyzing a sample containing more than one constituent, a number of peaks are observed in the Raman spectrum. The Raman peaks are characteristic of a specific type of molecule. Thus the constituents of a sample can be determined by analyzing the Raman spectrum and identifying the Raman peaks of a constituent. In Raman spectroscopy, we are looking at the vibration of the molecular bonds since we are unable to see atomic species.

### 3.6 Raman Spectrum

In  $\mu$ Raman spectroscopy, laser light is focused on the sample through a microscope to a spot size of  $\sim 1 \mu m$  in diameter. The confocal microscope, can be adjusted to analyze a surface with a spot size of about  $1 \mu m$  to a few  $\mu m$  [2]. A laser beam irradiates the sample material and the scattered light, which carries the Raman signals, is collected and directed into a spectrometer to be detected by a CCD array detector. The spectrometer measures the intensity of the Raman signal as a function of frequency. When the sample is unstressed, the spectrometer measures a reference spectrum whose center position is the peak frequency of an unstressed sample. When the sample material is placed in a stressed state, the Raman spectrum displays a shift in frequency with respect to the reference spectrum. This frequency shift is a result of the residual or induced stress in the sample material.

The scattered light consists of two types. The first, called Rayleigh scattering, is strong and has the same frequency as the incident beam ( $\omega_0$ ). The other, called Raman scattering, is very weak (intensity of  $\sim 10^{-5}$  when compared to the incident intensity) and has angular frequencies  $\omega_0 \pm \omega_m$ , where  $\omega_m$  is the vibrational frequency of a phonon [12]. The  $\omega_0 - \omega_m$  and  $\omega_0 + \omega_m$  lines are called the Stokes and anti-Stokes lines respectively. Thus, in Raman spectroscopy, one measures the vibrational frequency ( $\omega_m$ ) of molecules as a shift from the incident beam frequency ( $\omega_0$ ).

The Raman frequency shifts are independent of the frequency of the incident light. One factor that can influence the apparent Raman peak frequency is instability of the laser and spectrometer. Focusing changes of the laser on the sample may also result in a slight shift of the Raman peak obtained from crystalline silicon that has nothing to do with stress in the silicon material [27]. Another hazard lies in heating of the sample material by the focused laser beam. When the laser power is too high, the sample will be heated locally, resulting in a downshift of the Raman peak. Heating can change the local stress distribution, but can also falsify the stress results. The frequency of the Raman peak is both stress and temperature

sensitive. A difference in temperature of 4 °C induces a silicon-Raman peak shift of  $\Delta\omega = -0.01 \text{ Rcm}^{-1}$  (The unit 'Rcm<sup>-1</sup>' denotes "relative cm<sup>-1</sup>"; the frequency is always measured relative to the frequency of the laser light) [27]. A schematic of the excitation of a molecule resulting in a Raman spectrum is illustrated in Figure 3.1. Here the incident and Rayleigh scattering frequencies are the same and the Raman scattering is the frequency of the lattice vibrations.

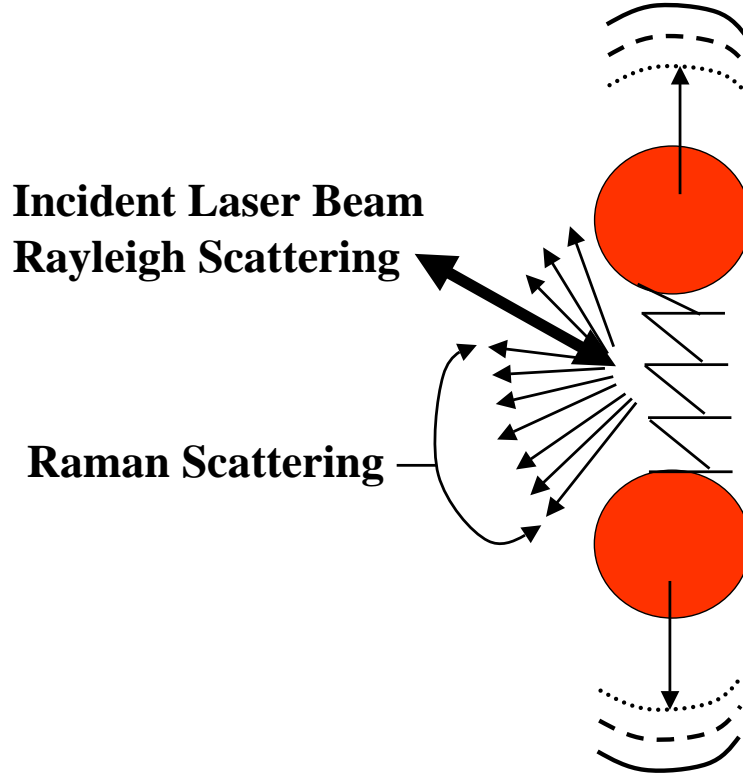


Figure 3.1: Schematic of the excitation of a molecule resulting in a Raman spectrum

During  $\mu$ Raman spectroscopy testing, the MEMS sample is moved in steps of about 1  $\mu\text{m}$  and a Raman spectrum is recorded at each step. A beam spot of  $\sim 1 \mu\text{m}$  diameter is used and has been verified using photosensitive material. The step size selected is the minimum resolution obtainable using Raman spectroscopy. This step size provides a reasonable stress profile for MEMS structures. A Lorentzian and/or Gaussian function is fitted to the measured Raman and laser peaks at each position

in order to determine the peak Raman frequency as accurately as possible. The shift of this frequency from the stress-free value,  $\omega_0$ , can be plotted as a function of the position on the sample where the corresponding spectrum was measured. To determine the sign and magnitude of the stress that corresponds to  $\omega_0$ , a hydrostatic pressure constant is used as described in Section 3.8.

Raman scattering arises from an inelastic interaction between photons (light of the incident laser) and phonons (vibrations of the crystal lattice) [27]. The frequency of the Raman signal,  $\omega_0$ , is related to the frequency of the natural lattice vibrations of the material. For unstressed crystalline silicon, the Raman peak is located at  $\omega_0 = 520 \text{ Rcm}^{-1}$  (triply degenerate) [27]. An example Raman spectrum for silicon is given in Figure 3.2. Since strain changes the frequency of the lattice vibrations, it will also shift the Raman frequency. An example Raman frequency shift for a polysilicon sample is shown in Figure 3.3. I obtain information on the local stress distribution by mapping the frequency shift,  $\omega_0$ , of the Raman peak at different positions on the sample.

*3.6.1 Benefits of Raman Spectroscopy.* There are several benefits to using Raman spectroscopy to measure the local stress in MEMS devices. The benefits include the following:

- Raman spectroscopy is a non-destructive and non-intrusive method. The observability depends on the ability to send photons to the sample and to collect those that are scattered.
- Samples can be studied in a controlled atmosphere.
- Raman spectroscopy can be easily coupled with other analytical methods.
- It offers the possibility of *in situ* stress monitoring.
- The technique is fast and relatively simple.

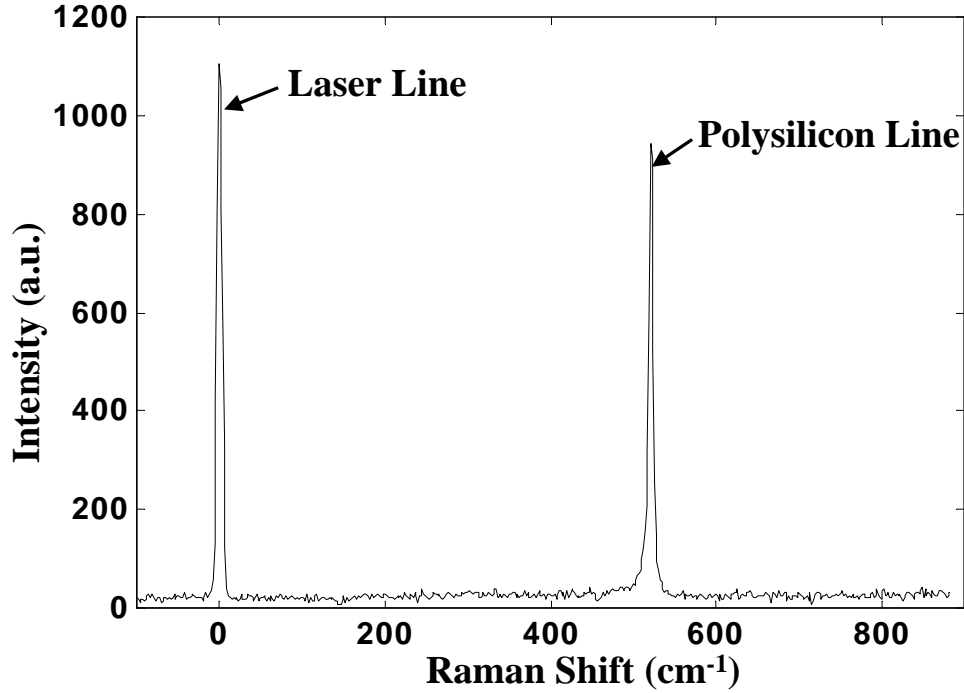


Figure 3.2: Raman Spectrum for bulk silicon using a 514.5 nm Argon ion laser excitation source.

### 3.7 Raman Frequency Shift Calculation

Mechanical strain or stress may affect the frequencies of the Raman optical phonons. For a cubic crystal, there are three independent components that are represented in the Raman secular equation along the diagonal of the matrix [2]. This equation yields the frequencies for the optical phonons in the presence of strain for a cubic crystal

My primary research goal is to show that  $\mu$ Raman spectroscopy can be used as an effective measurement technique to determine local and induced stress values in MEMS devices. Several papers have shown that  $\mu$ Raman spectroscopy is an effective measure of mechanical stress in silicon [5, 24, 25]. To achieve this goal, the focus is not on the precise value of stress, but rather on demonstrating that the stress profiles obtained from  $\mu$ Raman spectroscopy are both reasonable and helpful to the MEMS

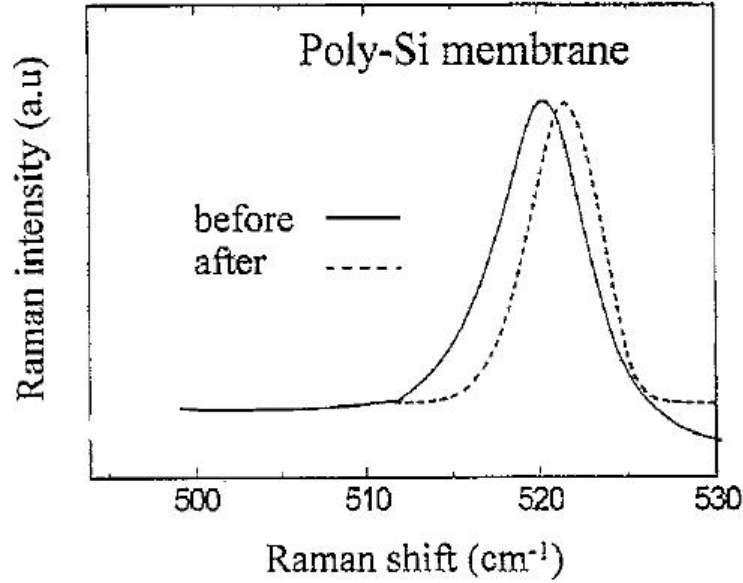


Figure 3.3: Example Raman spectral shift for a  $2.5 \mu m$ -thick polysilicon sample before and after annealing [15].

designer. However, to fully understand the data presented, it is necessary to develop the relevant theory.

Ganesan [13] was one of the first to show the effects of strain on diamond structured crystals. The Raman spectra of silicon has one peak at  $520 \text{ Rcm}^{-1}$ , which is comprised of three degenerate  $k = 0$  optical phonon modes. Using the following secular equation one can solve for the effect of strain on these optical modes:

$$\begin{vmatrix} p\epsilon_{11} + q(\epsilon_{22} + \epsilon_{33}) - \lambda_1 & 2r\epsilon_{12} & 2r\epsilon_{13} \\ 2r\epsilon_{12} & p\epsilon_{22} + q(\epsilon_{33} + \epsilon_{11}) - \lambda_2 & 2r\epsilon_{23} \\ 2r\epsilon_{13} & 2r\epsilon_{23} & p\epsilon_{33} + q(\epsilon_{11} + \epsilon_{22}) - \lambda_3 \end{vmatrix} = 0 \quad (3.1)$$

Equation 3.1 is called the Raman Secular Equation. The constants  $p$ ,  $q$ , and  $r$  are the optical phonon deformation potentials, and  $\epsilon_{ij}$  are the strain tensor components. Once Equation 3.1 is solved for the eigenvalues ( $\lambda_m$ ), it then represents

solutions to the shift in the Raman peak frequencies. In Equation 3.1, the  $e_{ij}$  (unitless) are the strain tensor components and the constants  $p$ ,  $q$ , and  $r$  (units of  $cm^{-2}$ ) are measured values for each type of crystal [25]. The difference between the Raman frequency of each phonon mode in the presence of stress,  $\omega_{m(m=1-3)}$ , and in the absence of stress,  $\omega_0$ , can be calculated from the eigenvalues  $\lambda_{m(m=1-3)}$  from Equation 3.1. The eigenvalues represent the frequency shifts [2, 25] where

$$\lambda_m = \omega_m^2 - \omega_0^2 \quad (cm^{-2}) \quad (3.2)$$

The relation between the Raman frequency of each mode and the components of the strain tensor is given by [2, 25]:

$$\Delta\omega_m = \omega_m - \omega_0 \approx \frac{\lambda_m}{2\omega_0} \quad (cm^{-1}) \quad (3.3)$$

After solving Equation 3.1 for the eigenvalues,  $\Delta\omega_m$  then provides a relation between the Raman frequencies of each of the three modes as a function of the strain. The modes, in the presence of stress, are described by the corresponding eigenvectors of the secular equation [26].

The Raman frequency shift ( $\Delta\omega_m$ ) depends on crystal symmetry, the polarization directions of the incident and detected light, and the propagation directions of the incident and detected beams with respect to the crystal axes as well as on the phonon modes of the crystal [7]. In silicon, there are three Raman optical phonon modes. In the absence of stress, these modes all have the same wavenumber  $\omega_0 = 520 \text{ Rcm}^{-1}$ ; two are transverse (TO) and one is longitudinal (LO) [7]. In the presence of stress the frequency of each of these peaks may change. In the backscattered geometry from a (100) silicon surface only the LO mode contributes to the Raman signal in the unstrained crystal. The presence of lattice strain shifts the degeneracy of these modes and changes their wavenumbers. The new wavenumbers are related to the lattice strains  $\epsilon_{ij}$  by solving the secular equation for the eigenval-

ues. The coefficients  $p$ ,  $q$ , and  $r$  are measured by observing the changes in Raman wavenumber induced by known strains. The three eigenvalues of the secular equation correspond to the shifts in Raman frequency of the three optical phonon modes.

### 3.8 Stress Calculation

From the Raman Secular Equation 3.1, under an incident laser, there will be up to three Raman frequency shifts. The frequency shifts are obtained from the elements along the diagonal of the matrix. The shifts are a function of the elastic strains in the cubic crystal, which are uniquely determined from the applied stresses. The strain components  $\epsilon_{ij}$  (unitless) are related to the stress components  $\sigma_{ij}$  (in units of Pa) by Hooke's law

$$\{\epsilon\} = [S]\{\sigma\} \quad (\text{unitless}) \quad (3.4)$$

where  $[S]$  ( $\text{Pa}^{-1}$ ) is the elastic compliance matrix for a cubic crystal structure [2,21]. For a cubic material such as silicon, the elastic compliance matrix has the following form [21]:

$$[S] = \begin{bmatrix} S_{11} & S_{12} & S_{13} & 0 & 0 & 0 \\ S_{12} & S_{22} & S_{23} & 0 & 0 & 0 \\ S_{13} & S_{23} & S_{33} & 0 & 0 & 0 \\ 0 & 0 & 0 & S_{44} & 0 & 0 \\ 0 & 0 & 0 & 0 & S_{55} & 0 \\ 0 & 0 & 0 & 0 & 0 & S_{66} \end{bmatrix} \quad (\text{Pa}^{-1}) \quad (3.5)$$

The Raman Secular Equation reduces to a cubic equation for given values of elastic strain associated with the corresponding stress field. By calculating the strain tensor components using Hooke's law, the following stress/strain relations are obtained:  $\epsilon_{11} = S_{11}$ ,  $\epsilon_{22} = S_{12}$ , and  $\epsilon_{33} = S_{13}$ . The  $S_{ij}$  are the elastic compliance tensor elements for silicon [2].

Under the assumption that stress in the sample is uniaxial or biaxial (confined along one or two axes of the cubic lattice in a cartesian coordinate system), the relation between Raman shift and stress is simply linear. Although this assumption is incorrect for many integrated semiconductor devices, it is often used as a first estimation of the magnitude of the stress in the sample material. In some structures, a significant rotational or translational stress component exists (i.e., gears, diaphragms, etc); thus, these components cannot be ignored. The uniaxial or biaxial assumption was found to be accurate for MEMS beam structures such as cantilevers, micro-bridges, and piston mirror flexures.

*3.8.1 Uniaxial Stress Calculation.* For uniaxial stress along the [100] x-direction, the Raman tensors and mode polarization vectors are not changed. The Raman spectra I obtain is not polarization dependent since we were capturing Raman data from various crystal orientations. I obtain an identical Raman spectra if polarization is used. Thus for back scattering from a (001) crystal surface, only the third Raman mode is observed. The relation between the frequency shift of this mode and the stress is given by Equation 3.3 [2, 25]. This component will provide the uniaxial stress value for the material along the x-direction, where  $\Delta\omega_1$  and  $\Delta\omega_2$ , corresponding to the phonon modes of the frequency shifts obtained from Equation 3.1, are given as

$$\Delta\omega_1 = \frac{\lambda_1}{2\omega_0} = \frac{\sigma}{2\omega_0}(pS_{11} + 2qS_{12}) \quad (cm^{-1}) \quad (3.6)$$

$$\Delta\omega_2 = \Delta\omega_3 = \frac{\lambda_i}{2\omega_0} = \frac{\sigma}{2\omega_0}[(pS_{12} + q(S_{11} + S_{12}))] \quad (cm^{-1}) \quad \text{where } (i = 2, 3) \quad (3.7)$$

Backscatter from a (001) crystalline surface corresponds to the TO phonons which represent the polarized x- and y-components. With polarization along the z-direction, this provides the Raman scattering by LO phonons.

*3.8.2 Biaxial Stress Calculation.* In the case of biaxial stress in the x-y plane, the Raman frequency shifts can be written as [25]:

$$\Delta\omega_1 = \Delta\omega_2 = \frac{\lambda_i}{2\omega_0} = \frac{\sigma}{2\omega_0}[p(S_{11}+S_{12})+q(S_{11}+3S_{12})] \text{ (cm}^{-1}\text{) where } i = 1, 2 \text{ (3.8)}$$

and

$$\Delta\omega_3 = \frac{\lambda_3}{2\omega_0} = \frac{\sigma}{\omega_0}[pS_{12} + q(S_{11} + S_{12})] \text{ (cm}^{-1}\text{)} \quad (3.9)$$

In the backscattered plane for polysilicon material, only the Raman scattering component in the z-direction will be visible. Thus the frequency shift associated with the z-direction is  $\Delta\omega_3$ . From the  $\Delta\omega_3$  expressions (Equation 3.7 and 3.9), compressive uniaxial or biaxial stress results in an increase in the Raman frequency, while tensile stress causes a decrease.

*3.8.3 Phonon Deformation Potential Experimental Determination.* To accurately determine the residual stress in the MEMS polysilicon structural layers, the determination of the phonon deformation potentials is necessary. Theoretical calculations and experimental Raman investigations on single crystal silicon have shown that a uniaxial strain along one of the  $\langle 100 \rangle$  or  $\langle 111 \rangle$  directions will result in the splitting of the triplet peak. The Raman spectra of silicon has one peak at  $520 \text{ Rcm}^{-1}$ , which is comprised of three degenerate  $k = 0$  optical phonon modes. Due to the uniaxial strain, the triplet peak is split into a singlet (one optical phonon mode) and a doublet (the remain two optical phonon modes) shifting with strain at two different rates. If a shear stress is applied, the degeneracy is completely removed meaning the triplet peak is split into three individual single optical phonon modes. One of the three single optical phonon modes will not shift with stress while the other two phonon modes will shift in two different directions. Both applied stress cases result in an observed increase in the silicon full-width-at-half-maximum (FWHM) spectrum under non-polarized Raman measurements. Hydrostatic pressure was found to

cause a linear shift in the triplet peak position without affecting its degeneracy [3]. The experimentally determined value of the phonon deformation potentials for single crystal silicon under hydrostatic pressure is [3]

$$\Delta\omega_H = 1.88 \pm 0.05 \text{ cm}^{-1}/GPa. \quad (3.10)$$

Based on measurements by Anastassakis and others, the elastic compliance constants  $S_{11}$ ,  $S_{12}$ ,  $S_{44}$  for crystalline polysilicon are nearly identical to those for silicon [3, 4, 6, 14, 27]. Thus, when performing Raman spectroscopy on polysilicon samples, it is common practice to use the cubic crystal equations developed for silicon. Therefore, I use the cubic crystal equations for silicon to model the Raman spectral data from the MEMS polysilicon layers to derive the residual stress values provided in this dissertation.

To determine the phonon deformation potentials for the MUMPs<sup>®</sup> structural layers, a set of Poly1 and Poly2 cantilevers were fabricated with dimensions of 100-200  $\mu m$ -wide by approximately 4000  $\mu m$ -long. The released cantilever structures were physically removed from the MEMS die and fastened to a plexiglass beam (plexiglass dimensions: 0.5 cm thick, 1 cm wide, and approximately 10 cm long) with commercially available spray on acrylic. A four-point bending test fixture was used to provide a known uniaxial strain on the MUMPs<sup>®</sup> Poly1 and Poly2 samples. The test set-up is depicted in Figure 3.4. The strain gage used in these experiments has a gage factor of  $2.080 \pm 0.5\%$  with a resistance of  $120.0 \pm 0.15\%$  ohms. The strain gage was cleaned and fastened to the plexiglass bar with M-bond 200 Adhesive (superglue). Contact leads were soldered to the strain gage and the resistance of the strain gage was measured using a digital multimeter to be  $120.1\Omega$ . The strain gage was then connected to a P-3500 strain indicator meter. The P-3500 is a precision instrument used with resistive strain gages for strain measurements. A zeroing potentiometer on the P-3500 was used to set the background strain to zero. Once the background strain

is set to zero, a background Raman spectrum of the polysilicon MEMS cantilever was taken to identify the initial stress state.

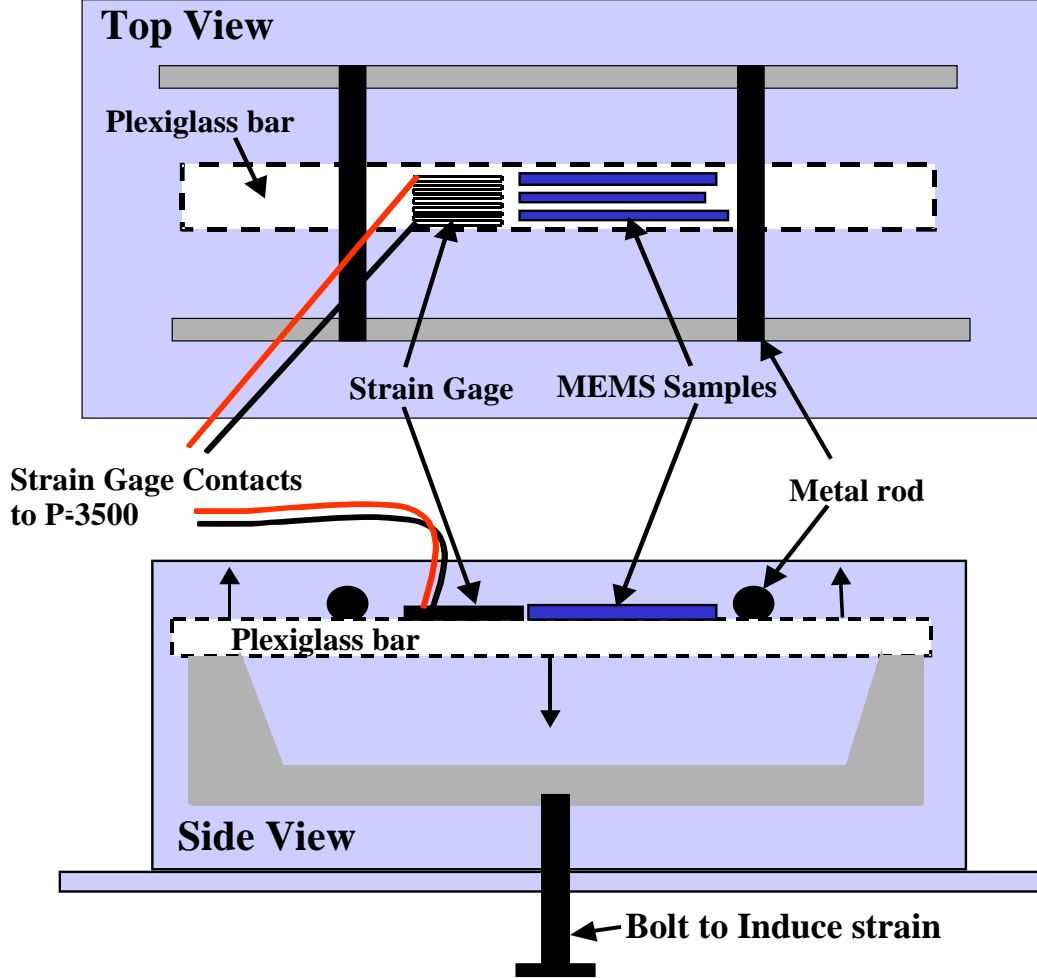


Figure 3.4: The four-point bending test fixture. (a) Top view and (b) Side view.

The induced strain tests are performed by creating a known bending moment strain on the plexiglass beam while monitoring the digital display on the P-3500 strain indicator. From controlled strain induction, the precise wavenumber shifts obtained using Raman spectroscopy can be correlated to the induced strain value. For this experiment, I adjusted the strain on the polysilicon samples in increments of  $100 \mu\epsilon$  (micro-strain (unitless)) up to  $1000 \mu\epsilon$  while capturing a single Raman spectrum at each strain level. Figure 3.2 shows typical Raman spectra used in

this study. The laser line is used to locally and individually calibrate each Raman spectrum used in this investigation.

Figure 3.5 shows the measured dependence of the polysilicon peak position on a uniaxial strain applied along the cantilever beam for polysilicon MEMS structures. Each spectral point in Figure 3.5 consists of the average of three spectra obtained from three different samples under test. The error bars in Figure 3.5 represent the variation in the peak location of the silicon peak. No change in the silicon peak FWHM was observed. It remained constant at  $5.9 \pm 0.15 \text{ cm}^{-1}$ . It should be noted that due to the average grain size of 30 nm in the polysilicon MEM structures [16], the Raman measurements obtained are averaged over a large number of randomly oriented crystals. Hence, in spite of the fact that the applied global strain is uniaxial, the observed Raman shift from local crystallites can be expected to simulate that of hydrostatic pressure. The strain dependence values obtained for Poly1 and Poly2 were  $2.19 \text{ cm}^{-1}/\text{GPa}$  and  $2.61 \text{ cm}^{-1}/\text{GPa}$  respectively. It is important to note that these values are higher than for single crystal silicon value of  $1.88 \text{ cm}^{-1}/\text{GPa}$ . This may be due to local stress concentrations expected in such loading conditions. Scatter in the data due to averaging over a large number of crystallites can also contribute to the observed high value. The difference in the strain dependence value between Poly1 and Poly2 is also expected due to differences in structural thickness and dopant concentration levels in the two cases that would lead to different local stress distribution under similar global applied strains. For all stress profiles reported in this dissertation, the experimentally determined values for polysilicon strain dependence are used to determine the localized stress in polysilicon MEMS structures.

*3.8.4 Raman Penetration Depth Calculation.* The Raman signal originates from a volume defined by the wavelength, the diameter of the laser beam, and the properties of the material under stress [25]. A short laser wavelength gives information on the stress closer to the surface since the penetration depth is inversely

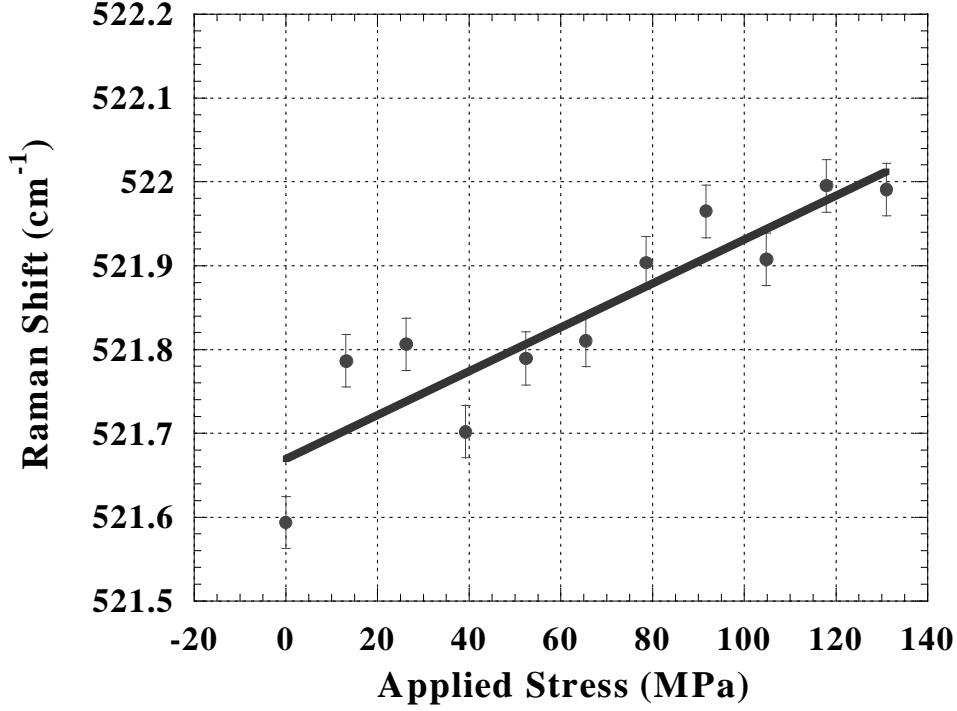


Figure 3.5: Frequency shift of the hydrostatic component for an applied uniaxial stress applied along a  $1.5 \mu m$ -thick Poly2 cantilever with dimensions of  $200 \mu m$ -wide by approximately  $4000 \mu m$ -long.

dependent on the absorption coefficient of the material [25]. A longer laser wavelength will increase the penetration depth and this results in the measured stress being a weighted average over the penetrated volume. The total scattered light intensity ( $I_s$ ) integrated from the surface to a depth  $d$  (nm), is given by

$$I_s = I_0 D \int_0^d \exp^{-2\alpha x} dx = \frac{I_0 D}{2\alpha} (1 - \exp^{-2\alpha d}) \quad (W/cm^2) \quad (3.11)$$

while that from the depth  $d$  to infinity is given by

$$I_d = I_0 D \int_d^\infty \exp^{-2\alpha x} dx = \frac{I_0 D}{2\alpha} (\exp^{-2\alpha d}) \quad (W/cm^2) \quad (3.12)$$

where  $I_0$  ( $W/cm^2$ ),  $D$  ( $cm^{-1}$ ), and  $\alpha$  ( $cm^{-1}$ ) are the incident light intensity, the Raman scattering cross section, and the photoabsorption coefficient of silicon [25]. If

the surface penetration depth,  $d_p$ , is given by the depth that satisfies the relationship  $I_d/(I_s + I_d) = 0.1$  (thus 90% absorbed within  $d$  from surface), this depth is then given by [25]

$$d_p = \frac{-\ln 0.1}{2\alpha} = \frac{2.3}{2\alpha} \quad (cm) \quad (3.13)$$

To obtain stress profiles at different depths within a material, the frequency of the laser can be adjusted to change the penetration depth. Several different laser wavelengths with associated penetration depths are shown in Table 3.1. The penetration depth for polysilicon is approximately 770 nm for a 514.5 nm laser

Table 3.1: Absorption coefficient ( $\alpha$ ) and penetration depth ( $d_p$ ) in crystalline silicon for various laser wavelengths ( $\lambda$ ) [25]

$\lambda(\text{nm})$	$h\nu$ (eV)	$\alpha 10^{-3} (cm^{-1})$	$d_p$ (nm)
514.5	2.410	14.96	770
488.0	2.541	20.18	570
457.9	2.708	36.43	320

### 3.9 Raman Spectroscopy Characterization

I performed Raman measurements with a Renishaw model 2000 Raman spectrometer equipped with a Leica microscope. The sample material is illuminated with an Ar+ laser operating at a wavelength of 514.5 nm. The Raman spectrometer collects the scattered Raman radiation which is analyzed with a monochromator and then collected by a CCD detector. Exact Raman peak positions were determined using a fitting software package (GRAMS 32) assuming a mixed Gaussian-Lorentzian peak profile [17]. I used two Renishaw model 2000 Raman spectrometers located at Wright State University (WSU) and at the Air Force Research Laboratory (AFRL). Both systems are nearly identical with the system at WSU being slightly newer. However, both Raman systems are configured, calibrated, and operated in exactly the same way during experimental testing.

Several potential conditions exist which can shift the Si-Raman peak including laser and spectrometer variations, sample heating, and laser focusing. Experimental and analytical calculations were performed to establish a baseline for Raman testing. I characterized both Raman spectroscopy systems before performing residual and induced stress analysis testing. Some of the characterization experiments included unstressed silicon testing, laser focusing, laser/spectrometer stability tests and analytical and experimental thermal tests.

*3.9.1 Unstressed Silicon Characterization.* Literature values for the Raman peak of unstressed silicon range from 519-523  $Rcm^{-1}$  [5, 6, 8, 26]. This spectral range variation equates to a stress value of approximately 2.0 GPa. Although most researchers use 520  $Rcm^{-1}$  as the value for unstressed silicon, I decided to measure my own value for unstressed silicon since the MEMS samples used in this research have low stress values (i.e. MPa of stress). Following significant research and experimental testing into the determination of the correct spectral constant for unstressed silicon, I found the value to be system dependant. I investigated an undoped electronic grade silicon wafer which should have minimal residual stress. I took a series of Raman spectra from the identical electronic grade silicon sample from each of the Raman systems. With the Raman laser line set to 0  $Rcm^{-1}$ , the Raman system at WSU provided an optimal value of approximately 521.0  $Rcm^{-1}$  for the electronic grade silicon test sample. The Raman system at AFRL initially provided an optimal value of 519.5  $Rcm^{-1}$  for the electronic grade silicon test sample.

The AFRL Raman system was later calibrated by a factory representative and the silicon peak was remeasured to be 520.5  $Rcm^{-1}$  [10]. Raman systems are commonly calibrated to detect unstressed silicon samples in the range of 520-521  $Rcm^{-1}$  [10]. The Renishaw representative also confirmed that changing the neutral density filters to assist in reducing the laser power does not affect the overall calibration of the system [10]. Following the calibration, the white light (camera) cross-hairs which are used for optical alignment on the sample and the spot location

of the laser beam were misaligned. This misalignment makes it difficult to establish the proper Raman scan line on the MEMS structures during Raman spectral analysis. Thus, I primarily used the Raman spectroscopy system at WSU for my dissertation research with the results presented in Chapters 4-7. For the WSU Raman system, I used the value of  $521 \text{ Rcm}^{-1}$  as the unstressed silicon peak frequency and confirmed this value through initial calibration and setup prior to performing daily Raman scans. These confirmation measurements ensure the calibration did not drift and the system is properly initialized.

*3.9.2 Laser Focusing.* Focusing changes of the laser on the sample material may result in a shift of the Si-Raman peak that has nothing to do with stress [27]. In typical Raman spectroscopy, where the sample is a wafer of fabricated electronic devices, the line or area scans employed by Raman spectroscopy are taken on a flat surface over the entire scan line or area. When using Raman spectroscopy for released MEMS structures, I no longer have a flat surface over the complete length of a cantilever, beam or flexure. This is true especially when the MEMS device is electrostatically actuated. A MEMS device fabricated using the MUMPs® foundry process can have a maximum deflection of  $2 \mu\text{m}$  for Poly1 structures and  $2.75 \mu\text{m}$  for Poly2 structures. Although the anchors of the structures are in focus, the remaining beam or flexure should become slightly out of focus as the MEMS structure is pulled closer to the substrate.

The majority of the Raman scans I performed were on unreleased MEMS structures. For unreleased structures, the Raman scans are similar to a wafer scan where the sample layer is a flat surface. For my released beam structures, the scan lengths are typically  $100 \mu\text{m}$ - $135 \mu\text{m}$ -long. Over this length, the beams' deflection is minimal and can be assumed to be flat. I periodically observed the spot size of the laser on the beam during a released and unreleased Raman scan. The spot size and focus of the laser on the sample remained constant through visual monitoring and with respect to the polysilicon peak intensity of the Raman spectra. If the intensity

of the silicon line decreases, the laser may not be focused properly. However, the intensity of the polysilicon line remained nearly constant over the scan length.

*3.9.3 Laser Stability.* During all Raman scans, both the silicon and laser lines are displayed for each Raman spectrum. From a single curve fit file, I am able to obtain the peak positions for both the laser line and the silicon line. The laser line is used as the reference point for all Raman spectra. I wrote a Matlab program to adjust the laser line to zero which corresponds to the frequency of the argon laser of 514.5 nm. The laser offset that I measured is used as a reference for each accompanying silicon spectral peak. This reference is used to adjust the location of the silicon peak prior to a calculation of the associated stress in the sample material. With the above technique, the location of the silicon peak is always referenced to the laser line ( $0 \text{ Rcm}^{-1}$ ). This technique helps reduce the variations which could occur due to laser or spectrometer instability.

To verify the laser stability, I conducted two separate experimental tests. The first test involved a series of 15 repeated Raman scans taken over the same  $100 \mu\text{m}$ -long by  $10 \mu\text{m}$ -wide Poly1 fixed-fixed beam. The laser beam was temporarily removed from the sample while the previous Raman spectrum was curve fitted and spectral maps generated. The off time was equivalent to approximately one minute. This would help prevent any possible thermal effects from altering the residual stress profiles.

The laser stability profile for a released Poly1 fixed-fixed beam is shown in Figure 3.6. The variation between all repeated Raman scans for the Poly1 beam are illustrated by the error bars. On average, the residual stress variations (error bars) are within approximately 80 MPa for all Raman scans. Figure 3.7 shows the residual stress variation for an unreleased  $100 \mu\text{m}$ -long by  $10 \mu\text{m}$ -wide Poly2 fixed-fixed beam. The variation for Poly2 beams is also approximately 80 MPa. From both figures, the stability curves obtained from Raman spectroscopy fall within the residual stress

variations of approximately 100 MPa. Thus, the drift in the spectrometer does not vary outside the measurement capabilities.

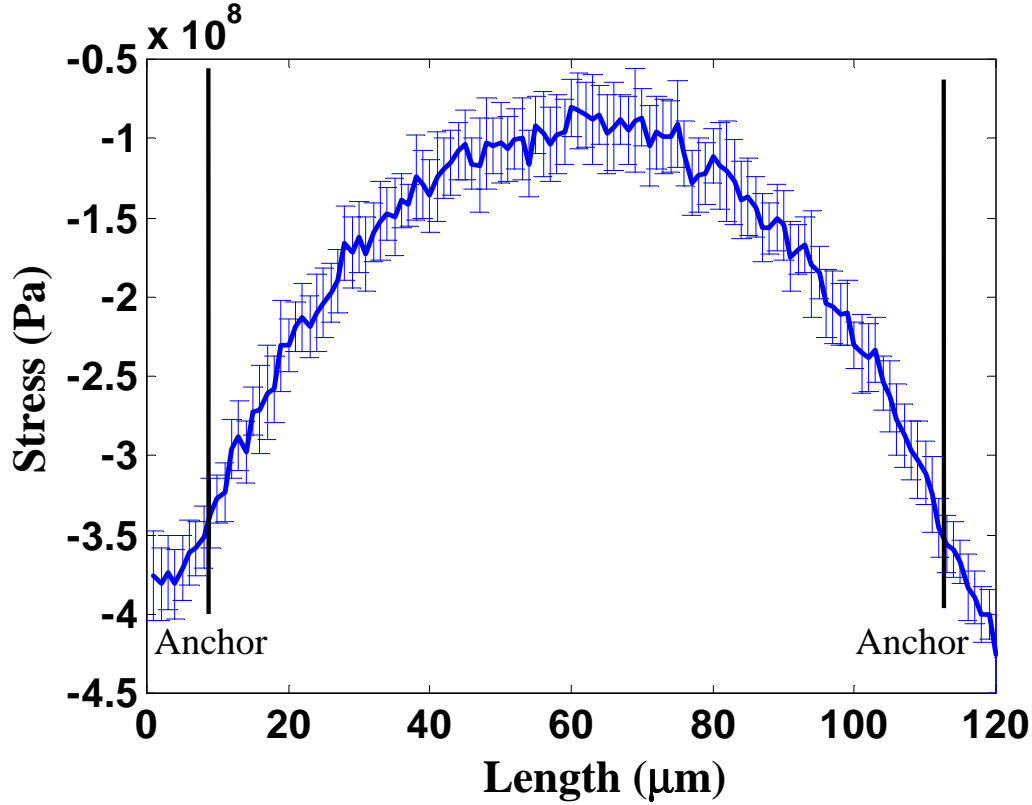


Figure 3.6: Laser stability stress curve for a 100  $\mu m$ -long by 10  $\mu m$ -wide released Poly1 fixed-fixed beam measured with the Raman spectroscopy system at WSU.

The second stability test consists of individual Raman scans of the same Poly2 fixed-fixed beam prior to each Raman test session. This test is used to identify spectrometer variations over time to ensure the  $\mu$ Raman spectrometer remains within the established test specifications. The plotted Raman scans shown in Figure 3.8 were obtained over a one year period. Figure 3.8 shows that the overall residual stress variations remained within approximately 100 MPa.

Although the laser power could not be readily monitored, the laser power was periodically checked between Raman scans to verify consistent laser power levels.

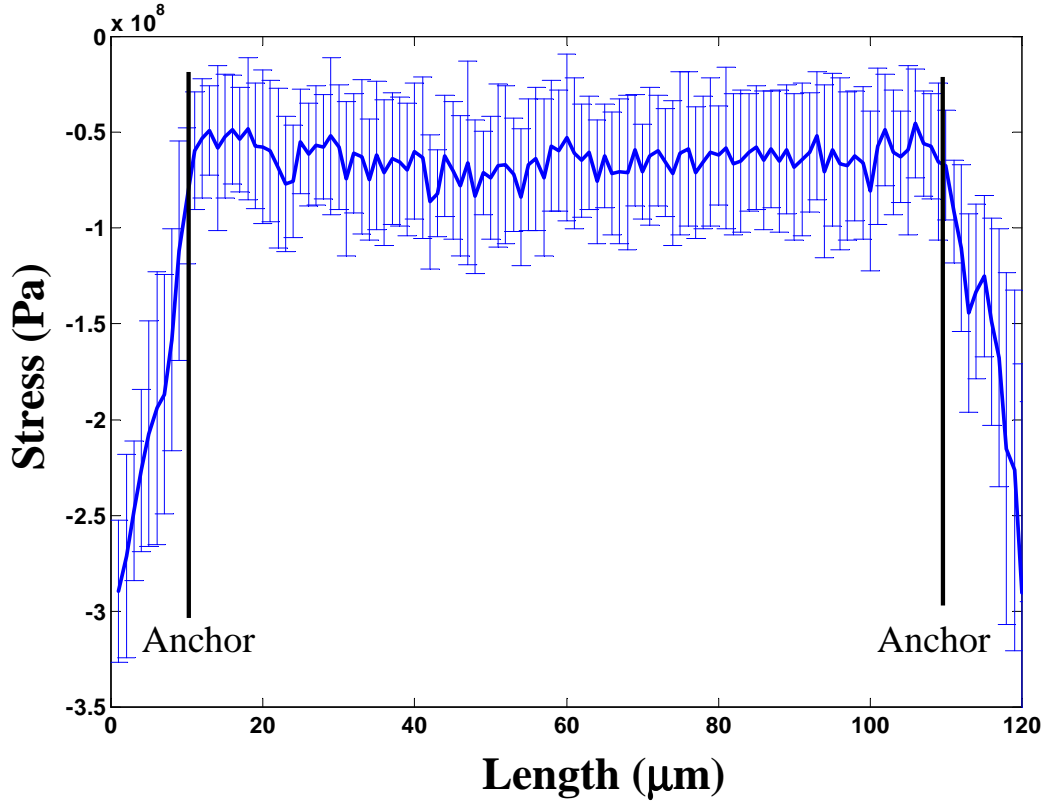


Figure 3.7: Laser stability stress curve for a 100  $\mu m$ -long by 10  $\mu m$ -wide unreleased Poly2 fixed-fixed beam measured with the Raman spectroscopy system at WSU.

This test was performed to eliminate possible abnormalities in the Raman spectra and limit potential thermal heating of the sample.

*3.9.4 Analytical Thermal Model.* Since the shifts in the Raman spectra are sensitive to both temperature and stress, I need to analytically determine the temperature rise of the MEMS fixed-fixed beam due to the laser beam while under test. One can derive an analytical thermal model based on the various mechanisms of heat loss in the structure. Figure 3.9 illustrates the possible mechanisms that will aid in reducing the temperature of the fixed-fixed beam structure [9, 19].

As shown in Figure 3.9, four heat loss processes exist for dissipating the heat build up in the fixed-fixed beam: (1)  $H_{bridge}$  - heat conduction through the

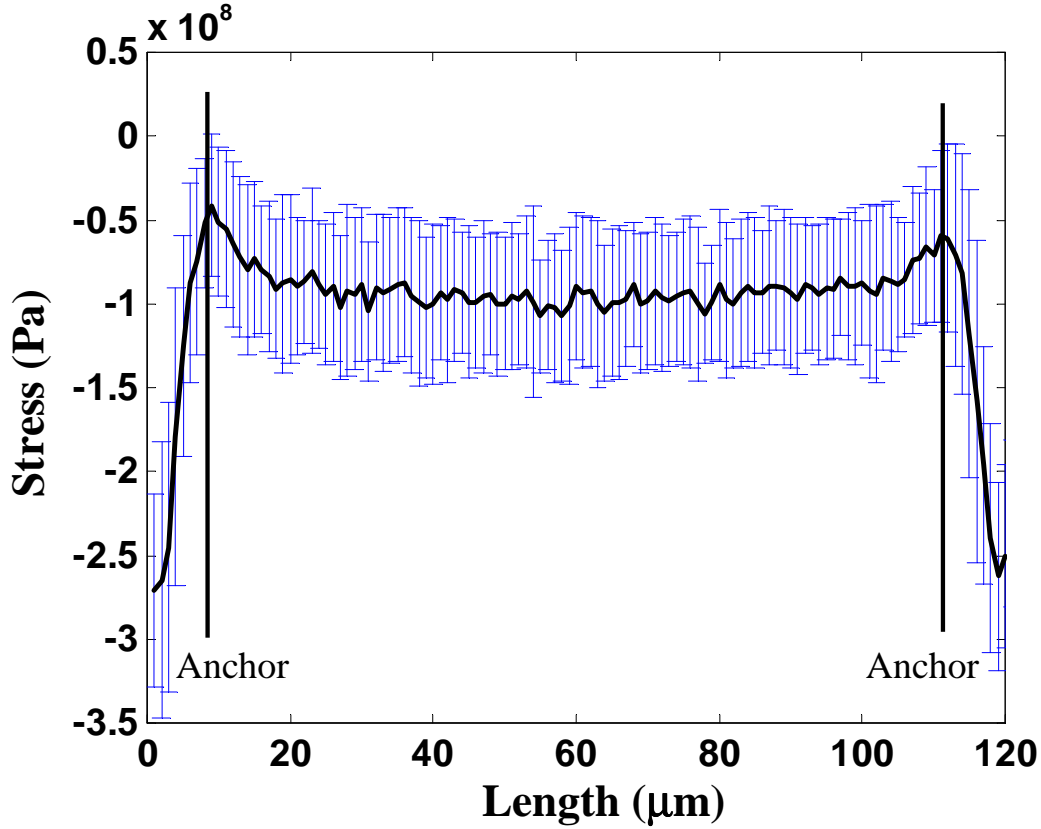


Figure 3.8: Laser stability variations for a Poly2 fixed-fixed beam as measured with the Raman spectroscopy system at WSU. (Obtained over a one year period and consists of 87 Raman beam scans)

bridge; (2)  $H_{conduction}$  - heat conduction through the surrounding gas into the substrate; (3)  $H_{convection}$  - heat loss through convection into the surrounding gas; and (4)  $H_{radiation}$  - heat loss through thermal radiation [9,19]. During my Raman tests, no gas flow is used as the fixed-fixed beam under test only has ambient air surrounding the structure. However, for future *in situ* tests, the MEMS structures could be placed in annealing test fixtures where  $N_2$  or argon gas flows can be used.

An equivalent thermal circuit model can be derived from the heat loss mechanisms and is shown in Figure 3.10. The various components of the thermal circuit model include the following:  $G_b$  - the thermal conductance for heat flow through the beam,  $G_g$  - the thermal conductance for heat flow through the surrounding gas

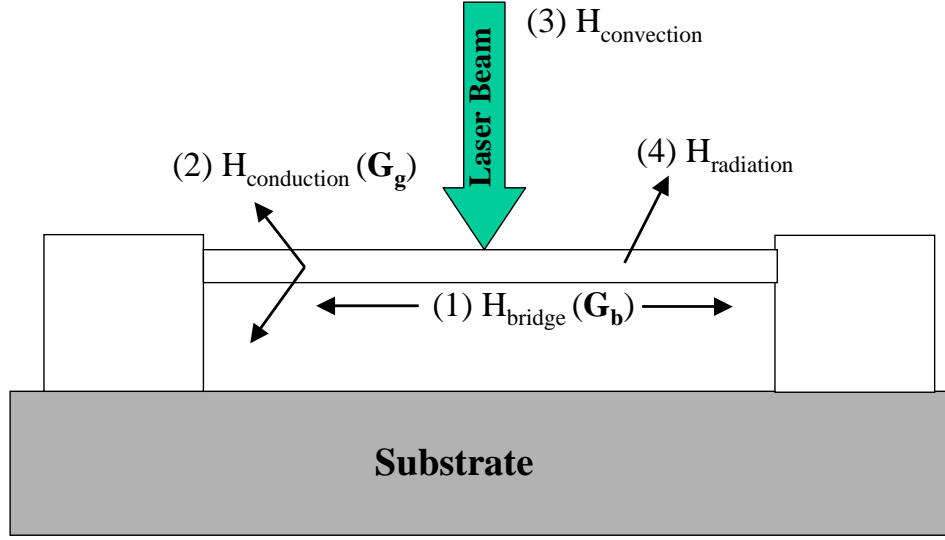


Figure 3.9: Heat loss mechanisms for a polysilicon microbridge [9, 19].

to the substrate,  $C_b$  - the thermal capacity of the beam,  $I_B$  - represents the power into the system,  $T_b$  is the temperature of the beam, and  $T_s$  is the substrate temperature [9, 19]. With the use of Raman spectroscopy, I need to eliminate or significantly reduce the level of heat generation due to the laser. Thus, the thermal radiation conductance can be omitted and is not shown in the thermal circuit model since this device will not operate at temperatures high enough to generate substantial thermal radiation.

The thermal circuit model shown in Figure 3.10 provides a means to estimate the temperature rise of the fixed-fixed beam due to the Raman laser. Similar thermal circuit models have been used to model the behavior of lateral thermal actuators and thermal piston micromirrors [9, 11]. The power provided to the system, represented by the variable  $I_b$ , is the optical power  $P_o$  not reflected by the beam surface and given by the following equation [11];

$$I_b = P_o(1 - R_{beam}) \quad (W) \quad (3.14)$$

where  $R_{beam}$  is the reflectance of the beam surface. I measured the reflectance of both Poly1 and Poly2 material layers to be approximately 31% at the Raman laser wavelength of 514.5 nm. The laser power was measured to be 2.4 mW on the surface of the Poly1 and Poly2 fixed-fixed beam samples.

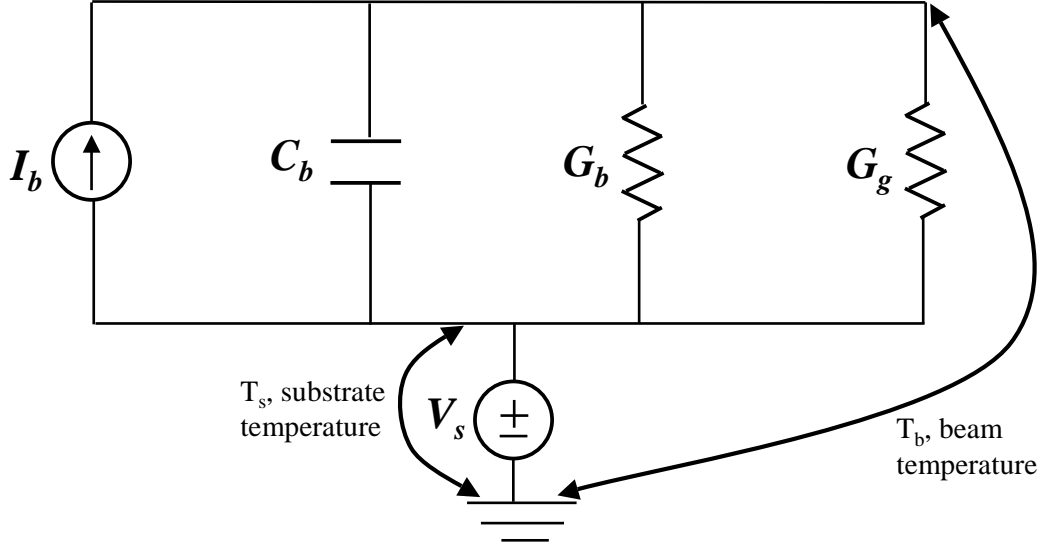


Figure 3.10: Equivalent thermal test circuit for a fixed-fixed beam [9, 11].

The thermal energy deposited on the beam is conducted primarily to the substrate through the polysilicon beam ( $G_b$ ) and at a far reduced level through the volume of gas directly beneath the beam ( $G_g$ ). Three assumptions are made to allow for this simplified model: (1) the beam has high thermal conductivity so its temperature remains fairly uniform; (2) the substrate is an infinite heat sink at room temperature (fixed at a constant  $25^\circ C$ ); and (3) the heat loss or transfer due to radiation is negligible.

The values of the components in Figure 3.10 are calculated using the physical dimensions of the structure and the material properties of polysilicon and the surrounding gas (ambient air). In the thermal model circuit, the equations to determine

$C_b$ ,  $G_b$ , and  $G_g$  are given as [9, 19]:

$$C_b = \rho_b C_p w t l \quad \left( \frac{kgm^2}{s^3K} \right) \quad (3.15)$$

$$G_b = \frac{N_{poly} w t}{l} \quad \left( \frac{kgm^2}{s^3K} \right) \quad (3.16)$$

$$G_g = \frac{F_s N_{air} w l}{h} \quad \left( \frac{kgm^2}{s^3K} \right) \quad (3.17)$$

where  $\rho_b$  is the density of the beam ( $2.33 \times 10^3 \text{ kg/m}^3$ ),  $C_p$  is the thermal capacity of the polysilicon beam ( $7.54 \times 10^2 \text{ JKg}^{-1}\text{K}^{-1}$ ), and  $N_{poly}$  (30 W/m-K) and  $N_{air}$  (0.02 W/m-K) are the thermal conductivities of the polysilicon and the surrounding gas [19].  $F_s$  (unitless) is the shape factor which accounts for the impact of the shape of the element on the heat-transfer to the gas, and  $h$  ( $\mu m$ ) is the gap distance between the beam and the substrate [9]. The length, width, and thickness are represented by  $l$ ,  $w$ , and  $t$  respectively. The values used in Equation 3.15, 3.16, and 3.17 are provided in Table 3.2.

Table 3.2: Material and Physical Parameters used in the Thermal Equations

Parameter	Value	Description
$h$	2.0 $\mu m$ or 2.75 $\mu m$	Elevation above substrate [1]
$C_P$	$7.54 \times 10^2 \text{ JKg}^{-1}\text{K}^{-1}$	Heat capacity of polysilicon [23]
$F_S$	1.6 (Poly1), 1.55 (Poly2)	Element shape factor [9]
$N_{air}$	$2.0 \times 10^{-2} \text{ Wm}^{-1}\text{K}^{-1}$	Thermal conductivity of air
$N_{poly}$	$30 \text{ Wm}^{-1}\text{K}^{-1}$	Thermal conductivity of polysilicon [11, 22]
$T_S$	25 $^{\circ}C$	substrate temperature

The shape factor  $F_s$  variable in Equation 3.17 accounts for fringing heat flux effects which are a function of the shape of the element and its elevation above the substrate [18, 19]. For arbitrary shapes,  $F_s$  is found by using computationally intense numerical methods or conformal mapping [19]. However, if a Manhattan (rectangular) geometry is assumed, the calculation for the shape factor can be accurately and

simply reduced to the empirical equation [9,18]:

$$F_s = \frac{t}{w} \left( \frac{2s}{t} + 1 \right) + 1 \quad (\text{unitless}) \quad (3.18)$$

where  $s$  is the elevation above the substrate and  $t$  and  $w$  are the thickness and width of the element. For Manhattan structures, this equation is accurate to within five percent of the answer obtained from the numerical method previously used by Mastrangelo [9,19]. For a typical 2  $\mu m$ -thick Poly1 fixed-fixed beam with dimensions of 10  $\mu m$ -wide by 100  $\mu m$ -long gives a shape factor of 1.6 and 1.55 for a 1.5  $\mu m$ -thick Poly2 beam.

From the thermal circuit model for the polysilicon beam in Figure 3.10, the temperature rise of the polysilicon beam is

$$T_b = P_o(1 - R_{beam})Z \quad (K) \quad (3.19)$$

where  $Z$  is equal to  $1/Y$ , and the value for  $Y$  is given by

$$Y = \sqrt{Z_1^2 + C_b^2} \quad \left( \frac{kg \ m^2}{s^3 \ K} \right) \quad (3.20)$$

where  $Z_1$  ( $kgm^2/s^3K$ ) is the parallel combination of the thermal conductance for heat flow through the element  $G_b$  and the thermal conductance for heat flow through the surrounding gas to the substrate  $G_g$ . Thus, the theoretically calculated temperature rise in a Poly2 beam for a Raman laser power level of 2.40 mW is approximately 1.381°C and 1.225°C for a Poly1 beam. An increase in the temperature of 4 °C results in a -0.01  $Rcm^{-1}$  shift in the Raman spectrum [27]. This shift equates to an increase in compressive stress of approximately -3.757 MPa. Thus, the theoretical temperature rise values will induce compressive stress values of approximately -1.726 MPa and -1.531 MPa respectively.

I experimented with a second laser-induced temperature rise calculation presented by Metzger [20] to further assess the thermal heating condition. Metzger's assumptions include: 1) the heat loss due to radiation and transport via the gas phase are neglected; 2) the laser beam profile is assumed Gaussian in intensity; and 3) the surface reflectivity and thermal conductivity are assumed to be independent of temperature [20]. Metzger's equation to calculate the temperature rise is [20]

$$\Delta T = \frac{P(1-R)}{2\sqrt{\pi}\omega K} \quad (K) \quad (3.21)$$

where  $P(1-R)$  is the absorbed laser power,  $R$  is the power reflectance of the absorbing surface,  $\omega$  is the  $1/e^2$  laser beam radius, and  $K$  is the thermal conductivity of the material [20]. By using the above equation, the temperature rise in the polysilicon material is calculated to be approximately  $0.043^\circ C$ . Although the Metzger model provides a lower temperature rise, this model assumes that the entire structure is attached to an infinite heat sink. For the MEMS structures that I analyzed, this is not the case. Thus the first model provides a better measure of the expected temperature rise during my Raman scans.

Both analytical models estimate a slight temperature rise in the polysilicon sample. The Poly2 layer has the largest increase in temperature with an estimated Raman frequency shift of  $0.0034 \text{ cm}^{-1}$  (equivalent to approximately -1.726 MPa of induced compressive stress). Since the current resolution of the  $\mu$ Raman spectroscopy systems at WSU and AFRL are approximately 40 MPa, the thermal effects are likely to be undetected. Several experimental tests are performed on the critical buckling beam arrays using the selected 2.40 mW laser power level. These tests will help assess the thermal affects and/or possible temperature rise of the MEMS buckling beam structures.

*3.9.5 Experimental Thermal Tests.* Raman spectroscopy is commonly used on microelectronic devices to determine ion implant locations and areas of high stress

within the microelectronic device. When using Raman spectroscopy in the above applications, thermal heating is minimal since the entire wafer can be considered an infinite heat sink. However, when using Raman spectroscopy for MEMS applications, thermal heating can be significant since an infinite heat sink no longer exists except at the anchor points. Due to the significant difference between the thermal conductivities of polysilicon (30 W/mK) and air (0.02 W/mK), the primary means of removing any generated heat will be via the MEMS structural material. Heat dissipation through the air will be minimal when compared to the structural material. Thus, the primary method of dissipating heat in the beam is via the beam material to the accompanying anchors.

Using the neutral density filters located on the spectrometer, the laser power can be reduced at the sample to eliminate structural heating. There are five possible neutral density filter positions for the WSU and AFRL Raman systems. The associated measured power levels are shown in Table 3.3. Both spectrometer systems used in this research have similar power levels at the MEMS sample when the power control knob on the AFRL laser is turned completely counterclockwise. This position corresponds to the lowest possible power level obtainable from the laser. Position #1 in Table 3.3 corresponds to the lowest possible power level of the laser without utilizing a neutral density filter. The laser power was measured using a Newport Model 840 hand-held optical power meter. To determine proper laser power levels for reliable and repeatable Raman spectra, several Raman scans were performed at each neutral density position. The collection on-times of the spectrometer were adjusted accordingly to permit proper phonon detection. Through these tests, I determined that the laser power required to obtain reliable and repeatable Raman spectral data on the polysilicon MEMS structures must be set to approximately 2.4 mW. At this power level, the signal-to-noise ratio is reasonable and the residual stress profiles from the Raman scans are repeatable. Lower power levels created unreliable and inconsistent results.

Table 3.3: Measured Raman Laser Power Levels for both Raman Systems.

Neutral Density Filter	Power Level (mW)
#1	2.40
#2	1.10
#3	0.42
#4	0.20
#5	0.04

To determine if the selected 2.40 mW laser beam causes thermal heating, several experimental tests were performed on both Poly1 and Poly2 fixed-fixed beams. Both structural layers were tested since the thickness of the material layers differ (Poly1 is 2  $\mu m$ -thick and Poly2 is 1.5  $\mu m$ -thick). Due to the significant impact heat generation has on the residual stress level, I performed several tests in an attempt to determine if the residual stress is increasing due to thermal effects from the selected laser power level. A series of Raman tests were performed on Poly1 and Poly2 fixed-fixed beams, (100  $\mu m$  long by 10  $\mu m$  wide) both before and after release. The thermal tests were performed by placing the laser beam in the center of the beam (both lengthwise and widthwise) and repeatedly taking a Raman spectrum at a rate of one spectrum per second. I performed the repeated spectral scans for five minutes since the beam should reach an elevated steady state temperature well within this time period. This test should create an increase in the compressive residual stress if localized heating occurs. This test also helps in determining laser and spectrometer stability for this time period. Under the assumption that both polysilicon structural layers in the MUMPs<sup>®</sup> process have identical thermal conductivities, with similar structural dimensions, the Poly2 beam will be more susceptible to laser heating due to its thinner structural layer. Figure 3.11 illustrates the raw and curvefit peak residual stress level at a single point on a Poly2 beam as a function of time. The x-axis correlates to a 5-minute scan period (300 Raman spectra).

From Figure 3.11, the stress level remains within 80 MPa over the complete 5-min time frame. The stress value initially decreases for the first minute and then

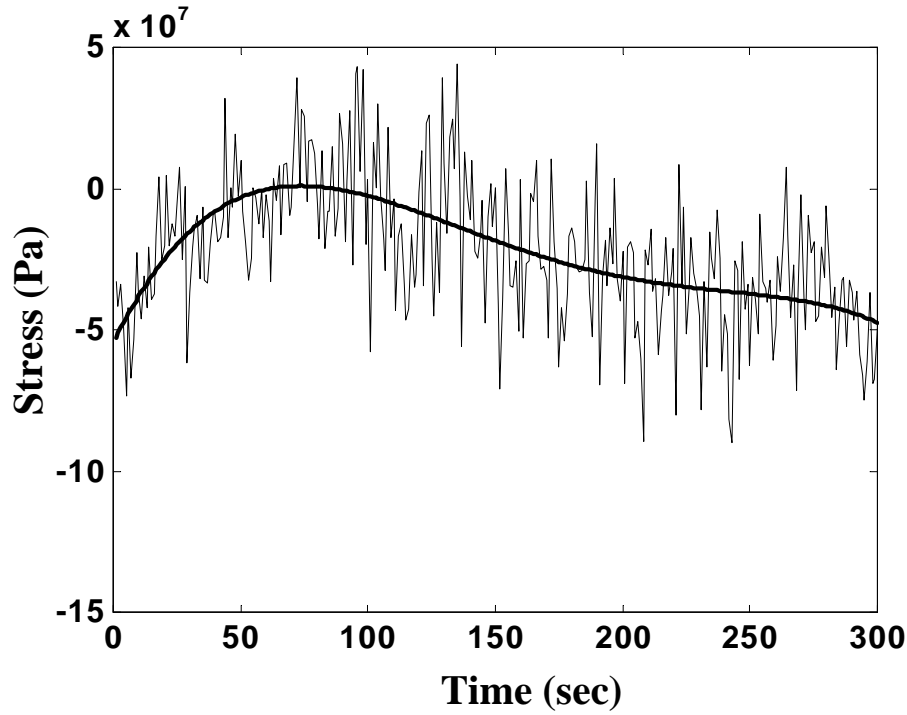


Figure 3.11: Thermal stability test (5-minutes) for repeated Raman scans on a Poly2 fixed-fixed beam

increases slightly over the remaining 4-minutes to approximately the initial residual stress value. If the beam was being heated, the residual stress would have increased initially and continued to increase until a steady state temperature is reached. Since this did not occur, it appears the beam is not heating up significantly. If I look at the variations in the stability of the Raman system for a Poly2 beam (Figure 3.7), the error bars are approximately 80-90 MPa. The thermal stress variation in Figure 3.11 falls within the approximate 100 MPa resolution of the spectrometer. Therefore, I cannot quantify if the beams are in fact being heated up due to the Raman laser and thermal heating cannot be confirmed from this test. A Poly1 beam was also tested under identical conditions with similar results. The stability of the spectrometer appears to be stable over the 5-min time period.

A 5-hour thermal and stability test was performed on the same Poly2 beam used earlier with the laser beam positioned in nearly the same location as the previous

test. The Raman scan rate was set to 30 seconds for the 5-hour time period. From Figure 3.12, the released beam stress profile again remains fairly constant with a slight increase in compressive stress for most of the time period. The maximum variation of the residual stress of the released beams is approximately 50-80 MPa. This again falls within the established error bars for the WSU Raman system and no thermal heating can be identified from this test. The Raman spectrometer appears to be stable over this 5-hour time period.

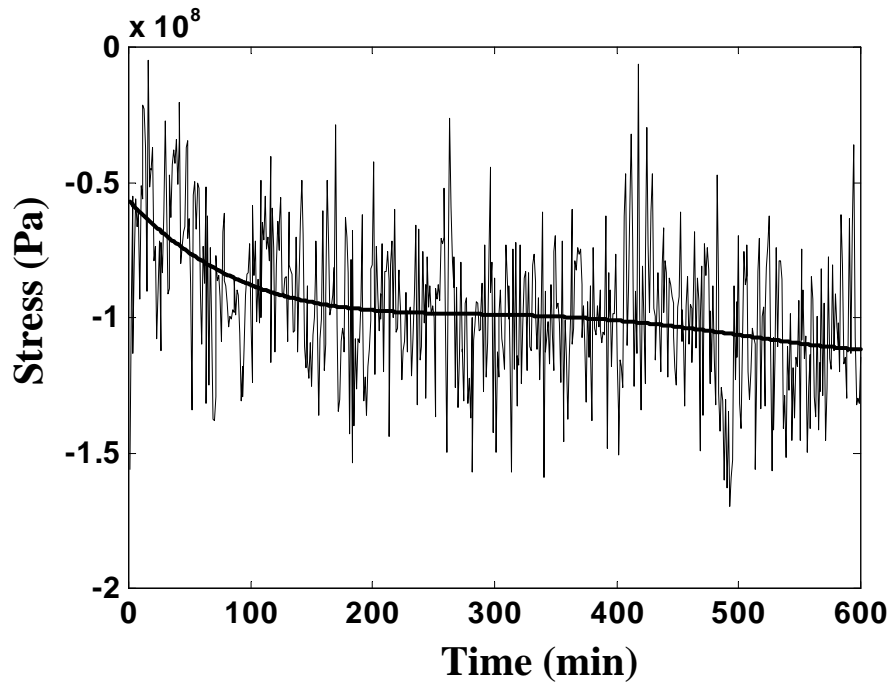


Figure 3.12: Thermal stability test (5 hours) for repeated Raman scans on a Poly2 fixed-fixed beam.

Although the analytical solution for the thermal effect of the laser beam on the MEMS sample appears to be minimal, a series of Raman scans were performed on released MEMS buckled fixed-fixed beam arrays. Through the use of an interferometric microscope (IFM), I determined the critical buckling lengths for both the Poly1 and Poly2 fixed-fixed beam arrays. I then performed a Raman scan on the first unbuckled beam. If the unbuckled beam heats up due to the laser, the beam will buckle since an increase in temperature results in an increase in the compres-

sive stress. By using the temperature/stress correlation presented by De Wolf [27], the measured stress can be determined by using 162 GPa as the measured value for Young's modulus for polysilicon. The compressive stress variation between the two Poly2 beams with lengths of 370  $\mu m$  and 380  $\mu m$  respectively is approximately -0.46 MPa (equivalent to a temperature increase of approximately 0.49  $^{\circ}C$ ). Since the unbuckled 370  $\mu m$  beam remained unbuckled (see Figure 3.13), no localized heating of the beam is present for this laser power level. If the beam would have buckled, the Raman spectrum would resemble the 380  $\mu m$  scan as shown in Figure 3.13.

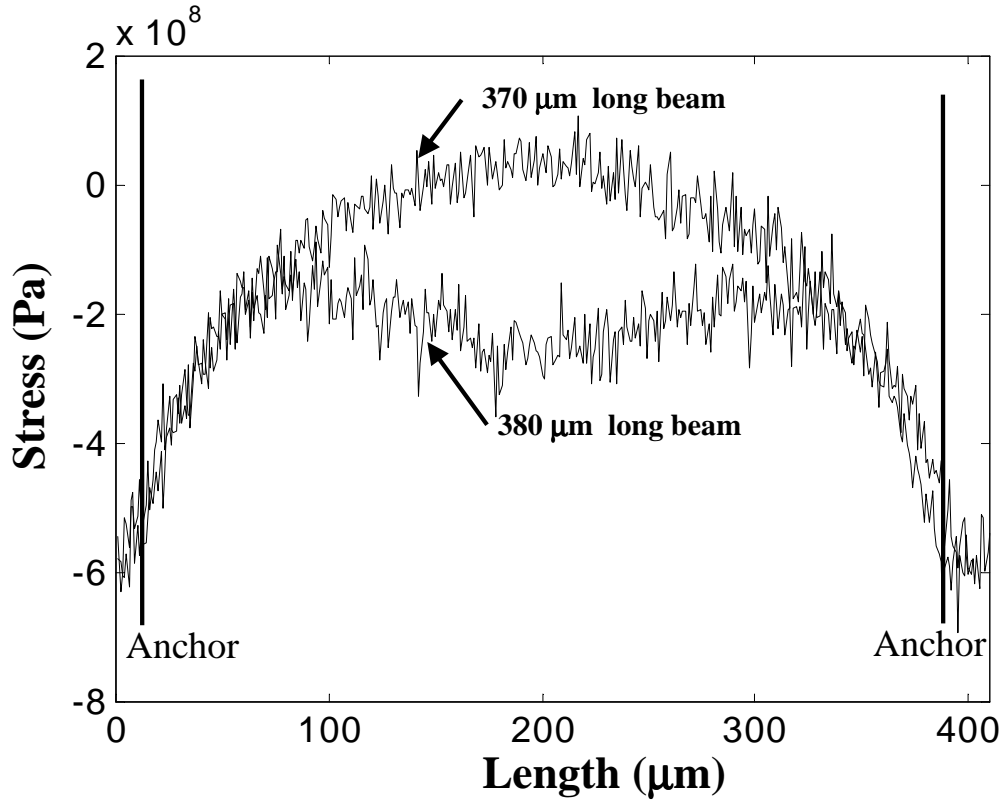


Figure 3.13: Thermal stability test on 370  $\mu m$  (unbuckled) and 380  $\mu m$  (buckled) Poly2 fixed-fixed beams

Identical Raman tests were performed on 490  $\mu m$  (unbuckled) and 500  $\mu m$  (buckled) Poly1 beams. The variation in compressive stress between these two beams using an experimentally determined value for Young's modulus of 131 GPa equates to -0.285 MPa. No localized heating was observed since the 490  $\mu m$  unbuckled beam

remained unbuckled following the Raman scans. Thus, I can conclude that significant thermal heating does not exist for the laser power level (2.40 mW) that I selected.

### 3.10 Summary of Chapter III

In this chapter, I provide a brief background on  $\mu$ Raman spectroscopy and the instrumentation which encompasses a Raman spectroscopy system. I performed a complete Raman spectroscopy characterization of my experimental systems to assess reliability, repeatability, thermal effects, and stability. The hydrostatic pressure constant is determined for both Poly1 and Poly2 structural layers from a MUMPs® test die. These are the first published values for these constants pertaining to the MUMPs® foundry fabrication process. The hydrostatic pressure constant is equivalent to the combination of the three phonon deformation potential constants ( $p$ ,  $q$ , and  $r$ ) used in the Raman secular equation. I used a simple thermal circuit model to estimate the temperature increase due to the laser beam. This model predicts a slight temperature rise; however, the increased temperature is unlikely to be detected with the current Raman system due to resolution limitations. In addition, I performed several experimental tests to assist in the identification of thermal effects on the Raman spectra. From both the analytical and experimental results, it does not appear the MEMS fixed-fixed beams in my MEMS test die are being significantly heated as a result of the laser used for my Raman measurements. Overall, the measurement accuracy of the  $\mu$ mRaman systems as stated in Renishaw literature is approximately  $0.1 \text{ Rcm}^{-1}$ . This value equates to approximately  $-38.3 \text{ MPa/cm}$  of stress. From Figure 3.5, the  $\mu$ mRaman resolution can be experimentally determined through interpolation of the change in stress to the change in the Raman frequency shift. From Figure 3.5, for an applied stress range from 0-120 MPa, the obtained Raman frequency shifted by approximately  $0.32 \text{ Rcm}^{-1}$ . This value equates to approximately  $38.4 \text{ MPa/cm}$  of stress. Thus, the smallest resolution we can attain is approximately  $40 \text{ MPa/cm}$ .

## Bibliography

1. Cronos, MUMP<sup>®</sup>s run data. [www.memsrus.com/cronos/svcsdata45.html](http://www.memsrus.com/cronos/svcsdata45.html), 2001.
2. S. T. Amimoto, D. J. Chang, and A. D. Birkitt. Stress measurements in mems using Raman spectroscopy. In *SPIE Conference on Materials and Device Characterization in Micromachining*, volume 3512, pages 123–129, Santa Clara, California, September 1998.
3. E. Anastassakis, A. Cantarere, and M. Cardona. Piezo-Raman measurements and anharmonic parameters in silicon and diamond. *Physical Review B*, 41(11):7529–7535, April 1990.
4. E. Anastassakis and E. Liarokapis. Polycrystalline Si under strain: Elastic and lattice-dynamical considerations. *Journal of Applied Physics*, 62(8):3346–3352, October 1987.
5. E. Anastassakis, A. Pinczuk, E. Burstein, F. H. Pollak, and M. Cardona. Effect of static uniaxial stress on the Raman spectrum of silicon. *Solid State Communications*, 8(2):133–138, 1970.
6. E. M. Anastassakis. *Dynamical Properties of Solids*. North-Holland Publishing Company, Athens 147, Greece, 1980.
7. A. Atkinson and S. C. Jain. Spatially resolved stress analysis using Raman spectroscopy. *Journal of Raman Spectroscopy*, 30:885–891, 1999.
8. M. S. Benrakkad, M. A. Benitez, J. Esteve, J. M. Lopez-Villegas, J. Samitier, and J. R. Morante. Stress measurement by micro-Raman spectroscopy of polycrystalline silicon structures. *Journal of Micromechanical Microengineering*, 5:132–135, 1995.
9. J. T. Butler. *Development and Packaging of Microsystems using Foundry Services*. PhD thesis, Air Force Institute of Technology (AETC), Wright-Patterson AFB OH, 1998. AFIT/DS/ENG/98-08.
10. Renishaw Corp. Private communication with Renishaw representative. Renishaw system calibration performance.
11. W. D. Cowan. *Foundry Microfabrication of Deformable Mirrors for Adaptive Optics*. PhD thesis, Air Force Institute of Technology (AETC), Wright-Patterson AFB OH, 1998. AFIT/DS/ENG/98-07.
12. J. R. Ferraro and K. Nakamoto. *Introductory Raman Spectroscopy*. Academic Press, Inc., San Diego, CA, 1994.
13. S. Ganesan, A. A. Maradudin, and J. Oitmaa. A lattice theory of morphic effects in crystals of the diamond structure. *Annals of Physics*, 56:556–594, 1970.

14. S. Greek, F. Ericson, S. Johansson, M. Fürtsch, and A. Rump. Mechanical characterization of thick polysilicon films: Young's modulus and fracture strength evaluated with microstructures. *Journal of Micromechanical Microengineering*, 9:245–251, 1999.
15. G. Kaltsas, A. G. Nassiopoulou, M. Siakavellas, and E. Anastassikis. Stress effect on suspended polycrystalline silicon membranes fabricated by micromachining of porous silicon. *Sensors and Actuators A*, 68:429–434, 1998.
16. D. A. Koester, 2001. Personal Phone Communications, Cronos Integrated Microsystems Technical Processing Engineer.
17. R. Krawietz, W. Pompe, and V. Sergo. Raman spectroscopic investigation of the stress state in silicon substrates near edges of Pt/PZT microstructures. *Crystal Research and Technology*, 35(4):449–460, April 2000.
18. L. Lin and M. Chiao. Electrothermal responses of lineshape microstructures. *Sensors and Actuators*, A55:35–41, 1996.
19. C. H. Mastrangelo. *Thermal applications of microbridges*. Ph.D. dissertation, University of California Berkeley, 1991.
20. D. Metzger and H. Reichl. Laser bumping process for GaAs devices. *Microelectronics Journal*, 28:475–487, 1997.
21. J. F. Nye. *Physical Properties of Crystals*. Oxford Science Publications, Oxford, 1964.
22. O. M. Paul, J. Korvink, and H. Baltes. Determination of the thermal conductivity of CMOS IC polysilicon. *Sensors and Actuators A*, 41-42:161–164, 1994.
23. W. Reithmuller and W. Benecke. Thermally excited silicon microactuators. *IEEE Transactions on Electron Devices*, 35(6):758–762, June 1988.
24. M. Siakavellas, E. Anastassikis, G. Kaltsas, and A. G. Nassiopoulos. Micro-Raman characterization of stress distribution within free standing mono- and poly-crystalline silicon membranes. *Microelectronic Engineering*, 41/42:469–472, 1998.
25. I. De Wolf. Micro-Raman spectroscopy to study local mechanical stress in silicon integrated circuits. *Semiconductor Science Technology*, 11:139–154, 1996.
26. I. De Wolf and H. E. Maes. Stress measurements in silicon devices through Raman spectroscopy: Bridging the gap between theory and experiment. *Journal of Applied Physics*, 79(9):7148–7156, May 1996.
27. I. De Wolf and H. E. Maes. Mechanical stress measurements using micro-Raman spectroscopy. *Microsystem Technologies*, 5:13–17, 1998.

## *IV. Stress in MEMS Structures*

### *4.1 Chapter Overview*

The properties of low pressure chemical vapor deposition (LPCVD) polysilicon are known to vary significantly, depending on the exact deposition conditions and the post-deposition processes. The control of stress in thin films is important in the processing of micro-electro-mechanical structures. Compressive stress may cause buckling of clamped freestanding films. Both tensile and compressive stress can affect the mechanical properties of devices such as the sensitivity of pressure sensors. Therefore, for both development and process control, it is important to determine the stress in thin films.

In this chapter, I briefly address some of the sources of residual stress and the effects this stress has on micro-electro-mechanical systems (MEMS) structures. Next, I address several quantitative methods to experimentally measure the localized residual stress and Young's modulus through on-chip test structures. I chose to use buckling beam arrays and comb drive resonators to measure the localized residual stress and Young's modulus. The buckling beam arrays and comb drive resonators are common test structures used in MEMS. From these test structures, I determine the residual stress and Young's modulus for both Poly1 and Poly2 structural layers made using the MUMPs<sup>®</sup> foundry process.

Additionally, I characterize the foundry-fabricated residual stress levels in Poly1, Poly2, and Poly1-Poly2 fixed-fixed beams, cantilevers and piston micromirror flexures through the use of  $\mu$ Raman spectroscopy. These are the first-of-their-kind published measurements using Raman spectroscopy on MUMPs<sup>®</sup> test structures. I generated line stress profiles for each of these MEMS structures to determine the stress magnitudes along the length of each MEMS structure. Stress maps are generated for a Poly1 fixed-fixed beam, cantilever, and micromirror flexure to illustrate the localized stress distribution with respect to the length and width of the test

structures. Finally, I measure the induced stress levels in a piston micromirror flexure during device electrostatic actuation and compare these results to a MEMCAD finite element model of the stress distribution in the flexures during actuation.

#### *4.2 Sources of Film Stress*

A typical polysilicon film used for MEMS devices consists of columnar grains that grow in a conical form out of a transition layer. The transition layer has small grains and resides at a polysilicon/silicon nitride interface [21]. This transition layer causes a high compressive stress. Further away from the underlying layer, the magnitude of the compressive stress decreases. Columnar grains are formed if one crystal orientation is preferred during film growth [21]. The initial distribution of grain orientations is random, but those grains with their preferred growth orientation parallel to the film normal dominate over the inclined grains during growth competition [21]. Once the columnar microstructure has been reached, atoms can immediately add to the fast-growing crystalline planes without inducing any compression.

Another possible origin of compressive stress in thin polysilicon films is impurities that are incorporated during deposition. Absorbed oxygen on the surface of the growing film decreases the surface mobility of the arriving silicon atoms. This results in a less ordered structure with vacancies and interstitial atoms. Figure 4.1 illustrates the origin of compressive stress in silicon due to interstitials in grain boundaries. Atoms in the grain boundaries and interstitials produce a high compressive stress, while vacancies can absorb a part of the compressive stress.

Stresses can develop in thin films due to mismatched lattice constants, different thermal expansion coefficients between different materials, and as a result of the growth process [14]. Stress gradients can be induced by variations in the deposition/growth process. Various problems associated with stress include nucleation, propagation of dislocations, and the formation of voids and cracks [14]. The residual stress in the thin films may influence dopant diffusion, affect hot carrier degradation,

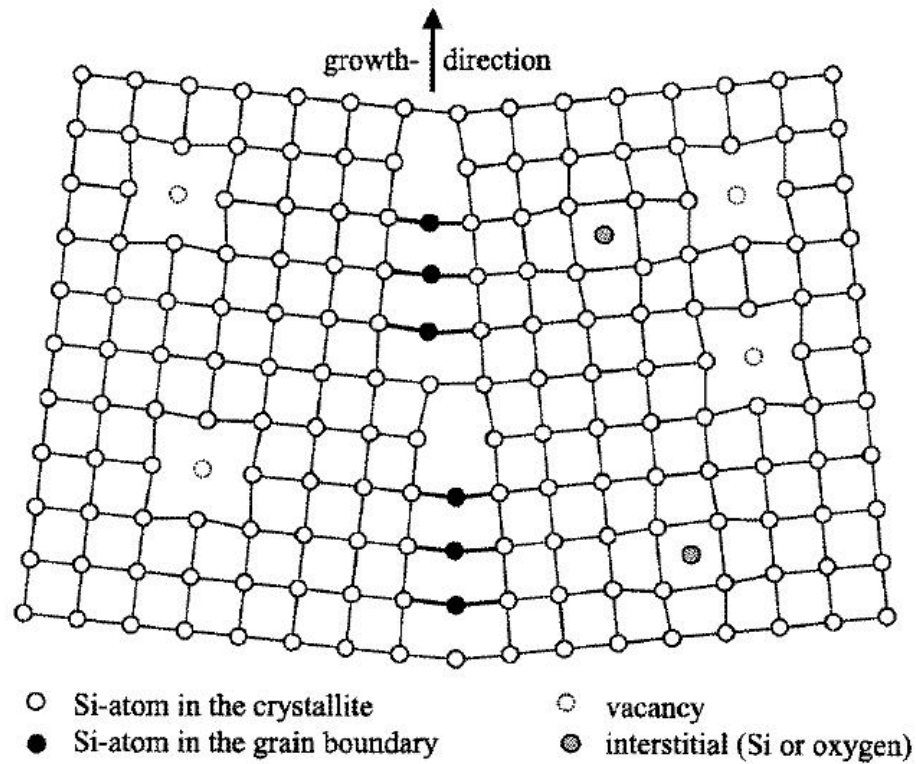


Figure 4.1: Known causes of stress in crystalline silicon. [21]

and jeopardize the oxide reliability. Many of these problems become more acute with the increasing complexity and miniaturization of the devices.

#### 4.3 Residual Stress

Residual stress and residual stress gradients through the thickness of the polysilicon film are critical constraints on microstructure designs. If the average stress is compressive, micro-bridges will buckle if longer than a critical length. Stress gradients generate an internal bending moment that causes cantilever beams to warp (up or down) out-of-plane upon release [13]. As deposited, undoped and non-annealed polysilicon is under compressive stress, for all deposition temperatures using chemical vapor deposition (CVD) [25]. The main factor that causes this stress is the grain boundary formation rather than the grain size [25]. The residual stress has a

significant dependence on the film thickness. The highest compressive stress during deposition is created in the first 200 nm of film thickness [21]. For thicker films, the compressive stress starts to decrease. The stress starts to relax significantly if the film becomes thicker than 350 nm [21].

Doped Polysilicon samples can have either a tensile or compressive residual stress level following deposition. Polysilicon that is annealed below the deposition temperature maintains its residual stress. If the polysilicon is annealed above its deposition temperature (typically 620 °C), the compressive stress starts to decrease with increasing temperature. It is not possible to induce tensile stress by annealing [3]. A structure with many crystal defects can have the resultant stress minimized through higher annealing temperatures. At higher temperatures, the atoms can rearrange themselves, thus the number of crystal defects decreases which reduces stress. The residual stress in polysilicon increasingly relaxes with a higher concentration of phosphorus. Doping and grain structure are important factors which affect the intrinsic stress in polycrystalline silicon [15].

#### *4.4 Background Raman Stress Profiles and Characterization*

Prior to investigating post-processing techniques, a background study was necessary to determine the residual stress profiles for unreleased and released MEMS test structures. I performed background Raman scans on fixed-fixed beams (Poly1, Poly2, and Poly1-Poly2 stacked), Poly1 and Poly2 cantilevers, and Poly1 and Poly2 piston micromirror flexures to identify the initial residual stress levels in these unreleased MEMS structures. Following the HF release of the MEMS structures as outlined in Appendix A, I again took Raman scans for the selected MEMS structures. I obtained Raman stress maps from each type of MEMS test structure to identify the stress distribution magnitudes along the length and width of the structures.

4.4.1 *Analytical Stress Model for a Fixed-Fixed Beam.* Before Raman stress profiles can be verified, an analytical fixed-fixed beam stress profile was generated. The analytical solution provides insight into the characteristic freestanding fixed-fixed beam residual stress profiles measured using Raman spectroscopy. The analytical model is based on a freestanding fixed-fixed beam with a uniform load distribution (gravity).

Figure 4.2 shows the analytical diagram used to determine the residual stress profile for a fixed-fixed beam with a uniform load. The load  $g$  is the distributed load due to gravity.  $R_1$  and  $R_2$  are the resultant forces, and  $M_1$  and  $M_2$  are the moments about the beam [23]. For a released fixed-fixed beam with a uniform distributed

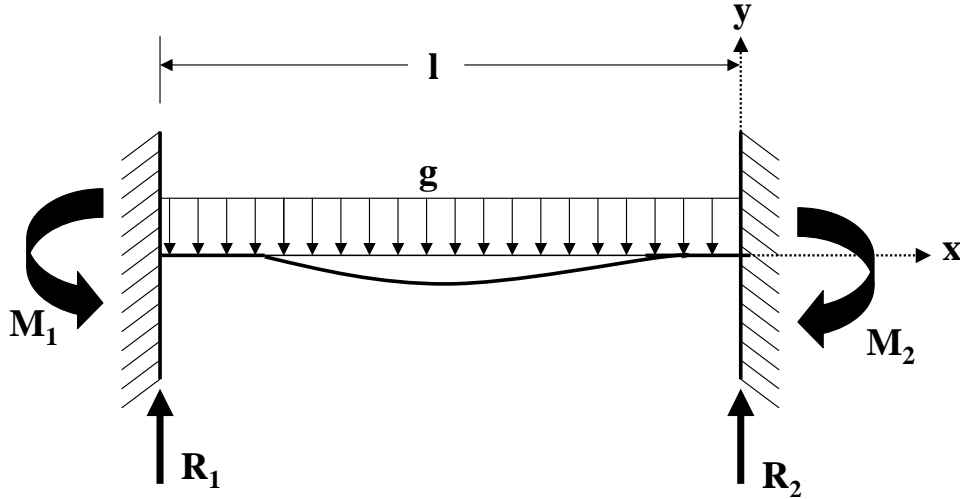


Figure 4.2: Analytical stress model for a MEMS fixed-fixed beam [24].

load, the residual stress can be calculated by the following equation [23]

$$\sigma = \frac{M(x)y}{I} \quad (Pa) \quad (4.1)$$

where  $M(x)$  is the moment about the beam and is given by [23]

$$M(x) = \frac{g}{12}(6lx - 6x^2 - l^2) \quad (N/m) \quad (4.2)$$

where  $g$  (N/m) is the distributed load,  $l$  ( $\mu m$ ) is the beam length, and  $x$  ( $\mu m$ ) is a selected position along the length of the beam respectively. For the analytical stress model calculation plotted in Figure 4.3, I stepped the value of  $x$  from 0-100  $\mu m$  (model beam length). The distributed load  $g$  for this beam model is given by

$$g = G\rho A \quad (N/m) \quad (4.3)$$

where  $G$  is the gravitational acceleration on earth ( $9.8066 \text{ m/s}^2$ ),  $\rho$  is the density of polysilicon ( $2.33 \times 10^3 \text{ kg/m}^3$ ) [18], and  $A$  is the cross sectional area of the beam ( $A = wh$  where  $w$  is the width and  $h$  is the thickness of the beam, respectively).

The compressive residual stress along the length of the beam can be considered a uniform load since this stress will produce a constant uniform applied force within the material layer (similar to Figure 4.2). The analytical fixed-fixed beam profile representing a uniform applied force due to gravity is shown in Figure 4.3. Although the stress due to gravity is 8-9 orders of magnitude less than what I am able to measure with  $\mu m$ Raman spectroscopy, the Raman stress profiles presented later for released fixed-fixed beams clearly resemble the stress profile shown in Figure 4.3 due to gravity. This model can be applied to all fixed-fixed beams with different lengths and/or thicknesses when a uniform load is applied.

*4.4.2 Fixed-Fixed Beams.* Several different fixed-fixed beam structures were designed having lengths of 100  $\mu m$ -long and widths ranging from 1 to 20  $\mu m$ -wide. The Raman experimentation for this section is limited to beams with widths of 10  $\mu m$ -wide. At this width, proper Raman scan alignment is readily obtainable. The Raman xyz-stage did not have a theta or rotational adjustment. I made the theta adjustment manually by rotating the MEMS test die positioned on the stage. The Raman assessment includes taking both background and post release Raman scans for both structural layers (Poly1 and Poly2) along with the Poly1-Poly2 stacked structural layer. The 100  $\mu m$ -long by 10  $\mu m$ -wide fixed-fixed beam arrays are the

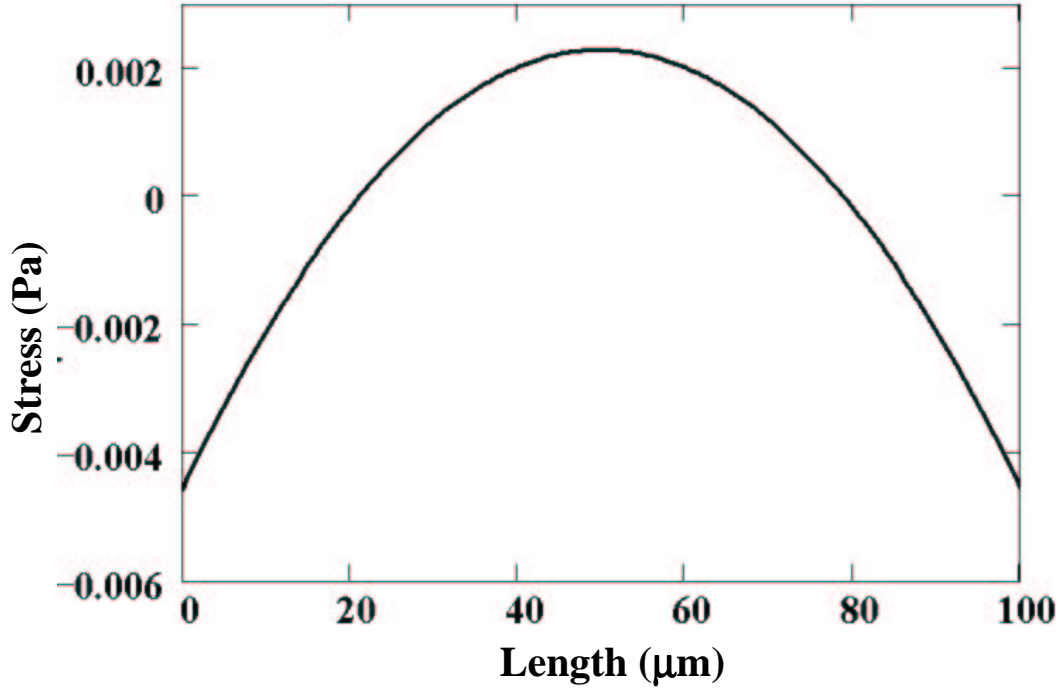


Figure 4.3: Analytical stress profile of a fixed-fixed beam with a uniform load.

primary test structures used in the annealing and doping residual relaxation assessments outlined in Chapters 4 and 5. The background scans establish a baseline for the residual stress prior to release. Figure 4.4 illustrates the residual stress profiles for the Poly1, Poly2 and Poly1-Poly2 stacked structural layers available in the MUMPs® foundry process. Each stress profile consists of the average of three repeated Raman scans to help eliminate spectral variations. Also each spectrum is referenced to the laser line to eliminate possible laser/spectrometer variations.

The residual stress measurements in Figure 4.4 display nearly identical stress profiles except for the stress magnitudes. This difference is due to the fabrication procedures (i.e. dopant concentrations and number of anneals performed during fabrication) for each structural layer.

Figure 4.5 illustrates several stress images of a 100  $\mu m$ -long by 10  $\mu m$ -wide Poly1 fixed-fixed beam. The stress images include: Figure 4.5a) the stress map of the residual stress for the beam with respect to its length and width; Figure 4.5b) the

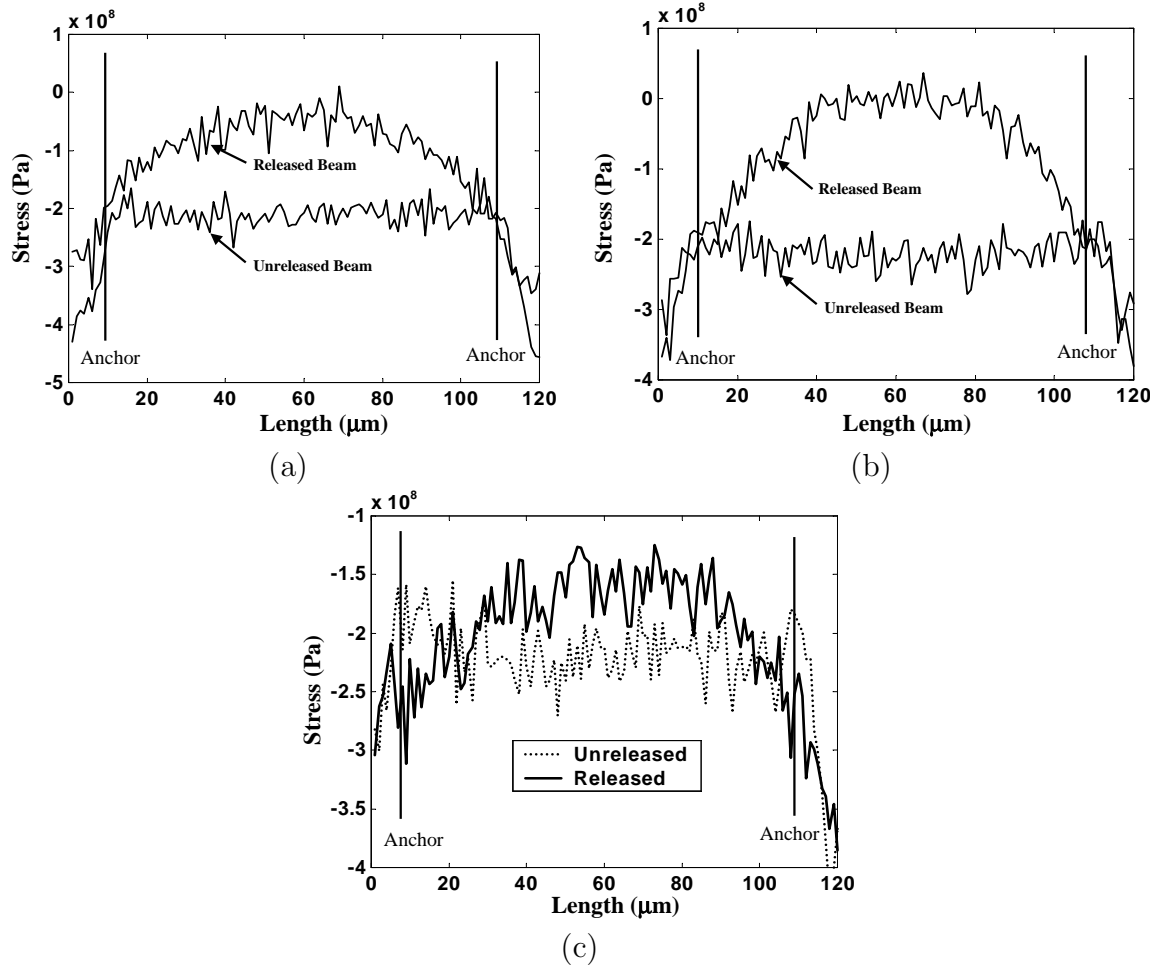


Figure 4.4: Background residual stress profiles for a 100  $\mu m$ -long by 10  $\mu m$ -wide unreleased and released fixed-fixed beam. (a) Poly1 beam, (b) Poly2 beam and (c) Poly1-Poly2 stacked beam.

camera image of the selected stress map area on the beam; Figure 4.5c) displays the 2D stress profile across the width of the beam; and Figure 4.5d) the 2D stress profile along the length of the beam. From Figure 4.5c), it is seen that the stress is nearly uniform across the width of the beam.

The stress map images shown in Figure 4.5 are generated by capturing a Raman spectra at each xy-location. For this map, the step size was set to 1  $\mu m$  in both the x (length) and y (width) directions. This is equivalent to approximately 960 Raman spectra for different locations on the beam. The maps shown in Figure 4.5 are not

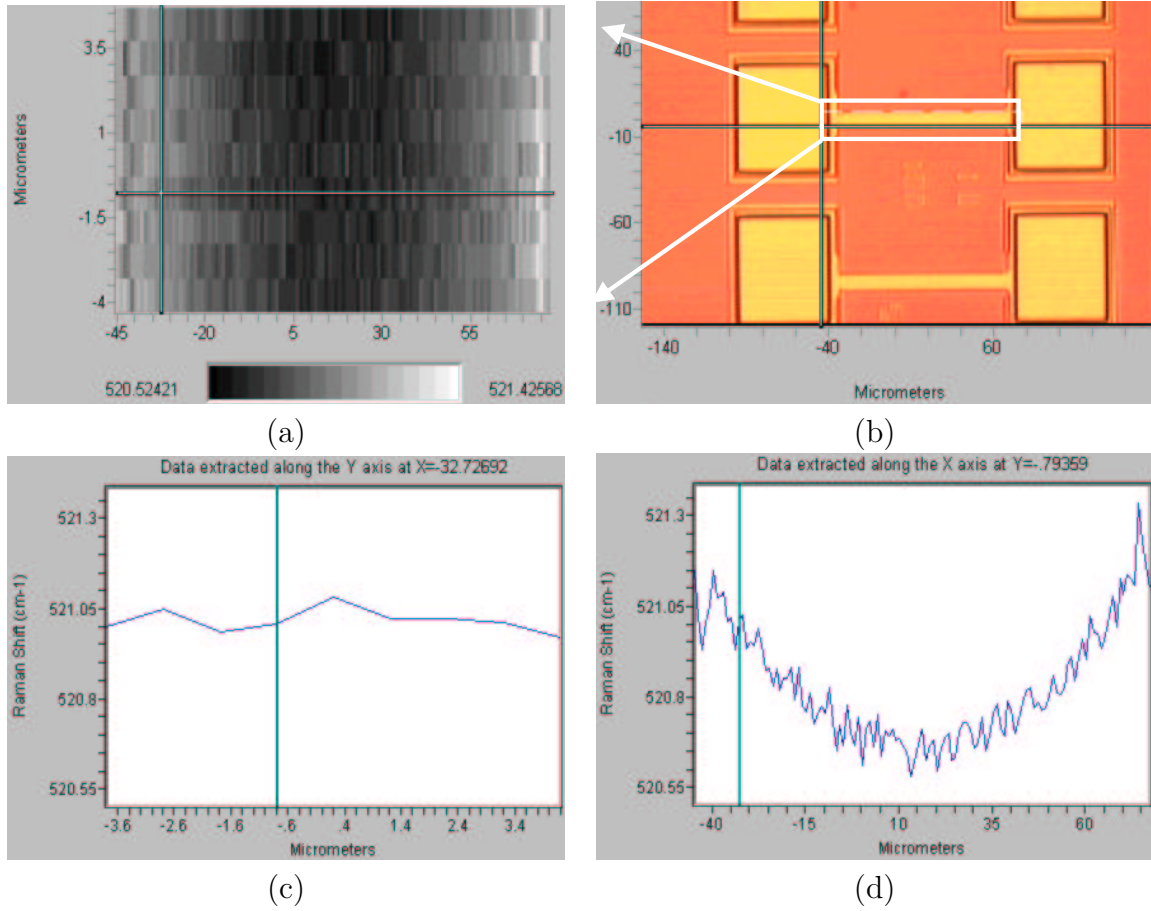


Figure 4.5: Raman spectral images for a 100  $\mu\text{m}$ -long by 10  $\mu\text{m}$ -wide Poly1 fixed-fixed beam (a) Raman spectra map, (b) Raman camera image of defined area, (c) 2D Raman profile across the beam, and (d) Raman along the length of the beam.

referenced to the  $\text{Ar}^+$  laser line. Referencing to the laser line will only shift the stress magnitude up or down according to the laser reference position and typically does not alter the stress profile.

From Figure 4.5, I can determine the uniformity of the stress across the width of the beam and down the length of the beam. This provides insight into the desired positioning of the laser beam on the MEMS structure. Since no significant stress variation is observed across the width of the beam in Figure 4.5c), this suggests that the Raman laser line scan does not have to be precisely positioned in the center of the beam to obtain the correct stress profile and stress magnitudes along the length

of the beam. The stress across the width of the beam should be nearly uniform until the beam becomes exceedingly wide (i.e. greater than approximately 40-50  $\mu m$ ).

A key observation concerning the characterization of residual stress in a fixed-fixed beam is that the residual stress profiles obtained using  $\mu$ Raman spectroscopy for the released fixed-fixed beam is nearly identical to the stress profile obtained through the analytical fixed-fixed beam model for a uniform applied load (see Figure 4.3). This helps to verify that the stress profiles obtained through  $\mu m$ Raman spectroscopy are representative of the uniform stress distribution within a fixed-fixed beam structure for a uniform applied load.

*4.4.3 Analytical Stress Model for a Cantilever.* An analytical stress model was generated to verify the  $\mu m$ Raman stress profiles. The analytical solution provides insight into the characteristic freestanding cantilever residual stress profiles measured using  $\mu m$ Raman spectroscopy. The analytical model is based on a free-standing cantilever with a uniform load distribution (gravity).

Figure 4.6 shows the analytical diagram used to determine the residual stress profile for a cantilever with a uniform load. The load  $g$  is the distributed load due to gravity.  $R_1$  is the resultant force, and  $M_1$  is the moment about the cantilever [23,24]. For a released cantilever with a uniform distributed load, the residual stress can be calculated by Equation 4.1 [23,24] where  $M(x)$  is the moment about the cantilever and is given by [23,24]

$$M(x) = -\frac{g}{2}(l-x)^2 \quad (N/m) \quad (4.4)$$

where  $g$  (N/m) is the distributed load,  $l$  ( $\mu m$ ) is the cantilever length, and  $x$  ( $\mu m$ ) is a selected position along the length of the cantilever respectively. For the analytical stress model calculation plotted in Figure 4.6, I stepped the value of  $x$  from 0-150  $\mu m$  (model cantilever length). The distributed load  $g$  for this cantilever model is given by Equation 4.3.

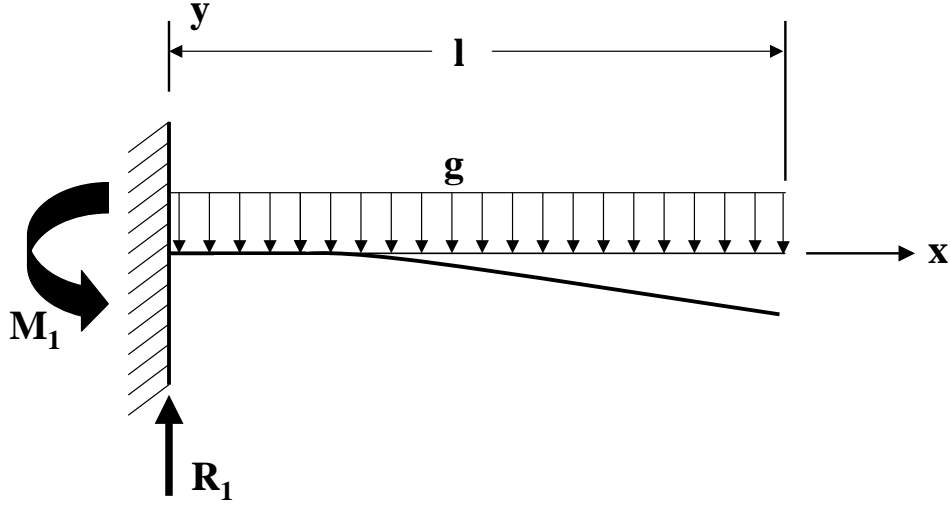


Figure 4.6: Analytical stress model for a MEMS cantilever [24].

The compressive residual stress along the length of the cantilever can again be considered a uniform load since this stress will produce a constant uniform applied force within the material layer (similar to Figure 4.6). The analytical cantilever stress profile representing a uniform applied force due to gravity is shown in Figure 4.7. The Raman stress profiles presented later for released cantilevers clearly resemble the stress profile shown in Figure 4.7. This model can be applied to all cantilevers with different lengths and/or thicknesses when a uniform load is applied.

*4.4.4 Cantilever.* I performed Raman scans on MUMPs® cantilevers just as I performed the scans for the fixed-fixed beams. A set of three repeated background Raman scans were again performed on pre and post released Poly1 and Poly2 cantilevers with structural dimensions of 100  $\mu m$ -long by 10  $\mu m$ -wide. Figure 4.8 shows a series of stress images for a Poly1 cantilever. Figure 4.8a) shows the background unreleased and released stress profiles for a Poly1 cantilever. As observed in Figure 4.8a), the released residual stress profile obtained by  $\mu m$ Raman spectroscopy clearly resembles the analytical cantilever model shown in Figure 4.7. The slope of the residual stress profile is due to the moment about the anchor of the cantilever. The residual stress in a cantilever can likewise be modeled as a uniform load dis-

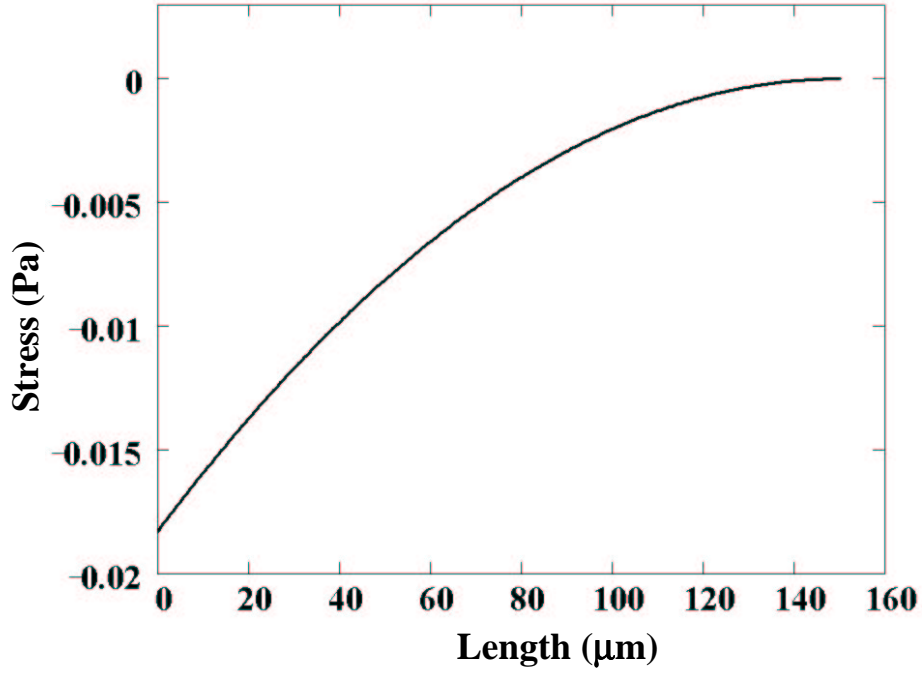


Figure 4.7: Analytical stress profile of a cantilever with a uniform load.

tribution along the cantilever length. Figure 4.8b) displays the residual stress map for a cantilever with respect to the length and width. Figure 4.8c) displays the 2D stress profile across the width of the cantilever. Finally, Figure 4.8d) displays the 2D stress profile along the length of the cantilever.

As seen in Figure 4.8c), the stress is again nearly uniform across the width of the cantilever. As before, the stress profiles in Figure 4.8b)- d) are not referenced to the laser line. The stress map in Figure 4.8b) is obtained with an xy step size of  $1\ \mu\text{m}$ . Measurements on Poly2 cantilevers yield nearly identical residual stress map profiles. The Raman unreleased and released stress profiles for a Poly2 cantilever are shown in Figure 4.9 to illustrate the stress magnitude similarities to the Poly1 cantilever layer.

*4.4.5 SUMMIT Cantilevers.* Several SUMMIT cantilevers are used to assess the residual stress levels in SUMMIT cantilever structures. Since the phosphorous doping is performed during polysilicon deposition in the SUMMIT process,

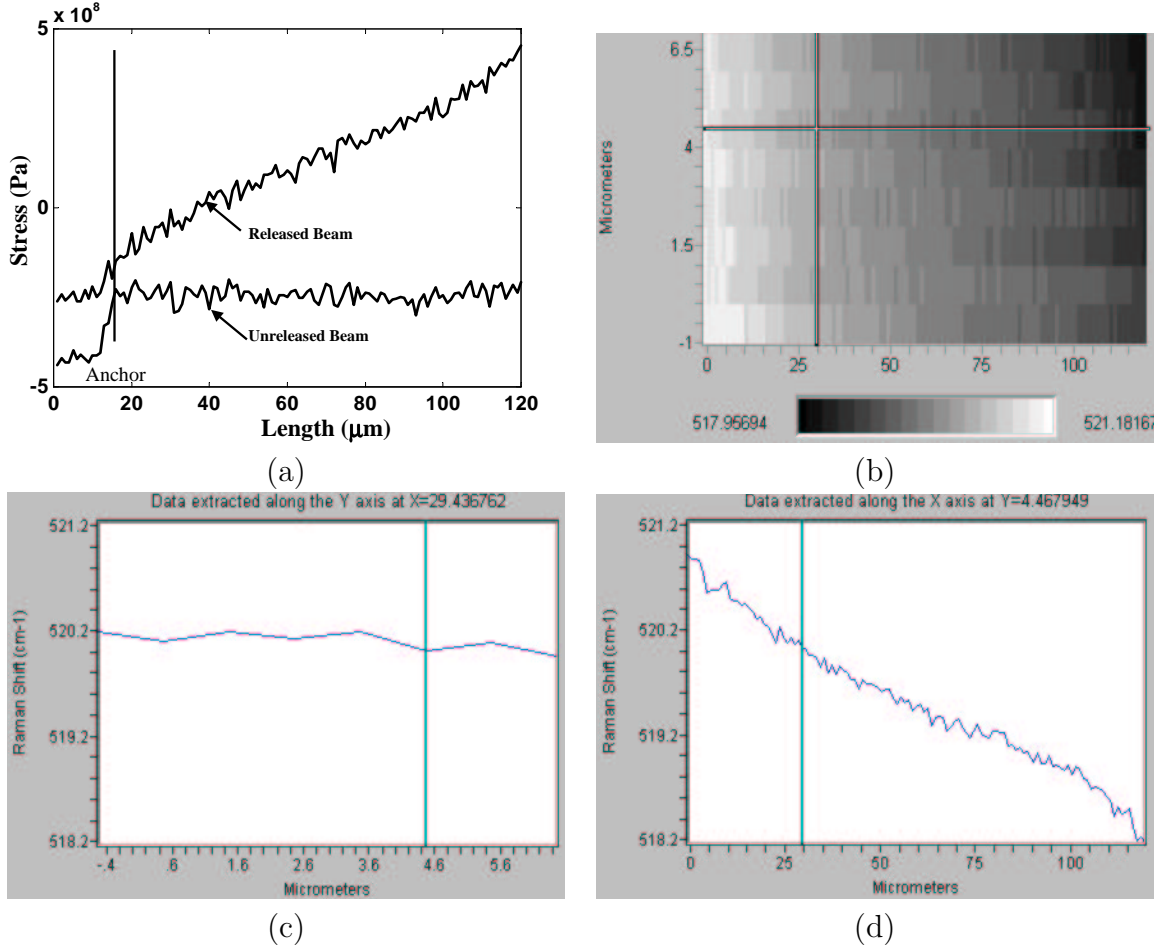


Figure 4.8: Raman stress images for a 100  $\mu\text{m}$ -long by 10  $\mu\text{m}$ -wide Poly1 cantilever: (a) background residual stress profiles for unreleased and released cantilever; (b) Raman spectra map; (c) 2D Raman profile across the beam (y-direction); and (d) Raman along the length of the beam (x-direction)

a very uniform doping concentration should exist in these structures. Figure 4.10 illustrates an IFM image of the SUMMIT cantilevers. As illustrated in Figure 4.10, the MPMOLY1 (bottom) cantilever is stuck to the substrate. The MPMOLY1+2 and MPMOLY1+2+3 cantilevers appear to be freestanding.

The Raman stress profiles on all three cantilever structures are illustrated in Figure 4.11. As illustrated in Figure 4.10, all cantilevers appear freestanding with the exception of the 240  $\mu\text{m}$ -long MPMOLY1 cantilever which is stuck to the

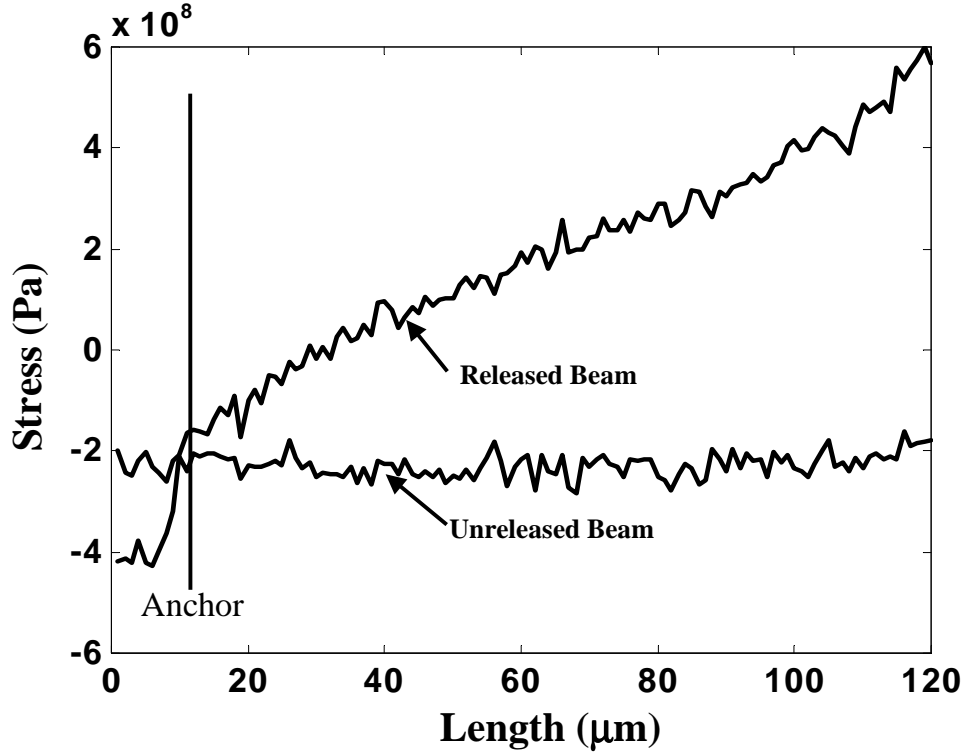
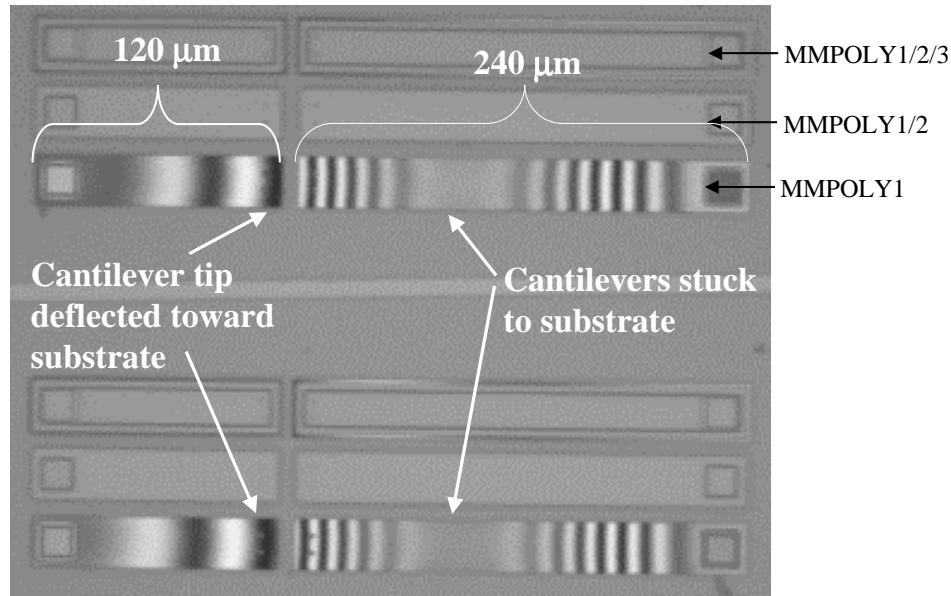


Figure 4.9: Background residual stress profiles for an unreleased and released 100  $\mu m$ -long by 10  $\mu m$ -wide Poly2 cantilever made in MUMPs<sup>®</sup> run #43.

substrate. (Figure 4.11a) and -b) illustrate a similar assessment with the 240  $\mu m$ -long MMPOLY1 cantilever shown in Figure 4.11b) as the only cantilever stuck to the substrate. The 240  $\mu m$ -long MMPOLY1/2 and MMPOLY1/2/3 cantilevers are freestanding as illustrated in Figure 4.10. The  $\mu m$ Raman stress profiles for these two cantilevers indicate a slight bend approximately 150  $\mu m$  down the cantilever length. This is likely due to the laser focusing on the sample. The SUMMIT die was mounted in a chip carrier which exhibited a slight tilt due to the crystal bond adhesive used to secure the die. I noticed the laser beam did become slightly out of focus during these Raman scans. Thus, the slight bend in the  $\mu m$ Raman stress profile for these two cantilevers is an artifact of improper laser focusing.

For the SUMMIT die tested, the various cantilevers illustrated were the only devices evaluated using Raman spectroscopy. Additional SUMMIT fabrication pro-



(a)



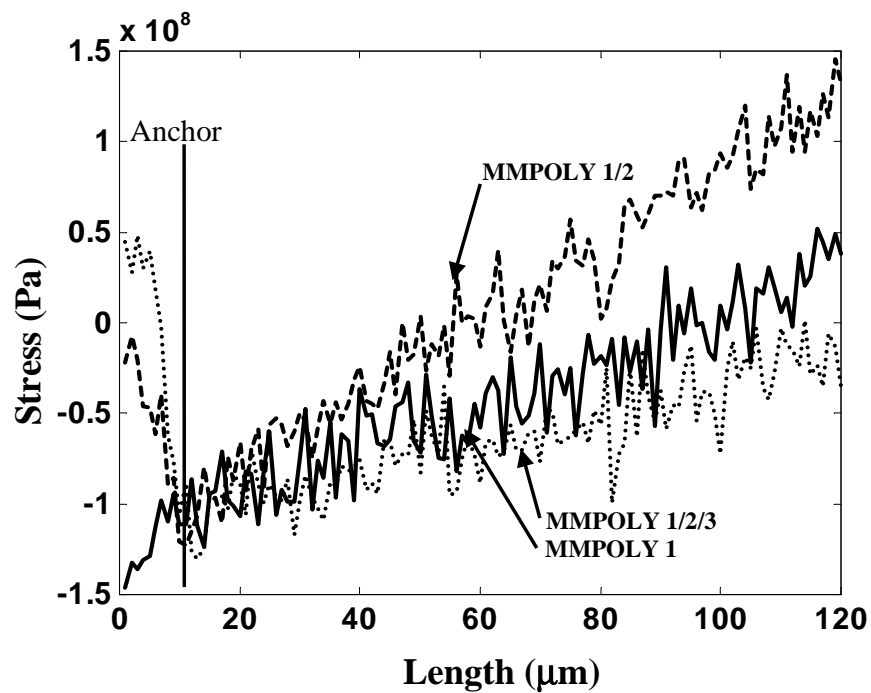
(b)

Figure 4.10: (a) IFM image of the SUMMIT 120  $\mu\text{m}$  and 240  $\mu\text{m}$ -long cantilevers illustrating curvature. (b) Illustration of the deflected cantilevers showing the difference in the fringe line patterns on the cantilevers

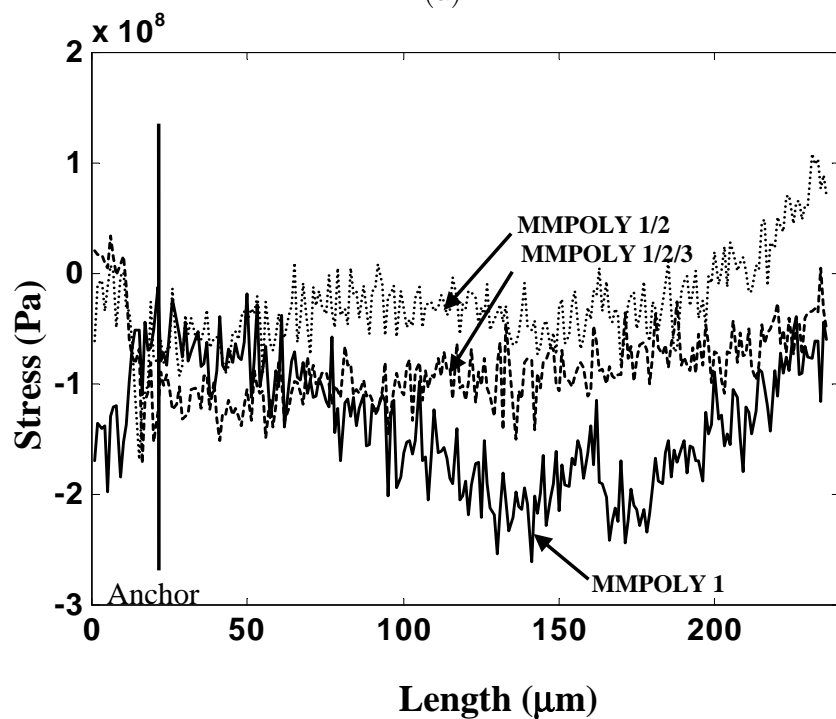
cesses were not pursued since the remainder of the experimentation focused on monitoring, measuring, and controlling the levels of residual stress relaxation by using Raman spectroscopy. Several additional reasons for not further pursuing the SUMMIT processes include:

- The primary reason is this foundry fabrication process is known to exhibit low stress levels. The post-processing techniques will provide minimal effects on the residual stress.

- With the stress resolution currently from Raman spectroscopy, this system is unlikely to detect the small stress changes.
- The turnaround time for the SUMMIT process is unpredictable.
- The SUMMIT process is expensive when compared to the MUMPs® process.



(a)



(b)

Figure 4.11: Raman stress profiles measured on SUMMIT cantilevers. (a) 120  $\mu\text{m}$ -long cantilevers, (b) 240  $\mu\text{m}$ -long cantilever.

*4.4.6 Micromirror Flexure.* I tested and analyzed several different flexure-beam micromirror designs. All micromirrors had similar design characteristics with the exception of flexure lengths and widths. Most flexures were designed with the Poly1 structural layer although a few micromirrors utilized the Poly2 structural layer. Identical Raman procedures were used for the micromirror flexures as for the fixed-fixed beams and cantilevers. I took unreleased and released background Raman scans on a 135  $\mu m$ -long by 13  $\mu m$ -wide Poly1 flexure. Figure 4.12 illustrates the generated stress profiles for the micromirror flexure: Figure 4.12a) shows the background stress profiles for a line scan for an unreleased and released Poly1 micromirror flexure. Figure 4.12b) displays the overall residual stress distribution of a flexure with respect to flexure length and width. Figure 4.12c) displays the 2D stress profile across the width of the flexure. Finally, Figure 4.12d) displays the 2D stress profile along the length of the flexure. Again, the stress profiles in Figure 4.12b)-d) are not referenced to the laser line. The stress map in Figure 4.8b) is obtained with an xy step size of 1  $\mu m$ . The Poly2 micromirror flexures provide nearly identical stress profiles.

The stress maps for all three structures (fixed-fixed beams, cantilevers, and micromirror flexures) experimentally verify that the stress across the width of the structures is approximately uniform.

*4.4.7 Induced Micromirror Stress Characterization.* Through the use of  $\mu$ Raman spectroscopy and finite element method models, the residual and induced stress profiles for the MEMS micromirror flexure are obtained. With these stress profiles, I can monitor the changes in stress due to an applied electrostatic actuation voltage. Through these measurements and subsequent calculation of induced stress, I can assess the sensitivity of the  $\mu$ Raman spectroscopy technique. A significant change in the stress profile should occur as the micromirror reaches the snap-down voltage level (approximately 16.5 V for the test structures).

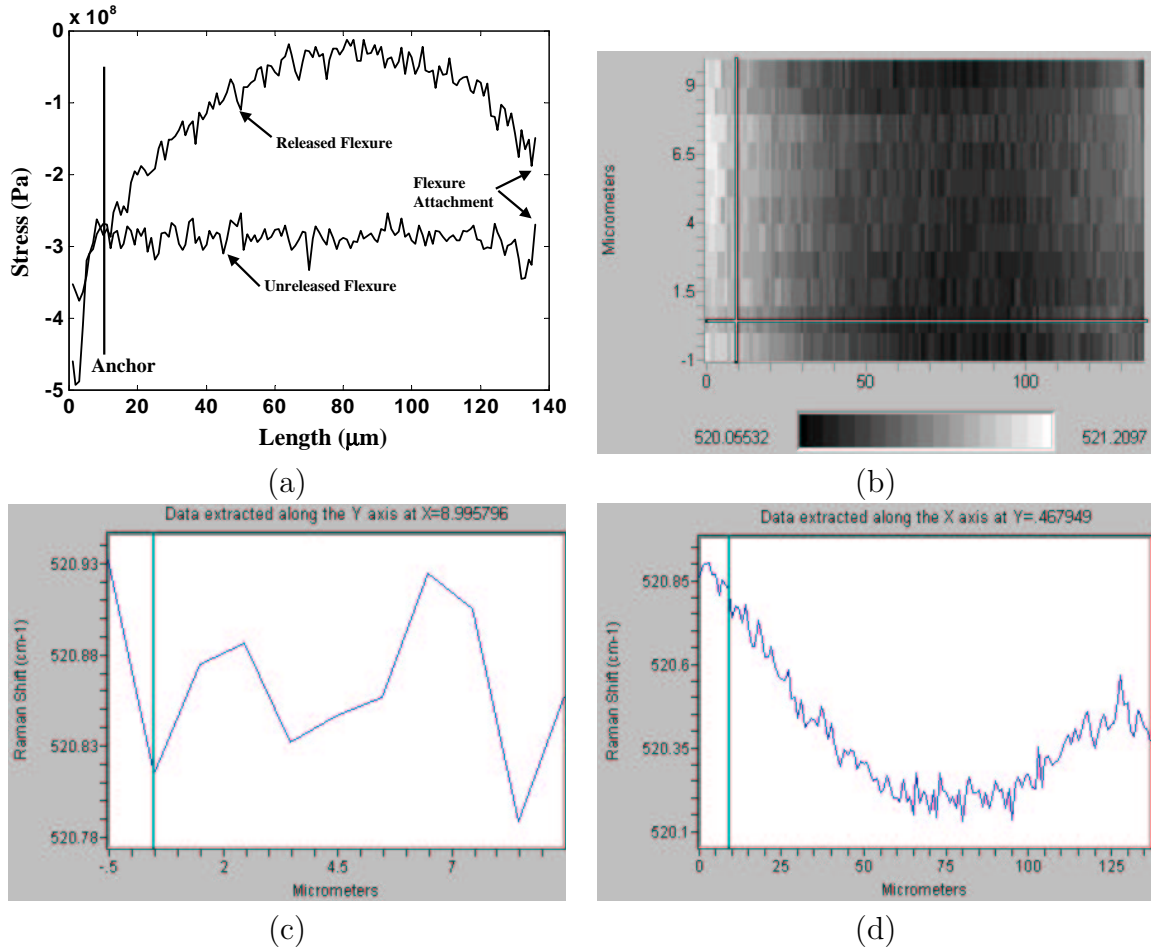


Figure 4.12: Raman stress images for a 130  $\mu\text{m}$ -long by 13  $\mu\text{m}$ -wide Poly1 micromirror flexure (a) background residual stress profiles for unreleased and released flexure, (b) raman spectra map, (c) 2D Raman profile across the flexure (y-direction), and (d) Raman along the length of the flexure (x-direction).

*4.4.8 Induced Stress on a Micromirror Flexure.* The MEMS micromirror shown in Figure 4.13 is a single element of a mirror array [6]. The mirror is actuated electrostatically through the use of an electrode pad located under the center of the mirror. As part of the MEMS design, dimples located under the flexures prevent electrical shorting and ‘stiction’ effects when snap-down occurs. The mirror is constructed using the MUMPs<sup>®</sup> fabrication process. The mirror is made of a stacked Poly1-Poly2 structural layer with a region of trapped Oxide2 with gold deposited in

the center of the micromirror. The mirror is designed with Poly1 flexures which are constrained from movement by anchors at one end and attached to the mirror at the other end. As seen in Figure 4.13, the flexure attachment to the mirror is solid. This will allow translation at the end of the flexure, but will resist rotation. The Raman scan line used to obtain the residual and induced stress profiles is identified in Figure 4.13.

Raman Scan  
line down center  
of mirror flexure

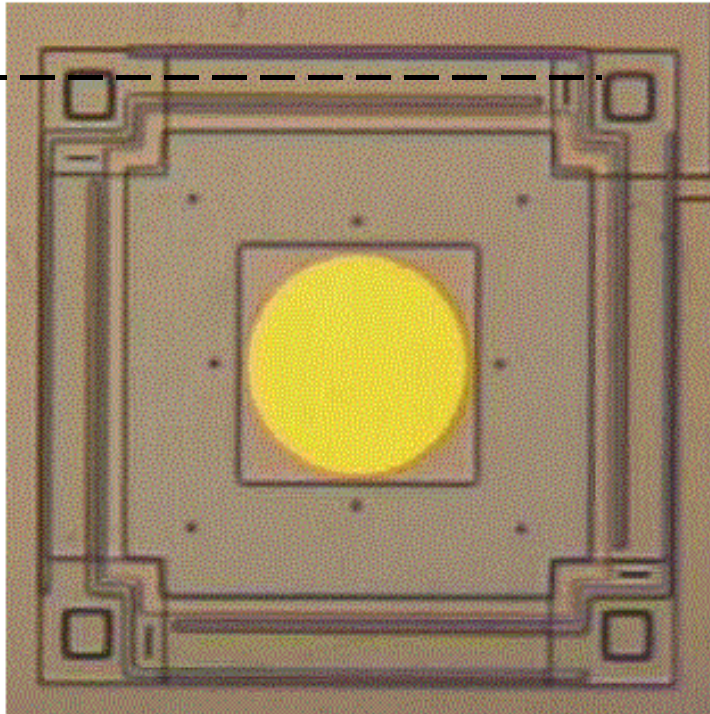


Figure 4.13: MUMPs® run #18 polysilicon piston micromirror designed with Poly1 flexures [6].

The micromirror flexure can be modelled as a beam as shown in Figure 4.14. As shown in Figure 4.14, the mirror is anchored to the substrate (left end of beam) and attached to the mirror at the opposite end. Since the mirror surface moves down when an electrostatic actuation voltage is applied, the flexure will bend as shown with the dotted line. Since the flexure to mirror attachment is solid, the attached end should remain relatively flat as shown by the flat region on the dotted line. As the actuated mirror flexes the beam downward, one would expect to see the induced

stress distribution on the top of the beam to be essentially a backward S-shape. A tensile stress section should exist close to the fixed end of the beam followed by an inflection point and a compressive stress near the end attached to the mirror.

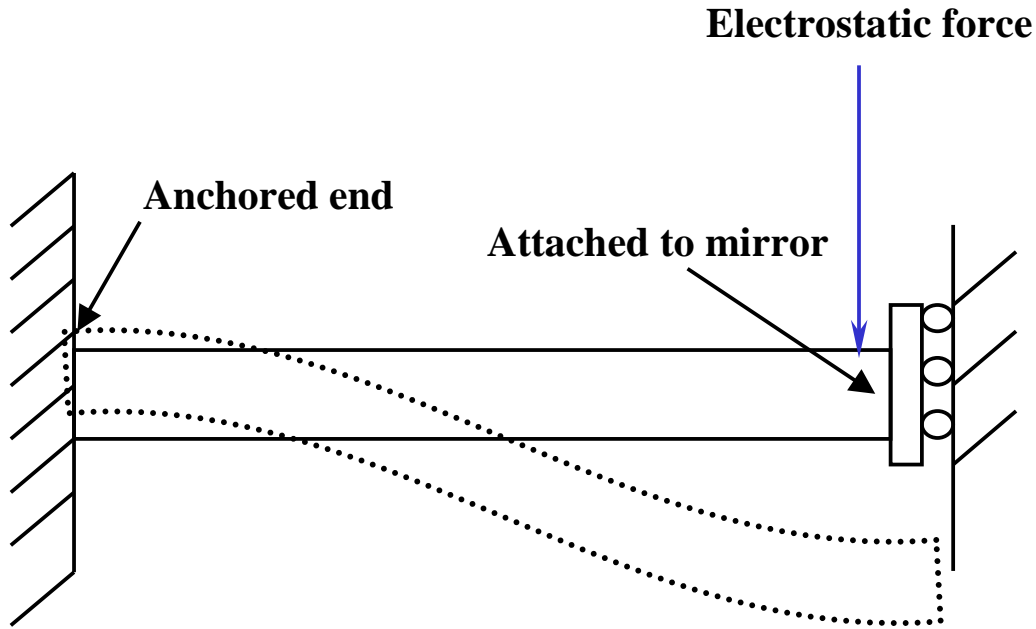


Figure 4.14: Mechanical beam model of a micromirror flexure

Raman stress measurements of this micromirror include both induced and residual stresses profiles. To accurately characterize the induced stress, one must first obtain the residual stress in the micromirror flexure. Figure 4.15 shows both the Raman frequency shift along the longitudinal axis of the flexure as well as the resulting residual stress calculated using the hydrostatic pressure constant of  $2.19 \text{ cm}^{-1}/\text{GPa}$ . The flat region on the left-hand side of both curves corresponds to the anchor of the flexure. The stress distribution starts with a small tensile stress close to the anchor and reaches a maximum of approximately 90 MPa just past the midpoint of the flexure, then begins to relax as it approaches the mirror attachment. One should note that the geometry of the mirror attachment will add some degree of torsion to the flexure.

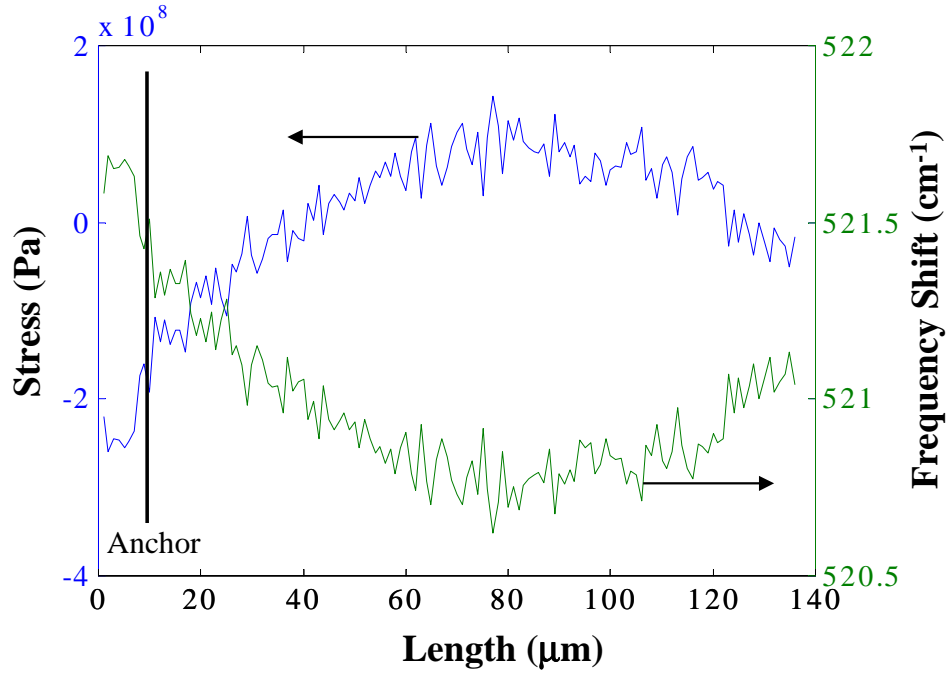


Figure 4.15: The residual stress distribution along the micromirror flexure shown in Figure 4.13.

To induce stress in the micromirror flexure, the micromirror is electrostatically actuated for voltage levels ranging from 1 V to 20 V. A representative schematic of a basic electrostatic piston micromirror is illustrated in Figure 4.16 showing how the mirror can be modelled as a mass-spring device. Through the applied voltage, one can calculate the amount of deflection as a function of the applied voltage. The amount of mirror deflection can be calculated from the following equation [5]

$$d = \frac{\epsilon_0 A V^2}{2k(h - d)^2} \quad \mu m \quad (4.5)$$

where  $A$  is the overlapping electrode area,  $\epsilon_0$  is the dielectric constant of air ( $8.854 \times 10^{-12}$  F/m),  $V$  is the voltage across the electrodes,  $k$  is the calculated spring constant, and  $h - d$  is the relative gap between the electrodes and is represented by the as-fabricated plate height minus the deflection of the plate [5]. The spring constant  $k$  is obtained from the following equation [5]

$$k = n \left[ \frac{Ewt^3}{l^3} + \frac{(1 - \sigma)wt}{2l} \right] \quad (N/m) \quad (4.6)$$

where  $n$  is the number of micromirror flexures,  $E$  is Young's modulus,  $\sigma$  is the residual stress value, and  $w$ ,  $l$ , and  $t$  are the flexures width, length, and thickness respectively.

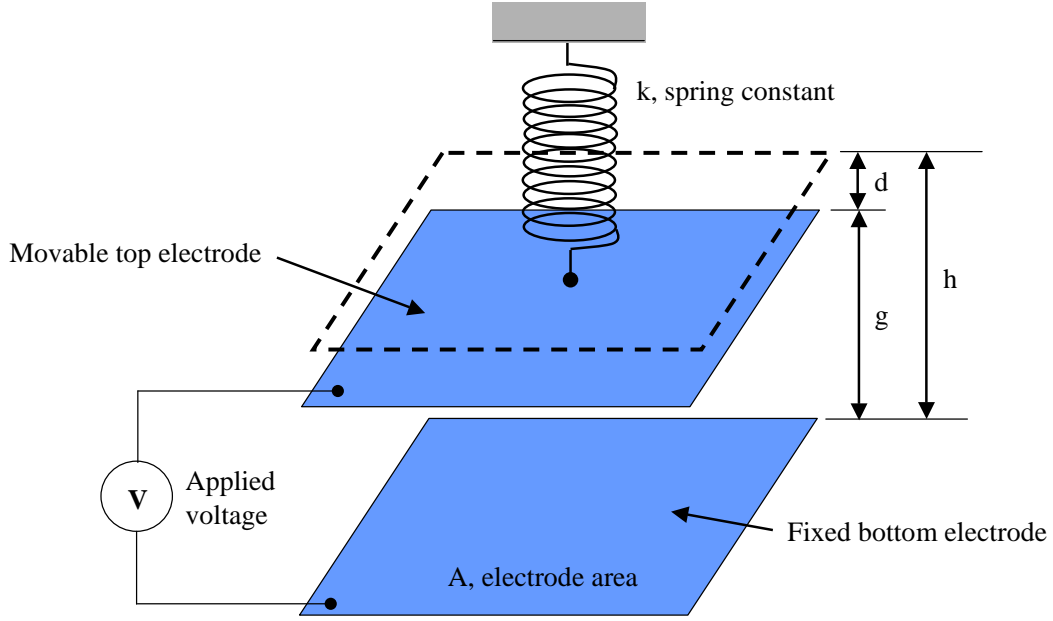


Figure 4.16: Schematic view of basic electrostatic piston micromirror [5].

The deflection equation (Equation 4.5) is used to analytically calculate the estimated snap-down of the micromirror. Snap-down for this particular micromirror is calculated to be 16.5 V. I experimentally measured snap-down of the micromirror to be approximately 15.96 V through the use of an interferometric microscope (IFM). By electrostatically actuating the micromirror, one can observe snap-down by monitoring the fringe lines on the micromirror flexures. Once snap-down occurs, the fringe lines are more numerous due to the height variation on the flexures (see Figure 4.17). Since snap-down of the mirror occurs around 16 V, this voltage level will assist in identifying the snap-down region of the micromirror in the induced stress image obtained by using Raman spectroscopy. To avoid hysteresis effects during the

actuation, care was taken to approach the voltage value from the lower side for all measurements. At each voltage setting, a single Raman line scan was taken across the same physical dimensions used to find the residual stress distribution in Figure 4.15. The residual stress (the stress measured with no electrostatic actuation) was subtracted from each of the corresponding stress distributions to yield the true induced stress profiles. To help analyze the induced stress curves obtained experimentally using  $\mu$ Raman spectroscopy, I used a MEMCAD finite element method (FEM) model. The FEM stress curves help to support the assumption of a nearly uniform stress across the width of the flexure. Based on FEM modelling (Section 2.6.5, the primary component of stress is in the x-direction (along the length of the flexure).

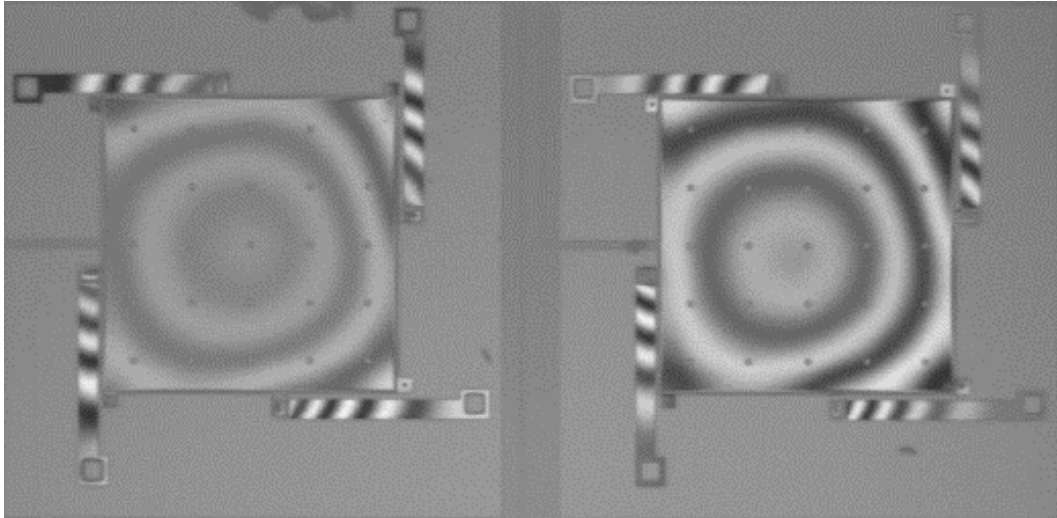


Figure 4.17: Interferometric microscope image of a set of micromirrors simultaneously in snap-down. Snap-down is observed by the multiple fringe lines on the micromirror surface and flexures.

The results of calculated 3-D induced stress is provided in Figure 4.18 and Figure 4.19 provides a third degree polynomial fit of the induced stress image shown in Figure 4.18. The third degree polynomial fit was selected since this fit the raw data properly. From the 3-D images, the micromirror snap-down region is observed at approximately 16 V for a flexure length of  $120\ \mu m$ . The flat region near the left sides of the plots corresponds to the anchored end of the flexure. As can be observed from

the images, the induced stress does increase as the applied voltage is increased and changes abruptly once snap-down occurs. Figure 4.18b) and Figure 4.19b), show the corresponding 2D induced stress map which clearly identifies the snap-down voltage level.

The calculated induced stress profiles for the piston micromirror are obtained using the MEMCAD FEM analysis software as outlined in Figure 4.20. A line marker is used to extract the FEM data as displayed across the micromirror flexure. The MEMCAD FEM stress curve for the 20 V (snap-down) condition is shown in Figure 4.21. The shape of the induced stress curve in the snap-down region conforms qualitatively to the expected S-shaped distribution from the analytical beam model shown in Figure 4.14. In fact, there is tensile stress close to the anchor (left) end of the flexure which decreases through an inflection point. This is followed by an increase in tensile stress near the right end of the beam. The shape of the curves corresponds well with the nature of electrostatic actuation. As illustrated in Figure 4.18, the shape of the stress curve changes minimally as the voltage is increased. Then, as the snap down voltage is approached, the shape of the curve changes abruptly corresponding to a large change in deflection over a short voltage range.

All of the Raman stress curves illustrated in this section are obtained through the use of the hydrostatic pressure Poly1 constant determined in Chapter 2. All stress profiles (unless noted) are referenced to the laser line and the average of three repeated Raman scans over the same structure. As determined by the Raman stress maps analysis, the stress occurs predominantly down the length of the flexure (x-direction). The stress across the flexure (y-direction) was minimal. Through the use of MEMCAD, these same structures are modeled. The generated MEMCAD stress profiles (see Figure 4.22) and the experimentally measured Raman map files of the MEMS structures for the y- direction illustrate the same result. These results from both Raman and MEMCAD indicate the stress across the MEMS structure is minimal and no significant change in the magnitude was noted across the width of

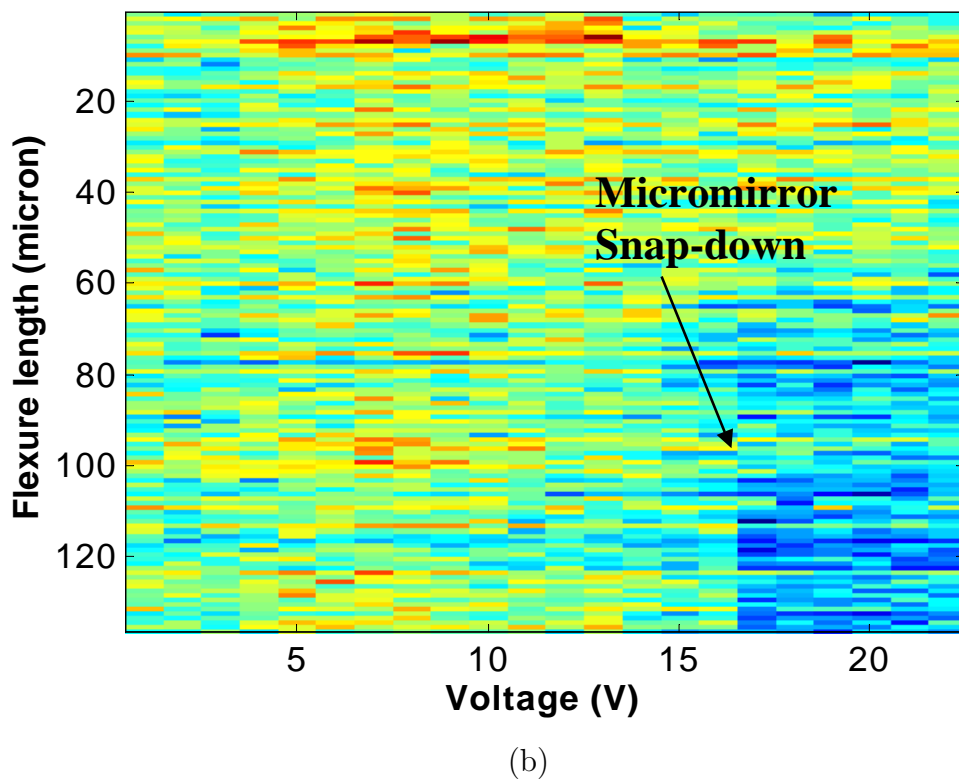
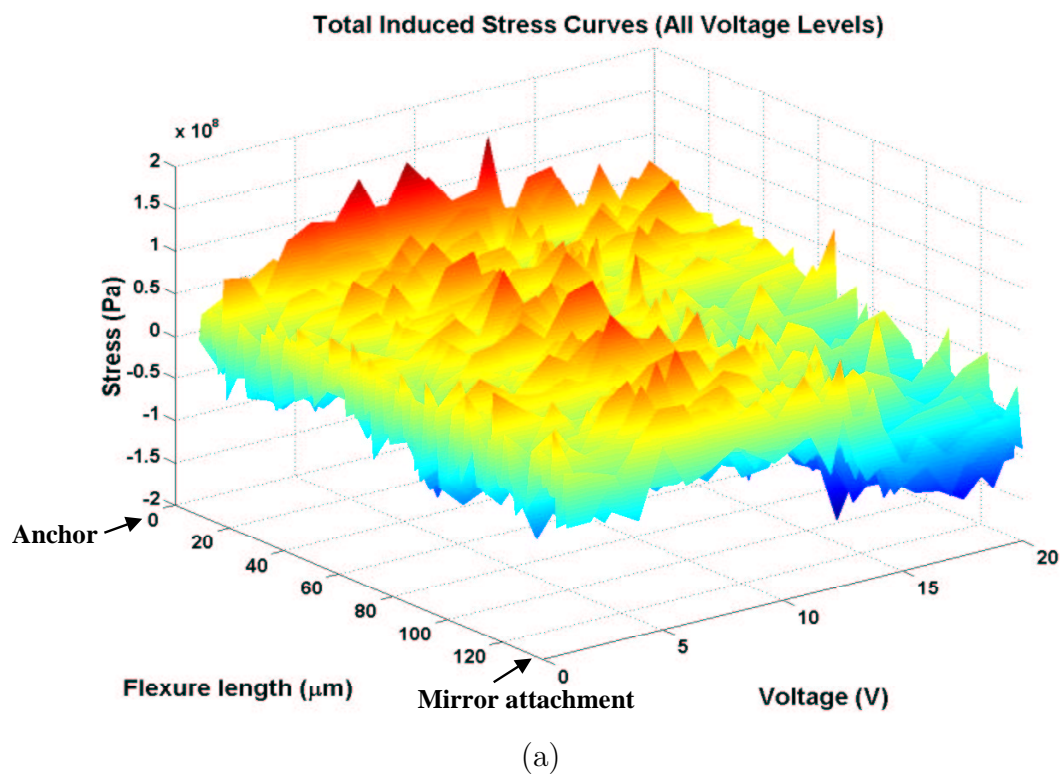


Figure 4.18: Induced stress profiles for a MEMS micromirror. (a) 3D stress map and (b) 2D stress map

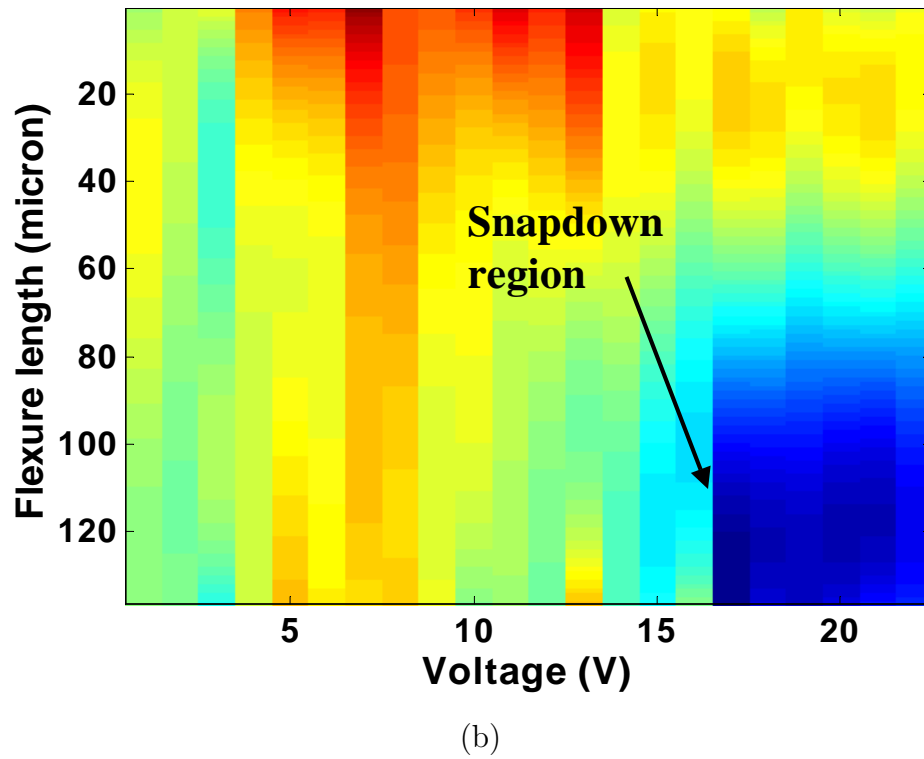
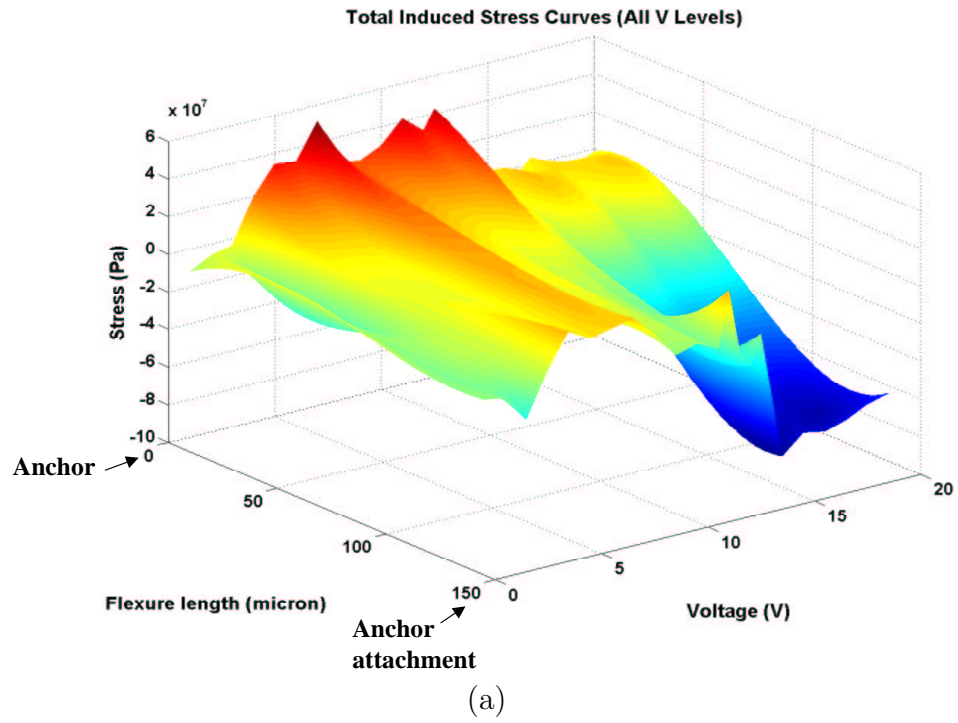


Figure 4.19: Induced stress profiles for a MEMS micromirror fitted with a third degree polynomial. (a) 3D stress map and (b) 2D stress map

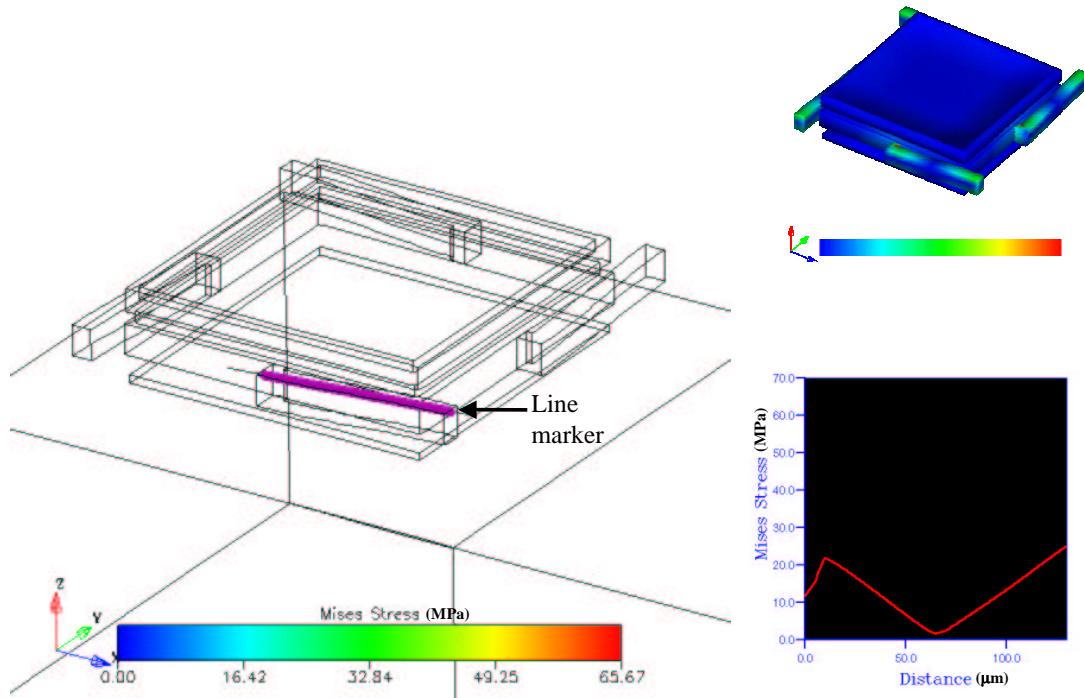


Figure 4.20: MEMCAD FEM data extraction technique for a micromirror flexure at snap-down.

the structures. In addition, both Raman and MEMCAD verify the primary element of the residual stress occurs along the length of the structure. Thus, the stress in the y- and z-directions is negligible when compared to the x-direction stress.

#### 4.5 Residual Stress Measurement Techniques

Several different measurement techniques are available to determine the residual stress values and Young's modulus for a particular materials deposition process. Some of the MEMS devices which can be used to determine the residual stress and Young's modulus include resonators, cantilevers, and microbridges. Each measurement technique is briefly described. I used these test structures to determine experimental values for residual stress and Young's modulus.

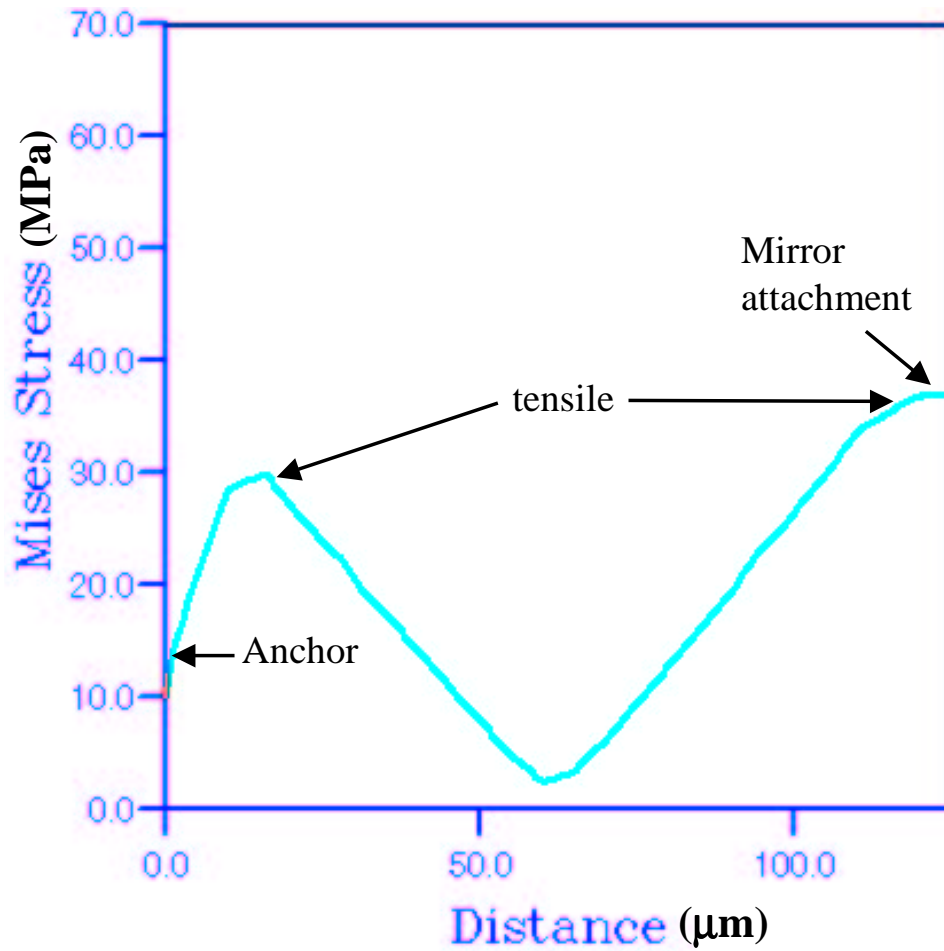


Figure 4.21: FEM induced stress in the micromirror flexure shown in Figure 4.20 at snap-down

*4.5.1 Beam Pull-in Measurement Technique.* The "beam pull-in" voltage method is based on the pulling down of the upper electrode (beam) towards the substrate. When the voltage between the ground electrode and the beam electrode exceeds a critical level, the beam will be pulled down to the substrate. Both tensile and compressive stress and the Young's modulus of a thin film can be derived using this method [28].

In this method, a voltage is applied across the gap between the free-standing beam and the substrate. The electrostatic force causes the beam to deflect toward the substrate. Figure 4.23 illustrates the basic design of the beam pull-in structure.

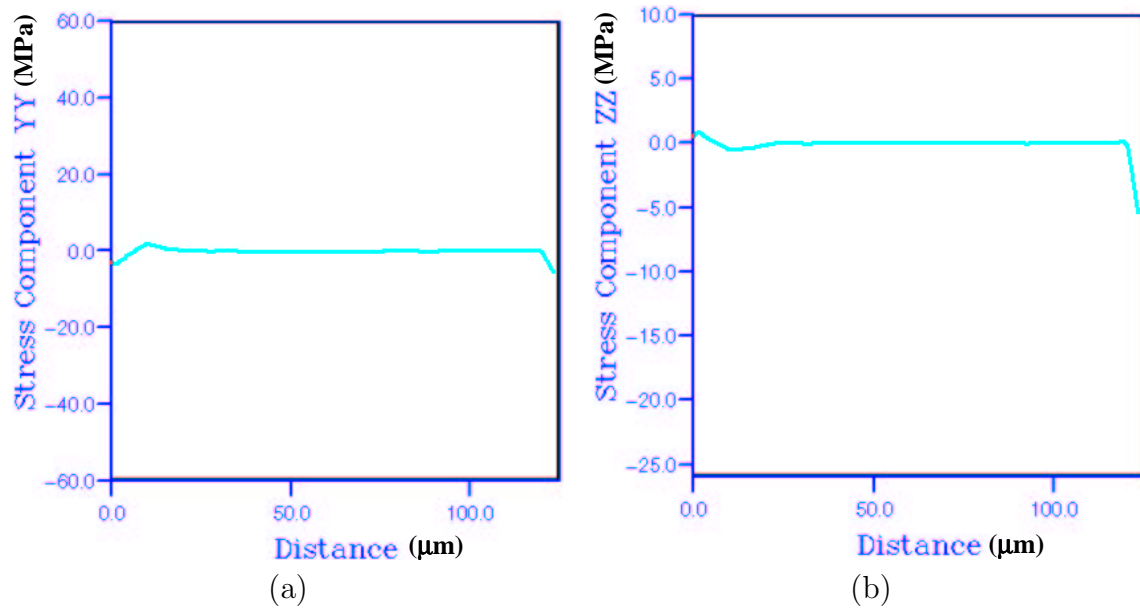


Figure 4.22: Y- and Z-stress components obtained from MEMCAD for the micromirror flexure shown in Figure 4.20 at snap-down. Figure (a) Y-Component and Figure (b) Z-Component

An increase of the deflection of the beam results in a decrease of the gap spacing and

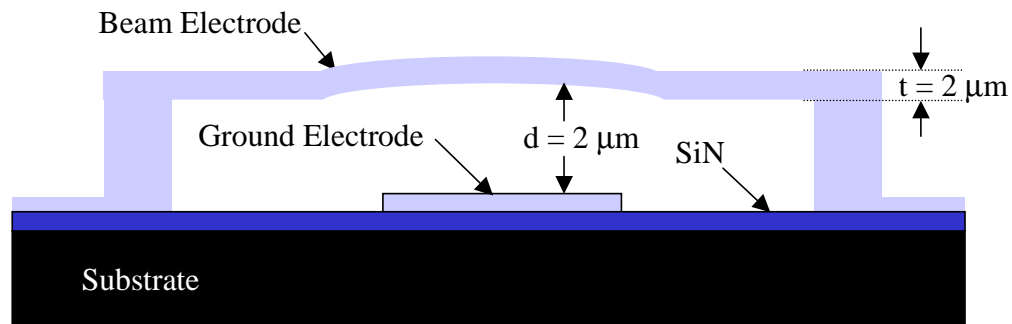


Figure 4.23: Schematic of MEMS Poly1 Microbridge for the “beam pull-in” measurement.

thus in an increase of the electrostatic force. If the applied voltage exceeds the pull-in voltage, the deflection does not reach an equilibrium position and will continue to increase until physical contact is made with the ground electrode (snap-down). Figure 4.24 illustrates the deflection of a beam with applied voltage. The pull-in voltage value depends strongly on internal stress. As a result, thin-film stress or

even Young's modulus of the material can be determined by measuring the pull-in voltage of the structure and the amount of deflection of the beam. Some assumptions to make include: 1) the beam material is uniform; and 2) the direction of the electric field in the air gap is always perpendicular to the electrode plates when the beam deflection occurs [28].

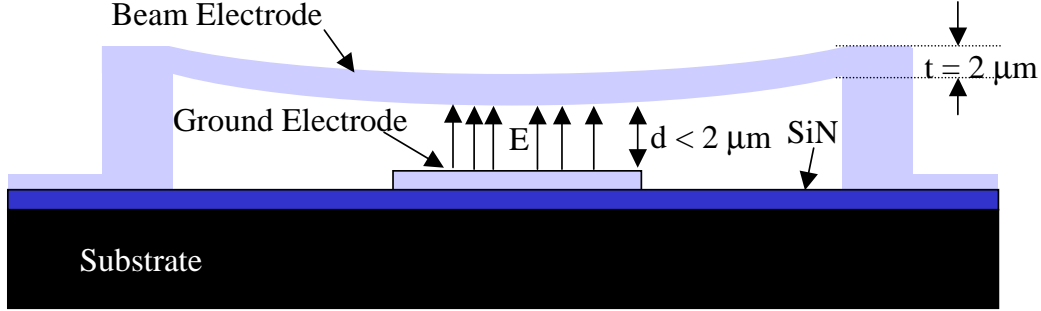


Figure 4.24: Actuated MEMS Poly1 microbridge

*4.5.2 Wafer Curvature Measurement Technique.* One of the most challenging aspect of micromachining is the measurement and control of the residual stress in the thin film materials employed. Current process control has failed to produce repeatable residual stress results in MEMS material layers. The wafer curvature technique is used to determine the residual stress values for the MUMPs® process at the foundry [17]. Figure 4.25 illustrates the wafer curvature stress measurement.

The Stoney Equation for the wafer curvature stress measurement is given by [5, 20]:

$$\sigma_f = \frac{E_s t_s^2}{6(1 - \nu_s) t_f R} \quad (Pa) \quad (4.7)$$

where  $E_s$  (MPa),  $\nu_s$  (unitless),  $t_s$  ( $\mu m$ ) are Young's modulus, the Poisson ratio, and the thickness of the substrate. Also,  $t_f$  ( $\mu m$ ) is the thickness of the film, and  $R$  ( $\mu m$ ) is the measured radius of curvature of the bowed wafer for bow  $B$  ( $\mu m$ ) much less than the deflection scan length  $L$  ( $\mu m$ ), where  $R \approx L^2/8B$  [7]. The Stoney Equation relates the radius of curvature (or wafer bow) due to the addition of a film to one side

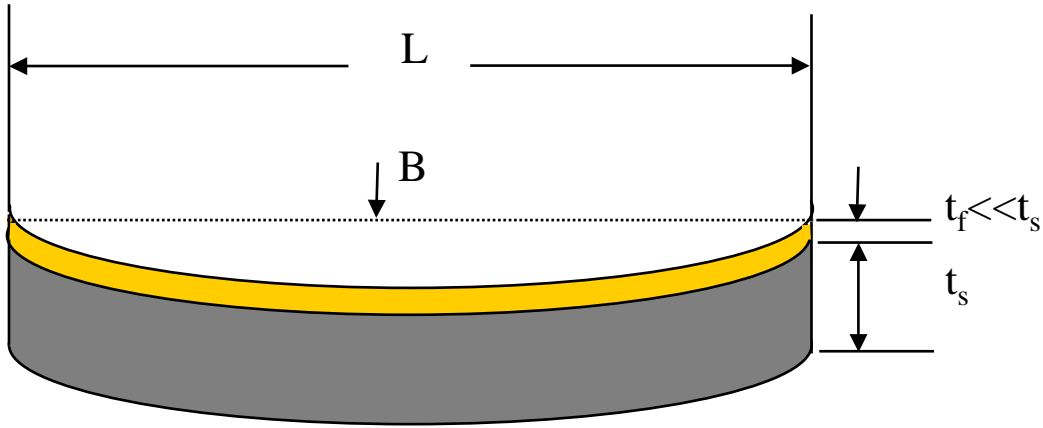


Figure 4.25: Wafer curvature measuring illustration

of the wafer, to the residual film stress [20]. In the Stoney Equation, it is assumed that the substrate thickness is much larger than the film thickness and the Young's modulus of the film is approximately equal to Young's modulus of the substrate. Two further assumptions are also made: 1) the film stresses are isotropic and constant; and 2) the elastic properties of the substrate plane are transversely isotropic. Bow measurements at the MUMPs® foundry are currently made using a Tencor FLX-2320 laser scanning thin film stress measurement system [17]. The Tencor measures substrate deflection across a single axis of the wafer and reports radius of curvature and wafer bow. Wafer bow measurements are performed on dedicated monitor wafers processed with each fabrication run. Poly1 and Poly2 monitor wafers are used to ensure that the film stresses measured are representative of the film stresses on the MUMPs® wafers [5]. Because films are deposited on both sides of the polysilicon monitor wafers, the bow measurement is performed by stripping the test film from one side of the wafer. After removing the cap oxide from both sides of the monitor using a wet etch the bow is measured [5]. The test film is then removed from one side of the wafer using reactive ion etching (RIE) and the bow is measured again [5]. The difference in the bow measurements represents the bow caused by stress in the test film.

Although the key advantage of the wafer bow method is low cost, there are several limitations of this technique including the following:

- The wafer curvature technique provides a mean value of film stress across the wafer rather than the local strain field. No localized stress information can be determined.
- The wafer curvature technique provides no information about residual stress variations across the wafer or any residual stress gradients (variations through a given film along the z-direction).

Table 4.1 provides a comparison between the residual stress values obtained from the wafer curvature technique performed by the MUMPs® foundry and the stress values I calculated from my MUMPs® buckled beam arrays and resonator devices. I derived the localized residual stress values by measuring the resonant frequency of comb drives (Section 4.6.1). From the comb drive resonant frequency equation (see Equation 4.11), I obtain the value of Young's modulus which is then applied to the critical buckling beam equation (see Equation 4.8). Using IFM, I am able to easily identify the critical buckling length of both the Poly1 and Poly2 fixed-fixed beams. From the critical buckling equation, I determine the localized residual stress value for each particular MEMS die.

To obtain the localized stress level in Table 4.1, I released two die from each MUMPs® run and measured the comb resonance and buckling beam lengths. I performed these tests to determine the variations in the localized residual stress levels between the MUMPs® runs.

As shown in Table 4.1 the residual stress levels are slightly different for each MUMPs® run. This is typically the case From the published MUMPs® foundry data [1], the stress in the Poly0 layer ranges from approximately -25-50 MPa (compressive) over the MUMPs® runs I used in this research. The tensile stress in the nitride insulating layer varied from 126-153 MPa [1]. The

Table 4.1: As Fabricated Compressive Residual Stress Comparisons.

MUMPs® Run (#)	Structural Layer	Wafer Curvature [1] MPa	Localized Stress MPa
38	Poly1	-8	-5.71
38	Poly2	-7	-13.48
41	Poly1	-8	-5.51
41	Poly2	-4	-13.48
42	Poly1	-9	-5.71
42	Poly2	-7	-15.48
43	Poly1	-9	-5.92
43	Poly2	-6	-12.63
44	Poly1	-10	-6.12
44	Poly2	-6	-14.43
45	Poly1	-17	-7.19
45	Poly2	-9	-16.65

*4.5.3 Fixed Beam Measurement Technique.* An array of fixed-fixed beam structures (micro-bridges) of lengths ranging from 100  $\mu m$  to 900  $\mu m$  in increments of 10  $\mu m$  are used to determine the residual stress of both Poly1 and Poly2 structural layers in the MUMPs® process. These structures will buckle for stress values above the critical Euler stress [10]. Although the buckling beam arrays require a significant amount of die space, they were my primary means of determining stress variations during my post-processing experimentation which is outlined in Chapters 4 and 5. Through the use of an IFM, the precise critical buckling beam length is readily determined. Figure 4.26 illustrates a schematic of a micro-bridge designed using the Poly1 structural layer.

The beam buckling equation, solved for length  $L$ , is given by [5,11]

$$L = \sqrt{\frac{\pi^2 t^2 E}{3\sigma}} \quad (\mu m) \quad (4.8)$$

where  $t$  ( $\mu m$ ) is the beam thickness,  $\sigma$  (Pa) is the residual stress, and  $E$  (GPa) is the Young's modulus of the material. The length  $L$  in Equation 4.8 is the maximum

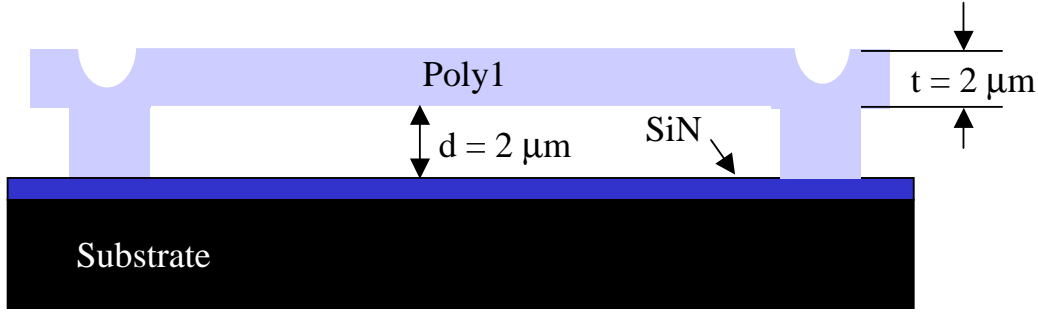


Figure 4.26: Schematic of a MUMPs® Poly1 microbridge

length before buckling occurs. By knowing the elastic modulus of the material, the localized residual stress can be determined for the MUMPs® die. Figure 4.27 illustrates an IFM image of buckled Poly1 and Poly2 fixed-fixed beam arrays. Figure 4.28 is a close-up scanning electron microscope (SEM) image of a set of Poly1 buckled beams stuck to the substrate.

The Poly1 and Poly2 buckling beam arrays illustrated in Figure 4.27 are nearly identical with the exception of the beam thickness  $t$  ( $2.0\ \mu\text{m}$  for Poly1 and  $1.5\ \mu\text{m}$  for Poly2) and the beam height above the substrate  $d$  ( $2.0\ \mu\text{m}$  for Poly1 and  $2.75\ \mu\text{m}$  for Poly2). Without an IFM microscope, it can be difficult to determine the first buckled beam in an array, as the change in height is typically limited by contact with the substrate to  $2.0\text{-}2.75\ \mu\text{m}$  in MUMPs®. An IFM allows easy identification of the first buckled beam length through the fringe lines on the test structures. The IFM image in Figure 4.27 illustrates the critical buckling beam lengths for the MUMPs® foundry fabricated test arrays (no post-processing performed on the die) following a supercritical carbon dioxide ( $\text{CO}_2$ ) dry. In Figure 4.27, all beams longer than the first buckled beam are buckled. The length of the first buckled beam in the Poly1 array is  $550\ \mu\text{m}$  and in the Poly2 array is  $310\ \mu\text{m}$  which correspond to residual stress values of  $-4.63\ \text{MPa}$  and  $-12.62\ \text{MPa}$  respectively.

Initially, four MUMPs® test die were used to determine the preliminary residual stress and Young's modulus values through the buckling beam arrays and comb

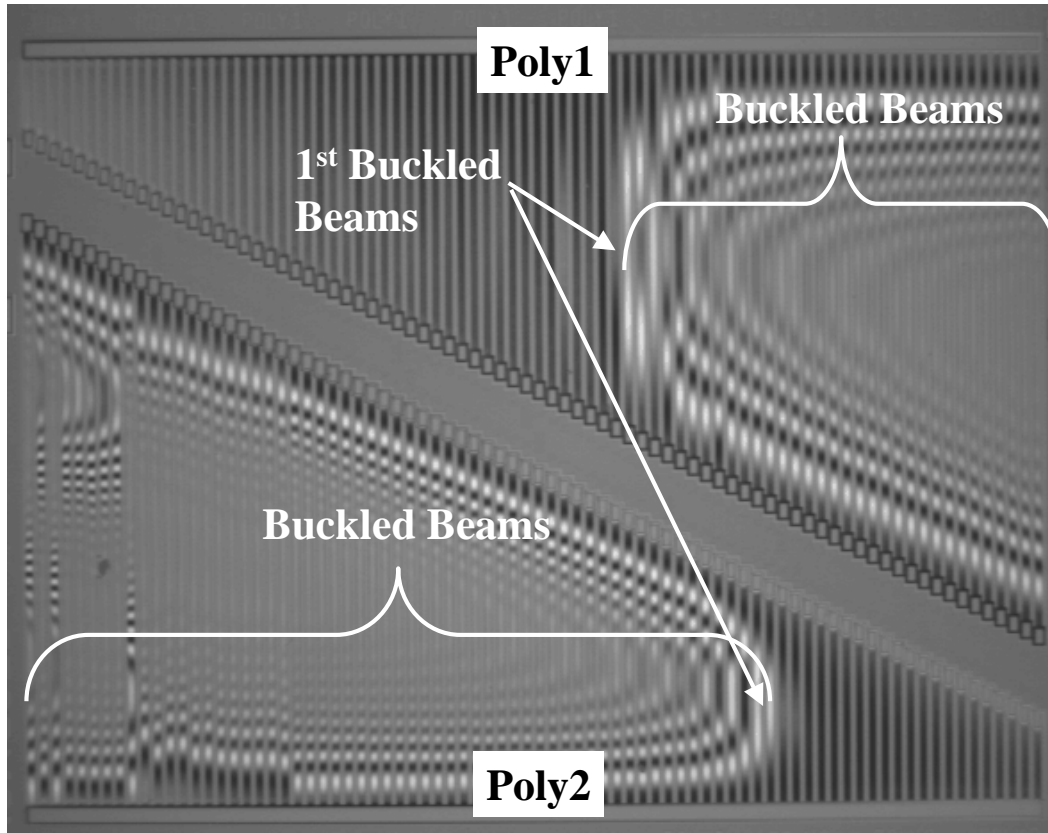


Figure 4.27: Interferometric microscope (IFM) image of buckled MUMPs® Poly1 and Poly2 beams

resonators. For these die, I used the release procedure outlined in Appendix A. Using a hotplate to perform the final dry yielded inconsistent results. From the four test die evaluated, the first buckled beam for Poly1 ranged from 160-500  $\mu m$  in length and for Poly2 ranged from 230-300  $\mu m$ . With an estimated Young's modulus value of 160 GPa, these beam lengths correspond to localized residual stress values ranging from -8.4 - -72 MPa for Poly1 and from -23 - -36 MPa for Poly2.

Since my primary research objective was to use  $\mu$ Raman spectroscopy as an experimental technique to measure and monitor the residual stress levels in released and unreleased MEMS structures, I needed a repeatable release process to quantitatively determine stress changes via the buckling beam arrays, cantilevers, and micromirrors. In an attempt to obtain repeatable results in the Poly1 and Poly2

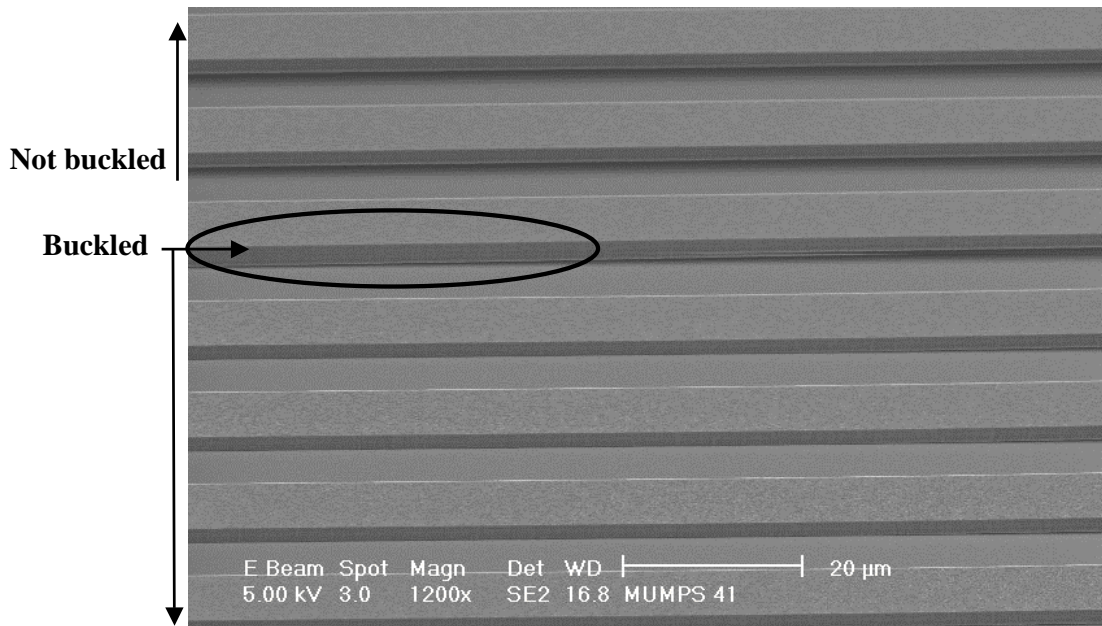


Figure 4.28: SEM image of buckled Poly1 beams

buckling beams and cantilevers, a supercritical  $CO_2$  dryer was purchased to alleviate the stiction problems encountered with the hotplate dry.

*4.5.4 Supercritical Carbon Dioxide ( $CO_2$ ) Drying.* A critical step in the surface micromachining of MEMS devices is the process that releases, cleans, and dries the flexible structures that are crucial to MEMS functionality. Stiction is one of the most problematic issues confronting producers of MEMS based products. MEMS devices are inherently sensitive to stiction because the polycrystalline structural members are relatively compliant and only a few microns above the substrate.

Stiction can occur as a consequence of poor packaging, handling, transportation, or device operation. Stiction typically occurs during the release of MEMS structures. Surface tension is the major culprit in process induced stiction. Following the sacrificial layer release with an HF dip (wet etch in HF), a solvent (methanol, isopropyl alcohol, etc.) rinse is used to remove the HF. This rinsing liquid gets trapped in the narrow gaps between the silicon wafer and the suspended MEMS structures. Interfacial forces generated when this trapped capillary fluid dries can cause the

microstructures to collapse and stick to the substrate or underlying layer [4]. The meniscus force between two flat polished surfaces with a liquid bridge is given by [4]

$$\nu = -\frac{\gamma A}{h}(\cos \theta_1 + \cos \theta_2) \quad (N) \quad (4.9)$$

where  $\theta_1$  and  $\theta_2$  are the contact angles of the liquid with the two solid surfaces,  $A$  is the shared area of the parallel surfaces, assuming the gap between them is flooded with capillary liquid,  $h$  is the average thickness of the liquid bridge, and  $\gamma$  (N/m) is the surface tension [4]. As seen in Equation 4.9, the attractive force is inversely proportional to the spacing between the structure and the substrate. This attraction is resisted by the bending stiffness of the structure. Since a decrease in gap spacing caused by the bending of the structure increases the surface tension, a stable equilibrium point may not exist. In this case, the structure will be pulled down to the substrate.

Supercritical  $CO_2$  drying has zero surface tension ( $\gamma = 0$ ), thus eliminating the capillary force from Equation 4.9 [4]. Research has shown that supercritical  $CO_2$  can be successfully used to alleviate stiction problems and provide clean, dry surfaces [9, 16]. In the supercritical  $CO_2$  process, the MEMS die are immersed in a shallow layer of methanol in the  $CO_2$  chamber at room temperature. Liquid  $CO_2$  displaces the methanol during a 5-min purge cycle. The temperature of the liquid  $CO_2$  is then raised above its critical point (Figure 4.29). The chamber is vented at a constant temperature of  $T > T_c$  ( $T_c$  is the critical temperature of  $CO_2$ ) and the  $CO_2$  escapes as a gas. A liquid to solid interface is never formed during the process, and hence surface tension is completely suppressed.

A model 815B supercritical  $CO_2$  dryer was purchased from Tousimis [27]. Beginning with MUMPs® run #41, the release etch procedure outlined in Appendix A was changed slightly. All release steps remained the same except the final hotplate

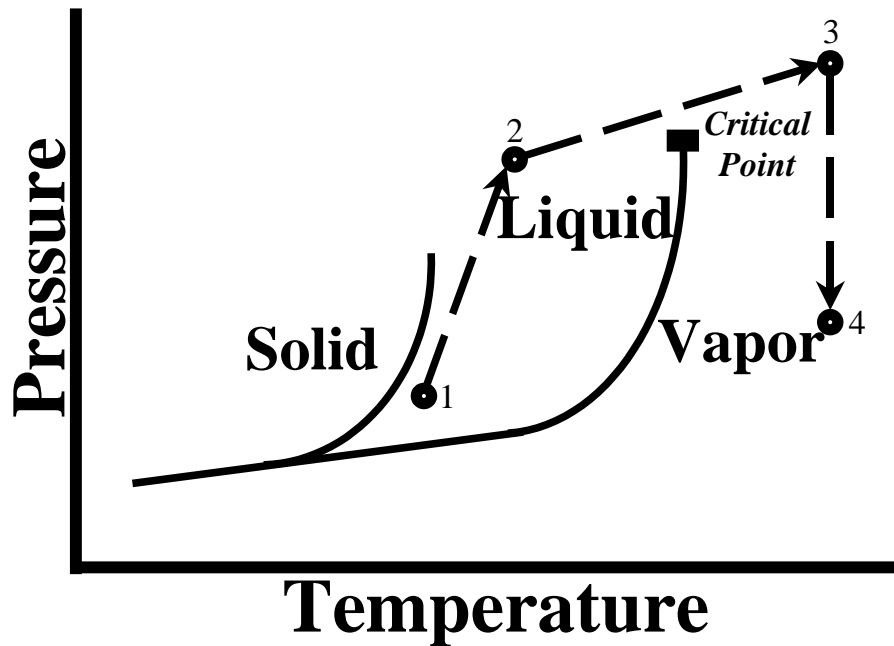


Figure 4.29: Phases of  $CO_2$  for various combinations of pressure and temperature with the regions used for release annotated, after [4, 18]. The release process begins at point 1, where liquid  $CO_2$  displaces methanol. The pressure of the drying chamber is raised (point 2) to prevent the liquid from evaporating in the normal fashion when the temperature is raised (point 3). The  $CO_2$  now exists in a supercritical state where it is both a liquid and a gas with no interface between the two. As the pressure is released the  $CO_2$  becomes all vapor and escapes from the drying chamber (point 4).

dry was replaced by drying using the Tousimis supercritical  $CO_2$  dryer in an attempt to reduce stiction effects.

Following the HF release etch and methanol rinses, the MEMS die is placed in the  $CO_2$  chamber with enough methanol to just cover the MEMS sample. The chamber is sealed with three fasteners and the supercritical  $CO_2$  drying process begins by pressing the “COOL” button on the  $CO_2$  dryer front panel. Once the temperature reaches approximately  $-7\text{ }^{\circ}C$ , the “FILL” button is pressed and the chamber begins to fill with liquid  $CO_2$ . From this point forward, the drying process is automatic until completed.

Prior to the  $CO_2$  purchase and installation, I had the MUMPs® foundry [1] release 15 MEMS die from MUMPs® run #41 with their supercritical  $CO_2$  dryer system. Through the use of an IFM, the Poly1 critical buckling beam lengths ranged from 550 to 570  $\mu m$  and for Poly2 ranged from 280 to 310  $\mu m$ . On these same die, I designed an identical Poly1 buckling beam array with an added dimple in the center of the beam length and width. This dimple should prevent premature buckling due to capillary forces and stiction. For this Poly1 structure, the buckling beam lengths ranged from 550 to 580  $\mu m$ . This is a good indication that stiction is not occurring since both types of Poly1 buckling beam array structures resulted in nearly identical results.

From these results, the buckling lengths are very repeatable and fairly consistent between MEMS die. The MUMPs® process is known to have small variations in residual stress from one wafer to the next and this may be a contributing factor in the slight variation observed in the buckling beam lengths. The slight variation in the Poly1 beam lengths is equivalent to a stress difference of 393 kPa and the variance in Poly2 beams is equivalent to -2.85 MPa of stress, respectively. This set of die was used as a baseline for subsequent supercritical ( $CO_2$ ) dries performed in AFIT's cleanroom.

When AFIT received and installed the  $CO_2$  dryer, I released several MUMPs® die to determine proper  $CO_2$  dryer operation, and also to observe the repeatability of the releases. The critical buckling lengths were measured with consistent and repeatable results between test die. The critical buckling lengths measured on these die fell within the range established from the MUMPs® foundry release.

Initially, Tousimis programmed the  $CO_2$  dryer for a purge time of 10-min, during which methanol is exchanged with liquid  $CO_2$ . At this setting, approximately 4-lbs of liquid  $CO_2$  is required for each dry cycle. Since the  $CO_2$  bottles require a dip tube, only half the  $CO_2$  in the bottle can be used. Therefore, for this setting, only 4-5 die could be dried per bottle of  $CO_2$ . With the small MUMPs® die size (0.5  $cm^2$ ),

I changed the  $CO_2$  dryer cycle to include only a 5-min purge instead of the 10-min purge. At this setting, a complete dry cycle requires approximately 1.5-lbs of  $CO_2$ . Again, several die were used to check for proper release of the MEMS structures and to verify that the critical buckling lengths were maintained. At this new setting, I received identical buckling beam lengths as previously measured. Thus, I performed all remaining MEMS releases using the  $CO_2$  dryer at the 5-min purge setting.

#### 4.6 *Young's Modulus*

Young's modulus is the proportionality constant which relates stress and strain in a material by:

$$E = \frac{\text{stress}}{\text{strain}} = \frac{\sigma}{\varepsilon} \left( \frac{N}{m^2} \right) \quad (4.10)$$

Most materials obey Hooke's law; that is, they deform linearly with load. Since the load is proportional to stress and the deformation is proportional to strain, stress and strain are linearly related. The larger the value of Young's modulus of a material, the less it will deform for a given stress, thus the material is stiffer.

The calculation of Young's modulus is directly related to the material density, which will be slightly different for films deposited under different conditions. The values and dimensions can also be affected by doping concentration and shrinkage or expansion during a diffusion process. For polysilicon, the density value of  $2.33 \text{ g cm}^{-3}$  of single crystal silicon is typically used [19]. Errors due to the inexact density and the non-true vertical sidewall profiles can range from 5-10% [19].

Doping, annealing, and film thickness do not significantly influence the measured value for Young's modulus [21]. Several studies were performed to determine the Young's modulus of LPCVD polysilicon films. However, the measured values of Young's modulus for polysilicon films deposited by LPCVD had a large variation from 40 to over 170 GPa [19].

Several different measurement techniques for the determination of Young's modulus in polysilicon exist. They include: 1) the bulge test of square and rectangular membranes; 2) the load deflection method; 3) the wafer curvature method; and 4) the ultrasonic surface wave method [19]. However, all these test methods give different results, and it is not clear which gives the correct Young's modulus.

*4.6.1 Resonator Measurement Technique .* The comb-drive resonator has been the most widely used MEMS device to measure Young's modulus [2, 12, 19, 22]. Tang [26] explored in detail the mathematical basis for resonance in a comb drive. Using the spring constant in the x-direction,  $k_x$ , the resonant frequency can be calculated as:

$$f = \frac{1}{2\pi} \sqrt{\frac{k_x}{M}} = \frac{1}{2\pi} \sqrt{\frac{24EI_z}{(M_p + \frac{1}{4}M_t + \frac{12}{35}M_b)L^3}} \quad (Hz) \quad (4.11)$$

where  $E$  (Pa) is Young's modulus,  $I_z$  ( $m^4$ ) is the cross sectional moment of inertia for the beam with respect to the axis,  $L$  ( $\mu m$ ) is the beam length, and  $M_p$ ,  $M_t$ , and  $M_b$  are the mass of the plate, trusses, and beams (kg), respectively [8, 26].

I obtained the Young's modulus for MUMPs® runs #38 and #41-45 through the use of comb drive resonators. The resonance was measured using an HP 4195A Network/Spectrum Analyzer. The measured resonant frequency for Poly1 comb drive resonators is approximately  $22.6 \pm 0.15$  kHz and for Poly2 is approximately  $18.9 \pm 0.15$  kHz. The resonant frequencies are used to determine Young's modulus for each particular layer. These resonant frequencies correspond to Young's modulus values of  $131 \pm 2.0$  GPa for Poly1 and  $162 \pm 2.0$  GPa for Poly2 respectively. The derived Young's modulus is then applied to the critical buckling equation to determine the localized residual stress level.

*4.6.2 Estimated Residual Stress Variation.* Throughout this research, I use the combination of comb drive resonators and buckling beam arrays to quantitatively

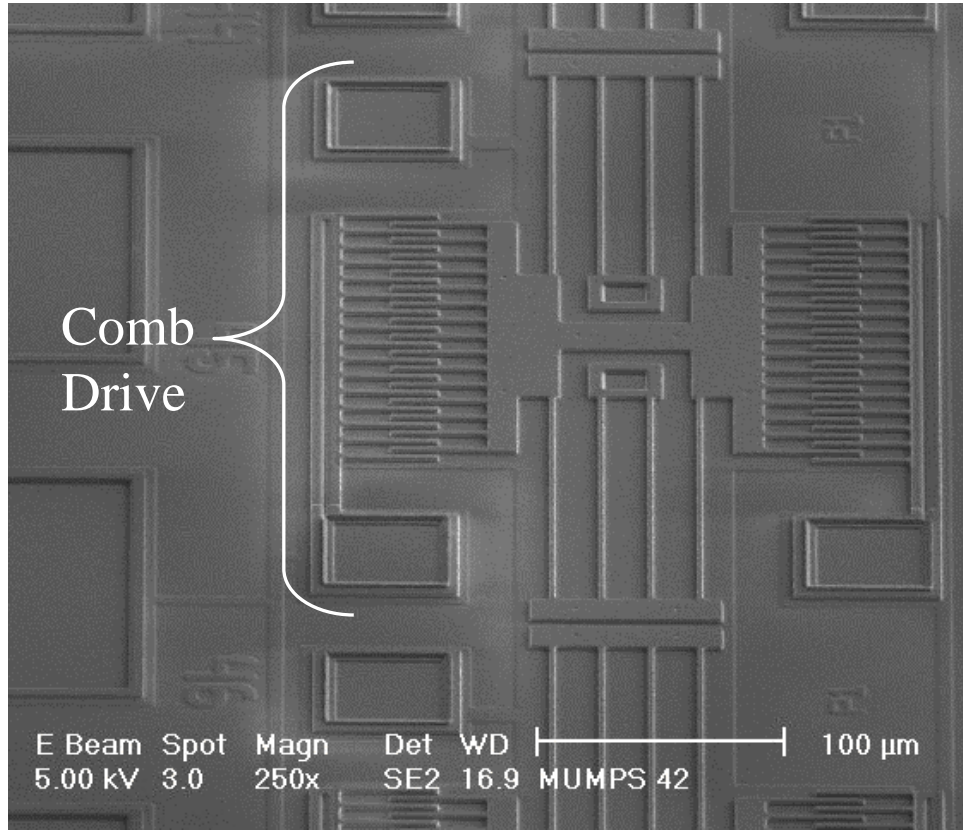


Figure 4.30: Poly1 comb drive resonator used to measure Young's modulus

determine the Young's modulus and localized residual stress values. To determine the estimated error variation in the measured residual stress values, I selected the worst and best case scenarios for the combined buckling beam length and comb resonance and used this as the typical error variation for the residual stress in standard MUMPS® test die.

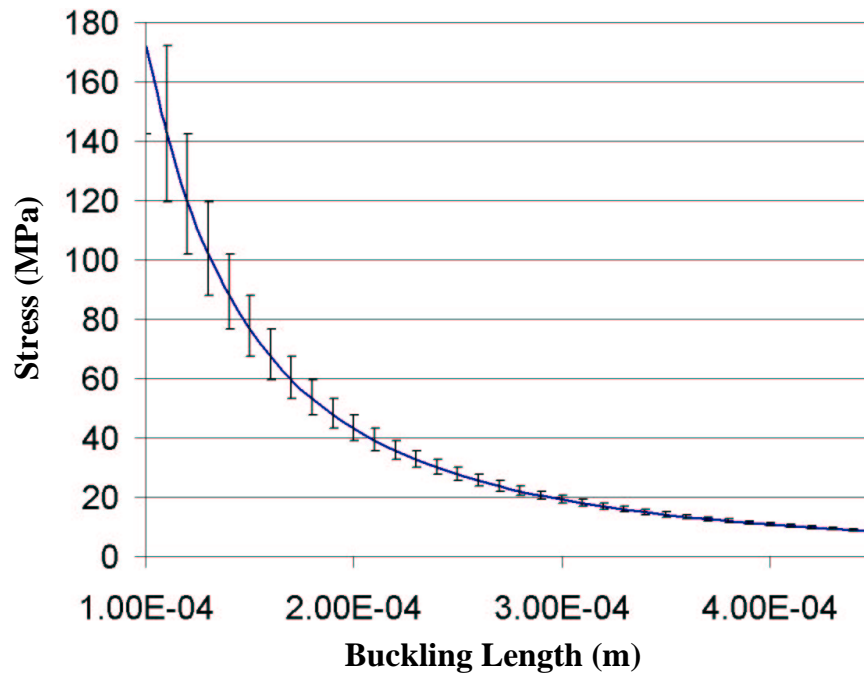
I estimated the residual stress variance due to system and material variations by using the average of 20 buckling beam arrays which did not have post-processing performed. The average buckling beam length for Poly1 is  $560 \pm 10 \mu m$  and Poly2 is  $290 \pm 10 \mu m$ . The resonant frequencies measured for these identical MEMS die are  $22.5 \pm 0.15$  kHz for Poly1 and  $18.9 \pm 0.15$  kHz for Poly2. From the shortest buckling beam length and the highest resonant frequency, the maximum stress value

for Poly1 is determined to be -5.789 MPa. The longest buckling beam and lowest resonant frequency provides the lowest residual stress value which is calculated to be -5.249 MPa. Thus for the average buckling beam, we obtain a stress value of  $-5.51 \pm 0.25$  MPa. By repeating the above procedures for Poly2, I obtain a stress variation of  $-13.8 \pm 1.6$  MPa. These error bars can be applied to all critical buckling stress values when post-processing is not performed. If post processing is performed, the buckling beam lengths change and thus new error bars are required. Figure 4.31 illustrates the expected variation in Poly1 residual stress at each buckling length. Figure 4.31a) provides the stress variation for 100  $\mu m$  to 450  $\mu m$  long buckling beams and Figure 4.31b) provides the stress variation for 450  $\mu m$  to 900  $\mu m$  long buckling beams. From Figure 4.31, the stress variation reduces significantly as the buckling beam length increases. Figure 4.32 illustrates the expected variation in Poly2 residual stress at each buckling length.

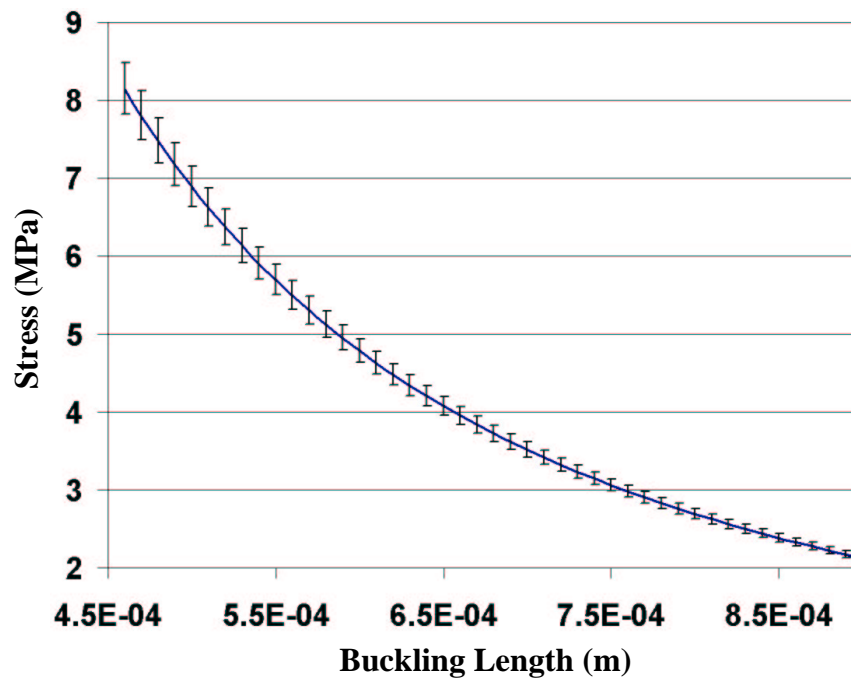
#### 4.7 *Summary of Chapter IV*

In this chapter I show that the localized residual stress levels in MEMS devices vary not only from one test die to another but also from one MUMPS® run to the next. With the stress variations in the foundry's fabrication processes, it is extremely difficult to design MEMS structures which provide repeatable operational results. I performed several experimental tests using  $\mu$ Raman spectroscopy to measure the background residual stress distribution in unreleased and released MEMS structures including conventional beams, cantilevers, and micromirror flexures. I generated stress map images to illustrate the stress variations across the width and length of these test structures. I compared my measured Raman stress map to results obtained from the MEMCAD FEM software. Both measured and numerical results clearly illustrate that the stress across the Poly1 and Poly2 flexures is minimal, as compared to the stress down the flexure lengths. I show that the measured and calculated values of stress are well correlated across the width of the structure (y-

direction) and along the length of the structure (x-direction). Both Raman and MEMCAD indicate minimal stress variations across the width of a structure with the primary stress component along the length of the test structure. The residual and induced stress profiles obtained from  $\mu$ Raman spectroscopy demonstrate a realistic representation of the stress distributions within the MEMS structures. I clearly show that  $\mu$ Raman spectroscopy is a viable, nondestructive, technique for measuring stress in MEMS.

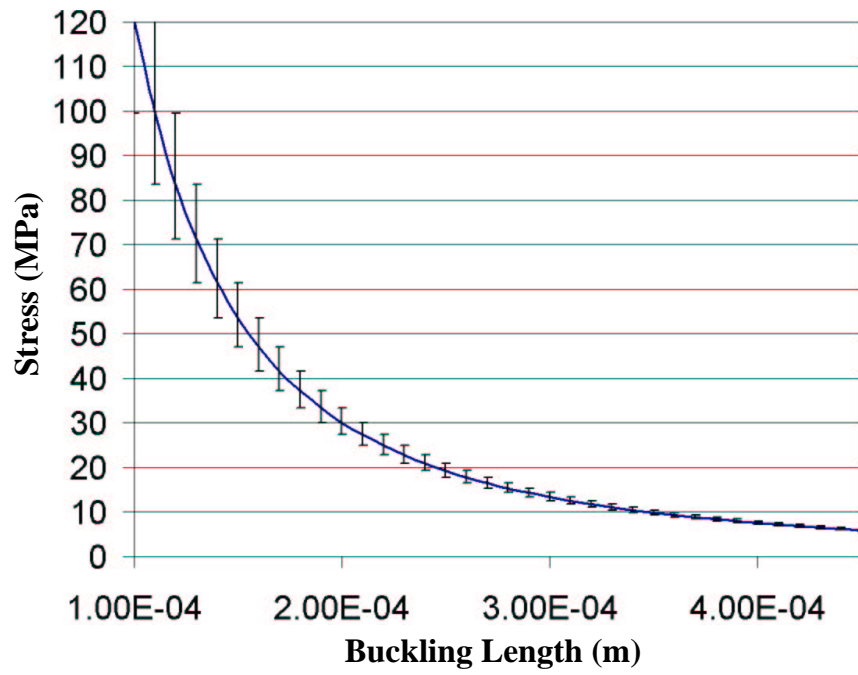


(a)

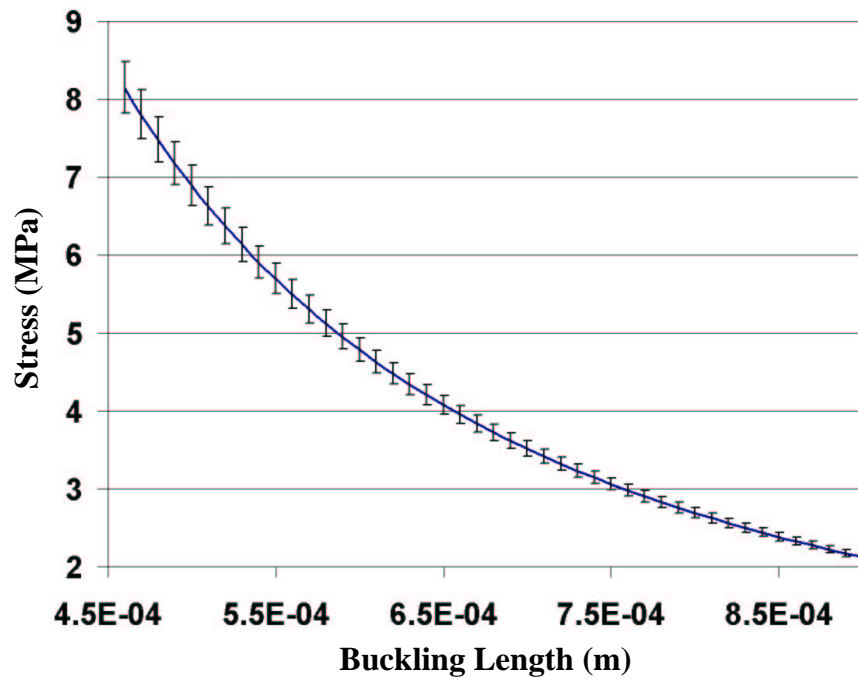


(b)

Figure 4.31: Poly1 residual stress variations as a function of the buckling beam lengths. a) stress variations for buckling beam lengths of  $100 \mu m$  to  $450 \mu m$ , b) stress variations for buckling beam lengths of  $450 \mu m$  to  $900 \mu m$



(a)



(b)

Figure 4.32: Poly2 residual stress variations as a function of the buckling beam lengths. a) stress variations for buckling beam lengths of  $100 \mu\text{m}$  to  $450 \mu\text{m}$ , b) stress variations for buckling beam lengths of  $450 \mu\text{m}$  to  $900 \mu\text{m}$

## Bibliography

1. Cronos, MUMP<sup>®</sup>s run data. [www.memsrus.com/cronos/svcsdata45.html](http://www.memsrus.com/cronos/svcsdata45.html), 2001.
2. M. G. Allen, M. Mehregany, R. T. Howe, and S. D. Senturia. Microfabricated structures for the *in situ* measurement of residual stress, Young's modulus, and ultimate strain of thin films. *Applied Physics Letters*, 51(4):241–243, July 1987.
3. M. A. Bentez, L. Fonseca, J. Esteve, M. S. Benrakkad, J. R. Morante, J. Samitier, and J. A. Schweitz. Stress-profile characterization and test-structure analysis of single and double ion-implanted LPCVD polycrystalline silicon. *Sensors and Actuators A*, 54:718–723, 1996.
4. B. Bhushan. *Tribology and Mechanics of Magnetic Storage Devices*. Springer Company, New York, NY, 1990.
5. W. D. Cowan. *Foundry Microfabrication of Deformable Mirrors for Adaptive Optics*. PhD thesis, Air Force Institute of Technology (AETC), Wright-Patterson AFB OH, 1998. AFIT/DS/ENG/98-07.
6. W. D. Cowan. Surface micromachined segmented mirrors for adaptive optics. *IEEE Journal of Selected Topics in Quantum Electronics*, 8:90–101, November 1999.
7. W. D. Cowan. Materials impacts on micro-opto-electro-mechanical systems. In *SPIE-MOEMS and Miniaturized Systems, Santa Clara, CA.*, volume 4178, pages 30–41, 18-20 Sept 2000.
8. G. C. Dalton. Artificial cochlea design using micro-electro-mechanical systems. Master's thesis, Air Force Institute of Technology, Wright-Patterson AFB OH, 1996. AFIT/GCS/ENG/96-07.
9. M. P. de Boer, P. J. Clews, B. K. Smith, and T. A. Michalske. Adhesion of polysilicon microbeams in controlled humidity ambients. *Materials Research Society Symposium*, 518:131–136.
10. L. Elbrecht, U. Storm, R. Catanescu, and J. Binder. Comparison of stress measurement techniques in surface micromachining. *Journal of Micromechanical Microengineering*, 7:151–154, 1997.
11. W. Fang and J. A. Wickert. Post buckling of micromachined beams. *Journal of Micromechanical Microengineering*, 4:116–122, 1994.
12. S. Greek, F. Ericson, S. Johansson, M. Fürtsch, and A. Rump. Mechanical characterization of thick polysilicon films: Young's modulus and fracture strength evaluated with microstructures. *Journal of Micromechanical Microengineering*, 9:245–251, 1999.

13. R. T. Howe, B. E. Boser, and A. P. Pisano. Polysilicon integrated microsystems: technologies and applications. *Sensors and Actuators A*, 56:167–177, 1996.
14. G. Kaltsas, A. G. Nassiopoulou, M. Siakavellas, and E. Anastassikis. Stress effect on suspended polycrystalline silicon membranes fabricated by micromachining of porous silicon. *Sensors and Actuators A*, 68:429–434, 1998.
15. M. Kawata, S. Nadahara, J. Shiozawa, M. Watanabe, and T. Katoda. Characterization of stress in doped and undoped polycrystalline silicon before and after annealing or oxidation with laser raman spectroscopy. *Research Center for Advanced Science and Technology*, pages 407–411, September 1989.
16. J. Y. Kim and C. J. Kim. Comparative study of various release methods for polysilicon surface micromachining. In *IEEE Micro Electro Mechanical Systems Workshop*, pages 442–447, Japan, 1997.
17. D. A. Koester, R. Mahadevan, B. Hardy, and K. W. Markus. MUMPs<sup>TM</sup> design handbook rev. 6, 2001. Cronos Integrated Microsystems, a JDS Uniphase Company, 3026 Cornwallis Rd., Research Triangle Park, NC 27709.
18. Gregory T. A. Kovacs. *Micromachined Transducers Sourcebook*. McGraw-Hill, New York, NY, 1998.
19. S. Lee, C. Cho, J. Kim, S. Park, S. Yi, J. Kim, and D. Cho. The effects of post-deposition processes on polysilicon Young’s modulus. *Journal of Micromechanical Microengineering*, 8:330–337, 1998.
20. G. J. Leusink, T. G. Oosterlaken, G. C. Janssen, and S. Radelaar. In situ sensitive measurement of stress in thin films. *Review of Scientific Instruments*, 63(5):3143–3145, May 1992.
21. D. Maier-Schneider, A. Köprülülü, S. Ballhausen Holm, and E. Obermeier. Elastic properties and microstructure of LPCVD polysilicon films. *Journal of Micromechanical Microengineering*, 6:436–446, 1996.
22. D. Maier-Schneider, J. Maibach, E. Obermeier, and D.A. Schneider. Variations in Young’s modulus and intrinsic stress of LPCVD-polysilicon due to high-temperature annealing. *Journal of Micromechanical Microengineering*, 5:121–124, 1995.
23. W. D. Pilkey. *Formulas for Stress, Strain, and Structural Matrices*. John Wiley & Sons, Inc., 1994.
24. Joseph E. Shigley and Charles R. Mischke. *Mechanical Engineering Design*. McGraw-Hill series in mechanical engineering. McGraw-Hill, Inc., New York, NY, 5th edition, 1989.
25. M. Siakavellas, E. Anastassikis, G. Kaltsas, and A. G. Nassiopoulos. Micro-Raman characterization of stress distribution within free standing mono- and

- poly-crystalline silicon membranes. *Microelectronic Engineering*, 41/42:469–472, 1998.
26. W. Chi-Keung Tang. *Electrostatic Comb Drive for Resonant Sensor and Actuator Applications*. PhD thesis, University of California, Berkeley, 1990.
  27. Tousimis, 2001. 2211 Lewis Avenue, Rockville, MD 20851.
  28. Q. Zou, Z. Li, and L. Liu. New methods for measuring mechanical properties of thin films in micromachining: beam pull-in (VPI) method and long beam deflection (LBD) method. *Sensors and Actuators A*, 48:137–143, 1995.

## *V. Post-Fabrication Anneals on Polysilicon MEMS Structures*

### *5.1 Introduction*

There are several post-fabrication processes which can influence the residual stress of MEMS devices. The two processes I focused on were post-fabrication annealing and phosphorous doping by diffusion and ion implants. These processes can be exploited to determine and obtain the required residual stress levels necessary for a particular MEMS design. For the MUMPs® foundry process, the residual stress in the thin film polysilicon structural layers is compressive. I first measured the magnitude of this compressive stress and then determined the amount of residual stress relaxation that occurs following a high temperature post-fabrication anneal.

In this chapter, I use a post-fabrication anneal technique to assess residual stress relaxation in MUMPs® Poly1 and Poly2 structural layers. I present *TSUPREM<sup>TM</sup>* modelling simulations for oxidized and unoxidized Poly1 and Poly2 layers. Stress profiles are measured by  $\mu$ Raman spectroscopy and compared to analytical residual stress levels obtained from critical buckling beam array test structures and cantilever deflection calculations. All MEMS die used in my post-processing anneal experiments are fabricated without metal. The gold metal used in the MUMPs® process would melt at the selected 1100 °C annealing temperature.

I am the first to measure, monitor, and reduce the residual stress in MUMPs® polysilicon structural layers by high temperature annealing. I verified the stress reduction through on-chip test structures. In addition, I demonstrated the use of  $\mu$ Raman spectroscopy to monitor and control the levels of residual stress relaxation in unreleased MEMS devices.

### *5.2 Thermal Annealing*

Post-processing furnace annealing is one technique I used in an attempt to reduce the residual stress in MEMS structures. From the MUMPs® fabrication

process, stress gradients exist in the polysilicon layers due to dopant irregularities, dopant uniformity, and peak dopant concentration levels. The annealing of these MEMS structures is expected to reduce the magnitude of the stress gradients, thus reducing the internal residual stress levels in the polysilicon layers.

From previous research, several significant characteristics are known concerning the thermal annealing of polysilicon. The annealing characteristics include the following facts:

- Compressive stress starts to decrease with annealing temperatures above the polysilicon deposition temperature of  $620\text{ }^{\circ}\text{C}$
- Some polysilicon films become nearly stress free after annealing at  $1100\text{ }^{\circ}\text{C}$  for 2-hours [5]
- It is not possible to induce tensile stress by annealing. This behavior indicates that the movement of dislocations in the grains and not the change in the film density is responsible for the stress relaxation [5]
- At temperatures above approximately  $750\text{ }^{\circ}\text{C}$ , silicon becomes increasingly ductile and the dislocations move in the direction of the stress gradient [5]. While moving through the crystal the dislocations reduce the stress. If the stress is nearly relaxed, there is no more driving force and the dislocations stop moving. Therefore it is not possible to convert a compressive stress into a tensile stress.
- Annealing below  $1000\text{ }^{\circ}\text{C}$  does not influence the grain size of as-deposited polysilicon film [4, 6].
- The grain size starts to increase when the annealing temperature is above  $1100\text{ }^{\circ}\text{C}$  [4]. From several studies on the grain size of polysilicon, an increased grain size will aid in reducing the residual stress [4, 6].

Post-deposition annealing to assist in stress reduction using conventional furnace annealing and rapid thermal annealing (RTA) has been investigated by Singh et

al. [6]. As-deposited polysilicon films show a significant amount of residual strain under all deposition conditions. The strain is reduced to approximately -20 MPa after a 100-min furnace anneal [6]. In the case of RTA, similar strain values are achieved in only 30-seconds of annealing. Post release annealing can lead to structural layer plastic deformation (cannot be recovered); thus, annealing must be performed before releasing the MEMS structures.

I use various MEMS structures fabricated in the MUMPs® fabrication process to determine if post-processing annealing will aid in the reduction of the residual stress common to polysilicon deposition. I performed post-processing tests using a mini BlueM annealing oven. RTA annealing was not performed since an RTA system compatible with the phosphorus dopant was not readily available. All post-process annealing experiments were performed on MEMS die prior to the HF release. Accurate annealing times and temperatures were documented so proper correlation between test die could be made. Since further annealing is not possible once the MEMS structures are released, initial  $\mu$ Raman scans are used to determine the foundry fabricated background residual stress levels prior to the 1100 °C anneals. Subsequent  $\mu$ Raman scans are performed following each timed anneal to determine the level of stress reduction associated for each anneal period.

I used die from several MUMPs® runs (#41 through #45) for the post-fabrication anneal studies. Prior to performing the post-fabrication anneals, several preparatory steps needed to be accomplished. First, a new annealing tube was obtained. Prior to use, the tube required cleaning and I performed a prebake to remove any contaminants and moisture. I cleaned the annealing tube according to the procedure outlined in Appendix A. Second, the protective photoresist covering all MEMS die was removed to prevent contamination and damage to the furnace tube. I used two separate 15-min acetone dips to remove the photoresist with an initial aggressive agitation for the first 3-min [3]. Following the acetone dips, the die are placed in methanol for 5-min and then dried on a hotplate at 60 °C for 1-min.

### 5.3 *TSUPREM<sup>TM</sup> Anneal Modelling*

From previous resistivity research on MUMPs<sup>®</sup> polysilicon, it was observed that phosphorous outgassing occurs when the temperature of the MEMS die is increased to 1100°C during the thermal anneals [1]. Since the buffered oxide etch performed at the MUMPs<sup>®</sup> foundry removes the second oxide layer exposing all Poly1 and Poly2 structures, I performed two separate *TSUPREM<sup>TM</sup>* simulations. One simulation employs an oxide cap and the other does not to illustrate the effects the oxide cap has on the dopant uniformity within the polysilicon layers.

Following several *TSUPREM<sup>TM</sup>* simulations with various oxide cap thicknesses, I determined that a 50 Å-thick or thicker cap on exposed polysilicon will nearly eliminate the phosphorous outgassing. Figure 5.1a) illustrates the *TSUPREM<sup>TM</sup>* simulation with the growth of a thin 50 Å-thick layer of oxide to cap off the exposed structures. Several timed 1100 °C anneals are then performed to promote further dopant diffusion to increase dopant uniformity. Figure 5.1b) illustrates the *TSUPREM<sup>TM</sup>* simulation for a 10 μm-wide Poly1 beam without an oxide cap. The identical 1100 °C anneals are simulated for this test.

As shown in Figure 5.1a), a thin 50 Å-thick layer of oxide grown over the polysilicon structures will nearly eliminate phosphorous outgassing. The oxide cap clearly promotes dopant uniformity throughout the 1100 °C anneal simulations. Without the oxide cap, phosphorous outgassing continues throughout the anneal periods. The outgassing causes the peak dopant concentration to decrease by approximately half an order of magnitude and the dopant never becomes uniform due to the continuous outgassing. Therefore, from the *TSUPREM<sup>TM</sup>* simulations for Poly1, the oxide cap promotes dopant uniformity which should result in a decrease in the residual stress. However, for Poly1 structures without the oxide cap, dopant uniformity cannot be achieved and the residual stress gradients may increase in the Poly1 structures.

An identical *TSUPREM<sup>TM</sup>* simulation was performed on a 10 μm-wide Poly2 beam with and without the oxide cap. Figure 5.2a) illustrates the oxidized beam

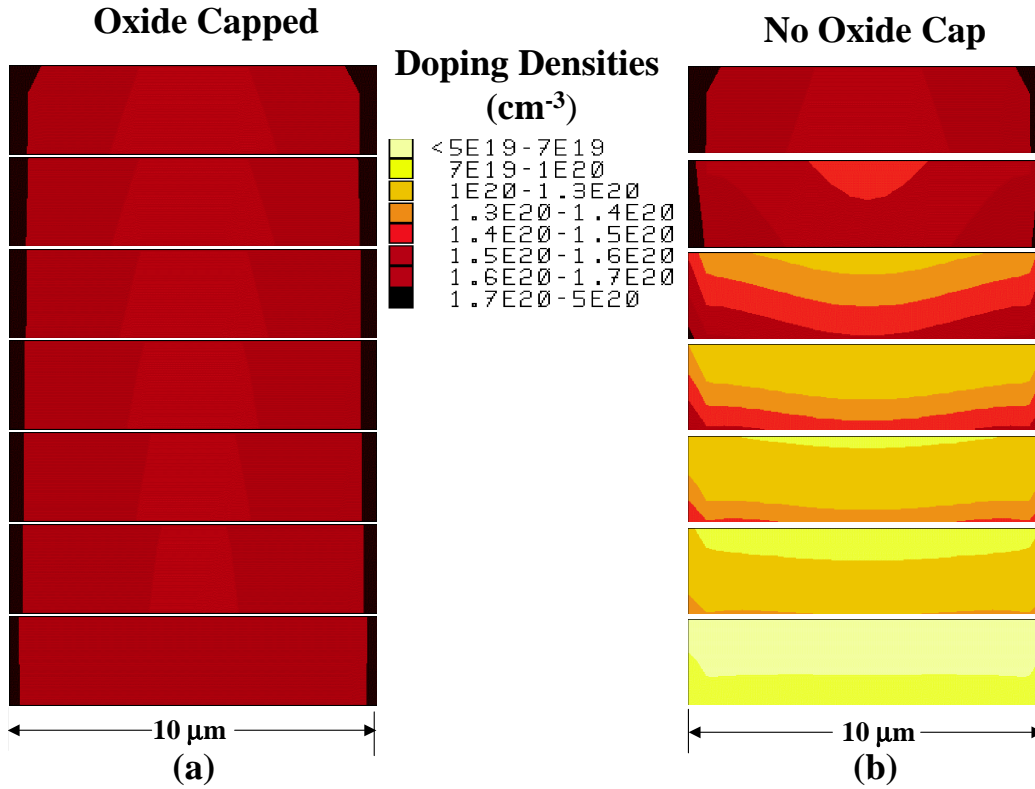


Figure 5.1: Cross-section *TSUPREM*<sup>TM</sup> simulations of the dopant density in oxidized and unoxidized Poly1 10  $\mu\text{m}$ -wide beams. Top-to-bottom anneal times (min): 0, 5, 10, 15, 20, 30, and 60-min. (a) with oxide cap, and (b) without the oxide cap.

and Figure 5.2b) shows the unoxidized beam. The results are similar to the Poly1 simulations. The oxidized beam promoted dopant uniformity and the residual stress is expected to decrease. The unoxidized beam continued to outgas and the dopant never becomes uniform. Thus, the residual stress is expected to increase.

#### 5.4 Oxidized vs. Unoxidized Stress Analysis

From the *TSUPREM*<sup>TM</sup> images shown in Figure 5.1b) and Figure 5.2b), I observed that the phosphorus dopant concentration decreases rather significantly for unoxidized polysilicon structures during the 1100  $^{\circ}\text{C}$  anneals. Since the MUMPs<sup>®</sup> foundry removes the second oxide exposing both the Poly1 and Poly2 structures,

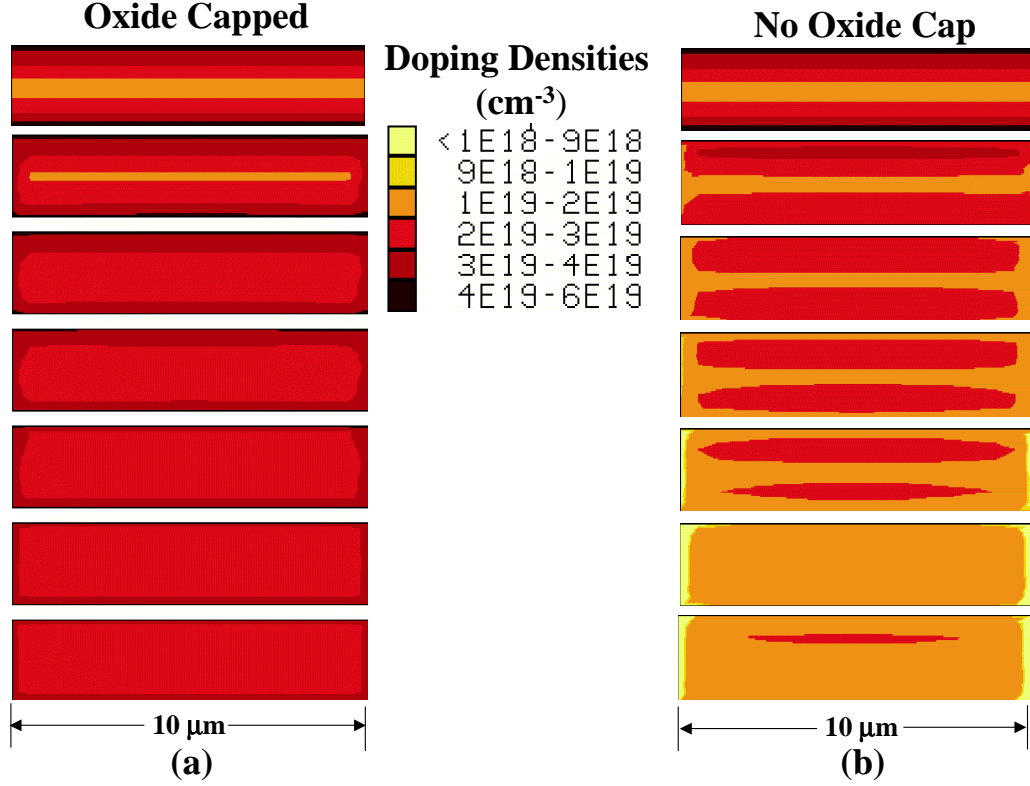


Figure 5.2: Cross-section *TSUPREM*<sup>TM</sup> simulations of the dopant density in oxidized and unoxidized Poly2 10  $\mu\text{m}$ -wide beams. Top-to-bottom anneal times (min): 0, 5, 10, 15, 20, 30, and 60-min. (a) with oxide cap, and (b) without oxide cap.

I performed a thermal oxidation to form an oxide layer on the exposed polysilicon layers prior to the 1100  $^{\circ}\text{C}$  anneals to reduce phosphorous outgassing. From the oxidation growth tables found in Sze [8], I selected a 900  $^{\circ}\text{C}$ , 30-min dry oxidation to grow the 50 Å-thick oxide cap. Following the thermal oxidation of the polysilicon, I performed controlled anneals on the individual MEMS die. I expected the anneals to increase dopant uniformity and reduce stress gradients.

Prior to performing the 1100  $^{\circ}\text{C}$  anneals, I verified that the 50 Å-thick oxide cap was sufficient to reduce the phosphorous outgassing. To measure the thickness of the oxide cap, I placed a sample MEMS die in the oxidation furnace at a temperature of 900  $^{\circ}\text{C}$  for 30-min with a 1 liter/min  $\text{O}_2$  gas flow rate. Following the oxidation,

I placed photoresist over one half of the die to create a protective mask. I removed the grown oxide layer with an HF vapor exposure (I suspended the die above an HF liquid layer) followed by a methanol rinse. The oxide cap was later measured to be 630 Å-thick with a Tencor profilometer. Although the oxide cap is thicker than the modeled value of 50 Å, this oxidation time period was selected to guarantee that a sufficient oxide cap is grown. Likewise, a thicker oxide cap should not significantly effect the 1100 °C anneals or the subsequent  $\mu$ Raman spectroscopy measurements.

To quantify the *TSUPREM<sup>TM</sup>* simulation results for the unoxidized and oxidized MEMS die, I selected a set of 6 oxidized and 4 unoxidized die for the anneal study. I performed a single anneal at 1100 °C for each pair of die (1-oxidized and 1-unoxidized) for anneal times of 5, 10, 15, and 20-min. I annealed the two remaining oxidized die for 30, and 60-min. Following the anneals, I performed  $\mu$ Raman spectroscopy.

### 5.5 $\mu$ Raman Spectroscopy Stress Analysis

$\mu$ Raman spectroscopy is used to obtain residual stress profiles from the unreleased MEMS test die. Prior to the oxidation and 1100 °C anneals, I performed a series of  $\mu$ Raman scans on 10  $\mu$ m-wide Poly1 and Poly2 fixed-fixed beams to determine the foundry fabricated background stress levels. Figure 5.3 shows a SEM image of the fixed-fixed beams selected for these Raman tests. Raman scans of the identical test beams are performed following the oxidation, and again after the 1100 °C anneals. All Raman stress profiles presented in this section are the average of three repeated  $\mu$ Raman scans.

Figure 5.4 illustrates the oxidized and unoxidized Raman stress profiles for 10  $\mu$ m-wide Poly1 unreleased fixed-fixed beams. The data for the oxidized Poly1 beam is shown in Figure 5.4a). From the Raman stress profiles, one notices that the residual stress actually increases during the oxidation and reaches an average maximum stress level of  $\sim$  -290 MPa. This is roughly -60 MPa higher than the foundry

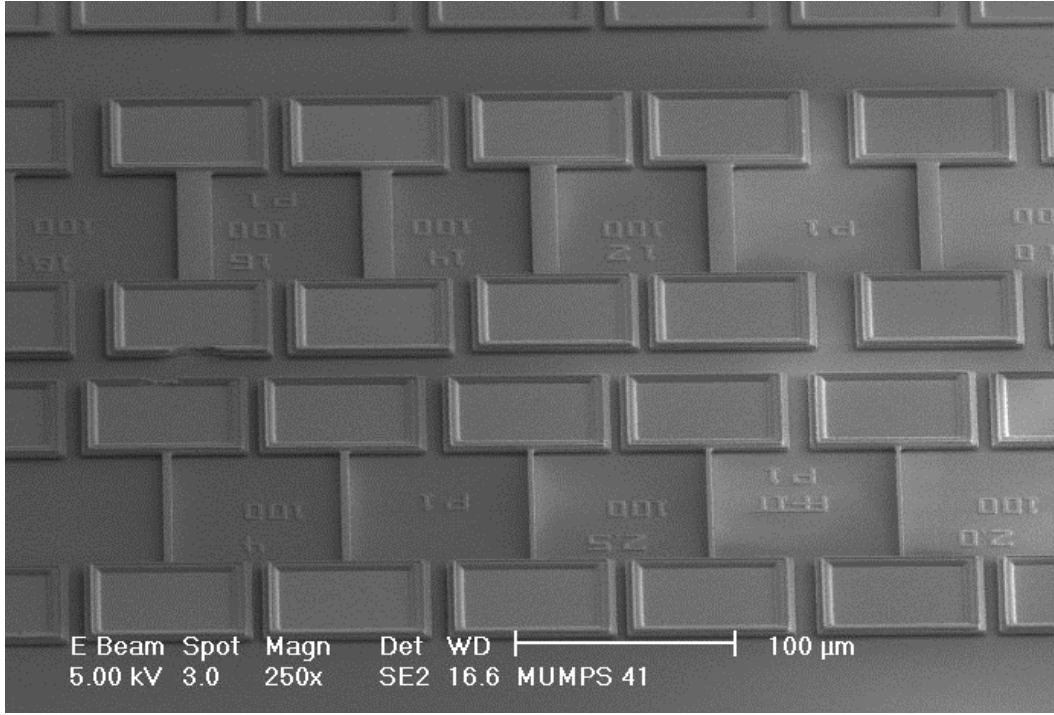


Figure 5.3: SEM image of Poly1 microbridges used for residual stress characterization.

fabricated stress level. The stress increase is probably due to initial phosphorous outgassing during the oxide growth. Oxidations are known to induce compressive stress; thus, the magnitude of the compressive stress is expected to increase [10]. Following the first 5-min anneal, the residual stress drops significantly to  $\sim -190$  MPa. The residual stress steadily decreases as the anneal time is increased. After 1-hour of annealing, the average residual stress reduces to  $\sim -80$  MPa.

The unoxidized Poly1 beam is shown in Figure 5.4b). The Raman stress profiles indicate a significant reduction in the residual stress within the first 5-min from  $\sim -220$  MPa for the foundry fabricated stress level to  $\sim -130$  MPa. Within 10-min, the residual stress reduces as far as possible to  $\sim -80$  MPa. Further anneals were performed with minimal changes observed. However, from my measurements it appears that the residual stress begins to slightly increase at longer anneal times. The residual stress probably decreases rapidly initially since the highest dopant concentrations

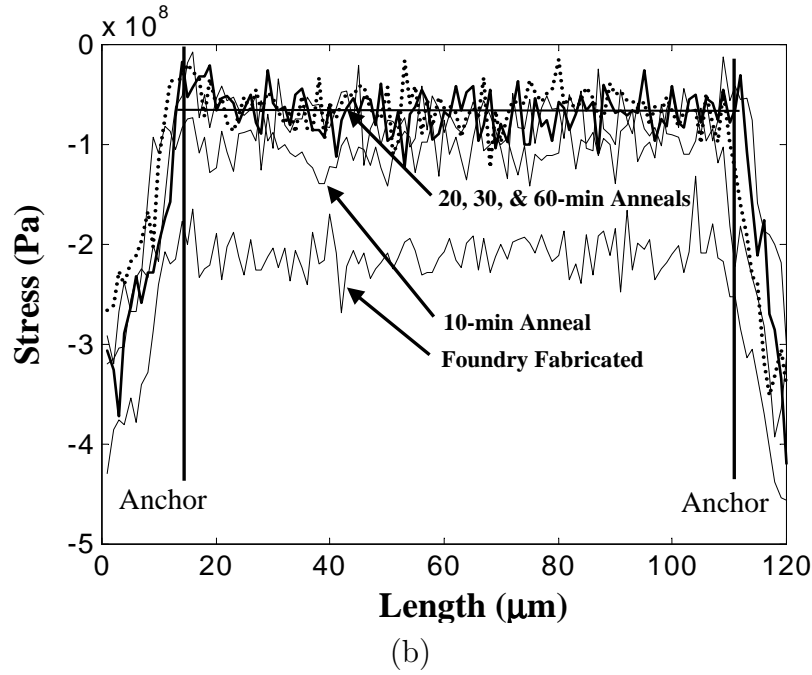
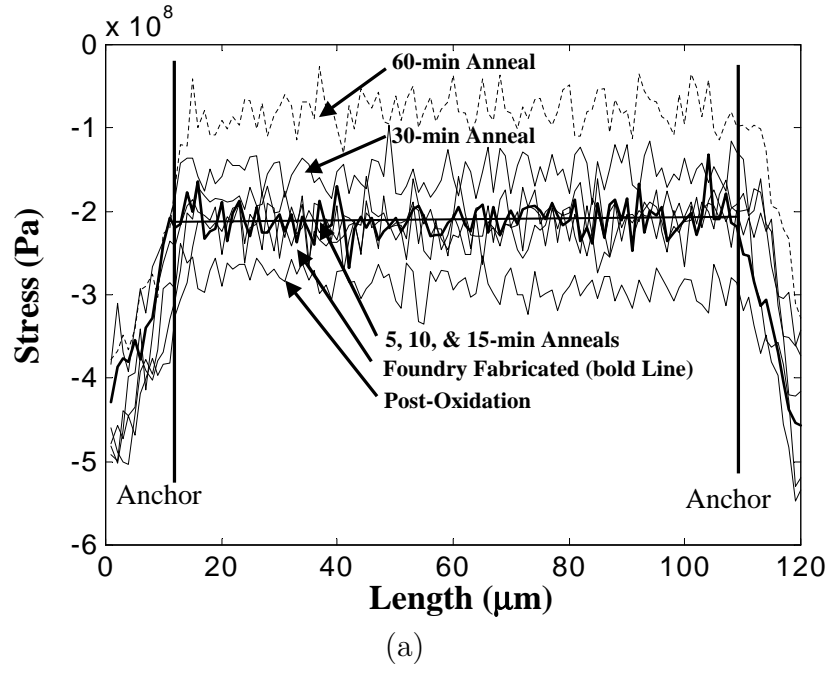


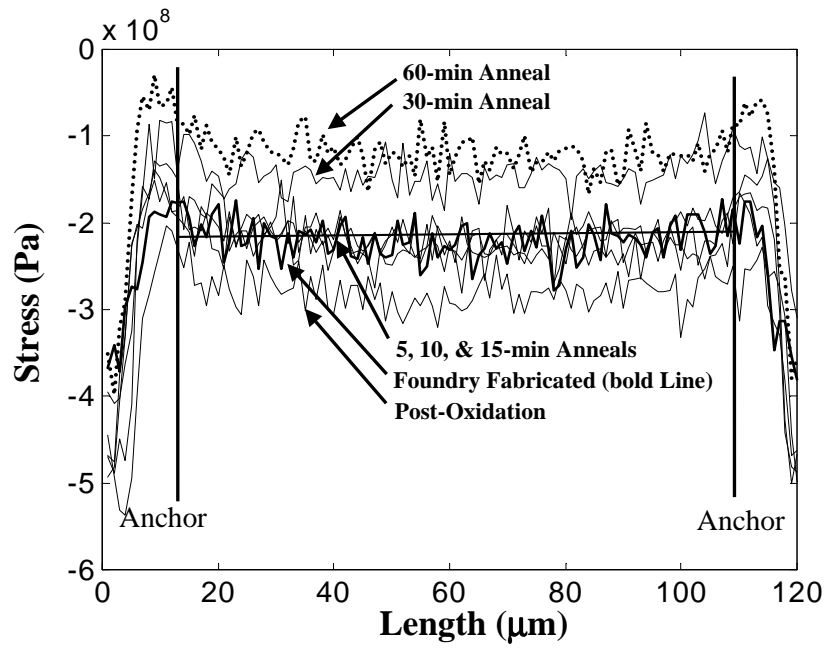
Figure 5.4:  $\mu$ Raman residual stress profiles for Poly1 10  $\mu m$ -wide oxidized and unoxidized beams (a) oxidized, (b) unoxidized.

are located near the surfaces of the Poly1 beam as illustrated in the *TSUPREM<sup>TM</sup>* beam model shown in Figure 5.1a) (top image).

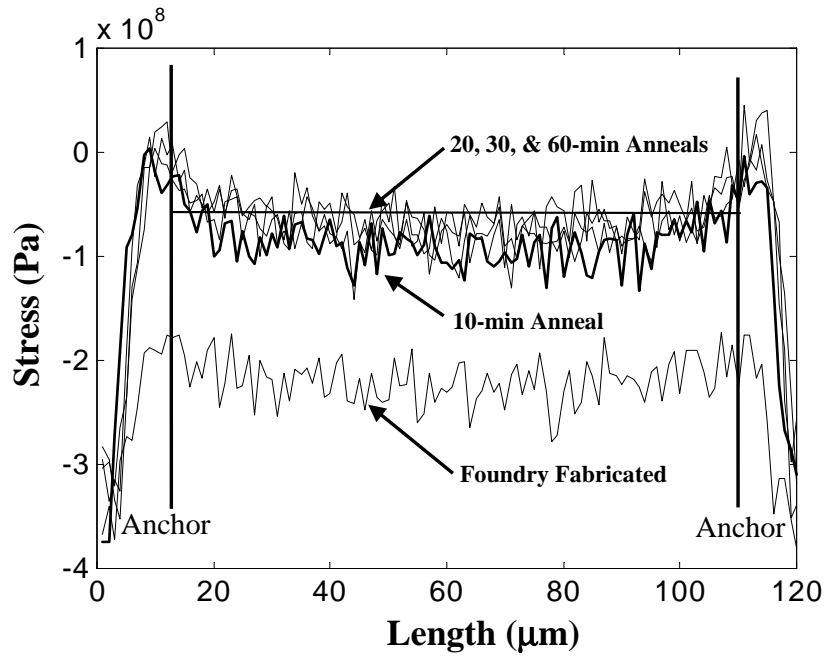
The stabilization of the residual stress after the first 10-min could result from the equilibrium of the dopant concentration along the length of the beam. Since  $\mu$ Raman spectroscopy probes the stress level at a specific depth in the material (770 nm for silicon) [9], the dopant uniformity at this established depth can remain fairly constant since the dopant diffuses from higher concentrations (bottom of the beam) to lower concentrations (top of the exposed beam). Eventually, I should obtain a dopant profile as illustrated in Figure 5.1b)(fourth image) where the dopant is uniform across the cross-sectional width of the beam but not uniform through the thickness of the beam. Thus, the residual stress may remain fairly constant under these conditions but the stress gradient through the thickness is likely to increase.

Figure 5.5 illustrates the oxidized and unoxidized  $\mu$ Raman stress profiles for 10  $\mu m$ -wide Poly2 unreleased fixed-fixed beams. The oxidized Poly2 stress profiles are shown in Figure 5.5a) and the unoxidized stress profiles are shown in Figure 5.5b). The Raman stress profiles obtained for the Poly2 beams are very similar to the Poly1 stress profiles for both the oxidized and unoxidized cases. The stress profiles look very similar with the exception that the peak residual stress after the 1-hour anneal is slightly higher in the Poly2 oxidized beam ( $\sim -100$  MPa in Poly2 compared to  $\sim -80$  MPa for Poly1). This may be a result of the lower dopant concentration level (approximately half an order of magnitude) in the Poly2 beam as compared to the Poly1 beam as modelled and shown in Figures 5.1 and 5.2.

Part of the observed residual stress relaxation could be a result of the 1100  $^{\circ}C$  anneals which increase the grain size of the polysilicon and promote residual stress relaxation [4, 6]. However, for the relatively short anneal times (5, 10, 15, and 20-min anneals), the grain size should not increase significantly. Thus, I expect that the majority of the observed stress reduction is due to increased dopant uniformity.



(a)



(b)

Figure 5.5:  $\mu$ Raman residual stress profiles for Poly2 10  $\mu m$ -wide oxidized and unoxidized beams (a) oxidized, (b) unoxidized.

## 5.6 Micromechanical Stress Measurements

Following the completion of the post-processing anneals and  $\mu$ Raman scans, I released the MEMS die as outlined in Appendix A. I performed the final dry by using the supercritical  $CO_2$  dryer. A series of oxidized buckled beam arrays for both the Poly1 and Poly2 structural layers is shown in Figure 5.6. The figures indicate the “critical buckling lengths for a given set of fixed-fixed beams.

The buckling beam arrays presented in Figure 5.6 correlate very well with the measured  $\mu$ Raman stress levels for the unreleased fixed-fixed beams. For example, the  $\mu$ Raman stress profiles, after oxidation indicated a fairly significant residual stress increase in both the Poly1 and Poly2 structural layers. From the critical buckling lengths illustrated in Figure 5.6b), the buckling lengths significantly decreased for Poly1 when compared to the foundry fabrication buckling lengths shown in Figure 5.6a). Although the Poly2 array indicates a small change in buckling beam lengths, the increased stress value is about the same as for Poly1. The calculated residual stress levels following the oxidation are -20.5 MPa for Poly1 and  $\sim$  -18 MPa for Poly2 beams. The remaining Raman stress profiles show a significant residual stress reduction causing an increase in the critical buckling length of the beams illustrated in Figure 5.6c)- f). One exception exists for the Poly2 beam array in Figure 5.6f) where the buckling length shortened which indicates an increase in the residual stress. This shorter buckling length could be a result of debris on the die as shown in Figure 5.6f). Although the entire Poly1 beam array remains unbuckled for all anneal times greater than 5-min, the Poly2 beam arrays never reach a fully unbuckled condition. Several reason exist which could result in this condition to include: 1) the dopant may never reach a uniform condition, 2) the dopant concentration may be too low to obtain a uniform concentration to reduce the stress gradients, and 3) phosphorous outgassing may be significant in the thinner Poly2 layer prior to the desired oxide growth thickness.

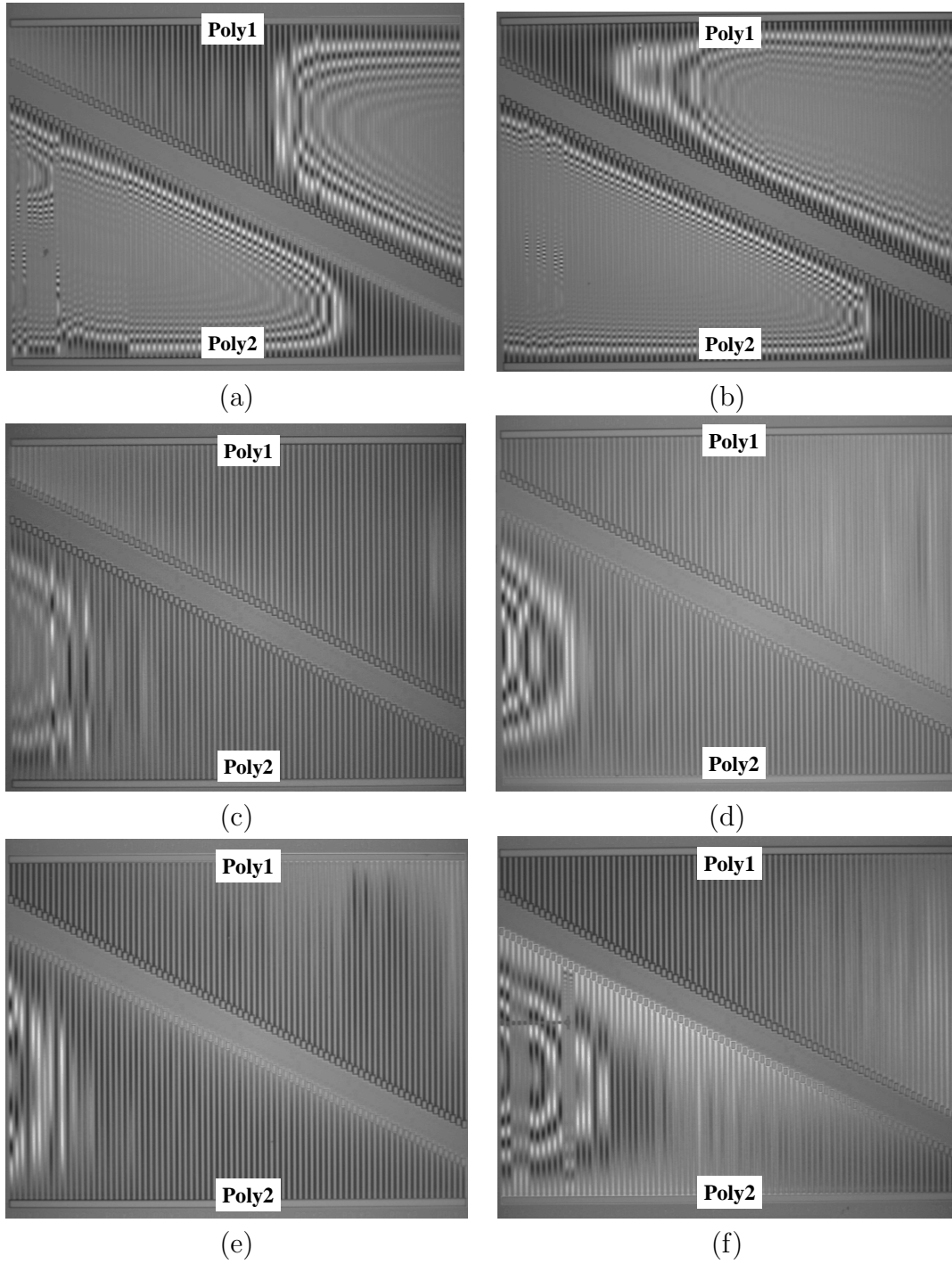


Figure 5.6: IFM images of oxidized Poly1 and Poly2 buckling beam arrays following 1100 °C anneals and HF release. Buckling beam arrays illustrated include: a) foundry fabrication; b) post 30-min oxidation; (c) post-oxidation and 5-min 1100 °C anneal; d) post-oxidation and 15-min 1100 °C anneal; e) post-oxidation and 20-min 1100 °C anneal; f) post-oxidation plus 30-min 1100 °C anneal

Next I used comb drive resonators to determine the value for Young's modulus for each structural layer Section 4.6.1. The resonant frequency did not significantly change due to residual stress relaxation. The resonant frequencies for both the oxidized and unoxidized die averaged approximately  $22.5 \pm 0.15$  kHz for Poly1 and  $18.9 \pm 0.15$  kHz for Poly2. The resonant frequencies correlate to Young's modulus values of approximately  $132 \pm 2$  GPa and  $162 \pm 2$  GPa respectively. By using the measured Young's modulus values, I calculated the analytical residual stress values for the oxidized critical buckling Poly1 and Poly2 beams shown in Figure 5.6. The calculated residual stress values are given in Table 5.6. In Table 5.6, the residual stress level does significantly increase following the oxidation and then rapidly decreases following the initial 1100 °C anneal.

Table 5.1: Oxidized buckled beam arrays residual stress values calculated from Figure 5.6

Image	Beam	Anneal Time (min)	Measured Buckling Length ( $\mu m$ )	Calculated Residual Stress (MPa)
Figure (a)	Poly1	foundry fab.	540	-5.9
Figure (a)	Poly2	foundry fab.	310	-12.6
Figure (b)	Poly1	30-min oxidation	290	-20.5
Figure (b)	Poly2	30-min oxidation	260	-17.9
Figure (c)	Poly1	5	900	-2.1
Figure (c)	Poly2	5	720	-2.3
Figure (d)	Poly1	15	900	-2.1
Figure (d)	Poly2	15	740	-2.2
Figure (e)	Poly1	20	900	-2.1
Figure (e)	Poly2	20	800	-1.9
Figure (f)	Poly1	30	900	-2.1
Figure (f)	Poly2	30	720	-2.3

The critical buckling beam arrays were designed with a maximum beam length of 900  $\mu m$ . The Poly1 beams remained unbuckled at this length following the 5-min 1100 °C anneal. Thus, this array provides no further indication of residual stress

relaxation for the longer anneal times. As a result, I used a Poly1 cantilever to further assess additional residual stress relaxation at the longer anneal times.

To determine if further residual stress relaxation occurs beyond the 5-min anneal time, a 150  $\mu m$ -long by 10  $\mu m$ -wide Poly1 cantilever was used. An IFM was used to measure the cantilever beam deflection to determine the residual stress. Figure 5.7 shows the IFM images. The images indicate a variety of deflection profiles for a cantilever array following oxidation.

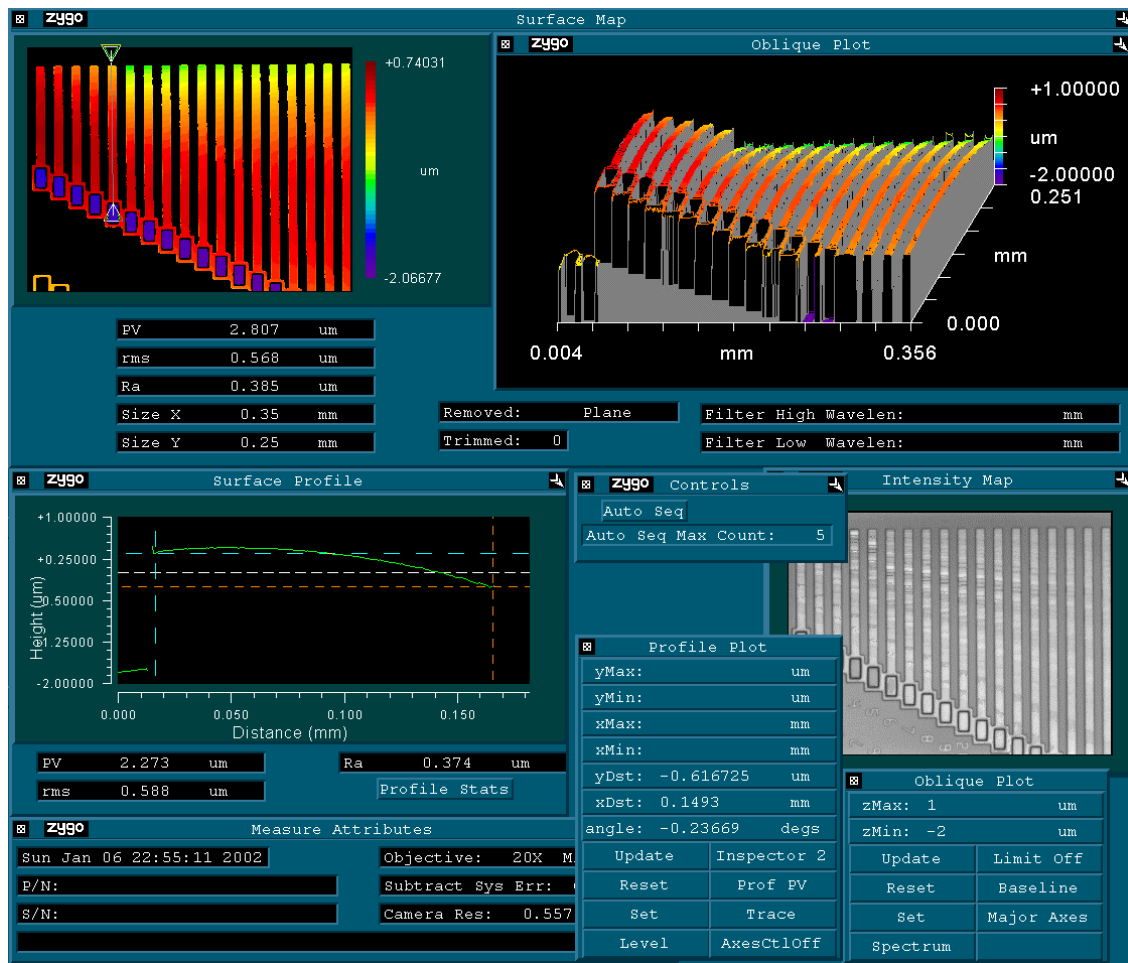


Figure 5.7: IFM image of a Poly1 cantilever array used for residual stress characterization.

Since internal stress is rarely uniform, but is instead a function of material thickness, many researchers are interested in the stress gradient within a material.

The stress gradient is calculated by looking at the change in stress over the change in film thickness. For a cantilever beam, the stress gradient can be analytically approximated by [7]:

$$\frac{d\sigma}{dt} = \frac{2yE}{(1-\nu)L^2} \quad (GPa/\mu m) \quad (5.1)$$

where  $y$  ( $\mu m$ ) is the deflection of the cantilever tip,  $t$  ( $\mu m$ ) is the film thickness,  $L$  ( $\mu m$ ) is the length of the cantilever,  $E$  (GPa) is Young's modulus, and  $\nu$  (unitless) is Poisson's ratio. While Equation 5.6 assumes a linearly varying stress field and does not take into account many of the irregularities considered in a finite element analysis, it does offer a good order of magnitude calculation for the stress field within thin films. Multiplying both sides of Equation 5.6 by  $dt$  and integrating yields the following equation for stress within a curled cantilever:

$$\sigma = \frac{2yEt}{(1-\nu)L^2} + c \quad (GPa) \quad (5.2)$$

where  $c = 0$  since  $\sigma(t = 0) = 0$ .

From the oxidized MEMS die, I measured the cantilever tip deflections for a 150  $\mu m$ -long by 10  $\mu m$ -wide Poly1 and Poly2 cantilever. The cantilevers are part of the Poly1 and Poly2 cantilever arrays fabricated on each MEMS die. All oxidized Poly1 cantilever deflections measured with the IFM are illustrated in Figure 5.8. This image shows the steady reduction in the deflection of the cantilever following the initial 1100  $^{\circ}C$  anneals and then begins to slightly increase for longer anneal times. The anchored end of the cantilever is located on the left-hand side of the figure. This image does not indicate the true height of the cantilevers above the substrate but only shows the relative deflection magnitudes of the cantilever beam. I also tested the deflections for Poly2 cantilevers measuring 150  $\mu m$ -long by 10  $\mu m$ -wide. The deflection images and residual stress levels for the Poly2 cantilevers were nearly identical to the results obtained for Poly1 cantilevers. Also, the buckling

beam array is still useful for the Poly2 structural layer since the maximum buckling length was not achieved. Thus, Poly2 cantilever results are not shown.

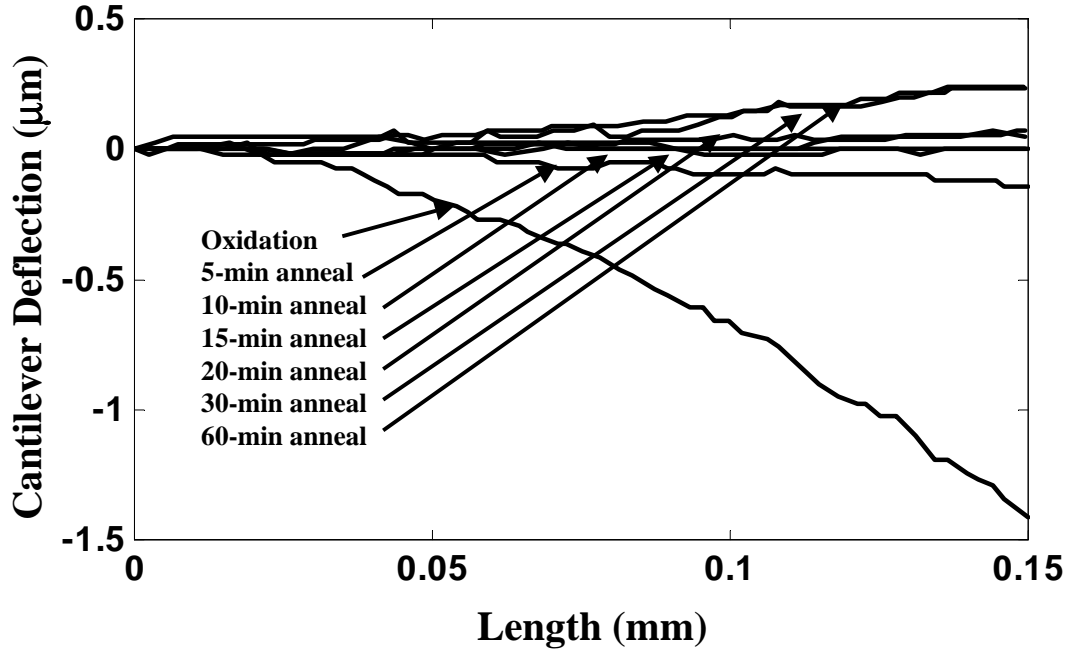


Figure 5.8: Cantilever deflection obtained from an IFM for all 150  $\mu m$ -long by 10  $\mu m$ -wide oxidized Poly1 cantilevers.

From the measured cantilever deflections for the oxidized MEMS die and using Equation 5.2, I calculated the residual stress for the Poly1 structural layer for the six anneal times. The calculated stress values for Poly1 cantilevers are provided in Table 5.2. The IFM precision is approximately  $\pm 1$  nm which give a residual stress variation of  $\pm 18$  kPa for Poly1 cantilevers.

As presented in Table 5.2, the residual stress continues to relax to a minimum value of -0.1 MPa after a 20-min anneal. For longer anneals, a slight increase is noticed. This increase could possibly be due to slight phosphorous outgassing or more likely from slight vibrations in the IFM measurement system. This situation does bear further investigation to identify what is causing the slight increase in stress at longer anneal times.

Table 5.2: Oxidized Poly1 cantilever residual stress values.

Beam	Anneal Time (min)	Measured Cantilever Deflection (nm)	Calculated Residual Stress (MPa)
Poly1	oxidation	1384	-20.94
Poly1	5	101	-1.52
Poly1	15	24	-0.37
Poly1	20	8	-0.12
Poly1	30	32	-0.48
Poly1	60	237	-3.58

To assess the unoxidized residual stress levels, the complete MEMS series of unoxidized buckled beam arrays for the Poly1 and Poly2 structural layers is shown in Figure 5.9. The images verify that residual stress relaxation occurs even though phosphorous outgassing occurs. The Poly1 beams are all unbuckled and the Poly2 beams are first unbuckled at a length of  $620\text{ }\mu\text{m}$  for a 10-min  $1100\text{ }^{\circ}\text{C}$  anneal and extend out to greater than  $900\text{ }\mu\text{m}$  for a 60-min  $1100\text{ }^{\circ}\text{C}$  anneal. Although the beams are not buckled, some of the beams have been slightly distorted. This is not the case for the oxidized die. Overall, from my visual inspection and my testing using electrostatic actuation, it appears that the oxide not only reduces outgassing but also provides structural protection during the  $1100\text{ }^{\circ}\text{C}$  anneals. Following the HF release, the oxidized die are significantly cleaner than the unoxidized die. Additionally, during electrostatic actuation testing on several micromirrors of the unoxidized die, although the residual stress appears to have been reduced, several micromirrors were physically warped to the point that actuation was not possible.

The measured critical buckling lengths for the unoxidized MEMS die shown in Figure 5.9 are listed in Table 5.3 with the corresponding calculated residual stress values. The  $\mu$ Raman stress profiles for the unoxidized Poly1 and Poly2  $10\text{ }\mu\text{m}$ -wide beams correlate well to the critical buckling beam lengths. By correlation, if the  $\mu$ Raman stress profile indicates an increase in the residual stress, the buckling beam array, once released shows a decrease in the buckling beam lengths which indicates

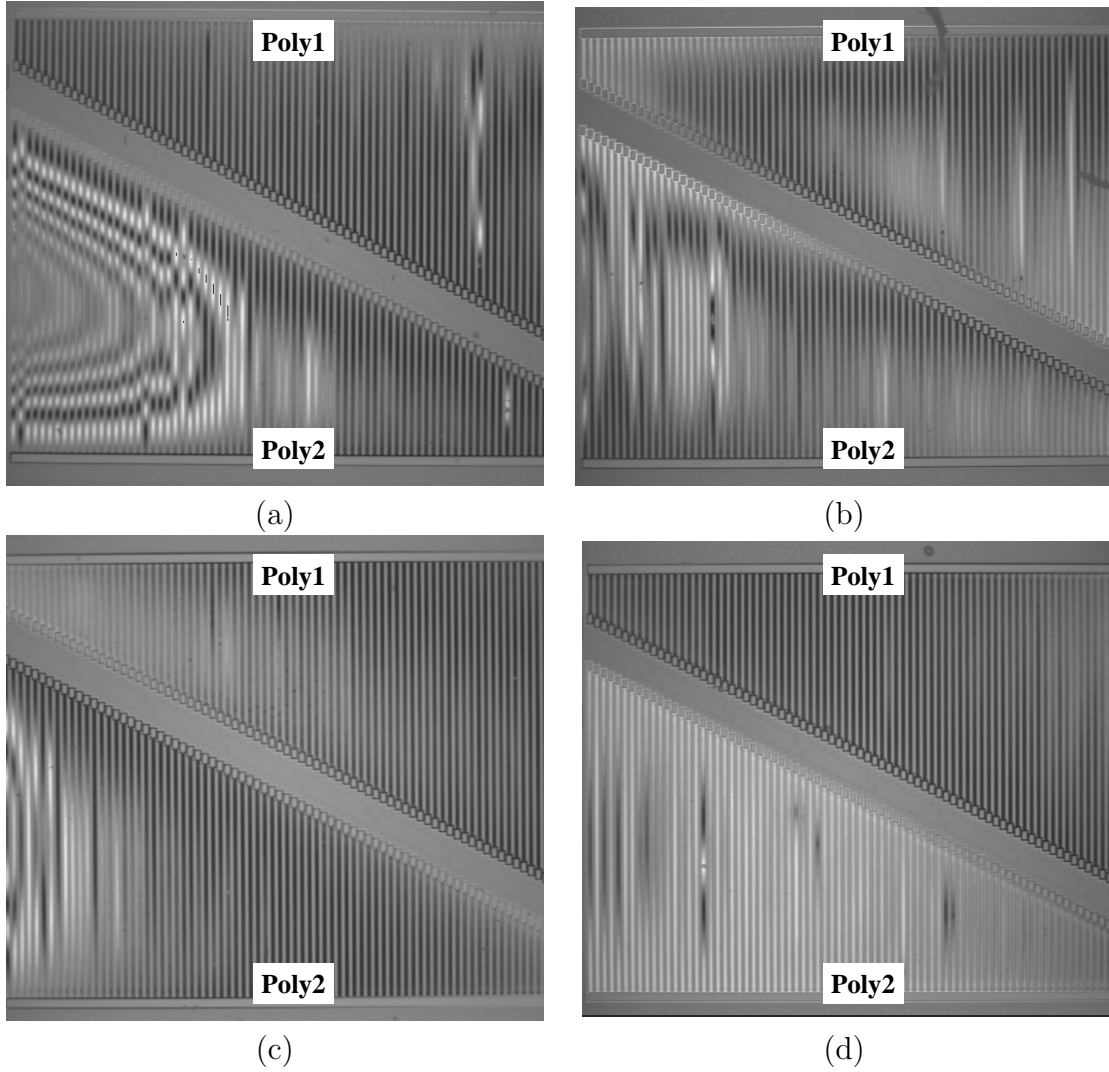


Figure 5.9: IFM images of unoxidized Poly1 and Poly2 buckling beam arrays following  $1100^{\circ}\text{C}$  anneals and HF release. Anneal times illustrated include: a) 10-min, b) 20-min, c) 30-min, and d) 60-min.

an increase in the residual stress. This scenario is reversed when the  $\mu\text{Raman}$  stress profile indicates a decrease in the residual stress, buckling beam length gets longer before buckling. The  $\mu\text{Raman}$  stress profiles indicate a significant stress reduction initially and then the stress remains fairly constant for the remaining anneals. This is also the case for the buckling beams and calculated residual stress values.

Table 5.3: Unoxidized buckling beam residual stress values from Figure 5.9

Image	Beam	Anneal Time (min)	Measured Buckling Length ( $\mu m$ )	Calculated Residual Stress (MPa)
Figure (a)	Poly1	10	900	-2.1
Figure (a)	Poly2	10	620	-3.2
Figure (b)	Poly1	20	900	-2.1
Figure (b)	Poly2	20	740	-2.2
Figure (c)	Poly1	30	900	-2.1
Figure (c)	Poly2	30	740	-2.2
Figure (d)	Poly1	60	900	-2.1
Figure (d)	Poly2	60	900	-1.5

As before, I used the cantilever deflection values obtained from IFM imaging to determine the residual stress levels in the unoxidized MEMS die. The cantilever deflections and calculated residual stress values are shown in Table 5.4. Since the IFM precision is approximately  $\pm 1$  nm, this gives a residual stress variation of  $\pm 14$  kPa for Poly2 cantilevers.

Table 5.4: Unoxidized Poly1 and Poly2 cantilever residual stress values.

Beam	Anneal Time (min)	Measured Cantilever Deflection (nm)	Calculated Residual Stress (MPa)
Poly1	10	153	-2.32
Poly2	10	279	-3.92
Poly1	20	9	-0.15
Poly2	20	190	-2.67
Poly1	30	59	-0.90
Poly2	30	171	-2.40
Poly1	60	93	-1.42
Poly2	60	89	-1.26

From the calculated residual stress values provided in Table 5.4, the stress fluctuates back and forth more then it decreases. These fluctuations are probably

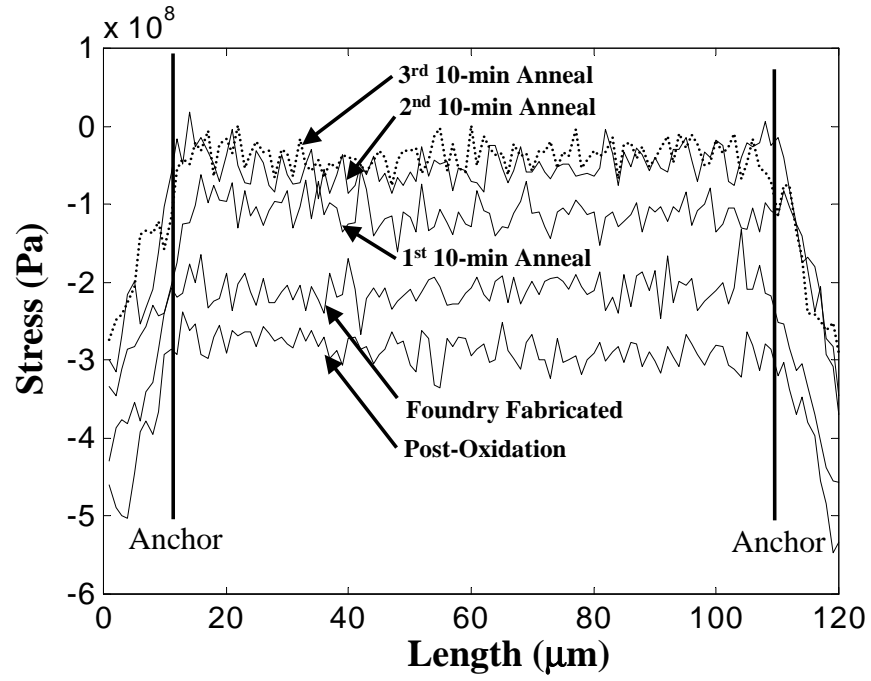
due to slight vibrations in the stage of the IFM or minor variations in the residual stress for different MEMS die due to the foundry fabrication processes.

### 5.7 Repeat Annealing

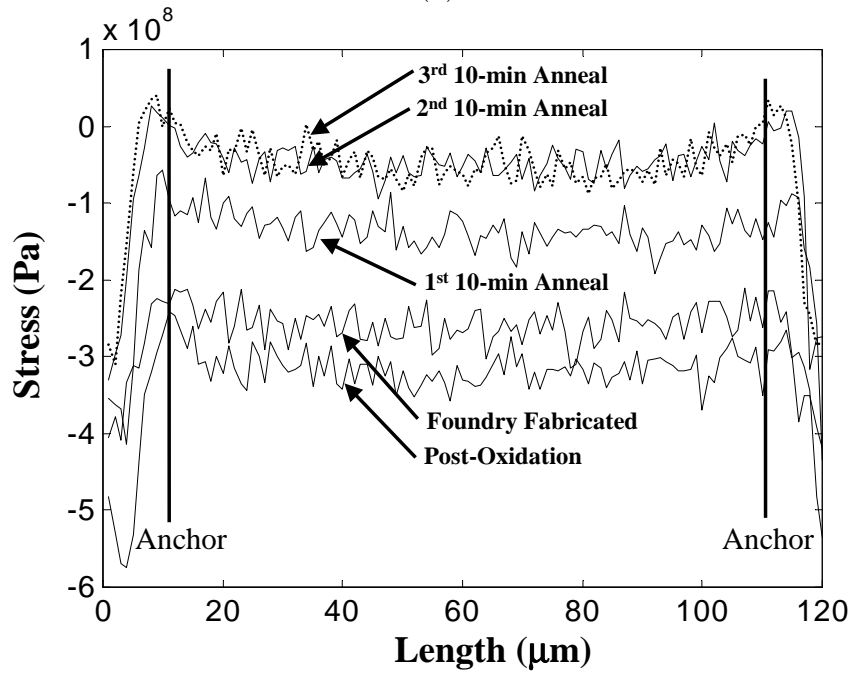
From the results of my thermal annealing analysis in the previous sections, I conclude that  $\mu$ Raman spectroscopy can be successfully used to monitor and measure the residual stress in unreleased MEMS structures. To further assess Raman spectroscopy as a residual stress measuring technique, I briefly examine the situation where the level of residual stress relaxation is not sufficient. I want to determine if repeat 1100 °C anneals on the same test die can produce further stress relaxation. To answer this question, I performed repeated 1100 °C anneals (three 10-min time periods) on two test die and measured a series of  $\mu$ Raman stress profiles following each anneal period. Figure 5.10 shows the  $\mu$ Raman stress profiles following each anneal period.

From Figure 5.10, it definitely appears that the residual stress can be further reduced following the initial 10-min anneal. The oxidation increased the stress in both Poly1 and Poly2 material layers to approximately -300 MPa. Following the initial 10-min anneal, the residual stress magnitude dropped to approximately -100 MPa for both material layers. After the second and third anneals, the stress reduced down to an average stress value of approximately -50 MPa. The final two anneals do not significantly reduce the stress further but this is expected. The compressive stress cannot change to tensile stress through these simple anneals. Also the stress gradients in the beams are progressively reduced. The dopant diffusion decreases as the dopant uniformity increases. The magnitude of residual stress relaxation also decreases progressively with each anneal.

Figure 5.11 illustrates the critical buckling beam array following HF release. By comparing the buckling beam array shown in Figure 5.11 with the buckling beam array obtained earlier for the oxidized 30-min 1100 °C anneal test die (Figure 5.6f), it



(a)



(b)

Figure 5.10:  $\mu$ Raman residual stress profiles for Poly1 and Poly2 10  $\mu m$ -wide oxidized beams with repeated 1100  $^{\circ}C$  anneals (a) Poly1, (b) Poly2.

is clear that the critical buckling beam lengths are nearly identical for Poly1 ( $900\ \mu\text{m}$ ) and Poly2 ( $720\ \mu\text{m}$ ) beams. From these results, I conclude that Raman measurements and anneals are a viable technique for achieving desired residual stress values. The  $\mu$ Raman spectroscopy stress profiles on unreleased MEMS structures present a clear representation of the residual stress levels in the structures when compared to released buckling beam arrays (i.e. if the Raman stress profile indicates an increase or decrease in the residual stress level, the buckling beam arrays likewise illustrate similar results).

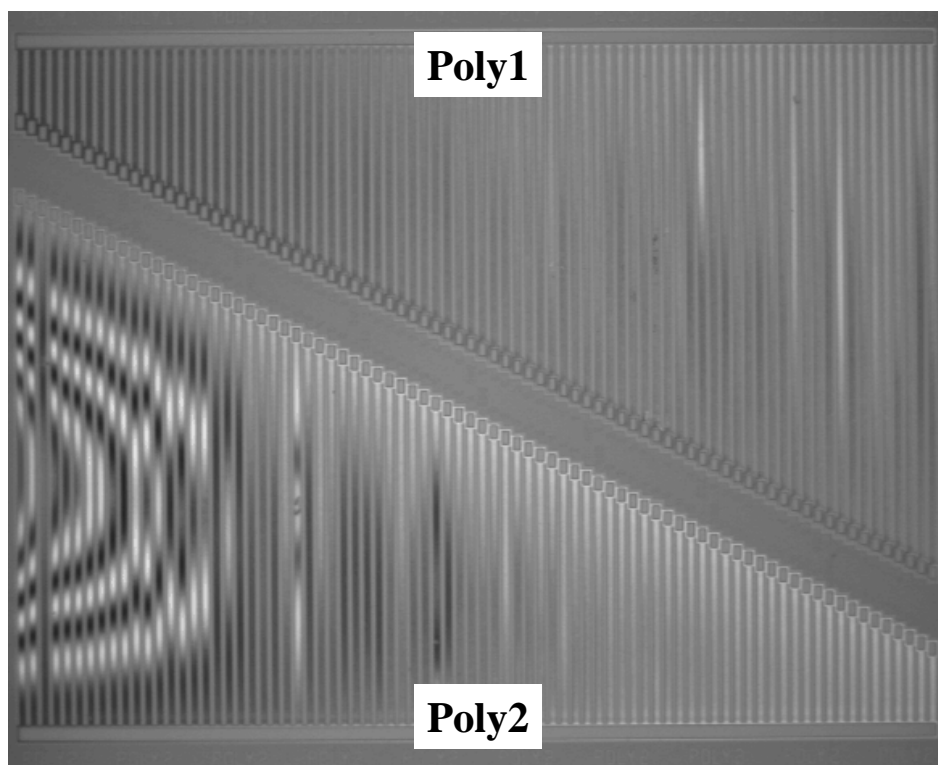


Figure 5.11: IFM image of buckling beam array for a repeated anneal.

### 5.8 Optical Characterization

Previous MEMS researchers determined that optically flat micromirrors are extremely difficult to attain with the MUMPs<sup>®</sup> foundry process [2]. The high residual stress levels inherent in the MUMPs<sup>®</sup> fabrication process are believed to cause

the mirror curvature. The residual stress deforms the optical surface making the micromirror essentially unusable. From my residual stress analysis of beams and cantilevers, it is clear that residual stress relaxation occurs with post-processing anneals at  $1100\text{ }^{\circ}\text{C}$ . To determine if this stress reduction aids in flattening optical mirror surfaces, I performed several optical surface flatness measurements on the micromirrors following the post-processing oxidation and  $1100\text{ }^{\circ}\text{C}$  anneals. I selected a Poly1 micromirror designed with Poly2 flexures as the optical flatness test mirror. The degree of deformation in a single layer micromirror is enhanced due to the thin Poly1 layer ( $2\text{ }\mu\text{m}$ ). An IFM image of an oxidized Poly1 micromirror prior to a  $1100\text{ }^{\circ}\text{C}$  anneal is shown in Figure 5.12.

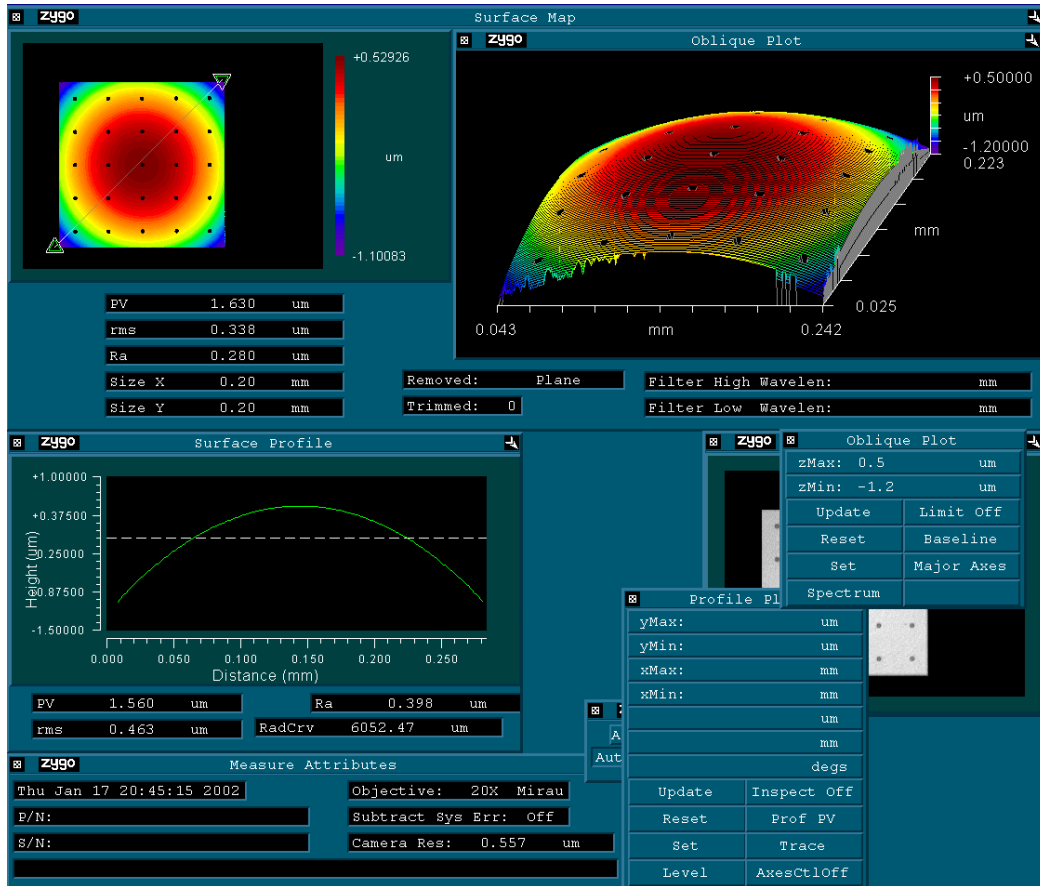


Figure 5.12: IFM optical flatness profiles for a  $200\text{ }\mu\text{m}$ -square oxidized Poly1 micromirror prior to post-processing anneals at  $1100^{\circ}\text{C}$ .

A series of IFM images for the oxidized micromirrors following the post-processing 1100 °C anneals are illustrated in Figure 5.13. The micromirror surface is bowed downward (concave) for all post-processing 1100 °C anneals but bowed upward (convex) following the oxidation process without an anneal. This is due to the oxide growth that was performed since the thermal oxidation process induces stress. Without the 1100 °C anneal, stress relaxation cannot occur. This results in very high stress gradients through the thickness of the Poly1 layer with the highest compressive stress level at the top surface of the mirror. With the highest compressive stress at the top surface, the mirror will bow upward as illustrated.

To further demonstrate the optical flatness of the post-processed MEMS micromirrors following the 1100 °C anneals, I show in Figure 5.14 two sets of micromirrors. The first set of micromirrors displayed in Figure 5.14a) were oxidized but no anneal was performed. The micromirrors are significantly curved as observed by the number of fringe lines displayed on the micromirror surface. The maximum peak deformation for this series of micromirrors is approximately 0.25  $\mu m$  at the mirror center. The second set of micromirrors shown in Figure 5.14b) treated with a 15-min 1100 °C anneal following the oxidation. As one can observe, there is minimal curvature to these micromirrors as verified by the lack of fringe lines on the mirror surface. The measured curvature for this micromirror is shown in Figure 5.15. The maximum deformation is approximately 10 nm at the center. This is a significant improvement from the previous flatness measurements observed for this fabrication process.

## 5.9 Summary of Chapter V

In this chapter, I demonstrated that residual stress relaxation is possible through the use of post-processing 1100 °C anneals and that this process can be monitored using  $\mu$ Raman spectroscopy. With the *TSUPREM<sup>TM</sup>* fabrication modelling software, I verified that an increased dopant uniformity in the polysilicon structural layers can

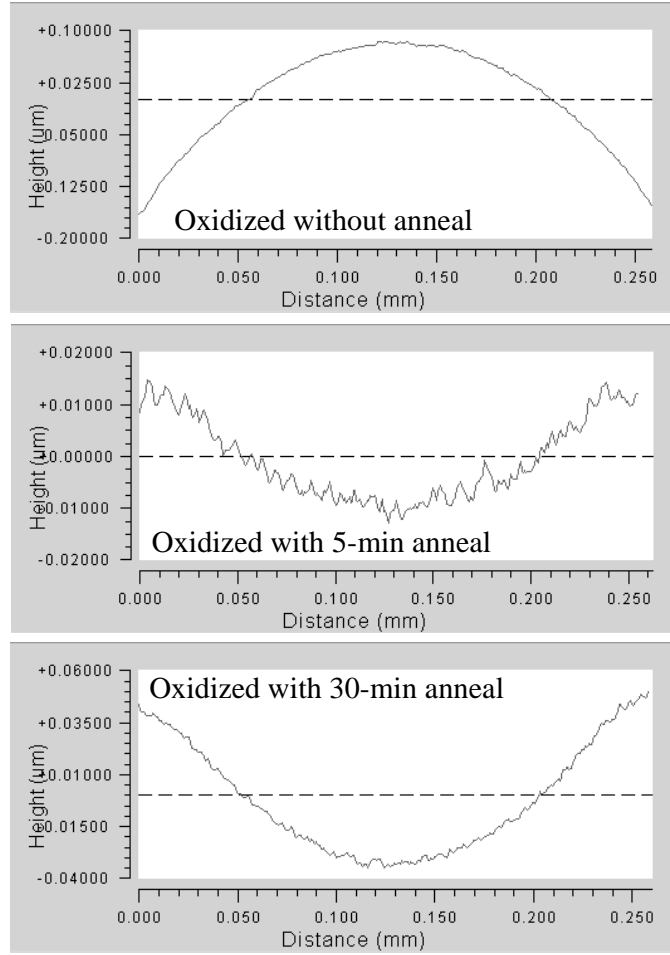


Figure 5.13: IFM optical flatness deflection profiles for three  $200\ \mu m$  by  $200\ \mu m$  oxidized micromirrors following post-processing  $1100\ ^\circ C$  anneals. Top-image - oxidized mirror without  $1100\ ^\circ C$  anneal, Middle-Image - 5-min anneal, and Bottom-Image - 30-min anneal.

be achieved with a thermal capping oxidation followed by  $1100\ ^\circ C$  anneals. The increased uniformity reduces stress gradients, thereby reducing the overall residual stress in the thin polysilicon layers. I measured the magnitude of stress reduction prior to the HF release through the use of  $\mu$ Raman spectroscopy. Following the HF release, the stress reduction was reassessed and verified through the use of critical buckling beam arrays, cantilevers, and micromirrors. By comparing the residual stress patterns obtained from  $\mu$ Raman stress profiles and released test structures, the stress profiles obtained from  $\mu$ Raman spectroscopy correlate very well with the

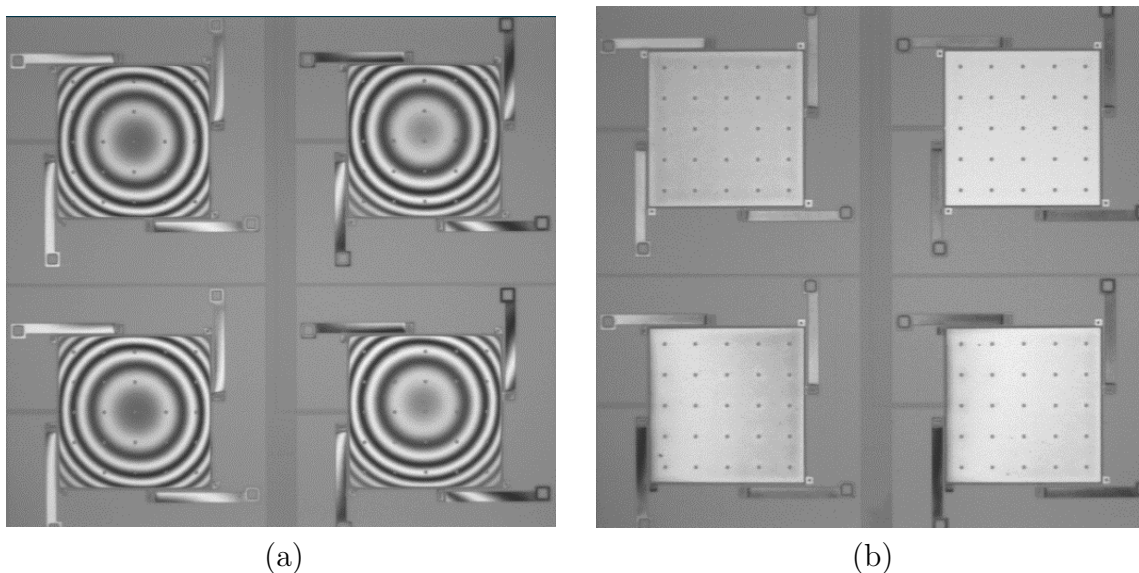


Figure 5.14: IFM micromirror images illustrating surface curvature for a  $200\ \mu\text{m} \times 200\ \mu\text{m}$  oxidized micromirror. (a) oxidized with no anneal, and (b) oxidized with a 15-min  $1100^\circ\text{C}$  anneal.

residual stress levels calculated from the released structures. Although the stress magnitudes between the two residual stress measurements differ by approximately an order of magnitude, an increase or decrease in the magnitude of the  $\mu\text{Raman}$  stress level correlates identically to the increase or decrease in the residual stress levels as analytically calculated from the released buckling beam arrays and cantilever deflections. Part of the residual stress magnitude difference is a result of the  $\mu\text{Raman}$  stress profiles are for unreleased fixed-fixed beams. The unreleased beams are not in a fully relaxed state, thus the beams should exhibit a slightly higher residual stress value. Finally, I found that the post-processing oxidation and anneals significantly reduce the deformation of MEMS micromirrors. The improved flatness enhances the optical capabilities of the micromirrors and most significantly demonstrates how  $\mu\text{Raman}$  spectroscopy and post foundry annealing can be used in real applications. Although the results from unoxidized test structures indicate stress relaxation, I would not recommend post-processing  $1100\ ^\circ\text{C}$  anneals on unoxidized

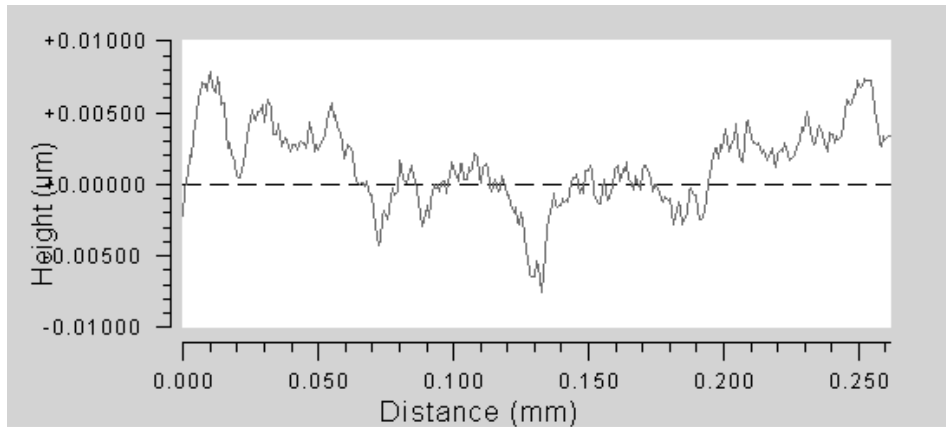


Figure 5.15: IFM optical flatness profile for a  $200\text{ }\mu\text{m} \times 200\text{ }\mu\text{m}$  oxidized micromirror following a 15-min post-processing  $1100\text{ }^{\circ}\text{C}$  anneal.

MEMS structures since it eventually results in damaged or warped MEMS devices unsuitable for testing.

## Bibliography

1. J. T. Butler. *Development and Packaging of Microsystems using Foundry Services*. PhD thesis, Air Force Institute of Technology (AETC), Wright-Patterson AFB OH, 1998. AFIT/DS/ENG/98-08.
2. W. D. Cowan. *Foundry Microfabrication of Deformable Mirrors for Adaptive Optics*. PhD thesis, Air Force Institute of Technology (AETC), Wright-Patterson AFB OH, 1998. AFIT/DS/ENG/98-07.
3. D. A. Koester, 2001. Personal Phone Communications, Cronos Integrated Microsystems Technical Processing Engineer.
4. D. Maier-Schneider, A. Köprülü, S. Ballhausen Holm, and E. Obermeier. Elastic properties and microstructure of LPCVD polysilicon films. *Journal of Micromechanical Microengineering*, 6:436–446, 1996.
5. D. Maier-Schneider, J. Maibach, E. Obermeier, and D.A. Schneider. Variations in Young’s modulus and intrinsic stress of LPCVD-polysilicon due to high-temperature annealing. *Journal of Micromechanical Microengineering*, 5:121–124, 1995.
6. J. Singh, S. Chandra, and A. Chand. Strain studies in LPCVD polysilicon for surface micromachined devices. *Sensors and Actuators A*, 77:133–138, 1999.
7. B. Stark. Mems reliability assurance guidelines for space applications. *JPL Publication 99-1*, pages 1–315, January 1999. Jet Propulsion Laboratory, Pasadena, CA.
8. S. M. Sze. *Semiconductor Devices - Physics and Technology*. John Wiley & Sons, New York, NY, 1985.
9. I. De Wolf and H. E. Maes. Mechanical stress measurements using micro-Raman spectroscopy. *Microsystem Technologies*, 5:13–17, 1998.
10. X. Zhang, Tong-Yi Zhang, M. Wong, and Y. Zohar. Residual-stress relaxation in polysilicon thin films by high-temperature rapid thermal annealing. *Sensors and Actuators A*, 64:109–115, 1998.

## VI. *Post-Fabrication Doping of MEMS Structures*

### 6.1 *Introduction*

In Chapter V, I demonstrated residual stress relaxation can be achieved with the use of post foundry processing anneals. From the *TSUPREM<sup>TM</sup>* images of the MUMPs<sup>®</sup> fabrication process, the images illustrate the nonuniformity of the phosphorous dopant within the polysilicon structural layers. A uniform dopant concentration was shown to assist in residual stress reduction. Some important material parameters of polysilicon films for sensor-actuator devices are the residual stress, stress gradients, Young's modulus, and resistivity. For most free-standing microstructures, it is important to reduce the stress in the thin film. In order to exploit the advantage of polysilicon for MEMS applications, it is essential to develop a process that results in low-stress polysilicon films. For the MUMPs<sup>®</sup> foundry process, the residual stress in the thin film polysilicon structural layers is compressive.

There are several post-fabrication processes which can influence the residual stress of MEMS devices. I show that post-fabrication phosphorous diffusion and phosphorous low dose ion implantation with a short 1100 °C anneal can significantly reduce the inherent residual stress in MUMPs<sup>®</sup> polysilicon structural layers. I prove that stress reduction does exist through the use of on-chip test structures. I am the first to use  $\mu$ Raman spectroscopy to measure, monitor and control the residual stress levels in MEMS structures. I demonstrate the feasibility of both doping techniques and that implants provide the largest levels of stress reduction. Both post-fabrication doping techniques I use are outlined in the following sections. I also briefly address the optical improvements obtained from micromirrors following phosphorous implants and accompanying anneals.

## 6.2 Doping Methods

There are two general methods of doping: impurity diffusion and ion implantation. Impurity diffusion occurs when the material to be doped is placed in a high temperature gaseous atmosphere containing the desired impurity atom. Impurity diffusion is the process by which impurity particles move from a region of high concentration near the surface, to a region of lower concentration in the structure. When the temperature decreases, the impurity atoms become permanently frozen into substitutional lattice sites.

Ion implantation generally takes place at a lower temperature than diffusion. A beam of impurity ions is accelerated to kinetic energies of 50 keV or greater and then directed toward the surface of the material to be implanted. The high-energy impurity ions enter the crystal and come to rest at some average depth from the surface. One advantage of ion implantation is that controlled numbers of impurity atoms can be introduced into specific regions of the crystal. A disadvantage of this technique is that the incident impurity atoms collide with the crystal atoms, causing lattice-displacement damage. However, most of the lattice damage can be removed by thermal annealing, in which the temperature of the crystal is raised for a short time. Thermal annealing is a required step following implantation.

Typically, deposited polysilicon films are doped by diffusion with  $POCl_3$  or phosphosilicate glass (PSG). In  $POCl_3$  diffusion doping, phosphorus-containing oxide films form at doping temperatures of 850 – 1000 °C. In PSG diffusion doping, the PSG films form at 350 °C [11]. Different phosphorus concentrations in the oxide films are present due to varying temperatures. PSG diffusion doping results in a lower doping concentration than that of  $POCl_3$  doping under the same conditions. MUMPs® employs the PSG diffusion doping method while  $SUMMiT^{TM}$  doping is performed while the polysilicon is being deposited. The  $SUMMiT^{TM}$  technique produces polysilicon layers with a very uniform doping concentration.

With a non-uniform doping profile, residual stress gradients are present. With additional doping, a higher dopant concentration can be obtained. Several different dopant doses at various implant energies were performed in an attempt to identify the dopant concentration effect on the residual stress.

*6.2.1 TSUPREM<sup>TM</sup> Phosphorus Diffusion Model.* Prior to the post-processing diffusion, I performed *TSUPREM<sup>TM</sup>* simulations to gain insight into the post-processing diffusion and anneal experiments. Several additional steps are added to the *TSUPREM<sup>TM</sup>* model outlined in Table 2.1 and are provided in Table 6.1. The post-processing steps are performed following the completion of the processes outlined in Table 2.1. The Poly1 beam is modelled with the oxide2 layer remaining as shown in Figure 2.3a).

Table 6.1: MUMPs<sup>®</sup> Post-Processing Phosphorus Diffusion as Modelled in *TSUPREM<sup>TM</sup>*.

Process Step	Time (min)	Temp (°C)
1. Phosphorus Diffusion	45-135	950
2. Drive in Anneal	120	950
3. High Temperature Anneal	60	1100

The experimental diffusion performed and outlined in the next section is modelled in *TSUPREM<sup>TM</sup>*. A step-by-step illustration of the diffusion process on a Poly1 20  $\mu m$ -wide beam is illustrated in Figure 6.1. The top beam (Figure 6.1a) represents the MUMPs<sup>®</sup> foundry processes final dopant representation. The second beam (Figure 6.1b) illustrates the effect of a 90 min, 950 °C phosphorous diffusion and the third beam (Figure 6.1c) shows the revised doping profile after a 950 °C two-hour activation anneal and a 1100 °C high temperature anneal for one hour. The non-uniformity of the phosphorous dopant is significantly reduced by this post-foundry diffusion process.

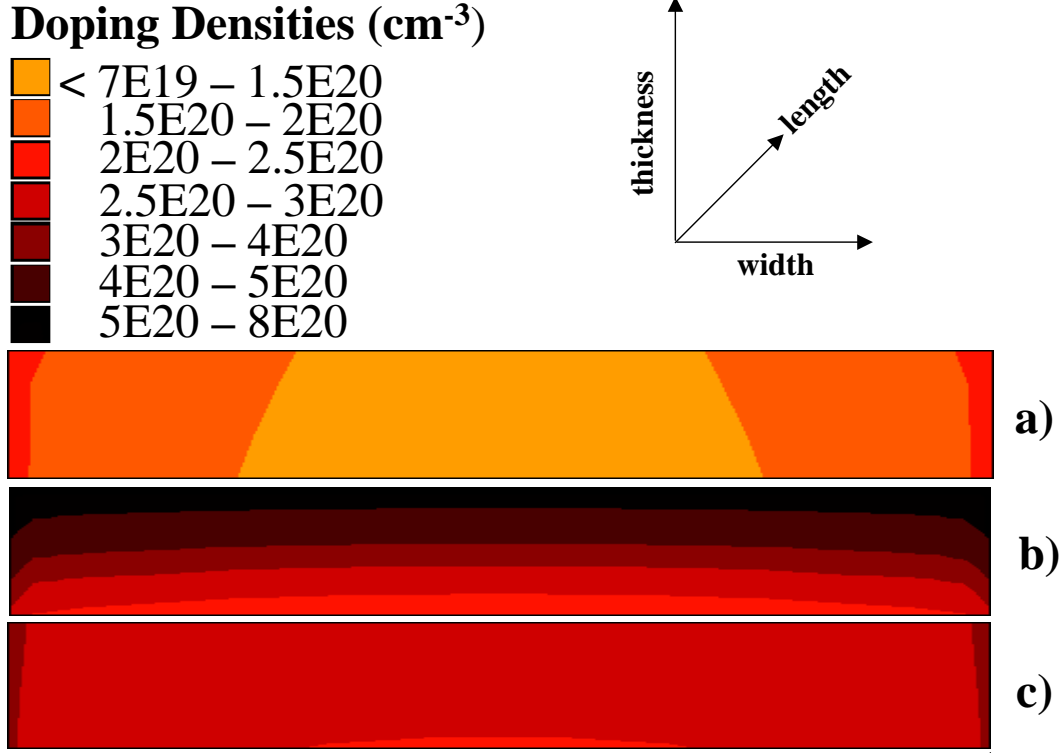


Figure 6.1: *TSUPREM<sup>TM</sup>* diffusion profiles of a Poly1, 20  $\mu m$ -wide beam cross-section following a 90-min phosphorous diffusion. Dopant concentration illustrations of (a) MUMPs<sup>®</sup> as grown, (b) two-hour 950  $^{\circ}C$  activation anneal, (c) one hour, 1100  $^{\circ}C$  post-oxidation anneal

Figure 6.2 illustrates the *TSUPREM<sup>TM</sup>* representation of the phosphorous diffusion for a 20  $\mu m$ -wide Poly2 beam. As before, the phosphorous dopant uniformity is significantly improved by the diffusion and annealing process. Previously, it was noted by Butler [4] that the MUMPs<sup>®</sup> Poly2 structural layer does not exhibit lateral diffusion; however, in the post-process diffusion experiment, lateral diffusion will exist since the sides and top of the beams are exposed to the phosphorous dopant. This is observed in the second beam cross-section Figure 6.2b).

*TSUPREM<sup>TM</sup>* modeling of various beam widths (2  $\mu m$  to 20  $\mu m$ ), shows that lateral diffusion will have a significant impact on the uniformity and dopant concentration in narrow Poly1 beams during device fabrication and in Poly2 beams during the post-processing diffusion. This corresponds well with previous research, where

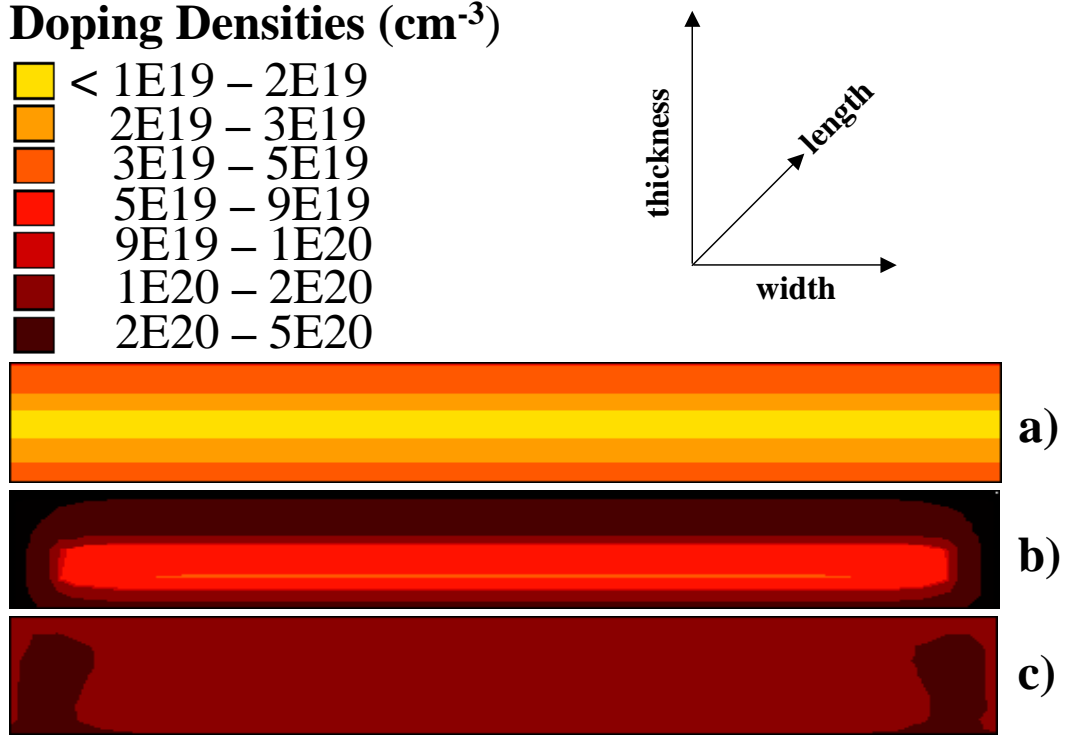


Figure 6.2:  $TSUPREM^{TM}$  diffusion profiles of a Poly2,  $20\ \mu\text{m}$ -wide beam cross-section following a 90-min phosphorous diffusion. Dopant concentration illustrations of (a) MUMPs<sup>®</sup> as grown, (b) two-hour  $950\ ^\circ\text{C}$  activation anneal, (c) one hour,  $1100\ ^\circ\text{C}$  post-oxidation anneal

the resistivity is lowest in narrow beams due to lateral diffusion [4]. Using  $\mu\text{Raman}$  spectroscopy, I experimentally verified these  $TSUPREM^{TM}$  results through the use of a series of Poly1 and Poly2 microbridge test arrays of varying widths ( $2\ \mu\text{m}$  to  $20\ \mu\text{m}$ ). These test arrays provide quantitative stress data to confirm the dopant irregularities observed in the  $TSUPREM^{TM}$  models.

### 6.3 Phosphorous Diffusion Set-up and Experimentation

I performed post-fabrication phosphorus diffusion doping on three die fabricated on MUMPs<sup>®</sup> run #21. The series of Poly1 and Poly2 structures are  $100\ \mu\text{m}$ -long microbridges with widths ranging from  $8$  to  $20\ \mu\text{m}$ . All test structures are anchored at each end to a silicon nitride layer deposited on the silicon substrate.

The Poly1 beams are suspended  $2\ \mu\text{m}$  above the substrate and the Poly2 beams are  $2.75\ \mu\text{m}$  above the substrate. Figure 6.3 is an SEM image of the polysilicon beams used in my diffusion experiments.

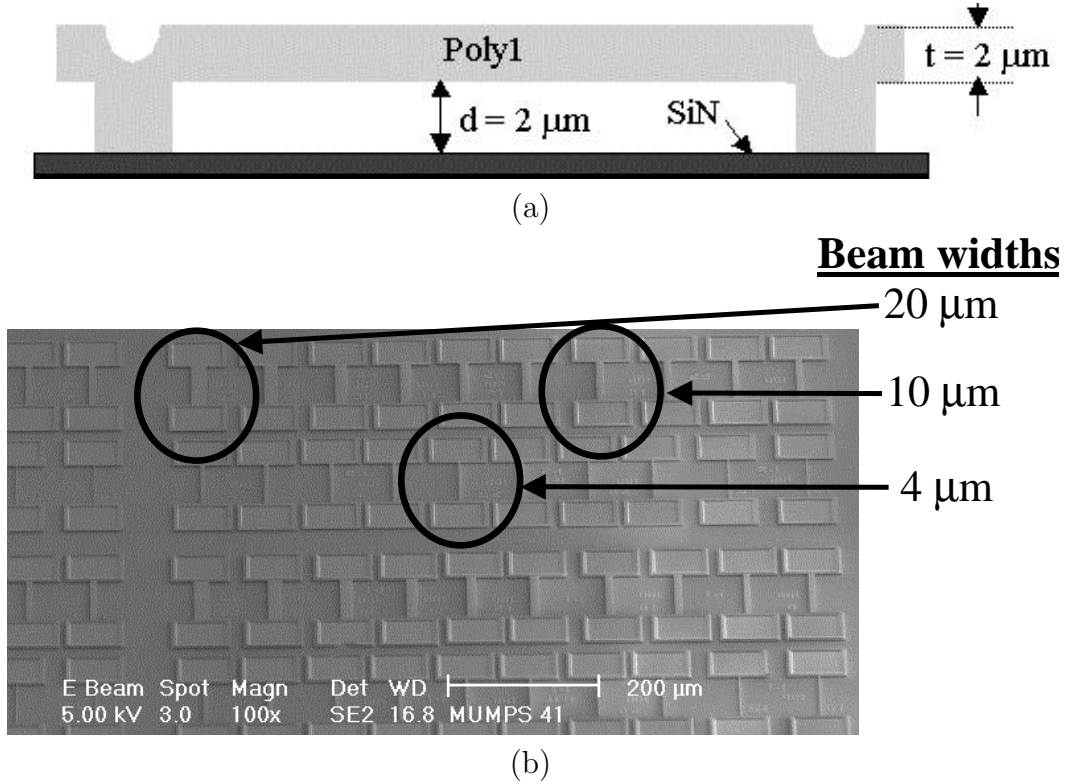


Figure 6.3: Images of polysilicon microbridges: (a) side-view of a Poly1 microbridge, (b) SEM image of microbridges with various widths.

I used PH-950 phosphorus wafers manufactured by Carborundum Products [5] as the dopant source. This dopant has a diffusion temperature range of 875 to 950  $^{\circ}\text{C}$ . From the PH-950 data sheet, the phosphorus wafers requires an 8 hour, 900  $^{\circ}\text{C}$  pre-bake to remove moisture which may be absorbed during storage. Prior to the phosphorus diffusion, the phosphorus wafers, quartz boat, silicon wafer, and the quartz plate were placed in the diffusion oven and baked for 48 hours at 900  $^{\circ}\text{C}$ . This bake was used to remove moisture and contaminants from the diffusion tube, phosphorus wafers, and quartz boat.

The MUMPs® fabrication process uses a PSG diffusion doping method. This doping technique is known to cause stress gradients in the polysilicon layers and it dopes the beams to a concentration level of approximately  $1\text{-}3 \times 10^{19} \text{ cm}^{-3}$  [10]. To increase the dopant concentration in the polysilicon beams, phosphorus diffusions were carried out prior to release at a temperature of  $900^\circ\text{C}$  for diffusion times of 45 (die #1) , 90 (die #2), and 135 minutes (die #3). A nitrogen flow rate of one liter per minute was used throughout the diffusion process. As a result of the varied diffusion times, a different dopant concentration level exists in all three samples. This provides insight into the relationship between dopant concentration and localized residual stress in the MEMS structures.

Figure 6.4 illustrates the set-up and orientation of the silicon pyrophosphate ( $\text{SiP}_2\text{O}_7$ ) wafers relative to the MUMPs® die during the diffusion process. At diffusion temperatures, the active component,  $\text{SiP}_2\text{O}_7$ , decomposes to form the desired dopant  $\text{P}_2\text{O}_5$ . Since the MUMPs® die are small (0.5 cm by 0.5 cm), a quartz plate was used to prop up the die in a vertical position during the diffusion process. The silicon wafer is used only to support the quartz plate during the diffusion to prevent the quartz plate and die from falling into the diffusion oven. The die were placed on the plate so the device side faced the phosphorus-oxide wafer to maximize the surface magnitude of the diffusing dopant.

Following the diffusion, the phosphorous-oxide wafers were removed and the MUMPs® die were annealed at  $900^\circ\text{C}$  for 2 hours in the diffusion furnace with a nitrogen flow rate of one liter per minute to activate and drive in the dopant. This anneal enhances dopant uniformity and helps eliminate potential stress gradients due to dopant irregularities. This low temperature activation anneal should not influence the grain size of the polysilicon film [13,16].

A one-hour high temperature furnace anneal was performed at  $1100^\circ\text{C}$  on the MUMPs® die following post-diffusion  $\mu\text{Raman}$  scans. At this temperature, further dopant diffusion occurs creating greater uniformity and the polysilicon grain size

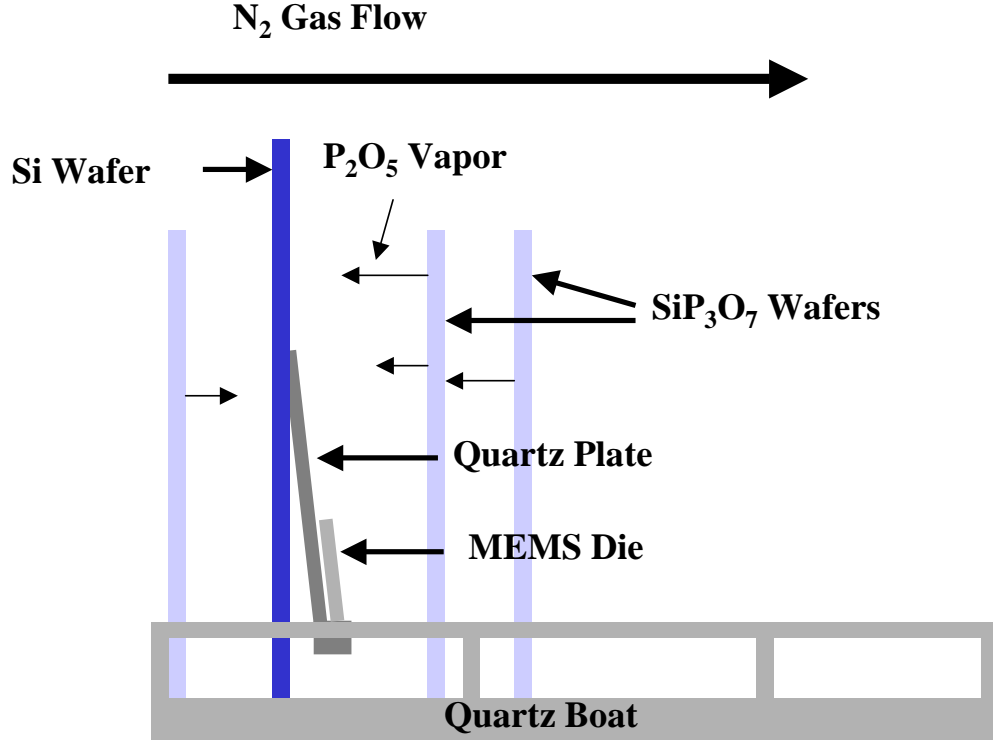


Figure 6.4: Illustration of the phosphorus diffusion process.

increases at this annealing temperature [13]. This increased grain size will aid in reducing residual stress [13,16].

I completed pre and post resistivity measurements on all Poly1 and Poly2, 10 and 20  $\mu m$ -wide beams before and after the diffusion. An HP4155A semiconductor parameter analyzer is used to supply the required voltages and also to measure the current through the beams. The following equation is utilized to calculate the resistance of the Poly1 and Poly2 beams

$$R = \frac{V}{I} \quad (\Omega) \quad (6.1)$$

where  $R$  is the resistance of the beam,  $V$  is the applied voltage, and  $I$  is the measured current. Since no gold is deposited on the beam anchors prior to the diffusion

experiments, the electrical probes were placed directly onto the ends of the microbridges.

From the measured current in the experimental circuit, the resistivity can be determined from

$$\rho = \frac{VA_B}{L_B I} \quad (\Omega \cdot cm) \quad (6.2)$$

where  $V$ ,  $I$ , and  $L_B$  are the applied voltage, measured current, and beam length respectively. The term  $A_B$  is the cross sectional area of the beam with  $A_B = wh$ , where  $w$  is the beam width and  $h$  is the beam thickness ( $2.0 \mu m$  for Poly1 and  $1.5 \mu m$  for Poly2). The test set-up is identical to a four-point probe test, eliminating contact resistance from the measured value.

Once the resistivity is determined, the average dopant concentration of each beam can be calculated from

$$N_D = \frac{1}{(\rho q \mu_n)} \quad (cm^{-3}) \quad (6.3)$$

where  $q$  is the electronic charge ( $q = 1.60218 \times 10^{-19} C$ ),  $\mu_n$  is the mobility constant for doped silicon ( $40 cm^2/Vsec$ ) [2,3], and  $\rho$  is the resistivity value calculated from Equation 6.2.

The pre-diffusion resistivity measurements are used to determine the background dopant concentration prior to the diffusion. This resistivity value is used later to determine the increase in the dopant concentration following the diffusion. Prior to the resistivity measurements for Poly1 microbridges, a short (15 sec) HF vapor exposure was performed to remove the Oxide2 layer from the surface of the Poly1 structures (**NOTE:** these MUMPs® die were fabricated prior to addition of the stringer removal etch at the foundry).

## 6.4 Diffusion Results and Analysis

Following the diffusion, resistivity measurements were repeated for all selected Poly1 and Poly2 beams. By comparing the measured resistivity following the diffusion to the background concentration, the increase in the dopant concentration is determined. Table 6.2 contains the resistivity values before and after the phosphorus diffusion.

Table 6.2: Resistivity values for 20  $\mu m$  wide Poly1 and Poly2 microbridges before the diffusion and again following both anneals (2-hours at 900  $^{\circ}C$  and 1-hour at 1100  $^{\circ}C$ )

Die	Beam	Resistivity(Pre) ( $\Omega \cdot cm$ )	Resistivity(Post) ( $\Omega \cdot cm$ )	Dopant Concentration ( $cm^{-3}$ )
#1	Poly1	0.013	0.007	9.581E19
#1	Poly2	0.022	0.005	2.761E19
#2	Poly1	0.012	0.005	1.268E20
#2	Poly2	0.022	0.004	1.717E20
#3	Poly1	0.013	0.005	1.286E20
#3	Poly2	0.021	0.003	1.786E20

As observed in Table 6.2, as the dopant concentration increases in the beams, the beam resistivity decreases. For Poly1 beams, the beam resistance varied from approximately 415  $\Omega$  before the diffusion to 115  $\Omega$  following the diffusion. The resistance of the Poly2 beams varied from approximately 820  $\Omega$  before to 109  $\Omega$  following the diffusion. From the calculated resistivity, the dopant concentration densities (shown in Table 6.2) were found to be approximately the same order of magnitude as in the TSUPREM models for both Poly1 and Poly2 structural layers (shown in Figure 6.1 and 6.2).

I performed a series of  $\mu$ Raman scans on Poly1 and Poly2 100  $\mu m$ -long microbridge beams with widths ranging from 8  $\mu m$  to 20  $\mu m$  prior to the diffusion, after the phosphorus diffusion, after the 1100  $^{\circ}C$  anneal, and again after the HF release. The pre-diffusion scans provide an initial residual stress level for each beam so a

reduction in stress can be determined. Figure 6.5 illustrates the raw Raman stress data with a 4<sup>th</sup>-order polynomial curve fit of the data overlaying the raw stress profiles. Since the 4<sup>th</sup>-order polynomial curve fit presents a dip in the middle of the beam length (artifact of a 4<sup>th</sup>-order polynomial, the stress level is linear across an unreleased beam), I present the raw  $\mu$ Raman data for the remainder of the diffusion experiments. I overlay a linear line to illustrate the approximate average of the stress data along the beam length for ease of comparison. The Raman stress profiles illustrated in this section are generated from a single  $\mu$ Raman scan of the microbridge structure. Figure 6.6 is a measurement of the residual stress in 10  $\mu m$ -wide Poly1 microbridges and Figure 6.7 represents the residual stress in 20  $\mu m$ -wide Poly2 microbridges. The residual stress variation for these test structures are accurate to within the resolution of the  $\mu$ Raman spectroscopy system. Thus the error for these  $\mu$ Raman stress profiles is approximately  $\pm 20$  MPa.

In Figure 6.6, the solid lines represent the background Raman scan of the residual stress level in the beams prior to post-fabrication processes. The dash lines indicate the post-diffusion residual stress level. The dotted lines relate to the post-high temperature anneal stress levels and the dash-dot lines correspond to the residual stress remaining in the beams following the HF release. For all the Raman stress profiles illustrated, the residual stress is a negative value (i.e. a negative stress value corresponds to compressive stress and a positive value corresponds to tensile stress). Therefore, as the stress level becomes less negative (i.e. closer to 0 Pa), the resulting compressive stress is reduced.

The residual stress profiles provided in Figure 6.6 illustrate the residual stress reduction for each post-processing step. By comparing the Raman scans obtained from the Poly1 beams shown in Figure 6.6, one notices the significant reduction in stress from the background residual stress levels to the post high temperature anneal stress levels for all three MEM test chips. From Figure 6.6, the post-processing step which appears to have the greatest impact on residual stress reduction is the

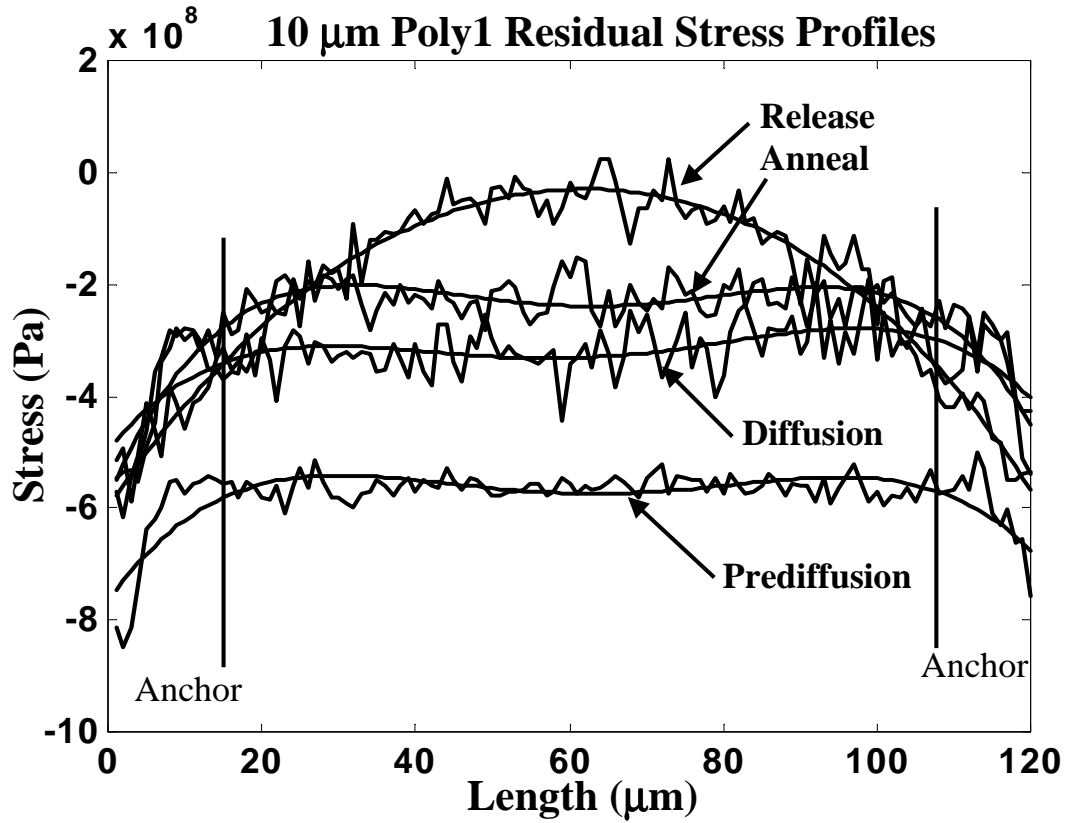
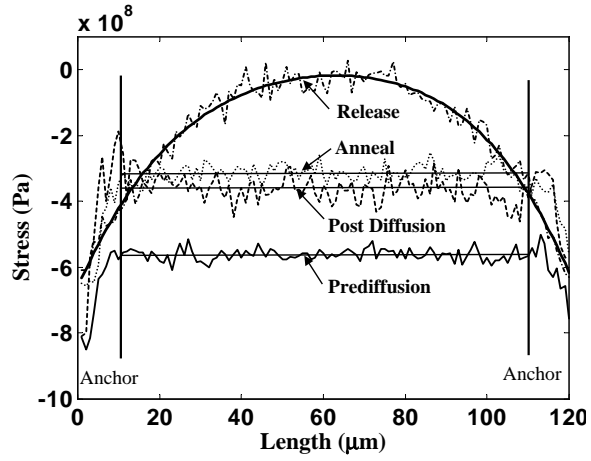


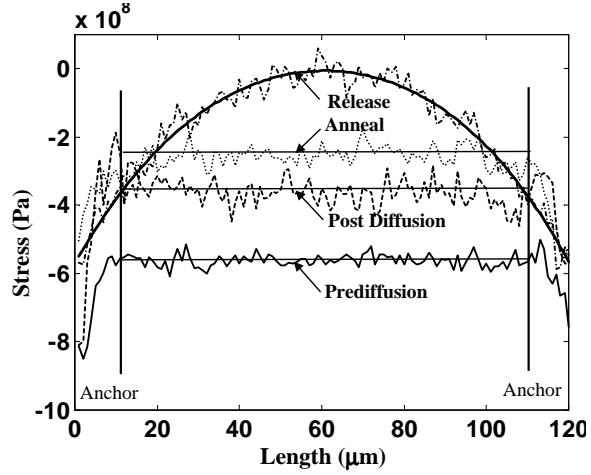
Figure 6.5: Raw Raman stress data and accompanying fourth order polynomial curve fits of the raw stress data.

increased doping concentration. Although the diffusion step accounts for nearly 20 to 30% of the actual stress reduction, one must take into account the temperature at which the diffusion took place. A significant amount of the reduced stress may be due to the elevated temperature during the diffusion process and associated activation anneal. During this time, the increased temperature permits greater dopant uniformity which results in stress gradient reduction.

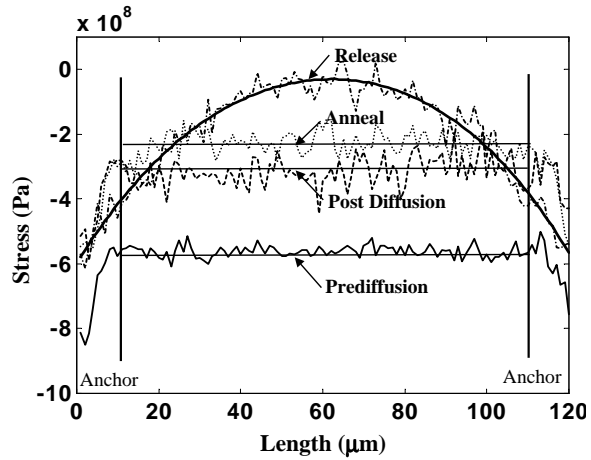
The post-processing experimental tests were designed to determine the level of residual stress reduction following the HF release. Figure 6.6 provides the final Poly1 residual stress profiles for the released 10  $\mu m$ -wide microbridges. The released stress level measured at the 60  $\mu m$  location in Figure 6.6) ranges from approximately



(a)



(b)



(c)

Figure 6.6: Residual stress profiles for 100  $\mu\text{m}$ -long by 10  $\mu\text{m}$ -wide Poly1 microbridges fabricated in the MUMPs<sup>®</sup> process. Phosphorous diffusion times are: (a) 45 min diffusion, (b) 90 min diffusion, and (c) 135 min diffusion.

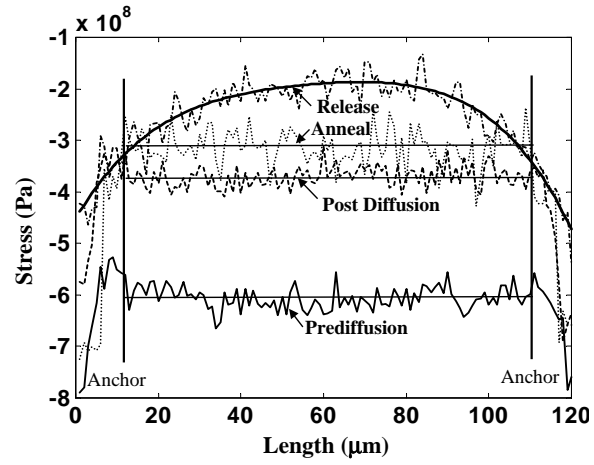
-5 to -40 MPa for all Poly1 10  $\mu m$ -wide microbridges. The minimum stress is in the device subjected to a 135-min diffusion.

I performed  $\mu$ Raman scans on the 20  $\mu m$ -wide Poly2 beams from each test die as shown in Figure 6.7. From these stress profiles, it is clear that the diffusion doping appears to have reduced the stress as the diffusion time is increased. The residual stress value following the high temperature anneal located in the middle of the beam (60  $\mu m$  from each edge) for Figure 6.7a) was approximately 300 MPa and the residual stress value for Figure 6.7c) is about 240 MPa. The final released Raman stress profiles also demonstrate a variation in the residual stress. The magnitude of the residual stress curve for the released Figure 6.7a) is approximately 220 MPa. Figure 6.7c) reduces down to about 75 MPa. These improved results are probably due to the longer diffusion which creates a higher and more uniform dopant concentration.

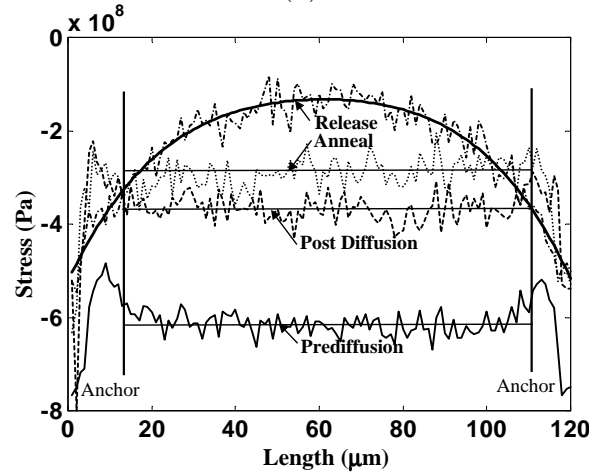
Since the MUMPs<sup>®</sup> fabrication process is known to exhibit material variations from one wafer to the next, the only way to generate a true comparison between the residual stress profiles for Poly1 and Poly2 test structures is to compare stress profiles from the same test die. Figure 6.8 is a combination of all Poly1 stress profiles from a single MEMS test die (die #1). The 8  $\mu m$ -wide beams have the lowest residual stress values. The residual stress increases as the beams become wider which supports my conclusions concerning dopant uniformity and concentration. This doping dependent stress variation held true for all Poly1 beam residual stress levels.

Figure 6.9 is a combination of all Poly2 stress profiles from the same MEMS test die (die #1) with similar results as for the Poly1 beams but at a lower stress level for each width. The two structural layers cannot be directly compared since each layer has different phonon deformation potentials (hydrostatic pressure constant). However, I noted that the residual stress changes similarly for both structural layers as illustrated in Figure 6.8 and Figure 6.9.

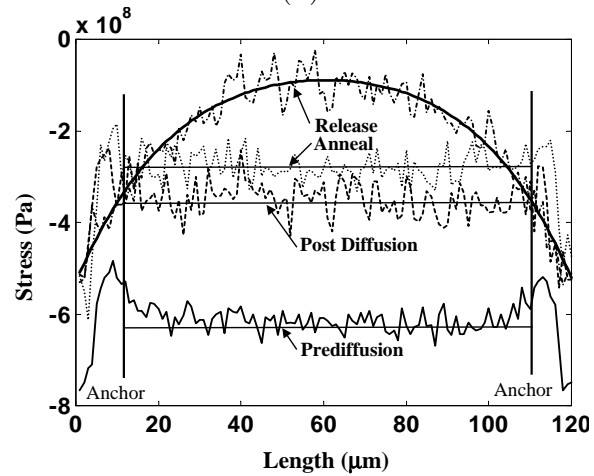
From my previous finite element method (FEM) modelling on actuated released structures (Chapter II), the magnitude of the residual stress profiles in the y- and z-



(a)



(b)



(c)

Figure 6.7: Residual stress profiles for 100  $\mu\text{m}$ -long by 20  $\mu\text{m}$ -wide Poly2 microbridges fabricated in the MUMPs<sup>®</sup> process. Phosphorous diffusion time frames are: (a) 45-min diffusion, (b) 90-min diffusion, and (c) 135-min diffusion.

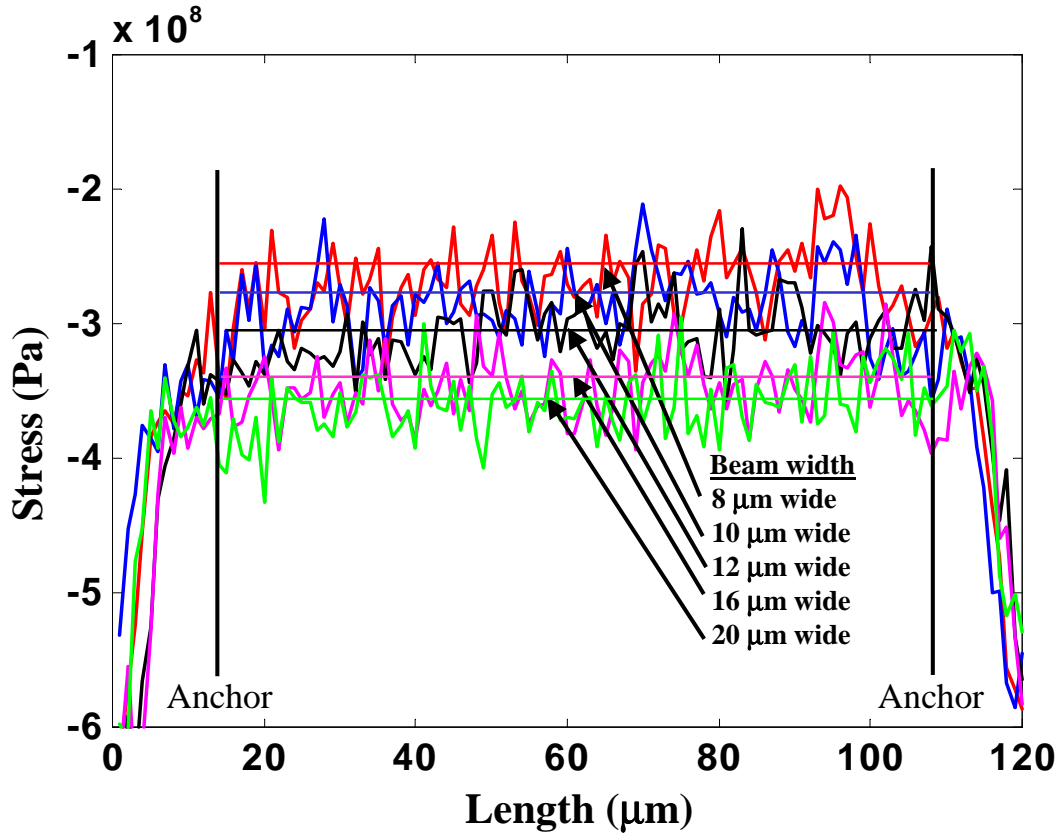


Figure 6.8: Residual stress profiles for all Poly1 100  $\mu m$ -long microbridges with varying widths following the 45-min diffusion and 1100  $^{\circ}C$  anneal.

directions are negligible when compared to the uniaxial FEM result along the length of the beams and flexures [7]. The residual stress values provide an approximation of the true stress values present in the MEMS structures since the  $\mu$ Raman spectroscopy system has a resolution of approximately 30-40 MPa.

The diffusion results herein are from a single phosphorous diffusion doping experiment. Other diffusion experiments were not possible since the diffusion furnace became unavailable. Following the diffusion experiments, I performed ion implantation experiments to study the effects of increased the dopant level in the polysilicon MEMS structures.

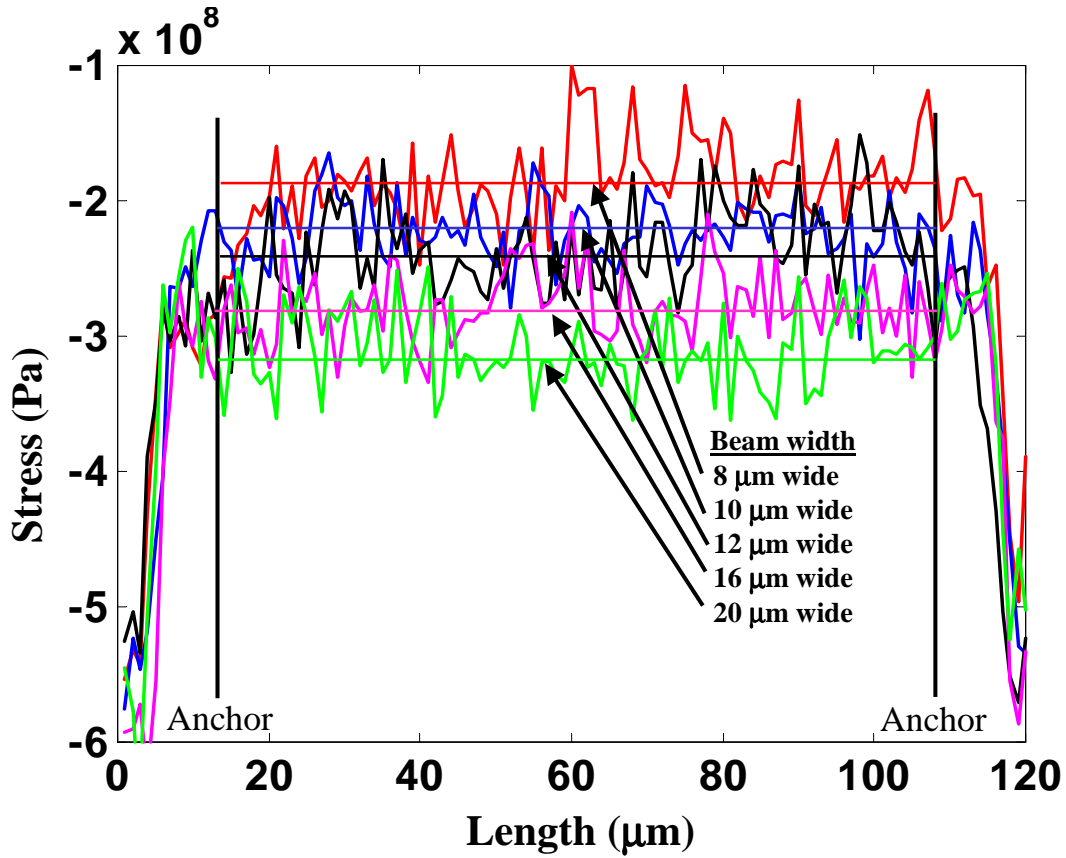


Figure 6.9: Residual stress profiles for a series of Poly2 100  $\mu\text{m}$ -long microbridges with varying widths following the 45-min diffusion and 1100  $^{\circ}\text{C}$  anneal.

### 6.5 Ion Implant Doping

Ion implantation is the second technique I used to increase the dopant concentration within the MEMS structures. This technique enables precise control of the dopant dose and peak concentration placement in the test structures. A series of implants were performed in an attempt to determine the optimum dopant concentration and peak concentration depth for maximum residual stress relaxation. I was able to vary several implant parameters to include implant energy and dopant concentration. These parameters allow for precise dopant placement vertically in the MEMS structural layers. The implant energy was set to 100 and 200 keV, and the dopant dose varied from  $5\text{E}15 \text{ cm}^{-2}$  to  $1\text{E}17 \text{ cm}^{-2}$ . This provides expected dif-

fused dopant concentration levels ranging from  $5\text{E}19\text{ cm}^{-3}$  to  $1\text{E}21\text{ cm}^{-3}$ . The post implant furnace anneal was at  $1100\text{ }^{\circ}\text{C}$  for 1-hour. The residual stress in polysilicon increasingly relaxes with a higher concentration of phosphorus. Doping and grain structure are important factors which affect the intrinsic stress in polycrystalline silicon [8].

## 6.6 Implant Modelling

To assess the characteristics from ion implants on the residual stress, I used two separate software packages to provide insight into the various implant doses and implant energy levels selected. I used *TSUPREM<sup>TM</sup>* to model the dopant concentration as a function of dopant dose, implant energy, and associated anneal times. I also used an implant modelling package available from Implant Sciences Corporation (ISC) [15] to determine the peak dopant concentration depth for the implants at different power levels. Each modelling program is briefly addressed in the next sections.

*6.6.1 TSUPREM<sup>TM</sup> Ion Implant Model.* The final post-processing technique, modelled in *TSUPREM<sup>TM</sup>* to illustrate dopant uniformity and concentrations, was a phosphorous implant. The phosphorous ion implants were followed by various anneals at  $900\text{ }^{\circ}\text{C}$  and  $1100\text{ }^{\circ}\text{C}$ . The  $900\text{ }^{\circ}\text{C}$  anneal/oxidation was used to activate the implant, grow the nominal  $50\text{ \AA}$ -thick oxide cap, and to repair the lattice structure damage due to the ion implant. The  $1100\text{ }^{\circ}\text{C}$  anneal was used primarily to further diffuse the phosphorous dopant to create greater uniformity. I added a few additional steps to the *TSUPREM<sup>TM</sup>* run file outlined in Table 2.1. The additional steps are provided in Table 6.3. These post-processing steps are performed following the completion of the processes outlined in Table 2.1.

Prior to the phosphorous implants, I used *TSUPREM<sup>TM</sup>* to simulate the various doses and energy levels available through ISC. Since the MUMPs<sup>®</sup> PSG

Table 6.3: MUMPs® Post-Processing Phosphorus Implant as Modelled in *TSUPREM<sup>TM</sup>*.

Process Step	Implant Power (keV)	Implant Dose ( $cm^2$ )	Time (min)	Temp ( $^{\circ}C$ )
1. Phosphorus Implant	100-200	5E15-1E17	-	-
2. Oxidation Growth/Anneal	-	-	30	900
3. High Temperature Anneal	-	-	5-60	1100

diffusion process provides dopant concentrations of approximately  $1\text{-}3E19\text{ cm}^{-3}$ , I had to provide at least an implant dose of  $5E15\text{ ions}/cm^2$  to approximately match the background concentration currently in the polysilicon [9]. I modelled several implant energy levels (100-400 keV). All my simulations predicted an increased and uniform dopant concentration following the  $1100\text{ }^{\circ}C$  anneals. The only significant benefit of implanting deeper into the material was that shorter anneal times were required to reach the overall dopant uniformity. Due to the high cost of high energy implants, I selected a series of doses implanted at 100 keV and 200 keV.

To determine the approximate post implant anneal times for maximum dopant uniformity for these two power levels, the *TSUPREM<sup>TM</sup>* model was used to generate a series of images at various post implant anneal times. From earlier *TSUPREM<sup>TM</sup>* simulations, I knew that phosphorous outgassing occurs during the post-processing high temperature anneals which inhibits dopant uniformity. I simulated a  $50\text{ \AA}$ -thick oxide cap over the structural surfaces to eliminate the phosphorous outgassing. Figure 6.10 is a *TSUPREM<sup>TM</sup>* representation of the  $1E16\text{ ions}/cm^2$  phosphorous ion implant for a  $10\text{ }\mu m$ -wide Poly1 beam. The simulated phosphorous dopant uniformity is significantly improved by the combined phosphorous implant, oxidation, and accompanying anneal.

Figure 6.11 is a *TSUPREM<sup>TM</sup>* representation of the  $1E16\text{ ions}/cm^2$  phosphorous ion implant for a  $10\text{ }\mu m$ -wide Poly2 beam. As before, the dopant uniformity

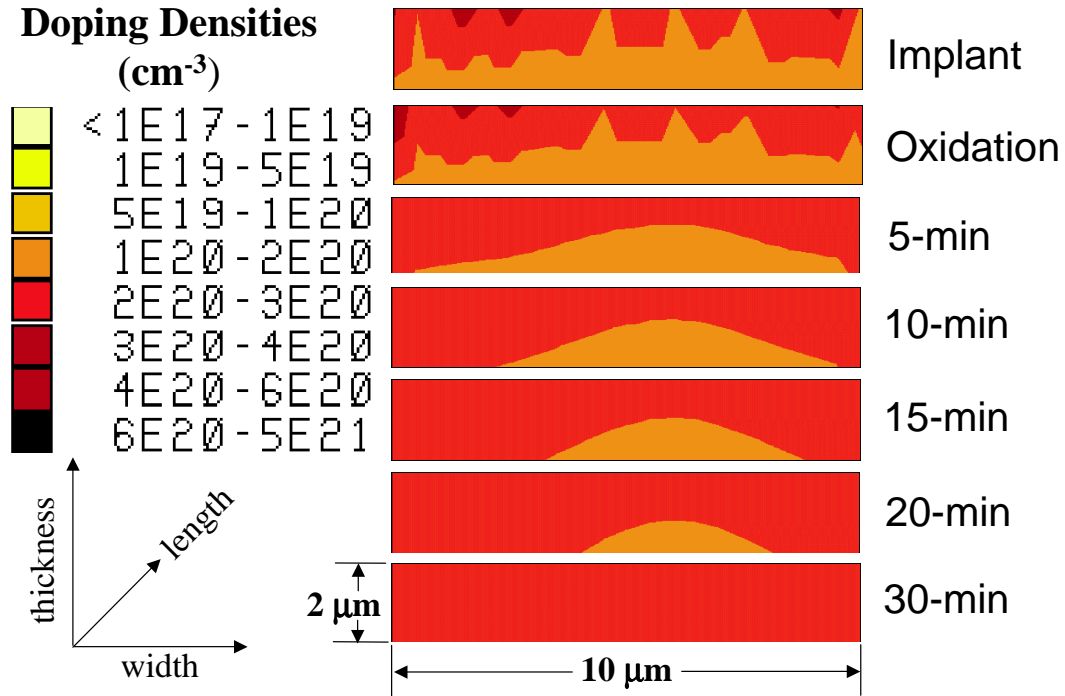


Figure 6.10: TSUPREM beam cross-section simulation of the 200 keV phosphorous implant ( $1\text{E}16 \text{ ions}/\text{cm}^2$  dose) with associated post implant anneal times at  $1100^\circ\text{C}$  for a Poly1  $10 \mu\text{m}$ -wide beam.

is improved through the combined implant and anneal. The increased uniformity should result in a decrease of residual stress.

**6.6.2 Ion Beam Profile Code.** An Ion Beam Profile Code model provided by ISC was used to determine the implant depths for the 100 and 200 keV implant energies. This model provides a Gaussian profile for the peak concentration of ions in the material due to the implant. From the ISC model, the 100 and 200 keV implant energies place the peak dopant concentration at depths of approximately 1353 Å and 2852 Å, respectively. An example Gaussian profile for a  $5\text{E}16 \text{ ions}/\text{cm}^2$ , 200 keV phosphorous ion implant as obtained from the ISC model is shown in Figure 6.12.

To obtain a sufficient dopant concentration variation between the different implant doses, I selected implant doses ranging from  $5\text{E}15 \text{ ions}/\text{cm}^2$  to  $1\text{E}17 \text{ ions}/\text{cm}^2$ . For these implant doses, the peak dopant concentrations range from approximately

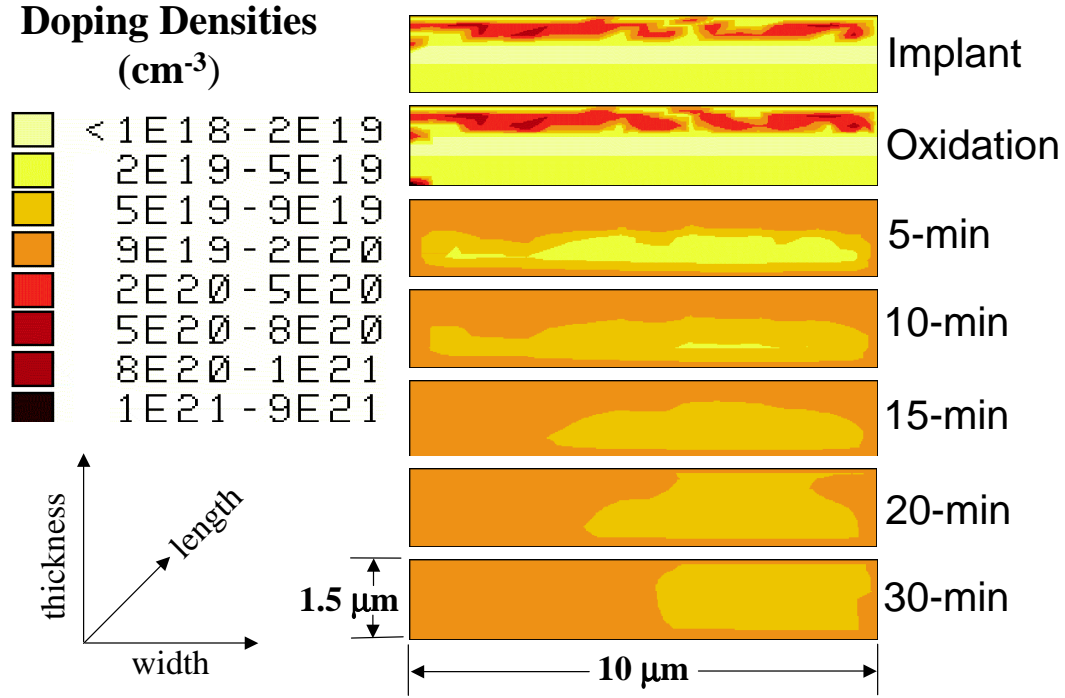


Figure 6.11: TSUPREM beam cross-section simulation of the 200 keV phosphorous ion implant ( $1\text{E}16 \text{ ions}/\text{cm}^2$  dose) with associated post implant anneal times at  $1100^\circ\text{C}$  for a Poly2  $10 \mu\text{m}$ -wide beam.

$2.67\text{E}20 \text{ cm}^{-3}$  to  $9.06\text{E}21 \text{ cm}^{-3}$ . The  $TSUPREM^{TM}$  simulations using these exact implant doses followed by the  $1100^\circ\text{C}$  anneal provides implant projected doping ranges from  $5\text{E}19 \text{ cm}^{-3}$  to  $1\text{E}21 \text{ cm}^{-3}$ . Table 6.4 shows all selected implant doses with corresponding peak dopant concentrations, and implant depths for the two implant power levels used in this research. All phosphorous ion implants were performed at a low temperatures ( $50^\circ\text{C}$ ) to prevent damage to the dice.

### 6.7 Implant Results and Analysis

Implant Sciences Corporation in Wakefield, MA performed all the implants used in this research. Prior to all implants, I recorded  $\mu\text{Raman}$  residual stress profiles for all selected MEMS structures to determine the background residual stress levels. Following all implants, I performed an oxidation/anneal performed at a temperature of  $900^\circ\text{C}$  for 30-min with a 1 liter/min  $\text{O}_2$  gas flow rate. The  $900^\circ\text{C}$ ,

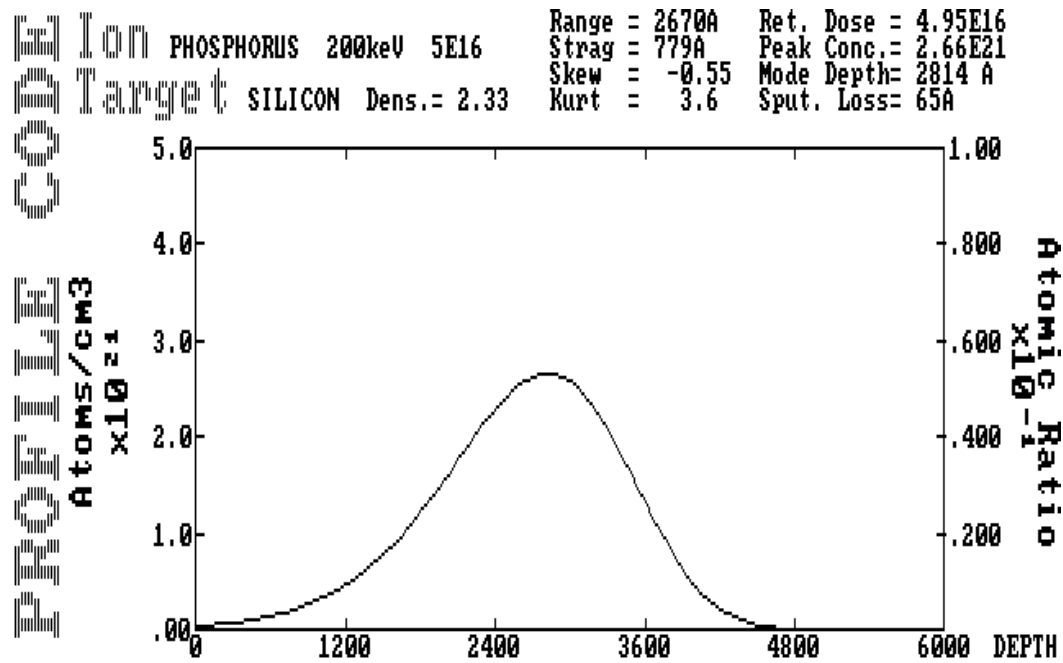


Figure 6.12: Gaussian profile for a  $5E16 \text{ ions/cm}^2$ , 200 keV phosphorous implant.

30-min oxidation/anneal step serves three purposes: 1) it helps to repair the crystal damage due to the implant; 2) it grows the nominal 50 Å oxide cap to help reduce phosphorous outgassing; and 3) it allows diffusion of the implanted phosphorous ions within the MEMS structure to aid in achieving uniform doping concentrations. Using a profilometer, I measured the oxide cap thickness to be 630 Å.

A significant part of my research was focused on selecting the proper implant doses. Since the implanting of post-fabricated MEMS structures has not been previously published, I set up my preliminary implant experiments to encompass a large range of implant dose levels to provide measurable residual stress changes. Therefore, my initial phosphorous ion implant study consisted of a set of 40 MEMS dice. The dice were divided into two sets. I implanted half at 100 keV and the other half at 200 keV. From each half set, the dice were divided further into 5 sets (corresponding to 5 different implant doses) with 4 die in each set. The die from each set were bonded to a 4-inch silicon wafer before implantation. Each of the four die is annealed

Table 6.4: Phosphorus Implant Parameters

Implant Energy (keV)	Implant Dose ( $\frac{ions}{cm^2}$ )	Calculated Peak Concentration ( $\frac{atoms}{cm^3}$ )	Calculated Implant Depth (Å)
100	5E15	4.57E20	1363
100	1E16	9.14E20	1353
100	3E16	2.74E21	1335
100	5E16	4.56E21	1319
100	1E17	9.06E21	1266
200	5E15	2.67E20	2852
200	1E16	5.33E20	2847
200	3E16	1.60E21	2840
200	5E16	2.66E21	2814
200	1E17	5.32E21	2788

for a different period of time (5, 10, 15, or 20-min) following the ion implant and oxidation. Table 6.5 provides a matrix of the experiment I performed.

Following the ion implants, I measured resistivity values for a set of die from each implant dose. Table 6.6 provides the measured resistivity values for selected Poly1 and Poly2 structural layers. I used an HP4155A semiconductor parameter analyzer to measure the resistivity values of the implanted and annealed microbridges. As listed in Table 6.6, as the dopant concentration increases, the beam resistivity decreases. For Poly1 beams, the beam resistance decreased from approximately 415  $\Omega$  before the implants to 86.5  $\Omega$  following the 1E17  $ions/cm^2$  implant. The resistivity of the Poly2 beams decreased from 820  $\Omega$  to 79.7  $\Omega$  following the 1E17  $ions/cm^2$  implant. Based on the resistivity measurements, I concluded that the final polysilicon doping densities match the levels predicted by my *TSUPREM<sup>TM</sup>* simulations.

After the foundry removes Oxide2, it then performs a timed BOE etch to reduce stringers. The BOE etch partially exposes both Poly1 and Poly2 structures. I perform an oxidation prior to the 1100  $^{\circ}C$  anneals to minimize the phosphorous

Table 6.5: Experimental phosphorous implant matrix.

Implant Energy (keV)	Implant Dose ( $\frac{ions}{cm^2}$ )	Anneal Time (min)			
		5-min	10-min	15-min	20-min
100	5E15	1	2	3	4
100	1E16	5	6	7	8
100	3E16	9	10	11	12
100	5E16	13	14	15	16
100	1E17	17	18	19	20
200	5E15	21	22	23	24
200	1E16	25	26	27	28
200	3E16	29	30	31	32
200	5E16	33	34	35	36
200	1E17	37	38	39	40

outgassing through exposed Poly1 and Poly2. I perform a dry oxidation at 900 °C for 30-min on all sample die to grow the nominal 50 Å thick oxide cap on the exposed polysilicon surfaces. All sample die in each set were then simultaneously annealed at 1100 °C for either 5, 10, 15, or 20-min. At this anneal temperature, the phosphorous dopant readily diffuses and thus increases the overall dopant uniformity.

### 6.8 Residual Stress Profiles for Ion Implanted MEMS by $\mu$ Raman Spectroscopy

$\mu$ Raman spectroscopy scans on all 10  $\mu m$ -wide by 100  $\mu m$ -long unreleased Poly1 and Poly2 fixed-fixed beams were performed. Through the use of the same fixed-fixed beam test structures,  $\mu$ Raman stress profile comparisons can be made to determine the implant affects on the polysilicon layers. All  $\mu$ Raman stress profiles presented in this section are the average of three repeated  $\mu$ Raman scans on the same beam and are computed using experimentally measured values for the phonon deformation potentials for Poly1 and Poly2 under hydrostatic pressure as provided in Chapter III [1].

Table 6.6: Measured resistivity values for 100  $\mu m$ -long by 10  $\mu m$ -wide Poly1 and Poly2 microbridges following a 200 keV phosphorous ion implant and a 15-min anneal at 1100°C.

Implant Dose ( $ions/cm^2$ )	MUMPs® Structural Layer	Measured Resistivity ( $\Omega \cdot cm$ )
Foundry Level	Poly1	0.013
	Poly2	0.022
5E15	Poly1	0.006
	Poly2	0.008
1E16	Poly1	0.005
	Poly2	0.007
3E16	Poly1	0.004
	Poly2	0.004
5E16	Poly1	0.002
	Poly2	0.003
1E17	Poly1	0.001
	Poly2	0.001

Figure 6.13 shows the Poly1 residual stress profiles obtained from unreleased 10  $\mu m$ -wide by 100  $\mu m$ -long microbridges following the phosphorous implants and a 15-min 1100 °C anneal. Each residual stress profile depicts a different implant dose. As illustrated in Figure 6.13, the compressive residual stress has been reduced in the low dose implants (5E15 and 1E16  $ions/cm^2$ ) where the stress level approaches 0 Pa. In the higher implant doses (3E16, 5E16, and 1E17  $ions/cm^2$ ), the residual stress shifts from a compressive (less than 0 Pa) to a tensile stress (greater than 0 Pa) and steadily increases as the implant dose is increased. Since the polysilicon grain size is similar in all dice due to the identical anneal times, the variation in measured stress profiles is due solely to minor variations in the MUMPs® foundry process between individual MEMS die and the increased dopant concentration in the beams.

Figure 6.14 shows the residual stress profiles obtained from unreleased 10  $\mu m$ -wide by 100  $\mu m$ -long Poly2 microbridges following the phosphorous implants and a 15-min 1100 °C anneal. Like the Poly1 structural layer illustrated in Figure 6.13,

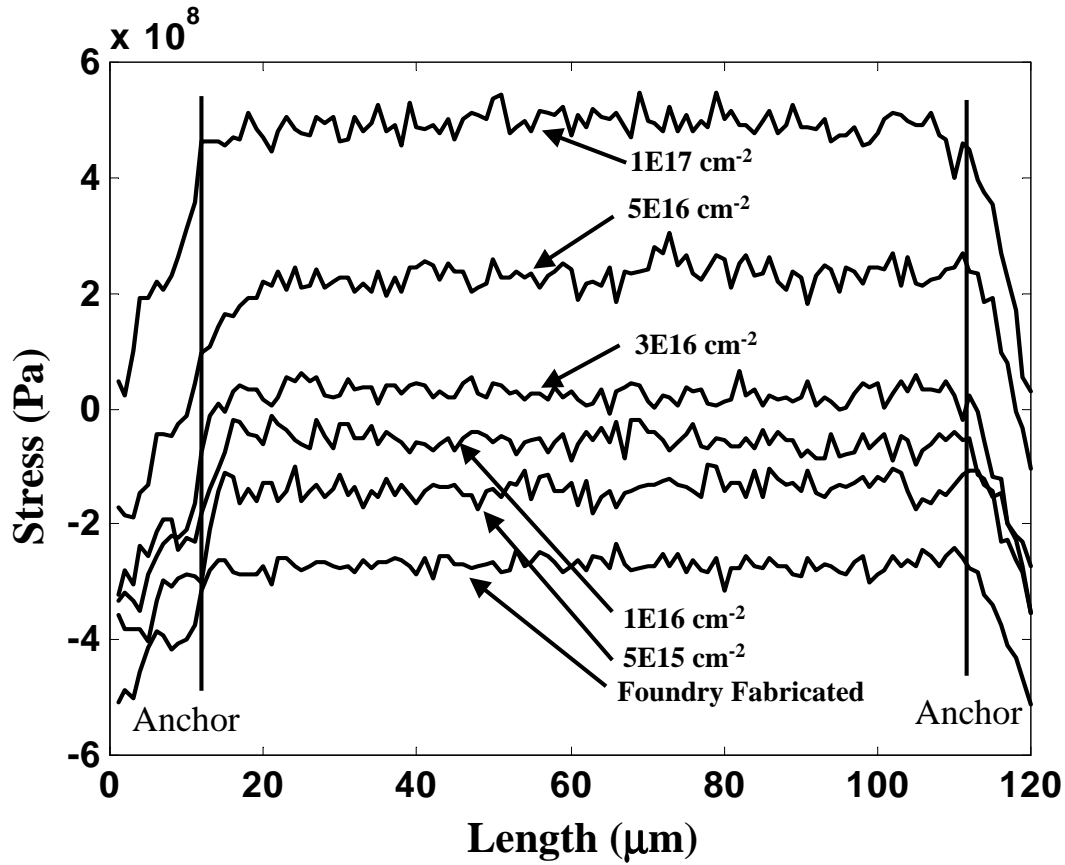


Figure 6.13: Poly1 residual stress profiles measured using  $\mu$ Raman spectroscopy for 100  $\mu m$ -long by 10  $\mu m$ -wide unreleased beams following the 100 keV phosphorous implants and a 15-min 1100  $^{\circ}C$  anneal.

the low dose implants exhibit a compressive residual stress reduction in the Poly2 layer. Likewise, as the phosphorous implant dose increases, the compressive residual stress shifts to a tensile stress and steadily increases with higher implant doses.

Figure 6.15 illustrates the residual stress variations between the 100 and 200 keV implant energy levels. As illustrated in Figure 6.15, the implant power level selected to perform the implants does not appear to have a significant effect on the residual stress. These results correlate very well with the *TSUPREM<sup>TM</sup>* simulations at these implant power levels. The bold lines in Figure 6.15 correlate to the implants performed at the 200 keV implant level.

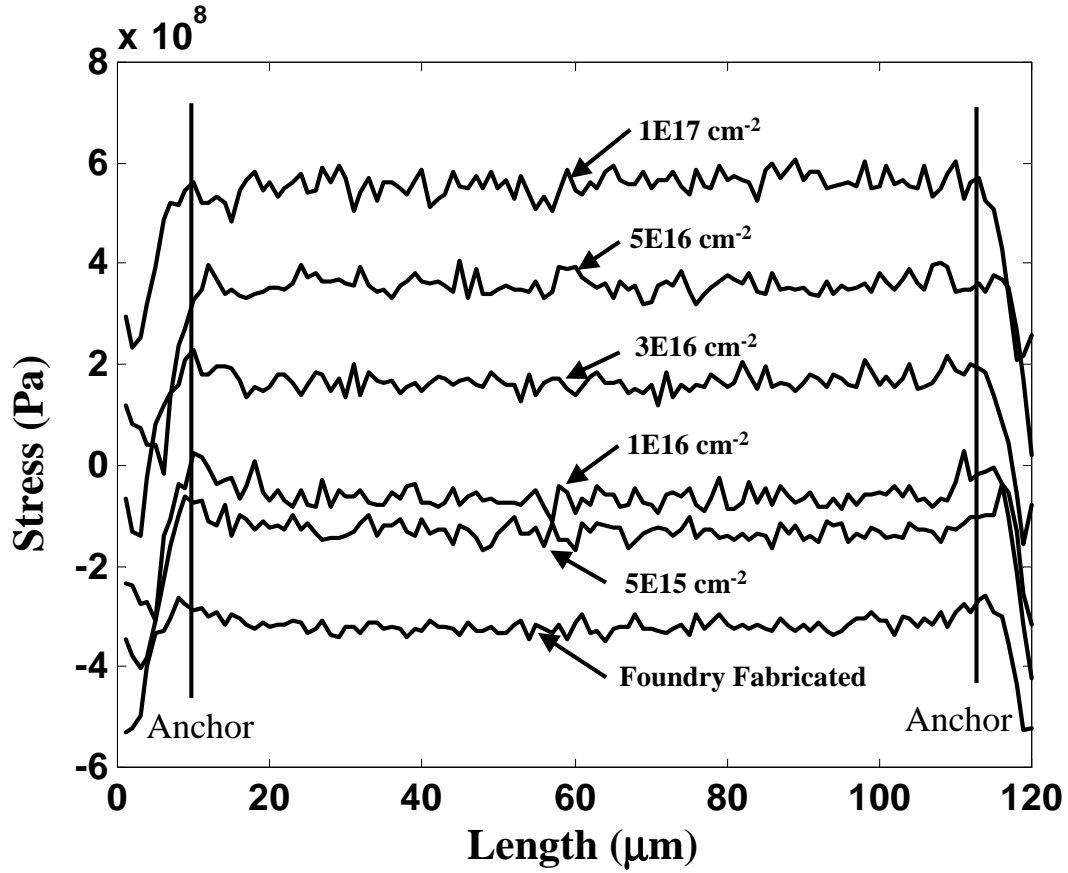


Figure 6.14: Poly2 residual stress profiles measured using  $\mu$ Raman spectroscopy for 100  $\mu\text{m}$ -long by 10  $\mu\text{m}$ -wide unreleased beams following the phosphorous implants for doses as listed and implant energy of 200 keV, followed by a 15-min 1100  $^{\circ}\text{C}$  anneal.

As illustrated in Figure 6.15, the residual stress converts to a tensile stress following the 3E16  $\text{ions}/\text{cm}^2$  implant doses. Since the Raman stress profiles for doses above 3E16  $\text{ions}/\text{cm}^2$  indicate tensile stress, the buckling beam arrays should not buckle for any of the tensile stress values. The critical buckling beam arrays only buckle under compressive stress. Thus I used cantilevers to assess the changes in residual stress. I obtained nearly identical Raman stress profiles as shown in Figure 6.15 for Poly2 fixed-fixed beams with similar stress magnitudes.

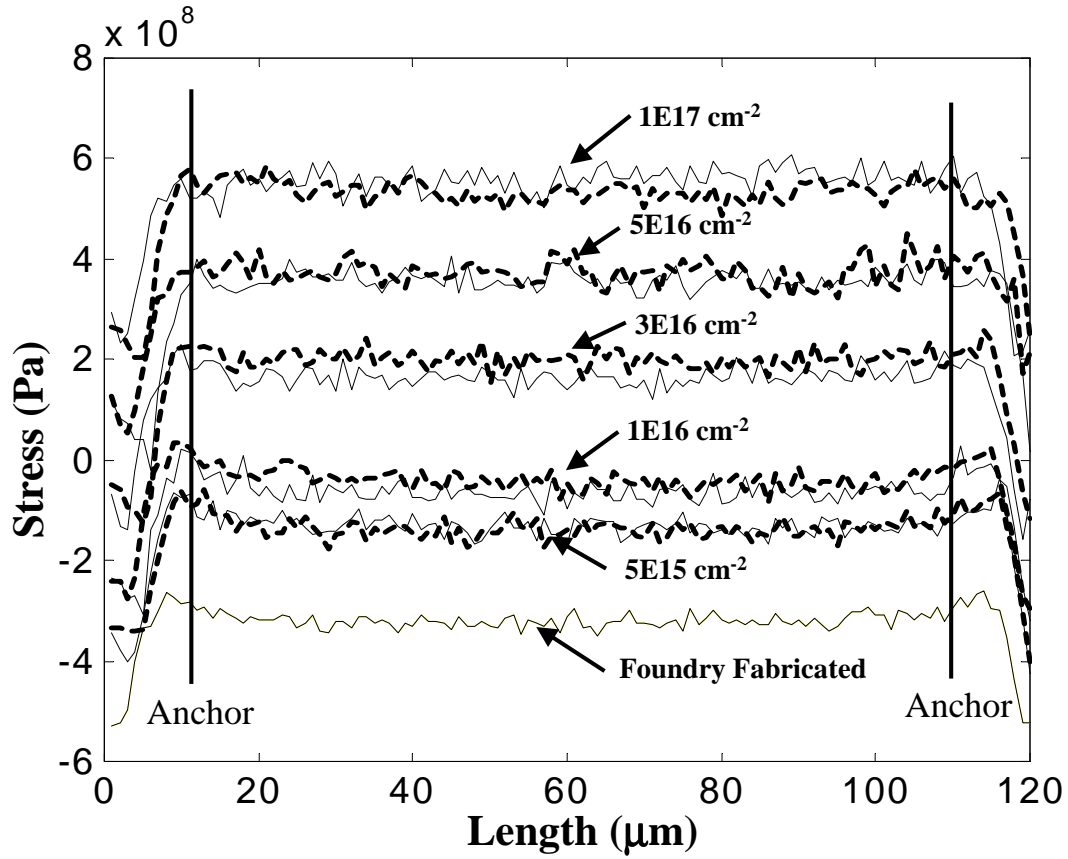
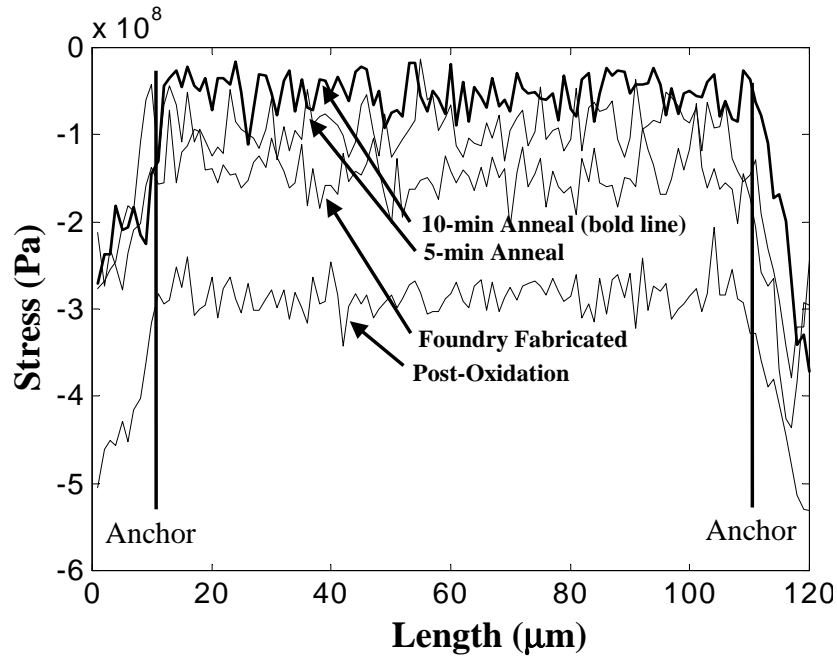


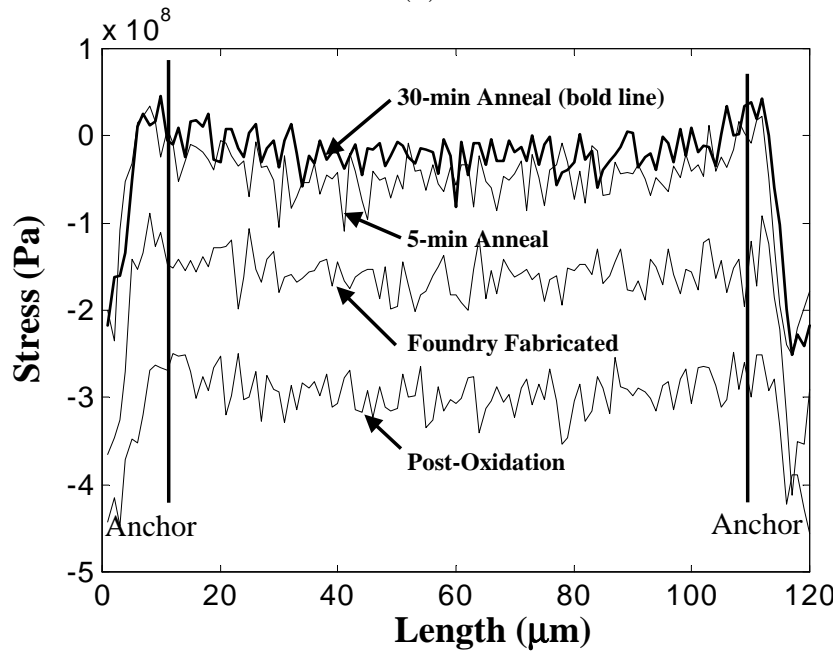
Figure 6.15: Poly1 residual stress profiles measured using  $\mu$ Raman spectroscopy for 100  $\mu\text{m}$ -long by 10  $\mu\text{m}$ -wide unreleased beams following the phosphorous implants at the doses listed for both the 100 keV (lighter line) and 200 keV (darker line) implant power levels followed by a 15-min anneal at 1100  $^{\circ}\text{C}$

Figure 6.16 illustrates the level of residual stress relaxation in both the Poly1 and Poly2 material layers resulting from a 1E16  $\text{ions}/\text{cm}^2$  phosphorous ion implant, oxidation, and subsequent 1100  $^{\circ}\text{C}$  anneals.

The previous research of Butler pertaining to resistivity in MUMPs<sup>®</sup> polysilicon found that (as expected) the resistivity of Poly1 and Poly2 increased as the beam width widened [4]. A possible reason for these results is the affects of lateral diffusion on Poly1 structures during the MUMPs<sup>®</sup> fabrication process. The MUMPs<sup>®</sup> fabrication process is modelled using  $TSUPREM^{TM}$  as outlined in Section 2.5. From  $TSUPREM^{TM}$ , lateral diffusion is evident and has the greatest affects in narrow



(a)



(b)

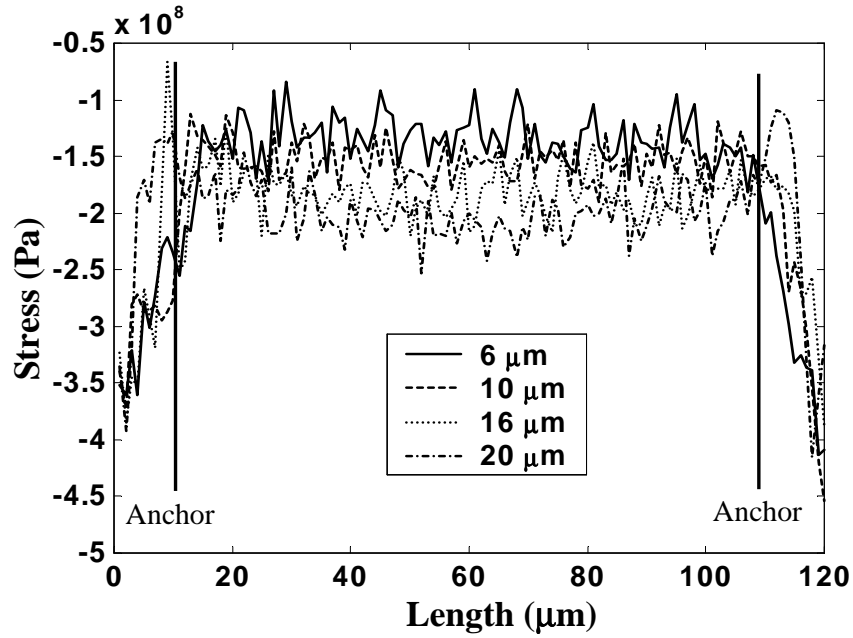
Figure 6.16:  $\mu$ Raman residual stress profiles illustrating stress changes in Poly1 and Poly2 material layers during the post-processing of a 200 keV,  $1E16 \text{ ions/cm}^2$  phosphorous ion implant. The  $\mu$ Raman stress profiles illustrate: (a) Poly1 material layers, and (b) Poly2 material layer.

beams. As the beams become wider, the affects of lateral diffusion are significantly diminished. If there is a dopant concentration difference, a possible shift in the  $\mu$ Raman stress profiles should be evident. I performed  $\mu$ Raman scans on Poly1 and Poly2 unreleased fixed-fixed beams with widths of 6, 10, 16, and 20  $\mu m$ -wide. I performed one set of  $\mu$ Raman scans on undoped MEMS beams to determine the foundry fabrication stress profiles. This same die was then implanted with phosphorous at a  $1E16 \text{ ions}/cm^2$  dose and annealed for 15-min at  $1100^\circ C$ . I then repeated the  $\mu$ Raman scans over the identical fixed-fixed beams. Figure 6.17 illustrates my measured residual stress levels for this series of Poly1 fixed-fixed beams.

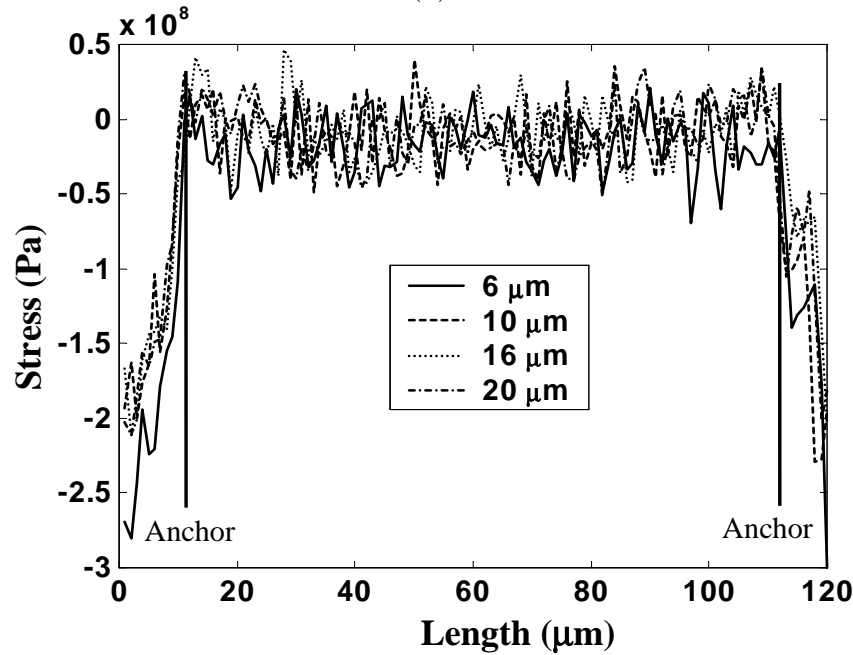
In Figure 6.17a), each beam width has a different residual stress level. However, Figure 6.17b) illustrates the residual stress levels in the same beams following a 200 keV,  $1E16 \text{ ions}/cm^2$  phosphorous implant and accompanying 15-min  $1100^\circ C$  anneal. From this plot, all beam widths provide nearly identical residual stress profiles. This indicates that the dopant concentration and dopant uniformity play an important part in residual stress reduction. Another important aspect of the post implant and anneal is that now, the entire wafer has nearly identical stress levels in both polysilicon structural layers. Thus, all Poly1 devices should operate nearly identically and the uniform stress should increase device yield. I performed similar experimental tests on Poly2 fixed-fixed beams with similar results.

### 6.9 Young's Modulus Measurements

Young's modulus decreases with increasing doping concentration in crystalline silicon . The reason is not entirely clear. Maier-Schneider [13] claims that even at a high doping concentration, only one percent of the Si-Si bonds are replaced by the dopant, and that this is not enough for a significant change in the Young's modulus [11]. However, in highly doped polysilicon, a significant fraction of dopant segregates to the grain boundary, which can have a significant affect on the value of Young's modulus [11].



(a)



(b)

Figure 6.17:  $\mu$ Raman residual stress profiles illustrating stress uniformity in Poly1 beams following a 200 keV,  $1\text{E}16 \text{ ions}/\text{cm}^2$  phosphorous ion implant. The  $\mu$ Raman stress profiles illustrate: (a) Poly1 foundry stress profiles, and (b) Post implant and 15-min  $1100^\circ\text{C}$  anneal.

For each of the MUMPs® die used in my implant study, a set of test structures (Poly1 and Poly2 buckling beam arrays [6], comb drive resonators [18]), and Poly1 and Poly2 cantilever arrays were fabricated and used to determine the material properties for each structural layer. I determined Young's modulus by measuring the resonance of comb drives before and after phosphorous ion implantation. The resonant frequency measured for Poly1 resonators for an  $5\text{E}15 \text{ ions}/\text{cm}^2$  implant dose averaged approximately  $22.52 \pm 0.15 \text{ kHz}$  which corresponds to a Young's modulus of  $129 \pm 2 \text{ GPa}$ . The Poly1 comb drive resonance for an  $1\text{E}16 \text{ ions}/\text{cm}^2$  implant dose averaged  $21.35 \pm 0.15 \text{ kHz}$  which gives a Young's modulus of approximately  $116 \pm 2 \text{ GPa}$ . Resonators on die with implant doses  $>1\text{E}16 \text{ ions}/\text{cm}^2$  would not resonate. This was due to a significant deformation (fingers curled downward following implant and accompanying oxidation) of the comb resonator after the implant (see Figure 6.18. Essentially, the comb fingers did not interleave any longer. The calculated Young's modulus value changed by approximately 13 GPa between the  $5\text{E}15$  and  $1\text{E}16 \text{ ions}/\text{cm}^2$  implant doses. From this, I conclude that the material's elasticity is weakening. A Poly2 resonator was not fabricated on this series of MUMPs® die, however I would expect analogous results.

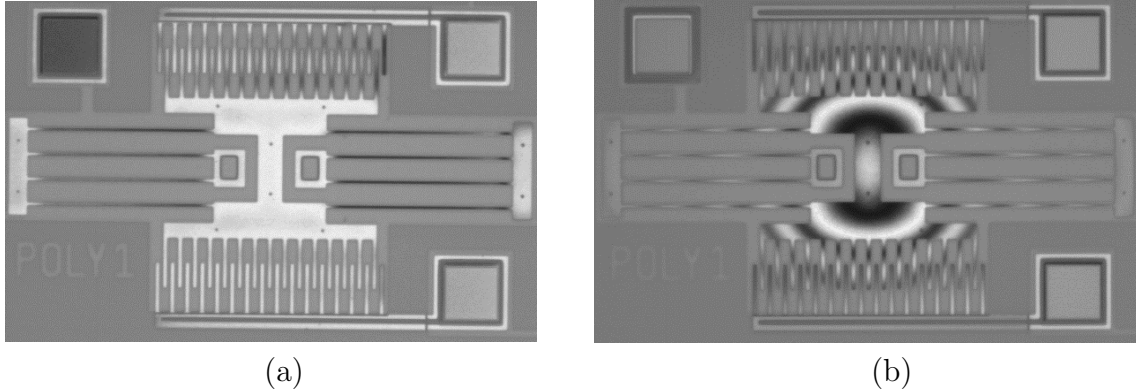


Figure 6.18: IFM image of Poly1 comb resonators: (a) image of foundry fabricated comb resonator, and (b) image following a 200 keV,  $3\text{E}16 \text{ ions}/\text{cm}^2$  phosphorous implant and 15-min  $1100 \text{ }^\circ\text{C}$  anneal.

### 6.10 Analytical Residual Stress Measurements

Following the HF and supercritical  $CO_2$  dry, I performed IFM measurements to determine the critical buckling lengths for polysilicon layers after the implant and anneal. The IFM images of the buckling beam arrays shown in Figure 6.19 demonstrate that residual stress reduction is achieved for the  $5E15$  and  $1E16$   $ions/cm^2$  dose phosphorous ion implants and accompanying 15-min  $1100\text{ }^\circ C$  anneals. The critical buckling lengths become shorter as the implant dose increases above  $3E16$   $ions/cm^2$  (see Figure 6.19 (d)-(f)). Figure 6.19 illustrates the critical buckling lengths of the MUMPs® foundry fabrication arrays for both Poly1 (top) and Poly2 (bottom) structural layers. From the critical buckling lengths and the measured Young's modulus for each layer, the residual stress levels can be determined.

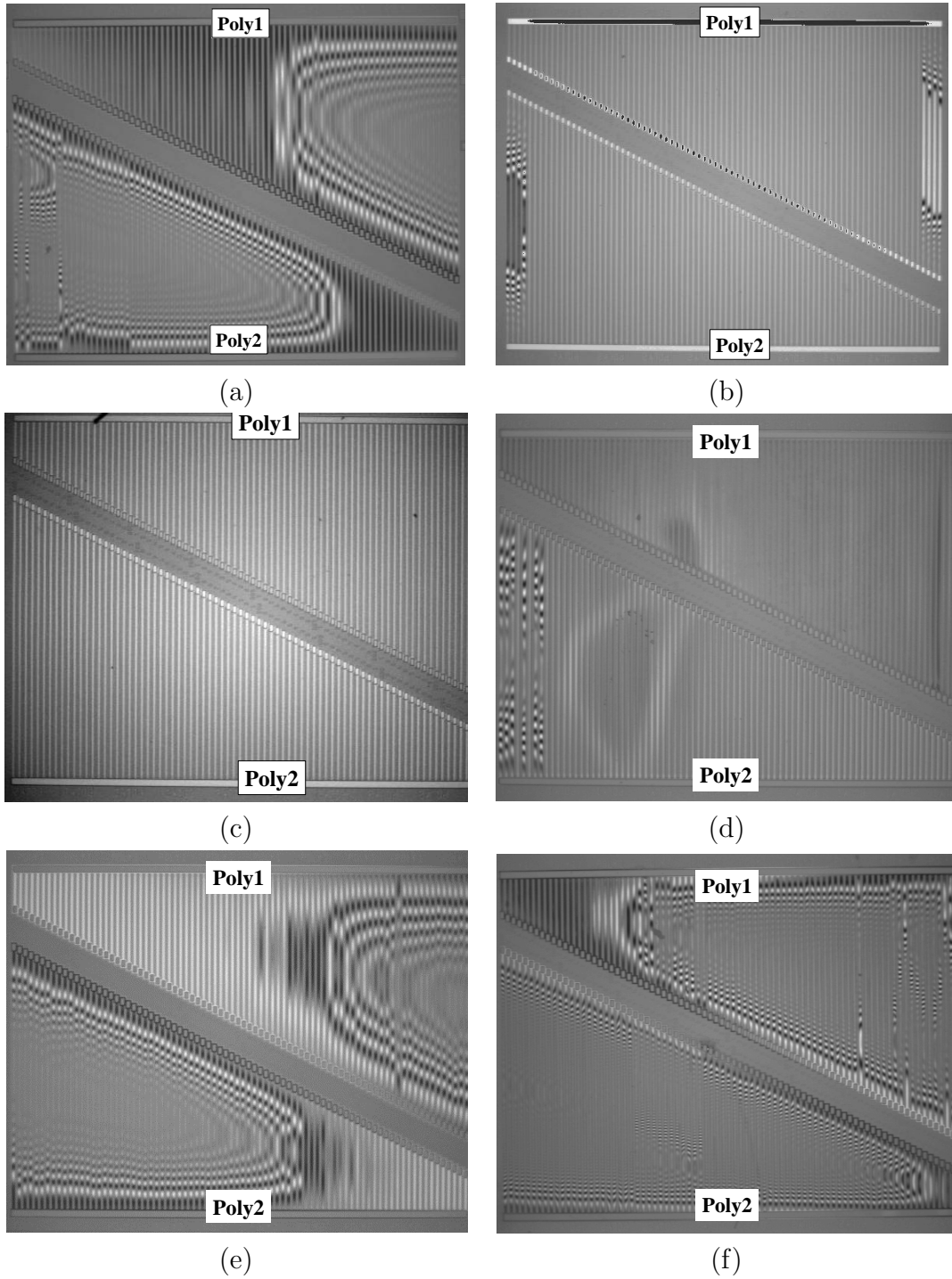


Figure 6.19: IFM images of Poly1 (top) and Poly2 (bottom) buckled beam arrays for various 200 keV phosphorous implants with an accompanying 15-min 1100°C anneal. The arrays presented illustrate: (a) foundry fabricated arrays, (b) 5E15  $\text{ions}/\text{cm}^2$  implant (c) 1E16  $\text{ions}/\text{cm}^2$  implant, (d) 3E16  $\text{ions}/\text{cm}^2$  implant, (e) 5E16  $\text{ions}/\text{cm}^2$  implant, and (f) 1E17  $\text{ions}/\text{cm}^2$  implant.

The corresponding residual stress values for each implant dose is calculated and presented in Table 6.7:

Table 6.7: Buckled beam lengths and corresponding residual stress values from Figure 6.19 for a 15-min 1100 °C anneal.

Image	Beam	Implant Dose ( $ions/cm^2$ )	Measured Buckling Length ( $\mu m$ )	Calculated Residual Stress (MPa)
Figure (a)	Poly1	background	510	-6.9
Figure (a)	Poly2	background	290	-14.3
Figure (b)	Poly1	5E15	860	-2.4
Figure (b)	Poly2	5E15	860	-1.6
Figure (c)	Poly1	1E16	900	-2.1
Figure (c)	Poly2	1E16	900	-1.5
Figure (d)	Poly1	3E16	900	-2.1
Figure (d)	Poly2	3E16	820	-1.8
Figure (e)	Poly1	5E16	590	-5.1
Figure (e)	Poly2	5E16	390	-7.9
Figure (f)	Poly1	1E17	340	-15.1
Figure (f)	Poly2	1E17	190	-33.6

The  $\mu$ Raman measurements in Figure 6.15 suggest that residual stresses for the 1E16  $ions/cm^2$  implant and 15-min anneal case are very near zero but still compressive. From my visual inspection of the buckling beam arrays, this also holds true for this implant dose. From the critical buckling beam arrays illustrated in Figure 6.19 with implants greater than 1E16  $ions/cm^2$ , the buckled beam lengths get shorter which correspond to the  $\mu$ Raman stress profiles where the data show a change from a compressive stress to a tensile stress.

One should notice that the  $\mu$ Raman stress profiles and the critical buckling lengths from the test arrays for the high implant doses do not agree with theory. For a beam with tensile stress, there is no buckling of the beams. A good example of tensile stress is a guitar string. As the tension is increased, the string gets tighter. This is similar to the buckling beam array such that tensile stress will not buckle the beam. However, from the buckling beam arrays illustrated in Figure 6.19 (d)-(f),

the beams are buckled. Thus, this intuitively tells me that the beams are not under tensile stress.

What experimentally appears to have happened during the high dose implants is that the polysilicon was inadvertently changed to a porous polysilicon. Porous polysilicon is a much weaker structural layer than polysilicon and results in shorter buckling lengths. This supports my measured results as the porosity of the polysilicon layer is increased due to the high implant doses, the beams become weaker and buckle at significantly shorter lengths. Previous research has indicated that the porous layer primarily depends on the doping level of the material layer [12]. Several other experimental tests and observations also support the polysilicon to porous polysilicon conversion to include the following:

- The reduced resonant frequencies with increased implant doses result in a decreased the elastic modulus. A lower Young's modulus reveals a weaker and more pliable material.
- The polysilicon material layers change from the usual yellowish color under a microscope to an increasingly darker brown color as the implant dose is increased. This brown color is a characteristic of porous silicon [12].
- The surface of the polysilicon structural material became increasingly pitted (similar to a sponge) as the implant dose increased. Pore sizes can range in diameter from 20 Å to 10  $\mu m$  [12]. This is a physical feature of porous silicon.
- The  $\mu$ Raman peak intensities decreased to approximately half the typical intensity of unimplanted MEMS.
- The FWHM of the  $\mu$ Raman polysilicon peak widened when compared to the typical polysilicon peak for the high implant doses. This agrees with the characteristics of porous silicon [17].
- Recent  $\mu$ Raman studies on porous silicon with respect to depth have found an increase in the phonon frequency at the interface which was attributed to

the lattice mismatch [14]. An increase in the phonon frequency could shift the frequency above the unstressed silicon value, thus making the stress appear tensile when in reality, it remains compressive. This could be why the high implant doses appear to induce tensile stress when measured by  $\mu$ Raman spectroscopy.

To reaffirm my conclusions from my preliminary studies of implant stress analysis, I implanted a second series of MUMPs® die. These die were implanted with doses of 5E15 and 1E16 *ions/cm*<sup>2</sup> at 200 keV. Prior to the oxidation and 1100 °C anneals, I recleaned the furnace tube as outlined in Appendix A to remove contaminants and outgassed phosphorous from the tube due to the previous anneals. I then performed the oxidation and applied various 1100 °C anneal periods on the MEMS die. Following the HF release, I performed IFM measurements on the test die. Figure 6.20 illustrates the results after both implant doses. As can be observed, both buckling beam arrays (Figure 6.20b) and d) remained unbuckled following a 5-min 1100 °C anneal.

*6.10.1 Residual Stress Calculation using Cantilever Deflection.* To further assess the residual stress relaxation for the 5E15 and 1E16 *ions/cm*<sup>2</sup> phosphorous ion implants for longer anneal times, I investigated Poly1 and Poly2 cantilever arrays. Table 6.8 provides the calculated values for the residual stress as measured by the deflection of the cantilevers using an IFM. All cantilevers for these implant doses curled downward. As the stress relaxed due to anneals, the magnitude of the downward deflection reduced.

When one compares the residual stress values measured by the cantilevers to those obtained from the critical buckling beam arrays, the cantilever values are slightly higher. This difference is probably due to the assumption made in the derivations of the cantilever and buckling beam equations. Also, the Young's modulus can vary slightly for the different implants and anneal times. However, the calculated

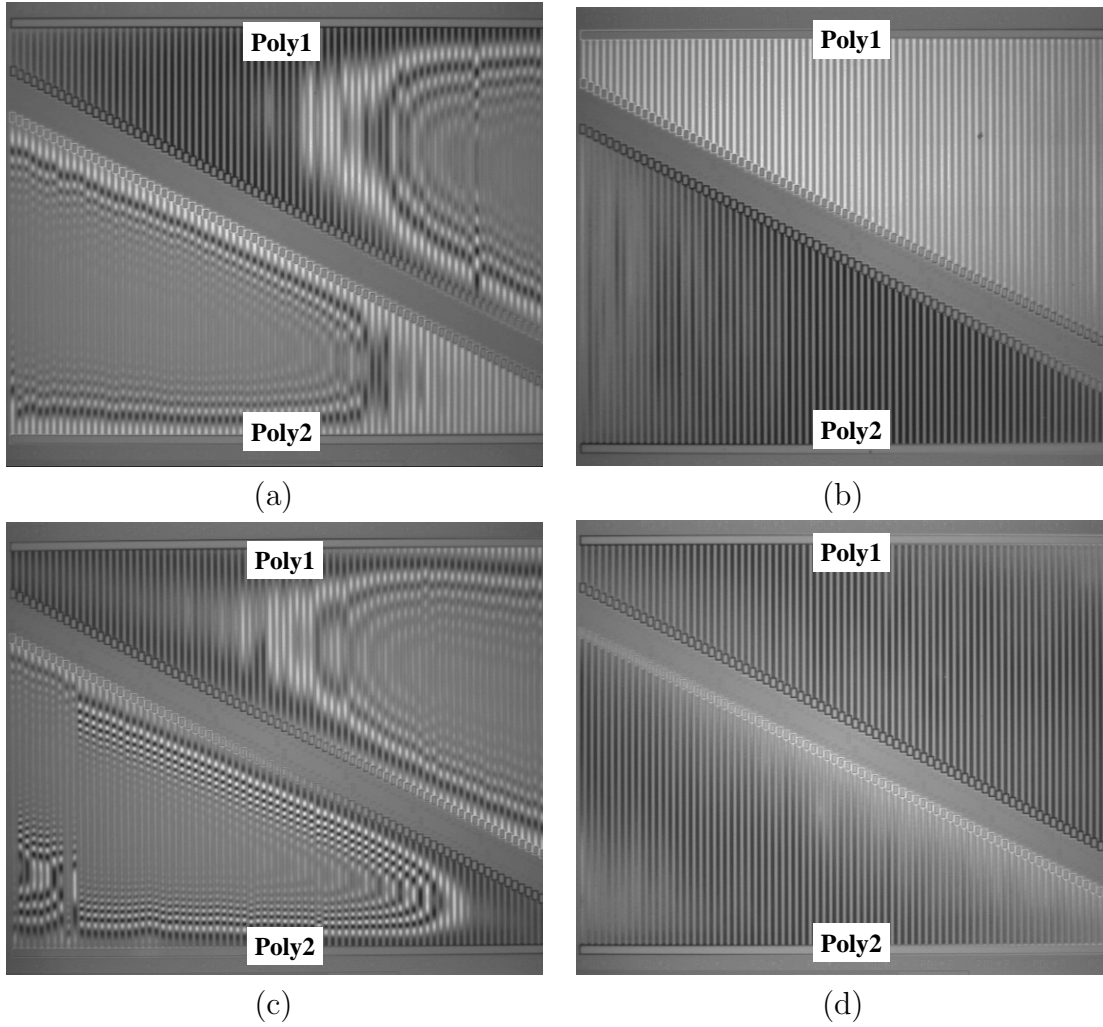


Figure 6.20: IFM images of buckled beam arrays representing changes in the residual stress for 200 keV phosphorous ion implants at doses of  $5E15 \text{ ions}/cm^2$  and  $1E16 \text{ ions}/cm^2$  and after a subsequent 5-min  $1100^\circ C$  anneal. (a)  $5E15 \text{ ions}/cm^2$  implant and oxidation (b)  $5E15 \text{ ions}/cm^2$  implant, oxidation, and 5-min anneal (c)  $1E16 \text{ ions}/cm^2$  implant and oxidation, and (d)  $1E16 \text{ ions}/cm^2$  implant, oxidation, and 5-min anneal.

values of residual stress in the cantilevers decrease as the anneal time increases. After a 30-min anneal, the residual stress levels are well below the minimum stress values detected via the buckling beam arrays.

Through both the IFM measurements and the  $\mu$ Raman stress profiles, the  $5E15$  to  $1E16 \text{ ions}/cm^2$  phosphorous ion implant range provides the minimal residual

Table 6.8: Poly1 and Poly2 150  $\mu m$ -long by 10  $\mu m$ -wide cantilever residual stress values for phosphorous ion implant doses of 5E15 and 1E16  $ions/cm^2$ .

Beam	Implant Dose ( $ions/cm^2$ )	Anneal Time (min)	Measured Cantilever Deflection (nm)	Calculated Residual Stress (MPa)
Poly1	5E15	5	0.365	-5.40
Poly2	5E15	5	0.772	-10.84
Poly1	5E15	10	0.237	-3.50
Poly2	5E15	10	0.573	-8.05
Poly1	5E15	15	0.185	-2.74
Poly2	5E15	15	0.566	-7.94
Poly1	5E15	20	0.157	-2.33
Poly2	5E15	20	0.353	-4.96
Poly1	5E15	30	0.141	-2.09
Poly2	5E15	30	0.396	-5.55
Poly1	1E16	5	0.586	-8.66
Poly2	1E16	5	0.928	-13.01
Poly1	1E16	10	0.227	-3.36
Poly2	1E16	10	0.555	-7.78
Poly1	1E16	15	0.237	-3.50
Poly2	1E16	15	0.655	-9.19
Poly1	1E16	20	0.143	-2.12
Poly2	1E16	20	0.505	-7.08
Poly1	1E16	30	0.143	-2.11
Poly2	1E16	30	0.108	-1.52

stress levels. The observed IFM images of the buckling beam arrays correlate well with the residual stress profiles obtained using  $\mu$ Raman spectroscopy for unreleased MEMS microbridges for low implant doses. From the  $\mu$ Raman stress profiles, the 1E16  $ions/cm^2$  phosphorous ion implant produces the minimal residual stress levels.

### 6.11 Optical Characterization

Following the implants, all micromirrors exhibited a concave (downward) surface curvature. The level of micromirror curvature varies by the implant dose and

the duration of the 1100 °C anneals. Figure 6.21 shows an IFM image of an array of micromirrors following the 5E15 and 1E16  $ions/cm^2$  phosphorous implants.

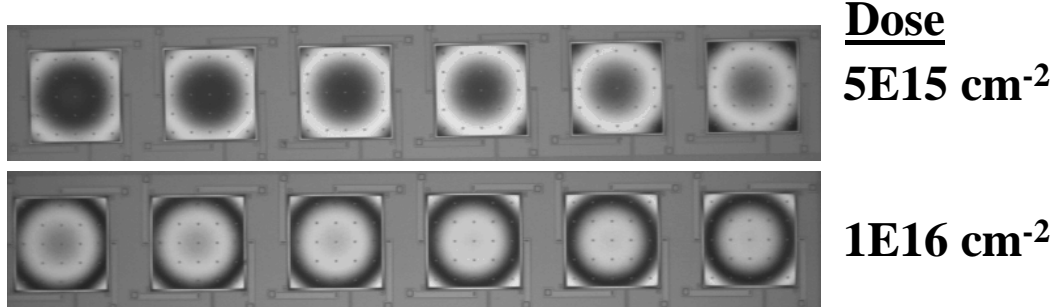
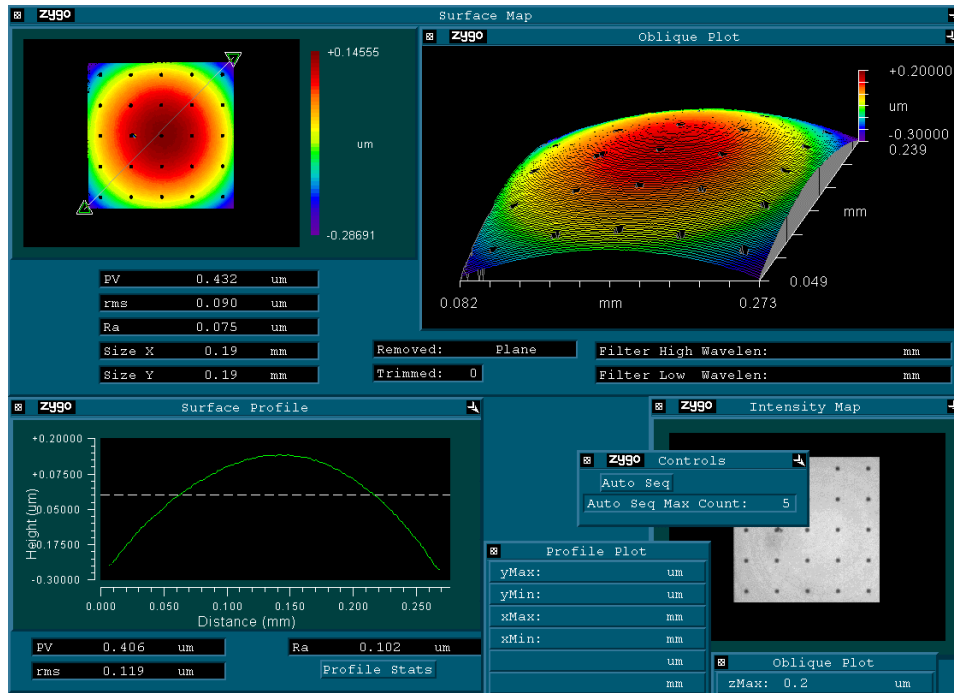
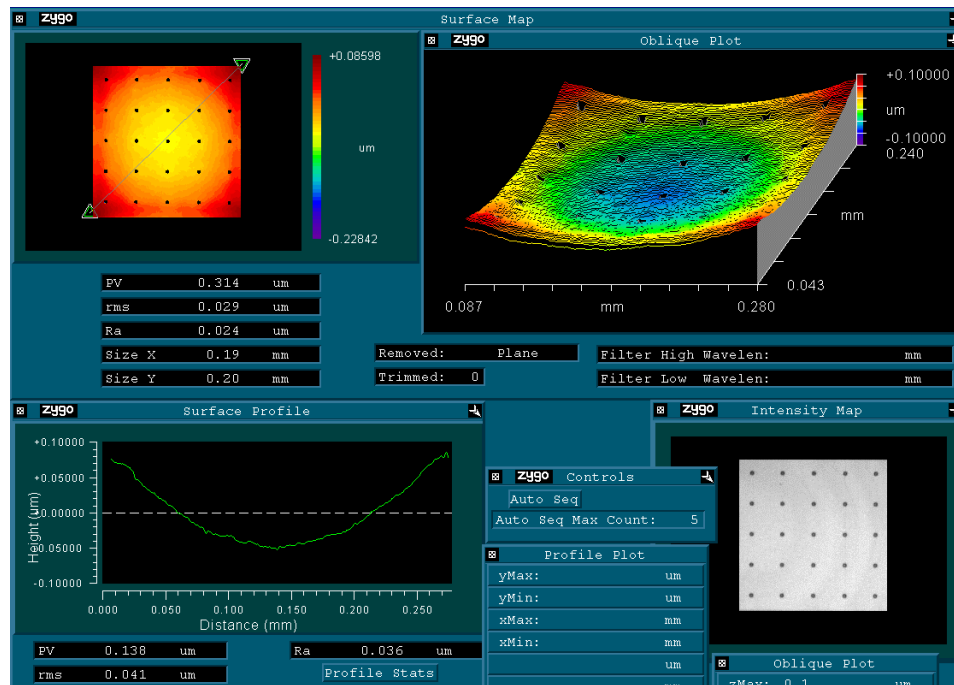


Figure 6.21: IFM image illustrating optical flatness for a 150  $\mu m$ -square oxidized micromirror with various implant doses and 5-min 1100 °C anneal.

As illustrated in Figure 6.21, following the anneals, the mirror curvature is curve upward (convex). The level of curvature decreases as the anneal time is lengthened. For example, a 150  $\mu m$  by 150  $\mu m$  square Poly1-Poly2 stacked micromirror has a background peak-to-valley upward bow of 0.406  $\mu m$  (see Figure 6.22a). Following a 1E16  $ions/cm^2$  phosphorous implant and 30-min 1100 °C anneal, the peak-to-valley upward bow decreases to 0.263  $\mu m$  (see Figure 6.22b). Thus, I conclude that by changing the stress gradient in addition to the stress level, the micromirror curvature in the MUMPs® fabrication process can be changed to either a concave or convex profile.



(a)



(b)

Figure 6.22: IFM image of 200 keV,  $1E16 \text{ ions}/\text{cm}^2$  phosphorous implant Poly1-Poly2 stacked micromirrors: Figure (a) implanted and oxidized, and (b) implant, oxidized and 15-min 1100 °C anneal.

## 6.12 Summary of Chapter VI

I verified that residual stress reduction is possible and controllable through the use of post-processing low dose ion implants and an accompanying 1100 °C anneal. Through the use of  $\mu$ Raman spectroscopy, I can monitor, measure and control the residual stress levels in the MEMS structures. The  $\mu$ Raman stress reduction was verified through on-chip buckling beam arrays and cantilevers. I showed that it is possible to “engineer” the stress in the polysilicon MEMS layers using  $\mu$ Raman spectroscopy to monitor the progress. The 1E16 *ions/cm<sup>2</sup>* phosphorous implant with associated anneals appears to produce the minimal residual stress levels. I verified that the Young’s modulus does indeed decrease with increasing phosphorous concentrations as stated by Maier-Schneider [13]. The Young’s modulus decreased by 13 GPa for the Poly1 structural layer between the 5E15 and 1E16 *ions/cm<sup>2</sup>* implant doses. I theorize that high implant doses inadvertently changed the material makeup of polysilicon to porous polysilicon. My idea is supported by the fact that porous polysilicon MEMS test structures become increasingly weak with higher implant doses and eventually fail to operate. My measurement techniques are useful because they can be used to develop fabrication techniques to design-in stress. My techniques can also be used for process control. Lastly, the optical characteristics of MUMPs® micromirrors can be improved through the use of post-processing techniques to reduce the inherent bow in as fabricated MUMPs® micromirrors.

## Bibliography

1. E. Anastassakis and E. Liarokapis. Polycrystalline Si under strain: Elastic and lattice-dynamical considerations. *Journal of Applied Physics*, 62(8):3346–3352, October 1987.
2. D. A. Antoniadis, A. G. Gonzalez, and R. W. Dutton. Boron in near-intrinsic 100 direction and 111 direction silicon under inert and oxidizing ambients - diffusion and segregation. *Journal of Electroanalytical Chemistry*, 125(5):813–819, 1978.
3. G. Baccarani and P. Ostojia. Electron mobility empirically related to the phosphorus concentration in silicon. *Solid-State Electronics*, 18:579–580, 1975.
4. J. T. Butler. *Development and Packaging of Microsystems using Foundry Services*. PhD thesis, Air Force Institute of Technology (AETC), Wright-Patterson AFB OH, 1998. AFIT/DS/ENG/98-08.
5. Standard Oil Semiconductor Products Division. PDS Phosphorus PH-950 n-Type Technical data sheet, 1985. P.O. Box 664, Niagara Falls, New York 14302.
6. W. Fang and J. A. Wickert. Post buckling of micromachined beams. *Journal of Micromechanical Microengineering*, 4:116–122, 1994.
7. L. Starman Jr., J. Busbee, J. Reber, J. Lott, W. Cowan, and N. Vandelli. Stress measurement in MEMS devices. In *4<sup>th</sup> International Conference on Modeling and Simulation of Microsystems*, Hilton Head, SC., pages 398–401, 17-22 Mar 2001.
8. M. Kawata, S. Nadahara, J. Shiozawa, M. Watanabe, and T. Katoda. Characterization of stress in doped and undoped polycrystalline silicon before and after annealing or oxidation with laser raman spectroscopy. *Research Center for Advanced Science and Technology*, pages 407–411, September 1989.
9. D. A. Koester, 2001. Personal Phone Communications, Cronos Integrated Microsystems Technical Processing Engineer.
10. D. A. Koester, R. Mahadevan, B. Hardy, and K. W. Markus. MUMPS<sup>TM</sup> design handbook rev. 6, 2001. Cronos Integrated Microsystems, a JDS Uniphase Company, 3026 Cornwallis Rd., Research Triangle Park, NC 27709.
11. S. Lee, C. Cho, J. Kim, S. Park, S. Yi, J. Kim, and D. Cho. The effects of post-deposition processes on polysilicon Young’s modulus. *Journal of Micromechanical Microengineering*, 8:330–337, 1998.
12. Marc Madou. *Fundamentals of Microfabrication*. CRC Press LCC, 2000 N.W. Corporate Blvd., Boca Raton, Florida 33431, 1997.

13. D. Maier-Schneider, A. Köprülü, S. Ballhausen Holm, and E. Obermeier. Elastic properties and microstructure of LPCVD polysilicon films. *Journal of Micromechanical Microengineering*, 6:436–446, 1996.
14. S. Manotas, F. Aquiló-Rueda, J. D. Moreno, F. Ben-Hander, and J. M. Martinez-Duart. Lattice-mismatch induced-stress in porous silicon films. *Thin Solid Films*, 401:306–309, 2001.
15. Ralph Sinclair. Implant sciences corporation, 2001. 107 Audubon road, #5, Wakefield MA 01880-1246.
16. J. Singh, S. Chandra, and A. Chand. Strain studies in LPCVD polysilicon for surface micromachined devices. *Sensors and Actuators A*, 77:133–138, 1999.
17. Z. Sui, P. P. Leong, and I. P. Herman. Raman analysis of light-emitting porous silicon. *Applied Physics Letters*, 60(17):2086–2088, April 1992.
18. W. Chi-Keung Tang. *Electrostatic Comb Drive for Resonant Sensor and Actuator Applications*. PhD thesis, University of California, Berkeley, 1990.

## VII. $\mu$ Raman Spectroscopy Results and Analysis

### 7.1 Introduction

In this dissertation, I present the first ever stress characterization measurements of silicon and gallium arsenide using the residual stress profiles obtained from MEMS structures via  $\mu$ Raman spectroscopy and the analytical residual stress values calculated from on-chip MEMS test structures (i.e. critical buckling arrays, cantilevers and comb resonators).  $\mu$ Raman stress profiles and the critical buckling lengths determined from buckling beam arrays show significant correlation. Correlation in these measurement techniques is presented as the magnitude of  $\mu$ Raman spectroscopy stress profiles increase or decrease, the buckling beam arrays indicate similar results. I showed that a first-order model of stress in cubic crystalline silicon is useful for the conversion of raw  $\mu$ Raman spectroscopy data into stress data. I demonstrate for the first time that it is possible to control or “engineer” the amount of strain in foundry MEMS structures by post-fabrication annealing and doping via ion implantation with diffusion. I conduct a series of annealing and implant/diffusion studies on a variety of polysilicon MEMS structures with varying lengths and widths. I show both experimentally and by numerical modelling that residual stress in polysilicon fixed-fixed beams and flexures is reduced. In this chapter, I address the stress magnitude variations and provide a prediction model to correlate the residual stress values obtained from  $\mu$ Raman spectroscopy for unreleased fixed-fixed beams to the localized residual stress values determined from buckling beam and cantilever arrays.

### 7.2 Stress Magnitudes

In general, the residual stress profiles obtained from  $\mu$ Raman spectroscopy are typically one or two orders of magnitude higher than the residual stress values calculated from either the buckling beam arrays or via cantilever deflection. The primary reason for this deviation is the fact that the  $\mu$ Raman stress profiles are

typically obtained from unreleased MEMS structures. The unreleased structures are not in a true relaxed stress condition. Although I can measure the residual stress in released MEMS structures, once the structure is released, I obtain a completely different stress profile for the same beam. For example, the typical  $\mu$ Raman test structure used in this research is the 10  $\mu m$ -wide by 100  $\mu m$ -long Poly1 and Poly2 fixed-fixed beam. Figure 7.1 illustrates the residual stress profiles for a Poly1 beam for pre and post release conditions.

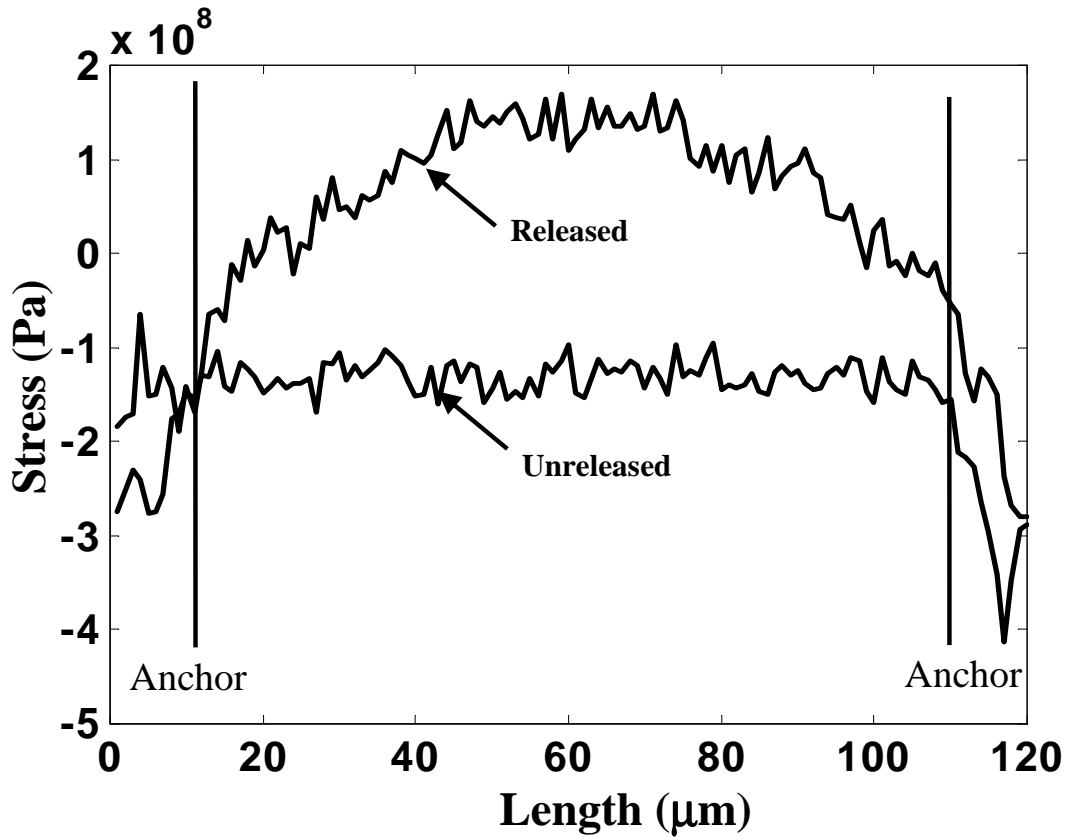


Figure 7.1: Unreleased and released  $\mu$ Raman stress profiles for a 10  $\mu m$ -wide by 100  $\mu m$ -long Poly1 fixed-fixed beam.

As illustrated in Figure 7.1, the residual stress profile for an unreleased beam is essentially a flat line with the exception of the anchors where the stress increases quite significantly. I obtain a flat  $\mu$ Raman stress profile since the polysilicon beam has a constant interface (attachment) to the sacrificial oxide beneath the beam. This

attachment prevents the beam from being fully relaxed. The anchors have a high residual stress partially because of the highly stressed SiN isolation layer deposited under the anchors. Once the beam is released, the residual stress profile takes on the shape of an upsidedown “U”. Mechanically, for a fixed-fixed released beam, the stress is highest in the anchored ends and in the middle (lengthwise). The stress is minimal along the linear regions of the beam prior to reaching the inflection points (points where the stress changes from a compressive value to a tensile level).

As Figure 7.1 illustrates, it is difficult to determine the true stress value for the released beam. To obtain a residual stress value for the released beam, I averaged the raw  $\mu$ Raman spectra from along the beam length (100-points) to obtain a single residual stress value. Due to symmetry of the beam, the averaged stress value should lie midway between the maximum and minimum stress levels (see Figure 7.1). The averaged  $\mu$ Raman stress value is calculated to be approximately -18.73 MPa to the critical buckling beam array stress value of -8.51 MPa. The calculated one order of magnitude difference between the two stress measurement techniques is presumed to be due to the resolution of the  $\mu$ Raman spectroscopy system since the critical buckling beam arrays provide a fairly accurate localized residual stress value. A small frequency shift in the  $\mu$ Raman spectrum results in a large stress value (e.g. a  $0.01\text{ cm}^{-1}$  frequency shift is approximately equal to a -4.5 MPa stress level). However, since I am interested in generating a predictive model to assist MEMS designers, I look for a means to correlate the stress I measure on unreleased MEMS structures using  $\mu$ Raman spectroscopy to the stress extracted from observations of released buckled beam arrays.

### 7.3 *Prediction Model*

In an effort to compare the magnitudes of the measured stress between the  $\mu$ Raman stress data to the analytical stress data obtained from the on-chip MEMS buckling beams, I use two different techniques. First, I use a graphing program to

analyze and curve fit the raw stress data values for both measurement techniques. Second I predict the buckling beam length by manipulation of the stress equations for both techniques.

*7.3.1 Raw Data Analysis.* I used a graphing software package [2] to generate the stress comparison images for the Poly1 and Poly2 structural layers. The prediction model is developed to relate the residual stress levels obtained from  $\mu$ Raman spectroscopy to the residual stress levels obtained from the fabricated MEMS test structures (buckling beam arrays, comb resonators, and cantilevers) on each die. I chose to relate the unreleased Raman stress profiles to the released MEMS test structures. By performing this relation, the  $\mu$ Raman stress profile can be used to predict approximately what the residual stress value is as determined by the buckling beam arrays. The primary benefit of this relationship is if the residual stress levels obtained via  $\mu$ Raman spectroscopy is not sufficient, the MEMS designer can perform a low dose implant and/or 1100 °C anneal to alter the residual stress to a desired level prior to the HF release. As stated earlier, post-processing techniques cannot be performed on released structures since structural deformation results.

To obtain the  $\mu$ Raman stress data values for use in the prediction model, I chose to use the middle 10-points in each unreleased 10  $\mu m$ -wide by 100  $\mu m$ -long fixed-fixed beam  $\mu$ Raman scan ( $\mu$ Raman spectral positions 55-64). For each unreleased beam, three repeated  $\mu$ Raman scans are performed with 120 spectra collected for each scan at a 1  $\mu m$  step interval. The three repeated scans are initially referenced to the laser line, then averaged together. I then average the middle 10-points of the averaged polysilicon line to obtain a single stress value. Averaging the 30-points (3 scans of 10 points each) will reduce the effects of a single high or low peak value and provide a truer residual stress level. The measured  $\mu$ Raman stress value is then compared to the buckling beam stress value determined through the use of the IFM and comb resonators. Figure 7.2 illustrates the corresponding residual stress values for the post-processing anneals and implants for the Poly1 structural layer.

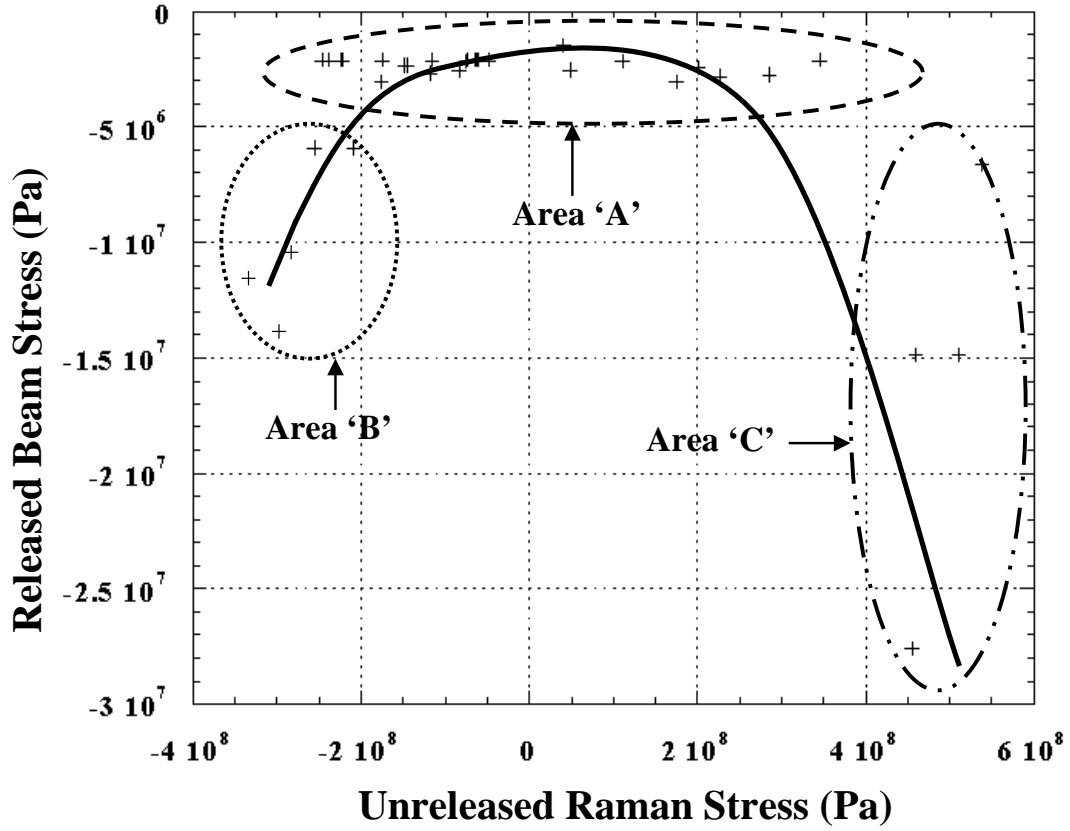


Figure 7.2: Comparison image of Poly1  $\mu$ Raman stress data to buckling beam stress data

Figure 7.3 illustrates the comparison of the  $\mu$ Raman residual stress values to the calculated buckling beam values for the post-processing anneals and implants for the Poly2 structural layer.

As can be observed from Figure 7.2 and 7.3 both structural layers provide similar results. These observations were typically the case throughout this research. The raw stress data plotted in Figure 7.2 and 7.3 is fitted with a 4<sup>th</sup> degree polynomial as this fit the measured data best.

As illustrated in Figure 7.2 and 7.3, the majority of the data points are located below the -5 MPa compressive stress level (area ("A")). The data points in location "A" correlate to the low dose implants ( $5E15$  and  $1E16\text{ cm}^2$ ) and the undoped high temperature anneals. The data points located in region "B" ( $-4$  to  $-2 \times 10^8$ (Pa)

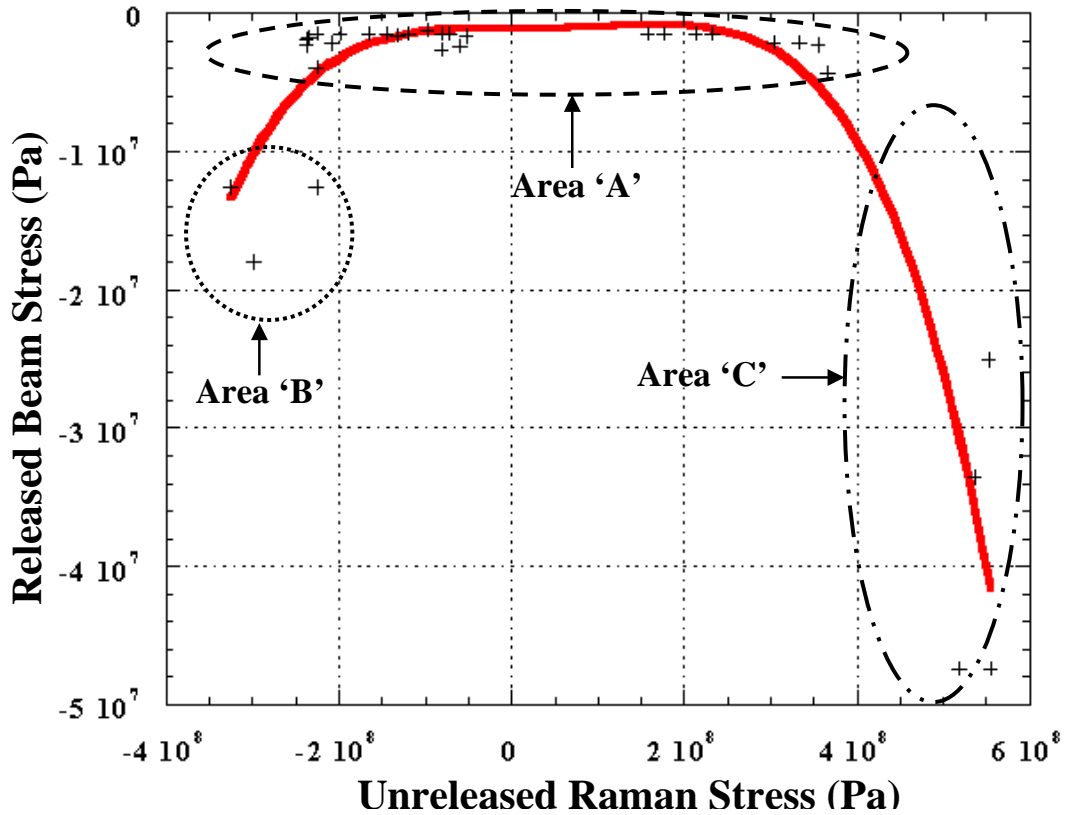


Figure 7.3: Comparison image of Poly2  $\mu$ Raman stress data to buckling beam stress data

along  $\mu$ Raman stress-axis) correspond to the increased compressive stress levels due to the oxidation. The data points located in region “C” ( $2$  to  $6 \times 10^8$ (Pa) along  $\mu$ Raman stress-axis) correspond to the high implant phosphorous doses ( $3\text{E}16$  to  $1\text{E}17 \text{ cm}^2$ ).

Following the residual stress analysis of the implant doses ( $5\text{E}15$  to  $1\text{E}17 \text{ cm}^2$ ), I conclude that implant doses greater than  $3\text{E}16 \text{ cm}^2$  will not result in residual stress relaxation. Therefore, since the polynomial curve fit in Figure 7.2 and 7.3 is altered due to the high implant dose data points (region “C”), I reanalyzed and plotted the raw stress data without the high implant dose data points (data points corresponding to the  $3\text{E}16$  to  $1\text{E}17 \text{ cm}^2$  implant doses). The modified prediction image for the Poly2 structural layer is shown in Figure 7.4. A second order polynomial was used to fit the data. As before, the points located in area “B” are from structures that have

been oxidized. Although the data points relate unreleased Raman data values to released buckling beam stress values, the prediction model needs to perform this relationship. The MEMS designer requires insight into the residual stress levels in the structures prior to release. From this, the designer can perform one or more of the post-processing techniques to reduce the residual stress to their desired levels.

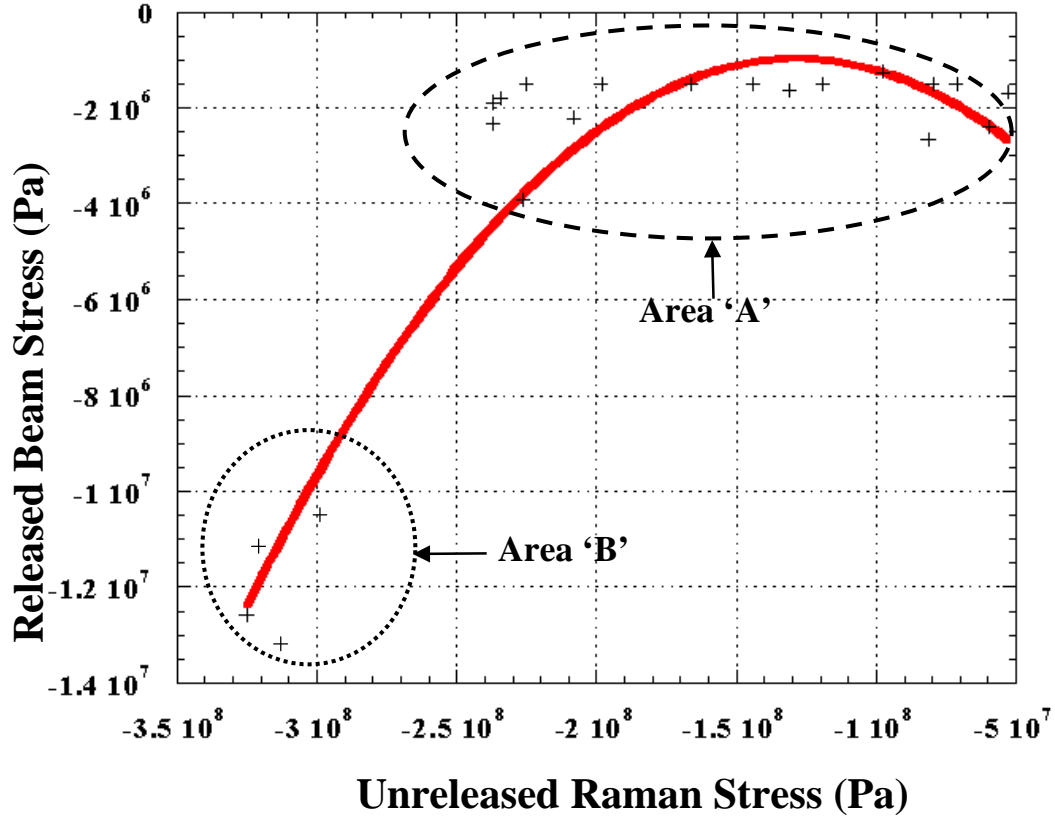


Figure 7.4: Comparison image of Poly2  $\mu$ Raman stress to buckling beam stress data for the 1100  $^{\circ}C$  anneals and implants of 5E15 and 1E16  $ions/cm^2$ .

*7.3.2 Buckling Beam Estimation.* The buckling beam model is based on the combination of the critical buckling beam length equation and the Raman stress equation. The  $\mu$ Raman stress equation relating the  $\mu$ Raman frequency shift to the unstressed silicon line is given by [3].

$$\sigma_{Raman} = \frac{Si - (P_{line} - L_{line})}{H_{constant}} \quad (Pa) \quad (7.1)$$

where  $Si = 521 \text{ cm}^{-1}$  (unstressed silicon value),  $P_{line} \text{ (cm}^{-1}\text{)}$  is the polysilicon peak frequency,  $L_{line} \text{ (cm}^{-1}\text{)}$  is the laser peak frequency, and  $H_{constant} \text{ (cm}^{-1}\text{GPa}^{-1}\text{)}$  is the measured hydrostatic pressure constant given in Chapter III.

The beam buckling equation [4, 5], solved for stress  $\sigma$ , is given by

$$\sigma = \frac{\pi^2 t^2 E}{3L^2} \quad (Pa) \quad (7.2)$$

where  $t \text{ (}\mu\text{m)}$  is the beam thickness,  $L \text{ (}\mu\text{m)}$  is the buckling beam length, and  $E \text{ (GPa)}$  is the Young's modulus of the material.

I set Equation 7.2 and Equation 7.1 equal to each other since the stress value in the  $\mu$ Raman equation should equal the stress value from the buckling beam equation. By setting Equation 7.2 and Equation 7.1 equal to each other and solving for the beam length, I get

$$L = \sqrt{\frac{\pi^2 t_b^2 E}{3 \frac{Si - (P_{line} - L_{line})}{H_{constant}}}} 10 \quad (\mu\text{m}) \quad (7.3)$$

Using MathCad [1], I allowed the value of  $P_{line}$  to vary between 519 and  $521 \text{ cm}^{-1}$ . This frequency shift will capture all relevant compressive  $\mu$ Raman stress data for the phosphorous implants ( $5\text{E}15$  and  $1\text{E}17 \text{ cm}^2$ ) and the high temperature anneals. Figure 7.5 illustrates the  $\mu$ Raman frequency shift vs. critical buckling beam length for a Poly1 beam.

Since the typical frequency shifts are significantly less in the high temperature and low dose implants, I reanalyzed the value of  $P_{line}$  to vary between 520.7 and  $521 \text{ cm}^{-1}$  (approximately 150 MPa of variation). This frequency shift will capture all relevant compressive  $\mu$ Raman stress data for the phosphorous implants ( $5\text{E}15$

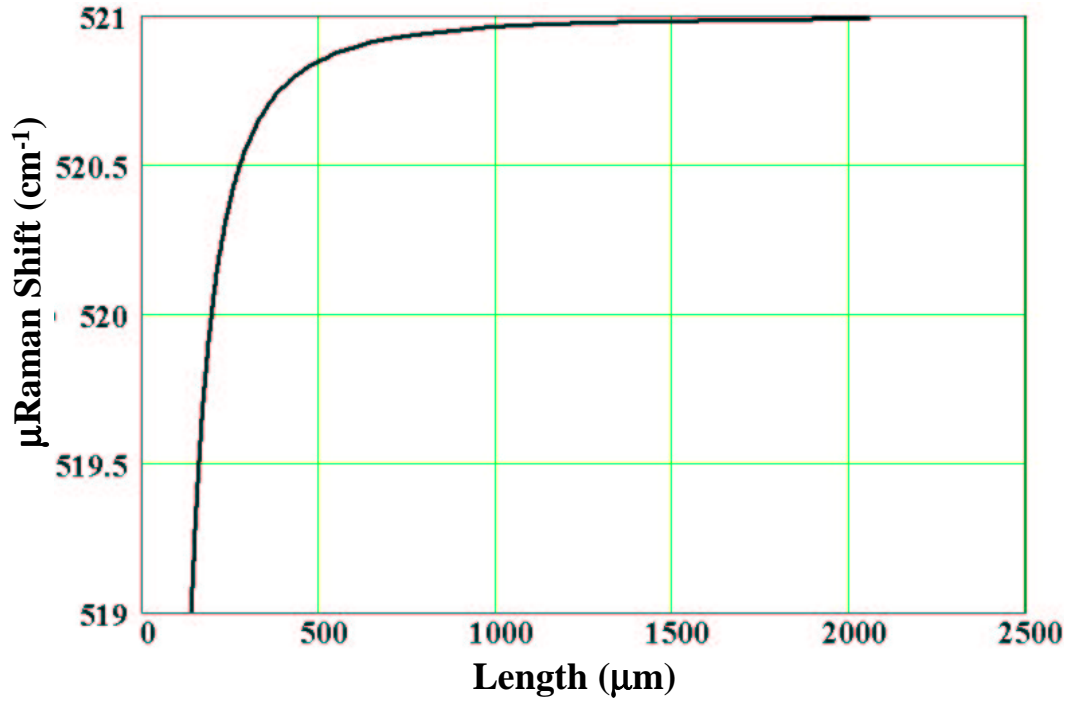


Figure 7.5: Buckling beam length prediction model for MUMPs® Poly1 (frequency shifts varies from 519 and 521  $cm^{-1}$ ).

and  $1E16\text{ }cm^2$ ) and the high temperature anneals. Figure 7.6 illustrates the  $\mu$ Raman frequency shift vs. critical buckling beam length for a Poly1 beam.

Since the Poly2 modeling result is essentially identical to the Poly1 result with the exception of the beam thickness and the value of Young's modulus, it is not shown. This model correlates the  $\mu$ Raman frequency shift to a buckling beam length. Thus, I can estimate the residual stress level in the MEMS beams prior to release by monitoring the frequency shift of the polysilicon peak in the  $\mu$ Raman spectra. For a single  $\mu$ Raman spectra, I can estimate the residual stress in the material by interpolating off Figure 7.5 or Figure 7.6 to identify an approximate beam length to within  $20 \pm 10\text{ }\mu m$ . If not at the desired target value, I could perform one or more of the post-processing techniques described earlier to reduce the stress to an appropriate level.

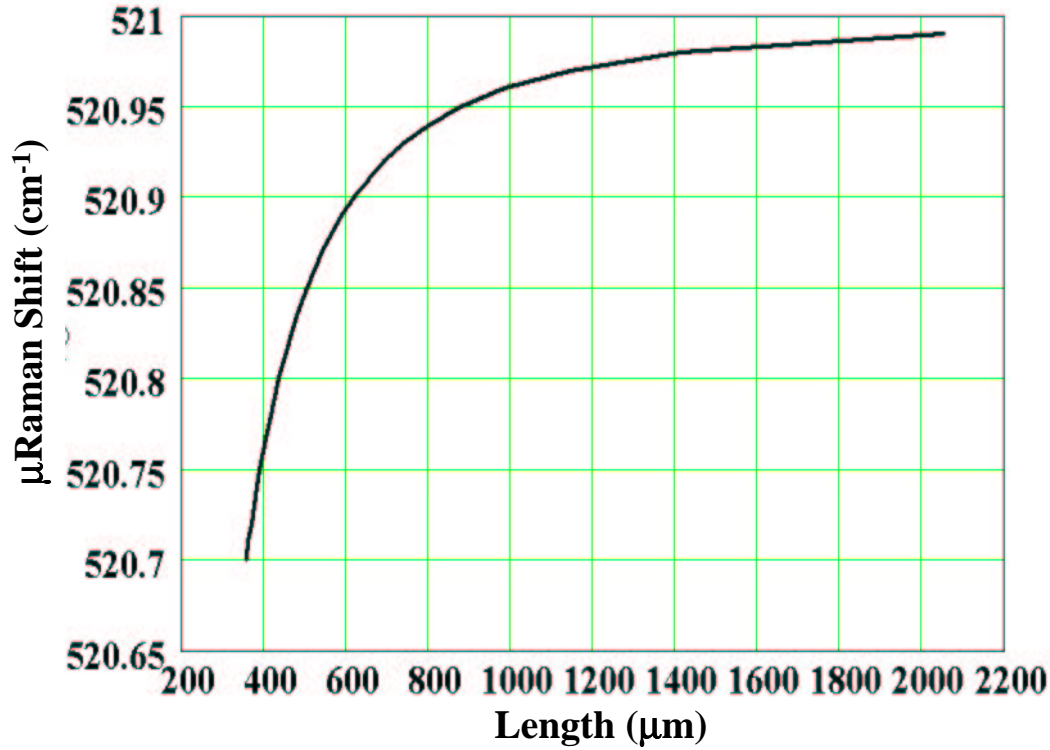


Figure 7.6: Modified buckling beam length prediction model for MUMPs® Poly1 (frequency shifts varies from 520.7 and 521  $cm^{-1}$ ).

#### 7.4 Summary of Chapter VII

In this chapter, I addressed the reasons for the variations in the residual stress magnitudes between  $\mu$ Raman spectroscopy and the MEMS test structures. The primary reason for the relatively large deviation in the stress values is due to the comparison of released stress levels to unreleased stress levels. The unreleased beams are not in a true relaxed state due to the underling sacrificial layer. I provided two different prediction methods for monitoring the residual stress levels as  $\mu$ Raman spectra are collected. From these methods, the MEMS designer has the ability to alter the residual stress levels through post-processing prior to releasing the MEMS structures.

## *Bibliography*

1. MathSoft Inc. 101 Main St. Cambridge, MA 02142.
2. Kaleidagraph software program, 2001. Air Force Research Laboratory, Wright-Patterson AFB, OH 45433.
3. E. M. Anastassakis. *Dynamical Properties of Solids*. North-Holland Publishing Company, Athens 147, Greece, 1980.
4. W. D. Cowan. *Foundry Microfabrication of Deformable Mirrors for Adaptive Optics*. PhD thesis, Air Force Institute of Technology (AETC), Wright-Patterson AFB OH, 1998. AFIT/DS/ENG/98-07.
5. W. Fang and J. A. Wickert. Post buckling of micromachined beams. *Journal of Micromechanical Microengineering*, 4:116–122, 1994.

## *VIII. Raman Spectroscopy on III-V MEMS Structures*

### *8.1 Introduction*

The most widely studied material used in the fabrication of MEMS is silicon. III-V compound semiconductors like GaAs and InP offer a number of material-related and technological advantages over silicon [7]. GaAs represents a technology with very promising applications such as infrared thermopiles, pressure sensors, and resonators [7]. On the other hand, InP seems to be a good candidate for optical devices mostly dedicated to long wavelength applications. For micro-optoelectronics applications like lasers, photodiodes or phototransistors, the use of III-V compound materials which exhibit a direct bandgap is mandatory [7].

At AFIT, research is currently being performed in the areas of MEMS tunable filters and tunable vertical cavity surface emitting lasers (VCSELs). These structures require a means of actuation, control, and tunability which requires some form of III-V MEMS structure. Currently AFIT colleagues are experimenting with beam type structures to include cantilevers, microbridges, and micromirrors. Since the control of residual stress plays a vital role in MEMS functionality, operability, and reliability. I present the first documented assessment of residual stress in GaAs MEMS through the use of  $\mu$ Raman spectroscopy. I am the first to measure and monitor the residual stress in GaAs fixed-fixed beams and micromirror flexures. In addition, I provide a brief background in the characterization of  $\mu$ Raman spectroscopy when performed on GaAs.

### *8.2 Background*

Raman scattering is of great interest for basic investigations of semiconductors since it yields information about phonon frequencies, energies of electron states, and electron-phonon interaction. It is also a powerful tool for the characterization of

semiconducting materials and devices. Raman can be used to determine the device's temperature, strain, carrier concentration, scattering time, impurity content, etc. [2].

$\mu$ Raman spectroscopy for measurements on GaAs is very similar to its use on silicon. The primary difference is in the Raman spectrum for crystalline GaAs in which two active modes are available. The two Raman peaks represent the LO and TO phonon modes with corresponding frequency values of  $269\text{ cm}^{-1}$  and  $292\text{ cm}^{-1}$ , respectively [3,9,13]. As with silicon, symmetry plays a large role in what modes are detected in the backscattering geometry. The symmetry selection rules for backscattering from “ideal” diamond and zincblende type semiconductors include [10–12]:

- (001) surface orientation - LO mode is allowed, TO mode forbidden.
- (110) surface orientation - LO mode forbidden, TO mode allowed.
- (111) surface orientation - LO and TO modes are allowed.

The Raman intensity ratios of the first-order LO and TO phonon mode lines in GaAs takes its origin through two different electron-phonon interactions. The first one is purely of vibrational nature and corresponds to the perturbation of the optical polarizability due to the atomic displacement deformation potential [1]. The second type takes its origin in the interaction of the electrons of the medium with the ‘local’ electric field induced by a polar longitudinal vibration [1]. This constitutes the electro-optic interaction which participates additively to the former channel to the LO intensity.

The frequencies of the LO and TO phonons are both sensitive to strain. Like silicon, a positive frequency shift relates to compressive strain and a negative shift to tensile strain. In GaAs in the backscattering geometry (with the incident and scattered photons along the [001]-direction), only the LO phonons are active. However, with the broadening of the peaks and the activation of the TO phonon mode for this geometry, this is indicative of structural disorder and defects in the GaAs lattice [11]. By observing the intensity of the TO phonon, the degree of disorder and

defects in the GaAs material can be determined since as the level of defects increase, the TO mode intensity increases.

The reported absorption coefficient ( $\alpha$ ) for GaAs at the 514.5 nm argon laser line is  $9E4 \text{ cm}^{-1}$  [5]. Therefore, for the 514.5, 488.0 and 457.9 nm lines of an argon ion laser, operating in the backscattering geometry, the penetration depths associated for these lines in crystalline GaAs are 50, 40, and 25 nm, respectively.

When performing  $\mu$ Raman spectroscopy measurements on a (001) surface, I expect to detect only the LO phonon line near  $292 \text{ cm}^{-1}$  on unstrained GaAs. By assuming a biaxial stress symmetry, the LO phonon line shift ( $\Delta\omega_{LO}$ ) is give by [6]

$$\Delta\omega_{LO} \text{ (cm}^{-1}\text{)} = -3.9\sigma \text{ (GPa)} \quad (8.1)$$

where  $\sigma$  is the stress calculated from the frequency shift of the LO phonon. When selective oxidation is performed, the AlAs or AlGaAs sacrificial layers are converted to AlOx and AlGaOx. During the oxidation, shrinkage is expected. From previous direct measurements performed on GaAs using transmission electron microscopy, a thickness contraction of 10%-20% was observed. Stress induced by lateral oxidation manifests itself as a mechanical instability of the multilayers for oxidized thicknesses of more than 300 nm. GaAs/AlAs multilayers were also shown to be mechanically unstable under thermal processing. Landesman et al. measured a  $0.4 \pm 0.05 \text{ cm}^{-1}$  frequency shift following oxidation which correlates to approximately 100 MPa of tensile deformation induced in the GaAs layer [6].

Several researchers have tried thermal annealing to restore the structurally disordered GaAs lattice at the surface [9–12]. They all obtained similar results with an emerging mode line at  $258 \text{ cm}^{-1}$  which is characteristic of the phonon from crystalline arsenium near the surface of GaAs. Both the LO and TO intensities decrease following the anneal. These results reveal that the annealing produces the migration of the As to the vicinity of the surface, where it crystallizes within the

GaAs matrix. This is common in III-V semiconductors and can be avoided if the annealing is performed under an overpressure of As [9, 11].

### 8.3 III-V MEMS Fabrication

A 2-inch GaAs wafer was received from the University of New Mexico (UNM-1186) [14] with the following layers grown on a (100) surface orientated wafer. The first layer grown is a 100 nm-thick n-doped GaAs buffer layer with a dopant concentration of  $2 \times 10^{18} \text{ cm}^{-3}$ . This is followed by a  $2 \mu\text{m}$ -thick layer of undoped AlAs which is used as the sacrificial layer. The final layer grown on the wafer is a  $2 \mu\text{m}$ -thick p-doped (carbon dopant at a concentration of  $3 \times 10^{18} \text{ cm}^{-3}$ ) GaAs structural layer.

Half of the wafer is patterned and mesas are etched using reactive ion etched (RIE) as outlined in the fabrication procedures provided in Appendix A. A selective water vapor oxidation was performed at a pressure of 5 Torr and  $395^\circ\text{C}$  for 31-min with  $\text{N}_2$  as the carrier gas passing through the  $\text{H}_2\text{O}$  bubbler. Following the oxidation, the MEMS structures are released using a KOH etchant as outlined in Appendix A. However, a residual film remains following the RIE and photoresist removal. This film prevents me from performing  $\mu\text{Raman}$  stress scans on the MEMS structures as the 514.5 nm wavelength does not penetrate through the film. Figure 8.1 shows an example test die with the film partially removed following an HF release.

Due to the residual film, I performed a mesa etch into the substrate on the second half of the wafer through a 1:1:10 volume ratio of sulfuric acid, hydrogen peroxide, and DIW. This etchant provides an etch rate of approximately  $1.14 \mu\text{m}/\text{min}$ . Following the etch, I removed the photoresist and dip the wafer in a diluted HF etchant (for 5-min) with a volume ratio of 1:3:6 (HF:isopropanol:DIW). The complete fabrication procedures are available in Appendix A.

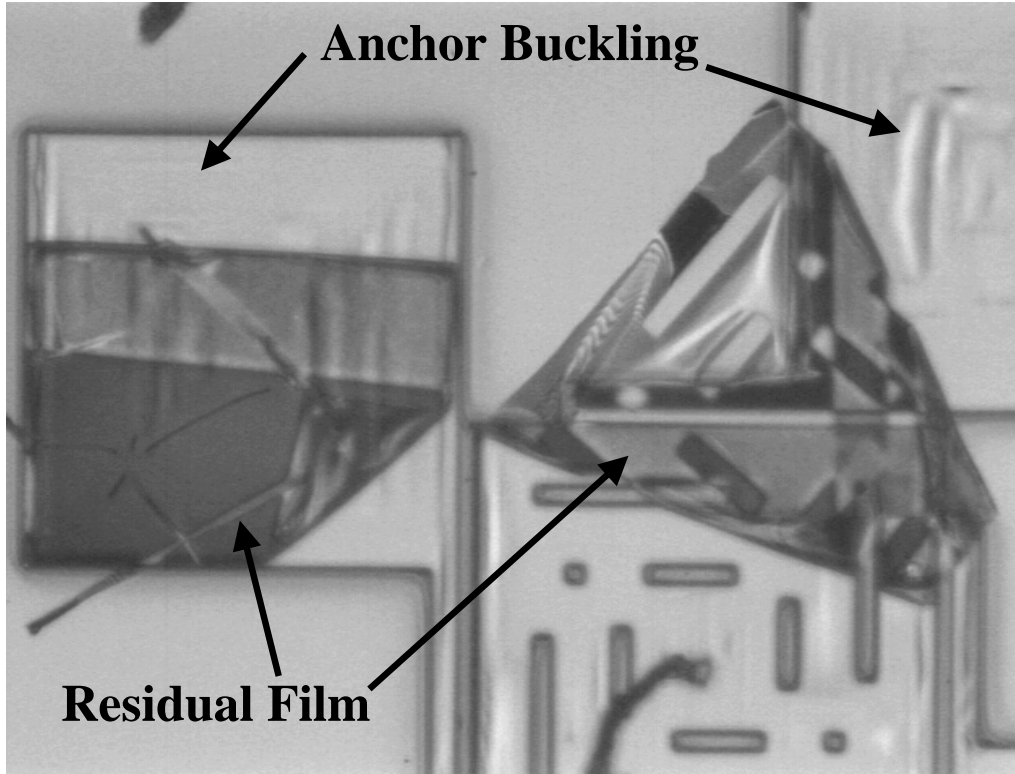


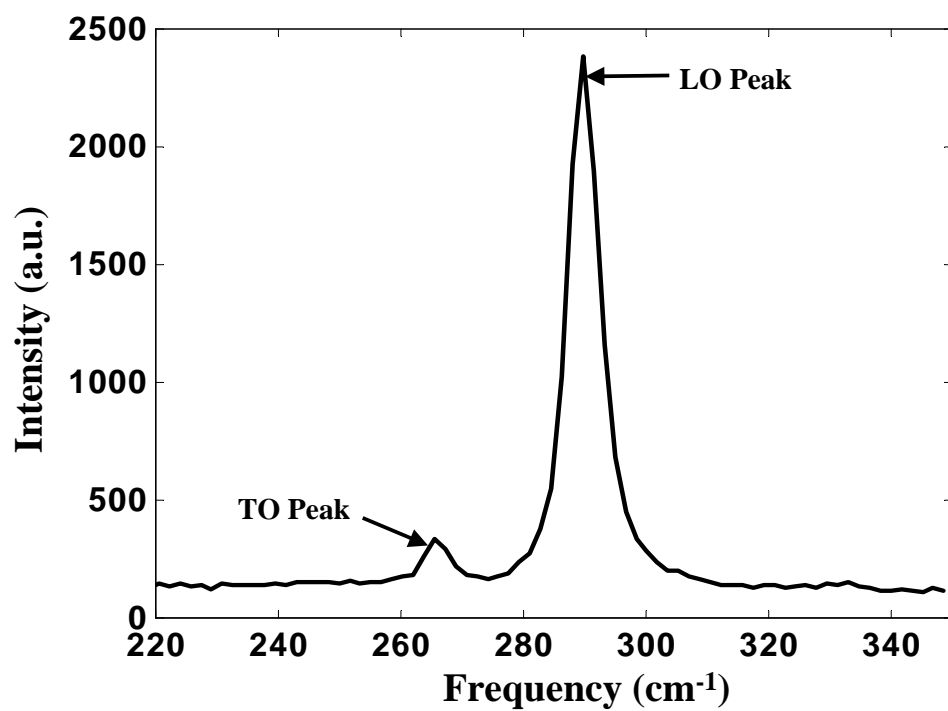
Figure 8.1: Residual film on the GaAs structural layer following the RIE etch

#### 8.4 Raman Residual Stress Characterization

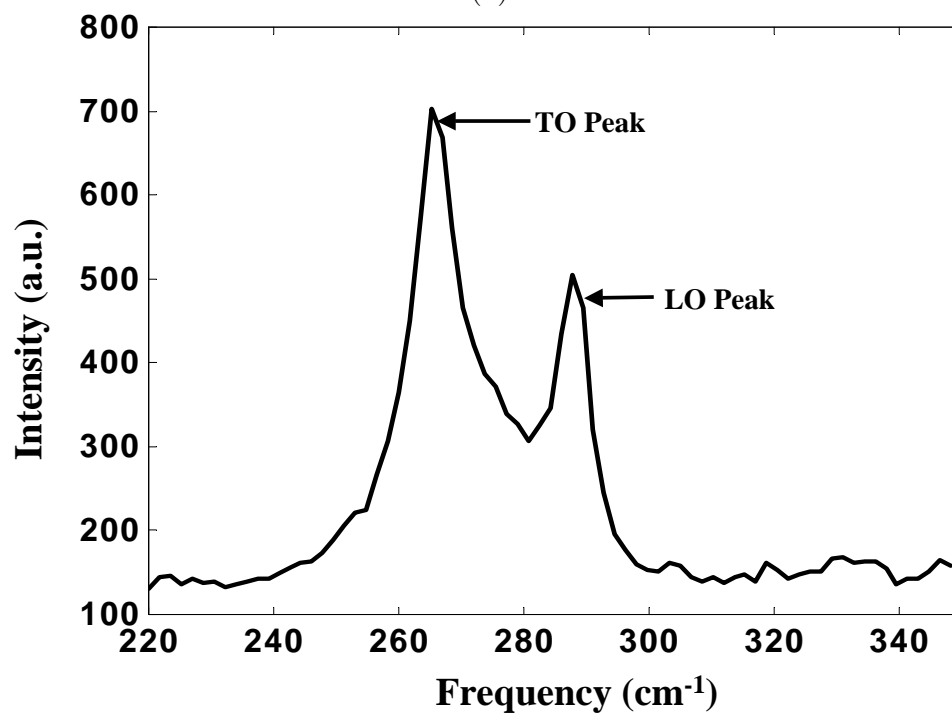
I performed the initial calibration on the  $\mu$ Raman system at AFRL/ML for GaAs by initially capturing the  $\mu$ Raman spectrum from a bulk GaAs wafer to determine the spectral intensities and peak locations of the LO and TO optical phonon modes. Prior to my  $\mu$ Raman experimentation on the GaAs samples, I calibrated the  $\mu$ Raman system to detect the laser line at  $0 \text{ Rcm}^{-1}$ . I again used the laser line as a reference point during my experimentation. I used the 50X microscope objective, an on-time of 25-seconds, and an extended scan from  $-100 \text{ Rcm}^{-1}$  to  $350 \text{ Rcm}^{-1}$  to capture the proper spectra (i.e. spectra contains the laser line, TO and LO peaks). Following the calibration, I performed a spectral scan on a highly polished (100) surface orientation sample of GaAs. I then took a  $\mu$ Raman spectrum of the GaAs substrate used for my fabricated MEMS structures. Figure 8.2 shows the two spectra collected for the GaAs samples. Since there is a slight mismatch ( $<1\%$ ) in

lattice constant between GaAs and AlAs, I expect a slight increase in the TO peak but the LO peak should remain dominant.

From Figure 8.2, the two spectrums are significantly different. For a highly polished GaAs sample, the spectrum should resemble the image in Figure 8.2a) where the LO phonon peak is dominant and the TO phonon peak is near the noise floor. The  $\mu$ Raman spectrum shown in Figure 8.2b) with the TO peak intensity higher than the LO phonon peak resembles a (110) surface orientation. I used x-ray diffraction to verify the UNM-1186 is a (100) surface orientation sample of GaAs. For the obtained spectrum with the TO phonon peak larger than the LO phonon peak for this surface orientation, this spectrum indicates a high defect sample with significant stress. The peak intensity locations for the highly polished sample are  $291.34 \text{ } Rcm^{-1}$  for the LO phonon peak and  $268.3 \text{ } Rcm^{-1}$  for the TO phonon peak. For the substrate used for my MEMS fabrication, the LO peak is positioned at  $289.81 \text{ } Rcm^{-1}$  and the TO peak is at  $266.79 \text{ } Rcm^{-1}$ . Using Equation 8.1, I obtain a stress value for the highly polished sample of -169.2 MPa and for the substrate to be approximately -561 MPa. The  $\mu$ Raman spectrum for the GaAs structural layer is approximately the same as the substrate value. A portion of the GaAs buckling beam array used to determine the localized residual stress is shown in Figure 8.3. This array was RIE etched, oxidized and then released.



(a)



(b)

Figure 8.2:  $\mu$ Raman spectrums for a (100) GaAs substrate. a) electronic grade GaAs wafer, b) UNM-1186 substrate

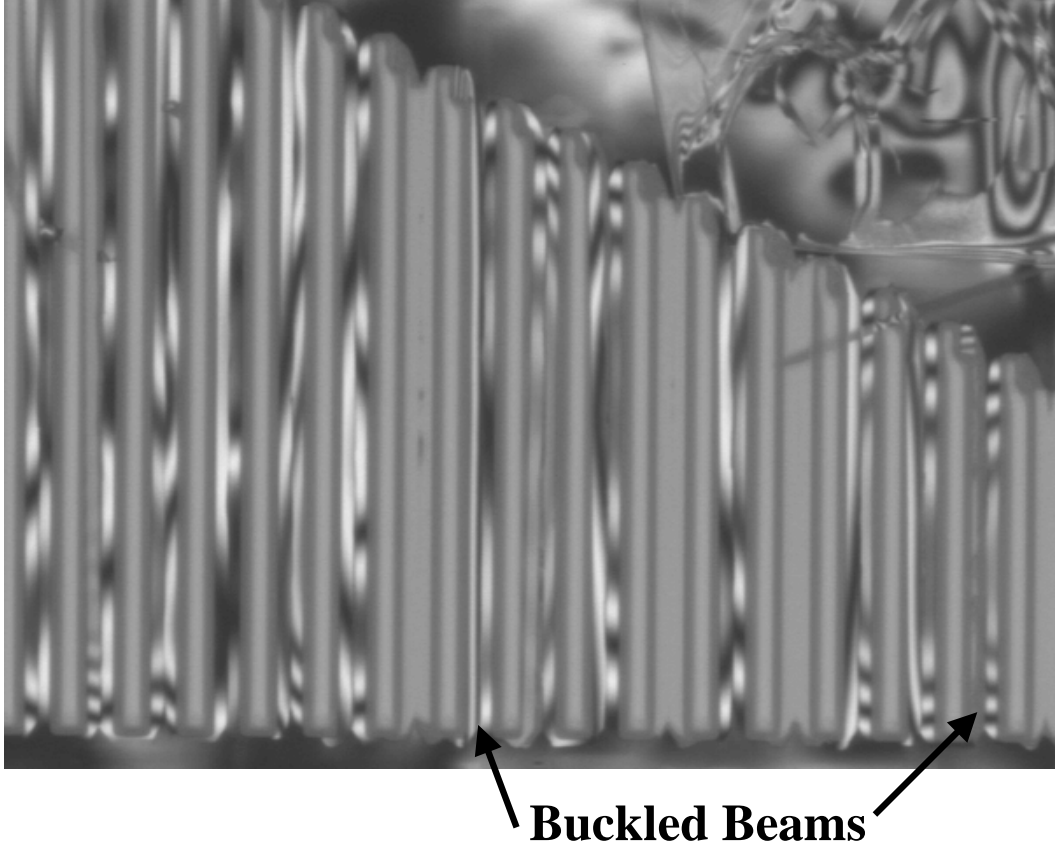


Figure 8.3: IFM image of a GaAs buckled beam array

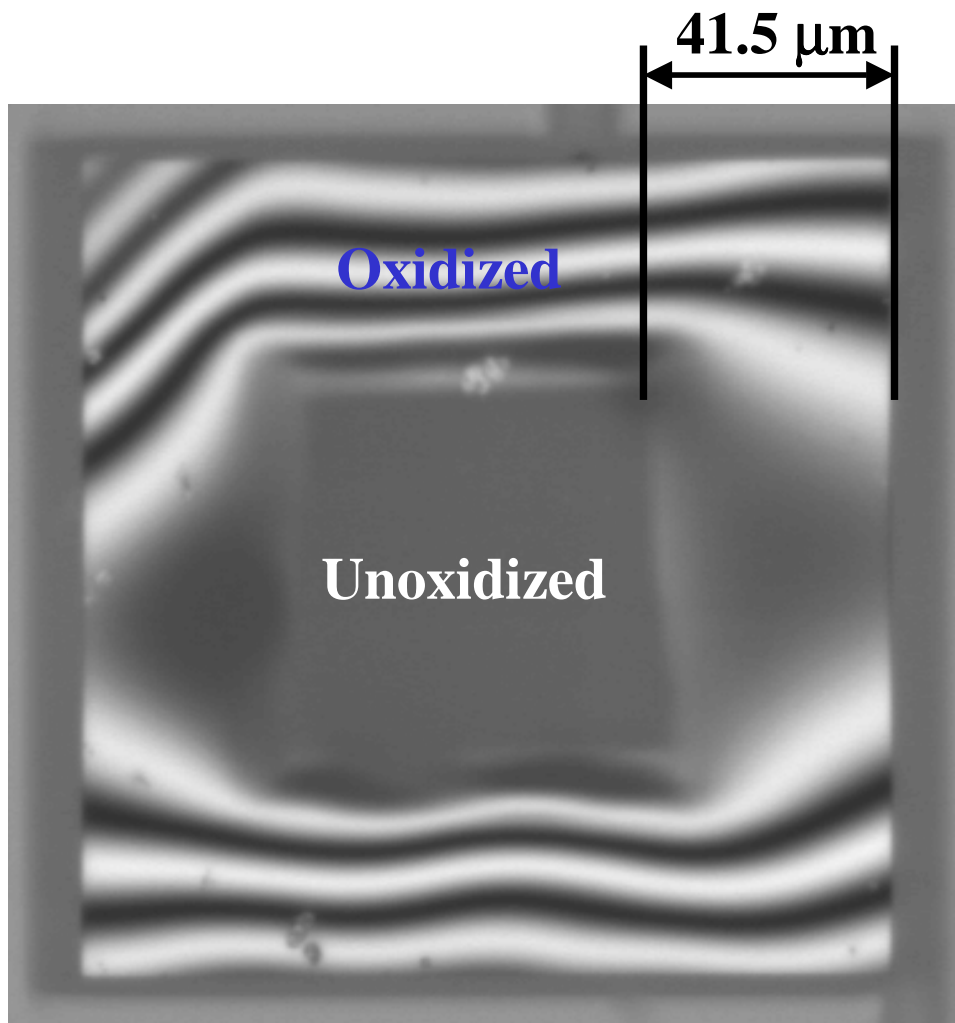
From Figure 8.3, all critical buckling beams are buckled. From the buckling beam equation (Equation 4.8), I used a Young's modulus value ( $E$ ) of 121 GPa for GaAs [4, 8], the buckling length ( $L$ ) as shown in Figure 8.3 is  $110\ \mu\text{m}$ . Using these values, I calculate the localized residual stress in the GaAs layer to be -133.4 MPa. The stress is likely to be higher in the GaAs layer, however I cannot verify this through the critical buckling test structure I fabricated on the MEMS wafer.

*8.4.1 Oxidation of MEMS Structures.* Since the sacrificial layer on my wafer is a  $2\ \mu\text{m}$ -thick AlAs layer, I performed an oxidation and then a release on the III-V GaAs fabricated MEMS structures. This oxidation results in the AlAs layer being converted to an AlO layer which can then be removed through a KOH etch. Figure 8.4 shows a  $150\ \mu\text{m}$  on a side square micromirror anchor which has been

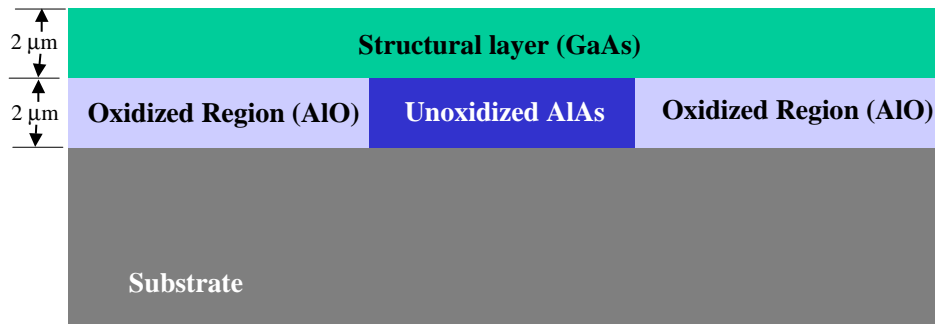
selectively oxidized for 31-min at 395 °C. As shown in Figure 8.4, the oxidation is fairly uniform from all sides and reached approximately 41.5  $\mu m$  into the anchor. Thus, the rate of oxidation for this experiment is approximately 1.34  $\mu m/min$ .

Figure 8.5 shows an IFM measurement of the identical micromirror anchor illustrated in Figure 8.4. From the IFM measurement, I measure the level of shrinkage (conversion of the AlAs layer to an AlO layer) in the sacrificial layer to be approximately 0.21  $\mu m$ .

As illustrated in Figure 8.6, many of the MEMS devices, accompanying anchors, and bonding pads are physically fractured due to the shrinkage and high levels of residual stress resulting from the oxidation. Thus, I conclude the oxidation of a 2  $\mu m$ -thick AlAs sacrificial layer is not a viable method to release my fabricated MEMS structures.



(a)



(b)

Figure 8.4: IFM image of an oxidized GaAs micromirror anchor, and (b) Illustrates the oxidation characteristics of the bonding pad.

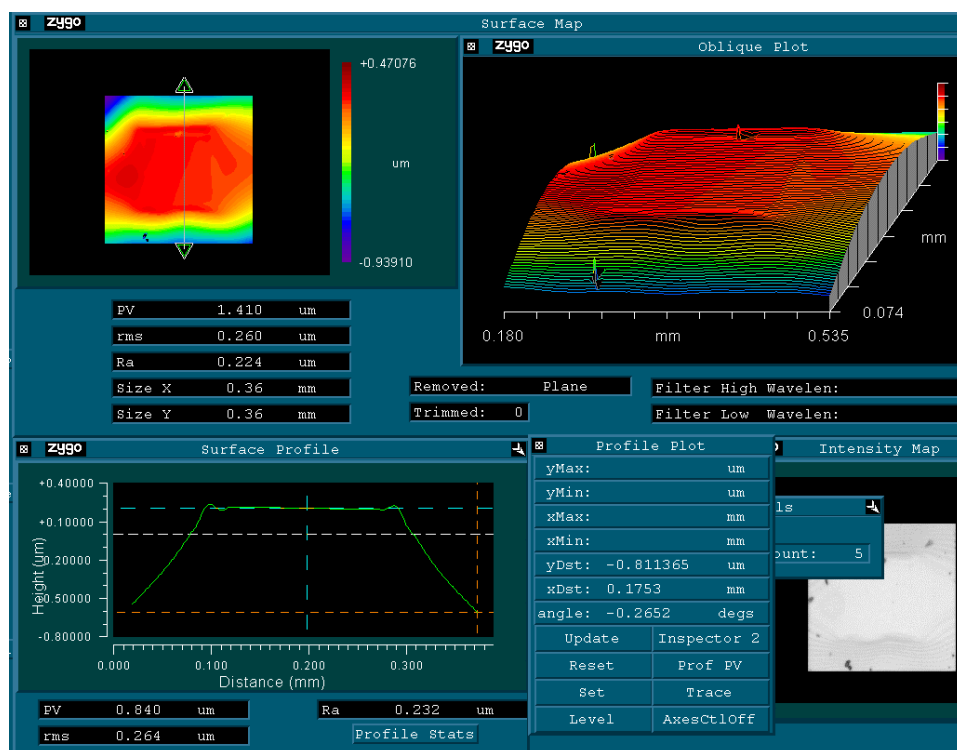
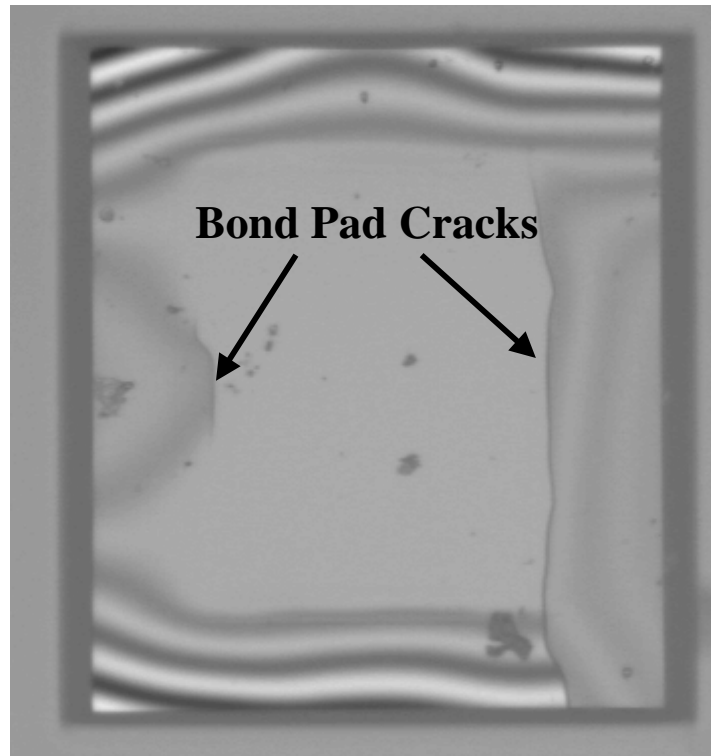
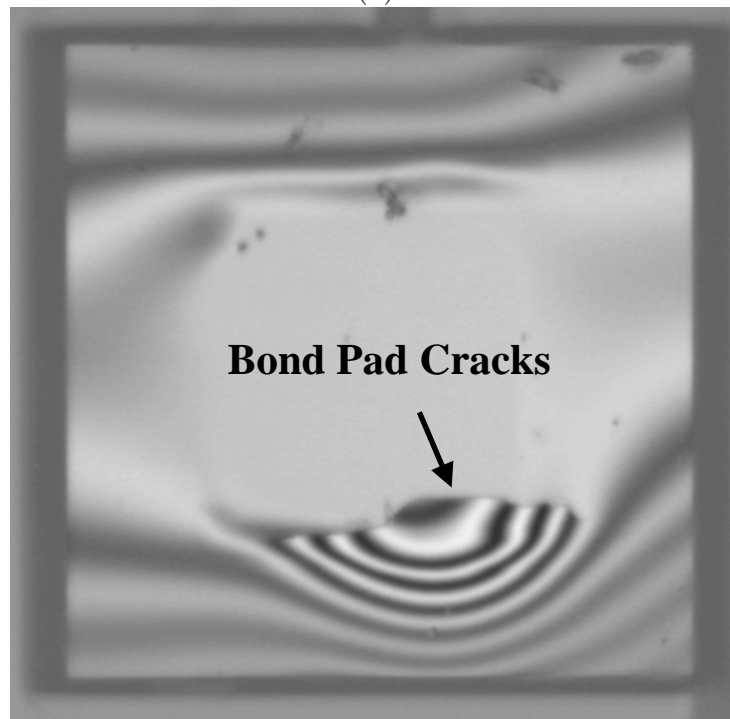


Figure 8.5: IFM 3D image of the oxidized GaAs micromirror anchor.



(a)



(b)

Figure 8.6: IFM images of bonding and micromirror cracks due to oxidation.  
a)  $150\ \mu\text{m}$ -square anchor pad, b)  $200\ \mu\text{m}$  by  $150\ \mu\text{m}$  bonding pad

I performed  $\mu$ Raman stress measurements on several fixed-fixed beams to verify the high levels of stress that exist in the MEMS structures. Figure 8.7 shows the  $\mu$ Raman stress profiles for a 400  $\mu\text{m}$ -long by 16  $\mu\text{m}$ -wide fixed-fixed beam. I was unable to perform  $\mu$ Raman scans on many of the MEMS structures due to a residual film which remained on the structural layer surfaces following the photoresist removal.

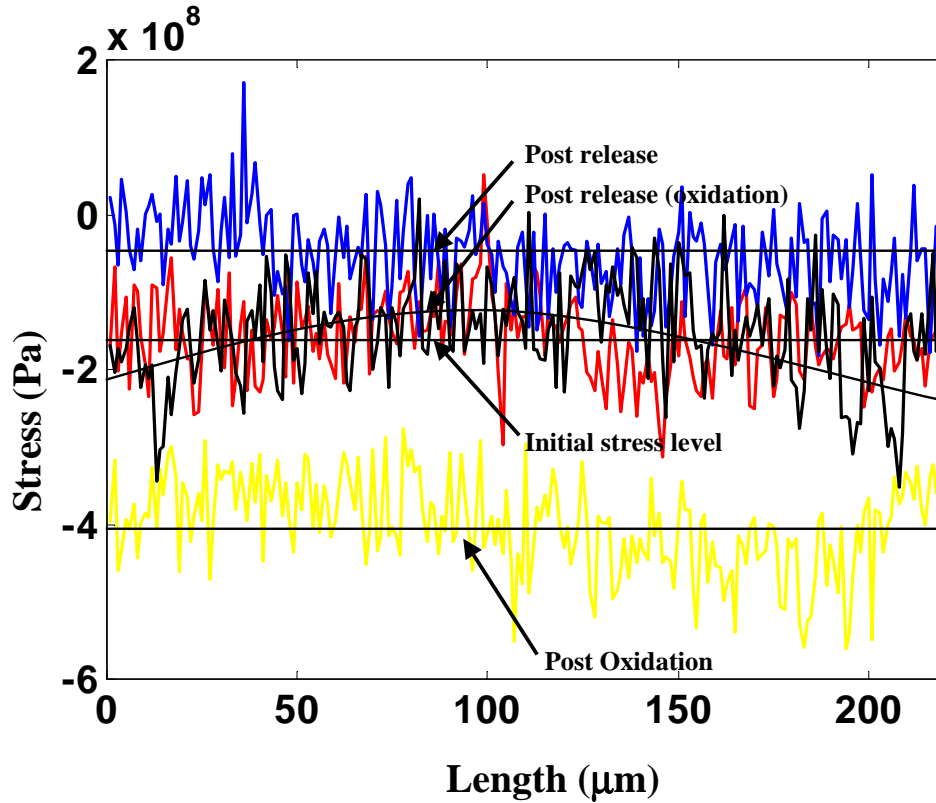


Figure 8.7:  $\mu$ Raman residual stress images of GaAs 400  $\mu\text{m}$ -long by 16  $\mu\text{m}$ -wide fixed-fixed beam.

As shown in Figure 8.7, the  $\mu$ Raman stress profiles indicate a significant level of stress in the GaAs structural layer following the oxidation. From Figure 8.7, the initial stress level in the structure is indicated by the red stress profile, post oxidation is shown in yellow, post oxidation release is shown in black, and the standard post release with HF is shown in blue. The post-released beam structure exhibits stress levels of approximately -400 MPa and post-oxidation release stress levels of approx-

imately -200 MPa respectively. The initial stress level of the GaAs structural layer is averaged to be approximately -170 MPa. Once the beam structure is released, the stress level reduces to about an average of -50 MPa. Since thermal oxidations result in significant residual stress increase in the MEMS structural layer for both the polysilicon and GaAs structural materials. Without performing post-processing on the oxidized structures, the released oxidized structure should have a significantly higher stress level in the post released beam structure when compared to the unoxidized released beam. The  $\mu$ Raman stress profiles verify this condition ( -50 MPa for unoxidized to -170 MPa in oxidized) in the measured beam structure.

The  $\mu$ Raman stress profiles for the released beams does not resemble the polysilicon stress curves. Some possible reasons for for this stress profile could include: 1) since the GaAs has a significant level of residual stress, many of the MEMS structures experience some degree of deformation due to the high levels of stress. If the structures are not normal to the laser beam, it will result in a variation in the LO and TO phonon modes. This could potentially alter the residual stress profile. 2) since the laser line cannot be used as a reference, I have no indication the spectrometer and/or laser are not drifting. From my experience with polysilicon, the laser line does drift over time. With an on-time of 25-sec for each  $\mu$ Raman spectrum, the total time to perform a line scan can range from 1-hour to several hours. Therefore, spectrometer/laser drift is a real possibility for these stress measurements.

*8.4.2 Optical Characterization of Fabricated Micromirrors.* From the residual stress measurements I performed in the previous section following an oxidation of the sacrificial layer and release, the feasibility of fabricating an optically flat micromirror from this technique is not promising. As shown in Figure 8.8, the micromirror surfaces are not optically flat. Therefore, a better technique would be to release the structures without performing an oxidation (i.e. a wet release followed by a supercritical dry). A wet release can eliminate the high stress levels due to

oxidation. This is shown in the  $\mu$ Raman stress profiles for the 400  $\mu m$ -long beams in Figure 8.7.

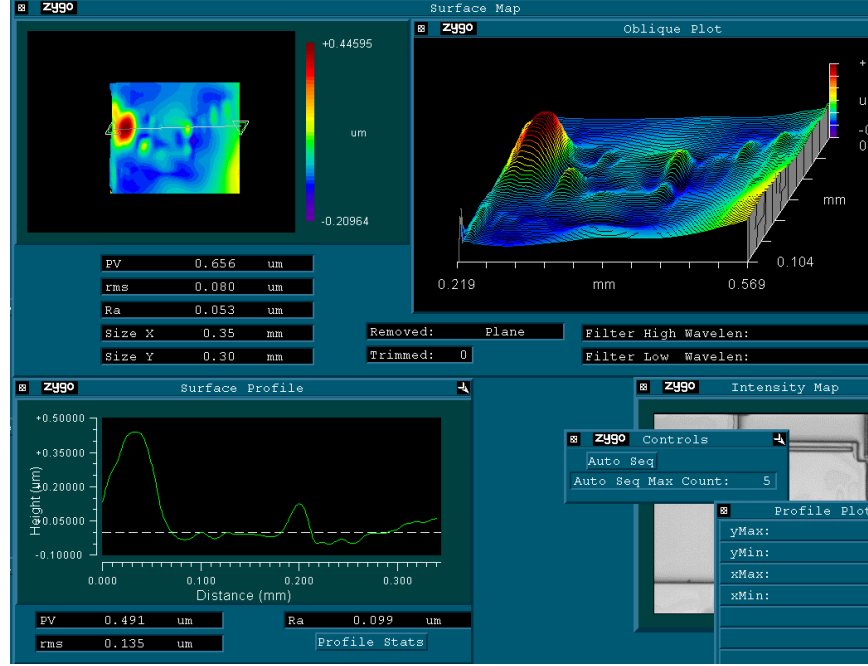


Figure 8.8: IFM 3D image of the surface of an oxidized GaAs micromirror

### 8.5 Summary of Chapter VIII

In this chapter, I presented the first ever residual stress assessment in GaAs MEMS structures through the use of  $\mu$ Raman spectroscopy. I presented two different means to mesa etch the structural layer to permit MEMS device release through diluted HF or oxidation with KOH as the etchant release. Through IFM measurements and  $\mu$ Raman spectroscopy stress profiles, I find the selective oxidation of a 2  $\mu m$ -thick AlAs release layer induces over -200 MPa of stress into the GaAs structural layer. In many instances, this stress level was high enough to physically crack the GaAs structural layer. A wet release of the fabricated MEMS structures without an oxidation provides the lowest stress levels in the released structures and is the recommended technique to release these MEMS structures. I conclude that oxidation is not a viable technique for the fabrication of MEMS with a thick (2  $\mu m$ ) AlAs

sacrificial layer. With a thinner  $\text{Al}(x)\text{Ga}(1-x)\text{As}$  sacrificial layer ( $0.9 \leq x \leq 0.98$ ) which is oxidized to form  $\text{Al}_x\text{Ga}_{1-x}\text{O}_y$ , the level of induced stress should be decreased and these layers deserve further investigation. From the  $\mu\text{Raman}$  stress profiles obtained from the GaAs 400  $\mu\text{m}$ -long beams, residual stress characterization in GaAs is possible and can provide invaluable information on the stress levels induced to the MEMS structures during and after release.  $\mu\text{Raman}$  spectroscopy can be used to optimize the release procedures to reduce or prevent inducing residual stress into the structures. Further  $\mu\text{Raman}$  characterization is necessary to verify the stress profiles are accurate for beams and other MEMS structures (cantilevers, micromirror flexures, etc).

## Bibliography

1. J. Biellmann, B. Prevot, and C. Schwab. First-order raman line intensity ratio in GaAs: A potential lattice perfection scale. *Journal of Physics C: Solid State Physics*, 16:1135–1142, 1983.
2. M. Cardona. Raman spectroscopy applied to the characterization of semiconductors and semiconductor microstructures. *SPIE Raman and Luminescence Spectroscopy in Technology*, 822:2–15, 1987.
3. L. Chu, A. Zrenner, M. Bichler, G. Böhm, and G. Abstreiter. Raman spectroscopy of In(Ga)As/GaAs quantum dots. *Applied Physics Letters*, 77(24):3944–3946, December 2000.
4. K. J. Hjort, F. Ericson, J. A. Schweitz, C. Hallin, and E. Janzen. Hardness, internal stress and fracture toughness of epitaxial AlGaAs films. *Thin Solid Films*, 250:157–163, 1994.
5. M. Ichimura, Y. Moriguchi, A. Usami, M. Tabuchi, and A. Sasaki. Characterization of GaAs heterolayers by micro-Raman spectroscopy. *Journal of Crystal Growth*, 149:167–174, 1995.
6. J. P. Landesman, A. Fiore, J. Nagle, V. Berger, E. Rosencher, and P. Puech. Local stress measurements in laterally oxidized GaAs/ $Al_xGa_{1-x}As$  heterostructures by micro-Raman spectroscopy. *Applied Physics Letters*, 71(11):2520–2522, October 1997.
7. J. L. Leclercq, R. P. Ribas, J. M. Karam, and P. Viktorovitch. Iii-V micromachined devices for microsystems. *Microelectronics Journal*, 29:613–619, 1998.
8. M. Y. Li. *Wavelength tunable micromechanical vertical cavity surface emitting lasers*. Phd dissertation, University of California, Berkeley, March 1999.
9. N. T. McDevitt and J. S. Solomon. Thermal oxide layers on GaAs studied by Raman and Auger spectroscopy. *Journal of Electrochemical Society*, 133(9):1913–1917, September 1986.
10. P. S. Pizani and C. E. M. Campos. Raman probing of thermal damage depth profile in annealed GaAs. *Journal of Applied Physics*, 84(12):6588–6591, December 1998.
11. P. S. Pizani, Jr. F. Lanciotti, R. G. Jasinevicius, J. G. Duduch, and A. J. V. Porto. Raman characterization of structural disorder and residual strains in micromachined GaAs. *Journal of Applied Physics*, 87(3):1280–1283, February 2000.

12. F. H. Pollak and R. Tsu. Raman characterization of semiconductors revisited. *SPIE Spectroscopic Characterization Techniques for Semiconductor Technology*, 452:26–43, 1983.
13. S. Saravanan, M. Adachi, N. Satoh, T. Soga, T. Jimbo, and M. Umeno. Stress reduction and structural quality improvement due to In doping in GaAs/si. *Materials Science and Engineering*, B68:166–170, 2000.
14. Andreas Stintz. PhD, January 2001. University of New Mexico.

## *IX. Conclusions, Contributions, and Future Work*

### *9.1 Contributions and Significance*

My primary contribution is that I demonstrated the successful use of  $\mu$ Raman spectroscopy technique as a viable means to measure and monitor the residual stress in MEMS devices. I used  $\mu$ Raman spectroscopy to monitor the residual stress following several different post-processing techniques. I showed that the stress profiles obtained from the  $\mu$ Raman spectroscopy system are valid representations of the stress profiles for released MEMS structures by comparing the measured results to microfabricated stress measurement structures. Several  $\mu$ Raman stress maps were generated to assess the stress distribution within select MEMS devices. These stress maps were verified through FEM modeling in the x- and y- directions to be reasonable. Both techniques illustrate the primary component of stress is down the length of the beam and nearly constant across the beam. I proved for the first time that through phosphorous implantation and annealing, the inherent residual stress in MEMS polysilicon structures can be reduced or altered. More importantly, through the use of  $\mu$ Raman spectroscopy, the residual stress of unreleased MEMS structures can be monitored. This monitoring tool coupled with the processes to adjust residual stress values can be exploited to vastly improve the yield, reliability, and functionality of MEMS devices.

### *9.2 Accomplishments*

I demonstrated the utility of  $\mu$ Raman spectroscopy for measuring residual and induced stresses in MEMS devices. Current stress measurements are limited to visual inspections of beam shaped devices (i.e., cantilevers, mirror flexures, and fixed-fixed beams). The devices have high aspect ratios so that the assumption of hydrostatic, uniaxial, or biaxial stress is reasonable. The FEM computer simulation tools are used to verify and assess the  $\mu$ Raman stress profiles to determine their validity. The

FEM models also provide valuable information to the MEMS designers for obtaining and measuring the actuation voltage requirements, stress fields, and displacement characteristics for their particular MEMS designs. I provided a simple thermal actuator model to demonstrate the functionality and modeling capabilities which can be used to assess MEMS devices prior to device fabrication. FEM modeling can also assist in determining the proper functionality and stress levels necessary for correct MEMS device operation. The combination of these modeling schemes should result in enhanced device performance and yield.

I performed several post-processing techniques (phosphorous diffusion and implant dopings and/or anneals) to assess the viability of  $\mu$ Raman spectroscopy as a monitoring technique. I proved for the first time that  $\mu$ Raman spectroscopy provides relative residual stress levels for the unreleased MEMS structures. Through the incorporation of post-processing techniques, the MEMS designer now has the ability to obtain the desired stress levels for a particular application. I compared the  $\mu$ Raman stress profiles to localized released stress levels I obtained from buckling beam arrays and cantilever deflections. Based on these comparisons, I conclude that stress data obtained with  $\mu$ Raman spectroscopy correlates very well to visual data obtained from released test structures.

Based on my stress measurement techniques, I created a prediction model relating the unreleased residual stress values obtained via  $\mu$ Raman spectroscopy to those obtained from released MEMS test structures. This model places the measured and calculated stress data points in three defined regions which designate the oxidation, low dose implants and anneals, and high dose implants. This simplified model provides insight into the localized residual stress levels prior to HF release. Based on the three defined regions, the high dose implants result in an increase in the stress. This is contradictory to what I set out to do to reduce stress. I removed this region and remodeled the stress values to obtain a more realistic model. This model is enhanced through the usage of an analytical model relating the Raman stress equations

to the critical buckling length equation. This model provides a direct relation of the frequency shift of the Raman spectra to the associated buckling length. The corresponding buckling length can be assessed to determine the localized residual stress level. Through this model, the MEMS designer can obtain the approximate residual stress levels remaining in MEMS devices prior to release. At this point, the MEMS designer can either release the structures or perform post-processing techniques (anneals and/or dopings) to further reduce the residual stress. I proved that  $\mu$ Raman spectroscopy gives the designer a means to qualitatively measure the residual stress in the unreleased structures. I analytically modeled the fixed-fixed beam and cantilever test structures to verify the residual stress profiles obtained from  $\mu$ Raman spectroscopy along the structures length were indeed stress values.

In addition, I solved for the phonon deformation potential constants for the MUMPs<sup>®</sup> polysilicon material layers. These material constants are necessary to accurately determine the magnitude of residual stress in the structures.

Finally, I applied the  $\mu$ Raman spectroscopy technique to III-V MEMS. This is the first documented attempt to use  $\mu$ Raman spectroscopy on GaAs MEMS. I fabricated and tested the viability of using  $\mu$ Raman spectroscopy to measure and monitor the residual stress levels in GaAs MEMS test structures. From the initial stress results I obtained from my fabricated GaAs MEMS,  $\mu$ Raman spectroscopy provides excellent stress detection capabilities and can provide invaluable stress information during the fabrication of MEMS for optical tuning applications.

### *9.3 Recommendations for Future Research*

Since  $\mu$ Raman spectroscopy is a new technique to measure the residual stress in materials, there are many new and exciting areas of research that could be performed in the future. Some of the possible upgrades and additional usages of  $\mu$ Raman spectroscopy include the following:

- To increase the accuracy and resolution of the prediction model, both Raman spectroscopy systems needs to be upgraded to include implementation of Fabry-Perot etalon filters and a finer resolution spectrometer. These upgrades would allow measurement of sub-MPa stress levels and should substantially improve the correlation of released to unreleased device stress. This upgrade in the  $\mu$ Raman spectroscopy system would provide a viable technique to measure, and monitor the deposition of materials in an *in situ* environment.
- In an attempt to predict the residual stress levels more accurately, the use of statistics software could be used to refine the experimental tests performed to increase stress control. The statistics program could help reduce the level of error in the experiments and identify which post-processing components (i.e. dopant concentration, anneal time, implant power, etc.) has the greatest impact on the residual stress in the MEMS structures. This program could also potentially assist in the prediction model to help determine the stress values for select experiments.
- The reduced stress devices require further assessment to verify that stress reduction does not interfere with the overall operations and functionality of the devices.
- Long term tests are necessary to determine reliability and degradation issues with reduced stress devices.
- With the significant interest in III-V MEMS for optical tuning, a thorough  $\mu$ Raman study could be performed to assess the viability of these materials. Further  $\mu$ Raman characterization of GaAs is necessary to assess the various release techniques to determine stress relationships and which release technique provides the lowest levels of induced stress. In addition, perform post-processing anneals and doping on III-V materials to assess stress reduction possibilities.

- Perform stress characterization on the MUSiC SiC structures currently being fabricated through both  $\mu$ Raman spectroscopy and on-chip test structures (buckling beams and comb resonators).
- Perform stress assessments on other MEMS structures in addition to classic beam type structures.
- Use  $\mu$ Raman spectroscopy as an *in situ* stress monitoring and control technique during material depositions to assess residual stress levels.

#### 9.4 Author's Publications

- L.A. Starman Jr., Stress Measurement in MEMS Devices, AVS 47th International Symposium on Thin films in MEMS/MOEMS, Oral Presentation, October 2000.
- J. Busbee, L. Starman, M. Amer, J. Reber, W. Cowan, and J. Maguire, "Utilizing Raman spectroscopy for stress imaging in MEMS devices," IFAC symposium AIRTC, Budapest, Hungary, October 2000, Submitted to Journal of Process Control.
- J.A. Lott, M.J. Noble, E.M. Ochoa, L.A. Starman, and W.D. Cowan, "Tunable red vertical cavity surface emitting lasers using flexible Micro-Electro-Mechanical top mirrors," 2000 IEEE/LEOS International Conference on Optical MEMS, Kauai, HI, USA, August 2000.
- L. Starman Jr., J. Busbee, J. Reber, J. Lott, W. Cowan, and N. Vandelli, "Stress measurement in MEMS Devices," 4<sup>th</sup> International Conference on Modeling and Simulation of Microsystems, Hilton Head, SC., 398-401, March 2001.
- L.A. Starman Jr., J.A. Lott, M.S. Amer, W.D. Cowan, and J.D. Busbee, "Stress reduction characterization using Raman spectroscopy measurements on MEMS devices," International Conference on Optical MEMS and Their Applications, Busena Terrace, Okinawa, Japan, September 2001.

- L.A. Starman Jr., E.M. Ochoa, J.A. Lott, M.S. Amer, W.D. Cowan, and J.D. Busbee, “Residual stress characterization in MEMS microbridges using micro-Raman spectroscopy,” 5<sup>th</sup> International Conference on Modeling and Simulation of Microsystems, San Juan, Puerto Rico, USA, April 2002.
- E.M. Ochoa, L.A. Starman Jr., W.D. Cowan, T.R. Nelson Jr., O. Blum Spahn, and J.A. Lott, “Polysilicon prototypes for flip-bonded hybrid MEM-tunable filters and VCSELs,” 5<sup>th</sup> International Conference on Modeling and Simulation of Microsystems, San Juan, Puerto Rico, USA, April 2002.
- L.A. Starman Jr., J.A. Lott, M.S. Amer, W.D. Cowan, and J.D. Busbee, “Stress characterization of MEMS microbridges by micro-Raman spectroscopy,” submitted to Sensors and Actuators A in January 2002. Currently in review.

## *Appendix A.*

In this appendix, I describe several etching and fabrication procedures for MEMS devices including: a MUMPs<sup>®</sup> polysilicon release with and without  $CO_2$  drying; AlGaAs MEMS fabrication and release; and the etching procedure for preparation of the furnace annealing tube.

### *A.1 MEMS Release Procedure*

To release the MUMPs<sup>®</sup> test chips, I used the initial release procedure outlined by Cowan. Following the initial die release, some steps required minor changes to fully release the MEMS structures. The release procedure outlined below was adhered to for test die from MUMPs<sup>®</sup> runs #21 and #38.

MUMPs<sup>®</sup> polysilicon release etch procedure using hotplate to dry:

- 6.5-minutes in 1st acetone (bulk photoresist removal).
- 7.0-minutes in 2nd acetone (final photoresist removal).
- 5-minutes in 1st methanol (acetone removal).
- Dry die on 60 °C hot plate for 1-minute.
- Place clean chip carriers on 120 °C hot plate and allowed to warm.
- Apply small amount of CrystalBond 509 hot melt adhesive to carrier.
- Place die in chip carrier, position, and remove from heat.
- Once cool, place packaged die in 49% HF for 2.5-minutes.
- Remove from 49% HF, place in 1st methanol for 5-minutes.
- Soak packaged die in 2nd methanol for 15-minutes then dry on 100 °C hot plate for 3-minutes.

Many of the test die that I released by following the above release procedure contained a fair amount of foreign material on the structures. The MUMPs® foundry recommended an acetone rinse for a minimum of 30-minutes to completely remove the protective photoresist. The foundry personnel also recommended that I agitate the die vigorously in the initial acetone dip for the first 2-4-minutes to remove possible silicon dust from the dicing procedure which may be on the surface of the die. Following these recommendations, the debris on the die was significantly reduced.

At first, I obtained inconsistent results from the buckling beam arrays (i.e. due to stiction during the final dry). The AFIT laboratory purchased a supercritical  $CO_2$  dryer to perform the final dry. The primary benefit of the supercritical  $CO_2$  dryer is that it replaces the methanol with liquid  $CO_2$  between the released MEMS structures. The dryer then increases the temperature and pressure of the  $CO_2$  to a level slightly above the critical point for  $CO_2$ . The  $CO_2$  is converted directly from the liquid phase to the gas phase. Thus, no liquid is present between the MEMS structures to permit stiction of the MEMS structures to the substrate. I developed the following MEMS release procedure outlined below and used this procedure to release all of my remaining MUMPs® test die.

MUMPs® polysilicon release etch procedure using  $CO_2$  dryer:

- 15-minutes in 1st acetone (bulk photoresist removal, initial 2-4-minutes with vigorous agitation by hand).
- 15-minutes in 2nd acetone (final photoresist removal).
- 5-minutes in 1st methanol (acetone removal).
- Place die in 49% HF for 2.5-minutes.
- Remove from 49% HF, place in 1st methanol for 5-minutes.
- Soak die in 2nd methanol for 15-minutes.
- Remove die and place in  $CO_2$  chamber with methanol (i.e. place enough methanol in  $CO_2$  chamber to just cover the MEMS die).

- Set the purge control knob to “1” (indicates a 5-min purge cycle for the exchange of the methanol with liquid  $CO_2$ )
- Press the “COOL” button (chamber temperature cools to approximately  $-5\text{ }^{\circ}C$ , takes approximately 70-sec to cool.)
- Press the “FILL” button (chamber begins to fill with liquid  $CO_2$ . The process is automatic at this point until dry cycle is complete) (Dry cycle takes approximately 30-minutes to complete).
- Place clean chip carriers on  $120\text{ }^{\circ}C$  hot plate and allow to warm to  $120\text{ }^{\circ}C$  (approximately 10-minutes).
- Apply small amount of CrystalBond 509 hot melt adhesive to carrier.
- Remove dried and released MUMPs<sup>®</sup> die and gently place on wax in chip carrier, position, and remove from heat and let cool to room temperature.

**NOTE:** Careful handling is required when packaging the  $CO_2$  dried die since the MEMS structures are released and can easily be damaged.

#### *A.2 GaAs MEMS Fabrication and Release Procedure*

The following fabrication and release procedures were used to fabricate the GaAs MEMS devices presented in Chapter VIII

## Oxidation Etch Study

<b>11 March, 2002</b>		<b>Piece ID:</b> <b>UNM Run 1186</b>
Init.	Process	Notes
	<b>Before Entering the Clean Room</b>	
	<b>Model RIE (Reflectivity for Mesa Etch)</b>	
	<b>Metalization</b>	
	<b>1) Prepare Wafer Surface</b> Cleave wafer and use one quarter for study Spin clean wafer with acetone, methanol, isopropyl alcohol, and DIW 30 seconds each @ 500 rpm N <sub>2</sub> blow dry 2 minute hot plate bake (HPB) @ 110° C ( <i>removes accumulated H<sub>2</sub>O</i> ) Cool	
	<b>2) XP LOR 3A Coat</b> Set spinner ramp rate = 200; spin 4000 rpm Coat sample with XP LOR 3A Spin 30 seconds @ 4K rpm 2 minute HPB @ 170° C Cool	
	<b>3) 1805 Coat</b> Set photoresist spinner ramp rate = 200; spin = 4000 rpm Flood wafer with 1805 Spin 30 seconds @ 4000 rpm 1:15 minute HPB @ 110° C Cool	
	<b>4) Edge Bead Removal</b> Flood expose edge bead mask for 2 min (2mw/cm <sup>2</sup> ) Develop for 30 seconds using LDD26W developer DI rinse, N <sub>2</sub> dry	
	<b>5) Metalization Contact Mask</b> Expose mesa contact mask for 17.5 sec (2mw/cm <sup>2</sup> , 405 nm) Spin develop for 75 seconds at 1000 RPM using LDD26W developer DI rinse for 30 sec, N <sub>2</sub> dry Microscope inspect to ensure alignment Clean mask using CA40, acetone wipe and N <sub>2</sub> dry	
	<b>6) Clean to ensure no photoresist in metal contact areas</b> 1 cycle in oxygen asher (4 minutes at 200 W)	
	<b>7) Place metalization order</b> Deposit 200 Å Ti, 1330 Å Au	
	<b>8) Remove oxide immediately prior to metal deposition</b> Dip 30 seconds in BOE:DIW 1:7 Rinse 3, 30 second cycles in DIW rinse tank Thoroughly N <sub>2</sub> blow dry	
	<b>9) Metal Lift Off</b> Acetone Spray lift off (as necessary, no more than 30 sec at a time) Methanol, Isopropanol rinse, 30 seconds each N <sub>2</sub> dry	

## Oxidation Etch Study

<b>11 March, 2002</b>		<b>Piece ID:</b> <b>UNM Run 1186</b>
Init.	Process	Notes
	<b>Before Entering the Clean Room</b>	
	<b>Model RIE (Reflectivity for Mesa Etch)</b>	
	<b>Metalization</b>	
	<b>1) Prepare Wafer Surface</b> Cleave wafer and use one quarter for study Spin clean wafer with acetone, methanol, isopropyl alcohol, and DIW 30 seconds each @ 500 rpm N <sub>2</sub> blow dry 2 minute hot plate bake (HPB) @ 110° C ( <i>removes accumulated H<sub>2</sub>O</i> ) Cool	
	<b>2) XP LOR 3A Coat</b> Set spinner ramp rate = 200; spin 4000 rpm Coat sample with XP LOR 3A Spin 30 seconds @ 4K rpm 2 minute HPB @ 170° C Cool	
	<b>3) 1805 Coat</b> Set photoresist spinner ramp rate = 200; spin = 4000 rpm Flood wafer with 1805 Spin 30 seconds @ 4000 rpm 1:15 minute HPB @ 110° C Cool	
	<b>4) Edge Bead Removal</b> Flood expose edge bead mask for 2 min (2mw/cm <sup>2</sup> ) Develop for 30 seconds using LDD26W developer DI rinse, N <sub>2</sub> dry	
	<b>5) Metalization Contact Mask</b> Expose mesa contact mask for 17.5 sec (2mw/cm <sup>2</sup> , 405 nm) Spin develop for 75 seconds at 1000 RPM using LDD26W developer DI rinse for 30 sec, N <sub>2</sub> dry Microscope inspect to ensure alignment Clean mask using CA40, acetone wipe and N <sub>2</sub> dry	
	<b>6) Clean to ensure no photoresist in metal contact areas</b> 1 cycle in oxygen asher (4 minutes at 200 W)	
	<b>7) Place metalization order</b> Deposit 200 Å Ti, 1330 Å Au	
	<b>8) Remove oxide immediately prior to metal deposition</b> Dip 30 seconds in BOE:DIW 1:7 Rinse 3, 30 second cycles in DIW rinse tank Thoroughly N <sub>2</sub> blow dry	
	<b>9) Metal Lift Off</b> Acetone Spray lift off (as necessary, no more than 30 sec at a time) Methanol, Isopropanol rinse, 30 seconds each N <sub>2</sub> dry	

## Oxidation Etch Study

<b>11 March, 2002</b>		<b>Piece ID:</b> <b>UNM Run 1186</b>
Init.	Process	Notes
	<b>Before Entering the Clean Room</b>	
	<b>Model RIE (Reflectivity for Mesa Etch)</b>	
	<b>Metalization</b>	
	<b>1) Prepare Wafer Surface</b> Cleave wafer and use one quarter for study Spin clean wafer with acetone, methanol, isopropyl alcohol, and DIW 30 seconds each @ 500 rpm N <sub>2</sub> blow dry 2 minute hot plate bake (HPB) @ 110° C ( <i>removes accumulated H<sub>2</sub>O</i> ) Cool	
	<b>2) XP LOR 3A Coat</b> Set spinner ramp rate = 200; spin 4000 rpm Coat sample with XP LOR 3A Spin 30 seconds @ 4K rpm 2 minute HPB @ 170° C Cool	
	<b>3) 1805 Coat</b> Set photoresist spinner ramp rate = 200; spin = 4000 rpm Flood wafer with 1805 Spin 30 seconds @ 4000 rpm 1:15 minute HPB @ 110° C Cool	
	<b>4) Edge Bead Removal</b> Flood expose edge bead mask for 2 min (2mw/cm <sup>2</sup> ) Develop for 30 seconds using LDD26W developer DI rinse, N <sub>2</sub> dry	
	<b>5) Metalization Contact Mask</b> Expose mesa contact mask for 17.5 sec (2mw/cm <sup>2</sup> , 405 nm) Spin develop for 75 seconds at 1000 RPM using LDD26W developer DI rinse for 30 sec, N <sub>2</sub> dry Microscope inspect to ensure alignment Clean mask using CA40, acetone wipe and N <sub>2</sub> dry	
	<b>6) Clean to ensure no photoresist in metal contact areas</b> 1 cycle in oxygen asher (4 minutes at 200 W)	
	<b>7) Place metalization order</b> Deposit 200 Å Ti, 1330 Å Au	
	<b>8) Remove oxide immediately prior to metal deposition</b> Dip 30 seconds in BOE:DIW 1:7 Rinse 3, 30 second cycles in DIW rinse tank Thoroughly N <sub>2</sub> blow dry	
	<b>9) Metal Lift Off</b> Acetone Spray lift off (as necessary, no more than 30 sec at a time) Methanol, Isopropanol rinse, 30 seconds each N <sub>2</sub> dry	

## Oxidation Etch Study

<b>11 March, 2002</b>		<b>Piece ID:</b> <b>UNM Run 1186</b>
Init.	Process	Notes
	<b>Before Entering the Clean Room</b>	
	<b>Model RIE (Reflectivity for Mesa Etch)</b>	
	<b>Metalization</b>	
	<b>1) Prepare Wafer Surface</b> Cleave wafer and use one quarter for study Spin clean wafer with acetone, methanol, isopropyl alcohol, and DIW 30 seconds each @ 500 rpm N <sub>2</sub> blow dry 2 minute hot plate bake (HPB) @ 110° C ( <i>removes accumulated H<sub>2</sub>O</i> ) Cool	
	<b>2) XP LOR 3A Coat</b> Set spinner ramp rate = 200; spin 4000 rpm Coat sample with XP LOR 3A Spin 30 seconds @ 4K rpm 2 minute HPB @ 170° C Cool	
	<b>3) 1805 Coat</b> Set photoresist spinner ramp rate = 200; spin = 4000 rpm Flood wafer with 1805 Spin 30 seconds @ 4000 rpm 1:15 minute HPB @ 110° C Cool	
	<b>4) Edge Bead Removal</b> Flood expose edge bead mask for 2 min (2mw/cm <sup>2</sup> ) Develop for 30 seconds using LDD26W developer DI rinse, N <sub>2</sub> dry	
	<b>5) Metalization Contact Mask</b> Expose mesa contact mask for 17.5 sec (2mw/cm <sup>2</sup> , 405 nm) Spin develop for 75 seconds at 1000 RPM using LDD26W developer DI rinse for 30 sec, N <sub>2</sub> dry Microscope inspect to ensure alignment Clean mask using CA40, acetone wipe and N <sub>2</sub> dry	
	<b>6) Clean to ensure no photoresist in metal contact areas</b> 1 cycle in oxygen asher (4 minutes at 200 W)	
	<b>7) Place metalization order</b> Deposit 200 Å Ti, 1330 Å Au	
	<b>8) Remove oxide immediately prior to metal deposition</b> Dip 30 seconds in BOE:DIW 1:7 Rinse 3, 30 second cycles in DIW rinse tank Thoroughly N <sub>2</sub> blow dry	
	<b>9) Metal Lift Off</b> Acetone Spray lift off (as necessary, no more than 30 sec at a time) Methanol, Isopropanol rinse, 30 seconds each N <sub>2</sub> dry	

### *A.3 Annealing Tube Preparation*

Prior to the post-fabrication high temperature anneals, a new annealing tube was acquired and a thorough cleaning was performed to remove possible contaminants. The following procedure was used to clean the annealing tube.

- Perform a triethylchloride (TCE) rinse (approximately 1-minute)
- Perform a acetone rinse (approximately 1-minute)
- Perform a methanol rinse (approximately 1-minute)
- Perform an aqua-regia etch - fill annealing tube with a volume ratio of 3:1 hydrochloric acid (HCl) to nitric acid and let set for 10-minutes
- Rinse thoroughly with DIW for 5-minutes
- Perform an hydroflouric acid (HF) etch - fill tube with a volume ratio of 1:1 HF and DIW and let sit for 1-minute
- Rinse thoroughly with DIW for 5-minutes
- Blow dry with low pressure nitrogen gas

## *Appendix B. MEMS Test Chips*

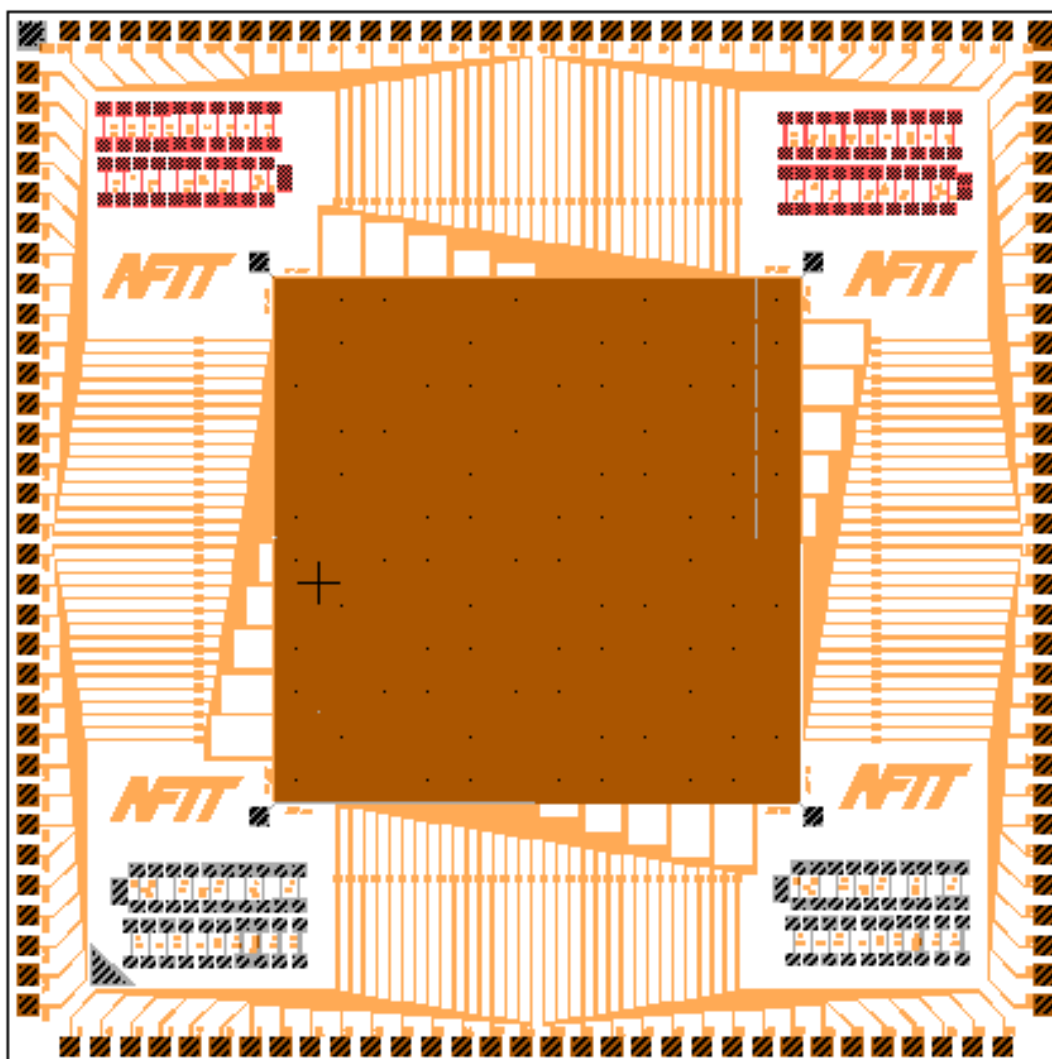
The primary purpose of this appendix is to identify the individual MUMPs® chips I used and designed specifically for my research on stress. I characterize the chips to determine important material parameters such as Young's modulus and residual stress. The hydrostatic pressure and uniaxial stress assumptions are used to determine localized residual stress using  $\mu$ Raman spectroscopy. These same test structures are used to evaluate the influence of post processing techniques (i.e. high temperature annealing and/or phosphorous diffusion) on the localized residual stress values. The MUMPs® 21 test chips I obtained from Cowan are used for phosphorous diffusion doping experiments. I used these chips to perform my initial assessment of residual stress characterization by  $\mu$ Raman spectroscopy. The MUMPs® #21 (designed by Paul Kladitis) and MUMPs® #38 (designed by William Cowan) test chips were designed by other AFIT students. From the MUMPs® 21 die, only the 100  $\mu m$  Poly1 and Poly2 fixed-fixed beams are used. I used other MEMS chips and structures thereon, fabricated via MUMPs® primarily for residual stress characterization and for my post-processing experiments. Similar MEMS test structures used in the MUMPs® fabrication method were fabricated in GaAs and SiC.

MUSiC is a developmental foundry fabrication based on the MUMPs® fabrication process but uses SiC as the structural material layer. Images of all fabricated dies and masks are provided along with a brief description of the primary test structures and their suggested usage.

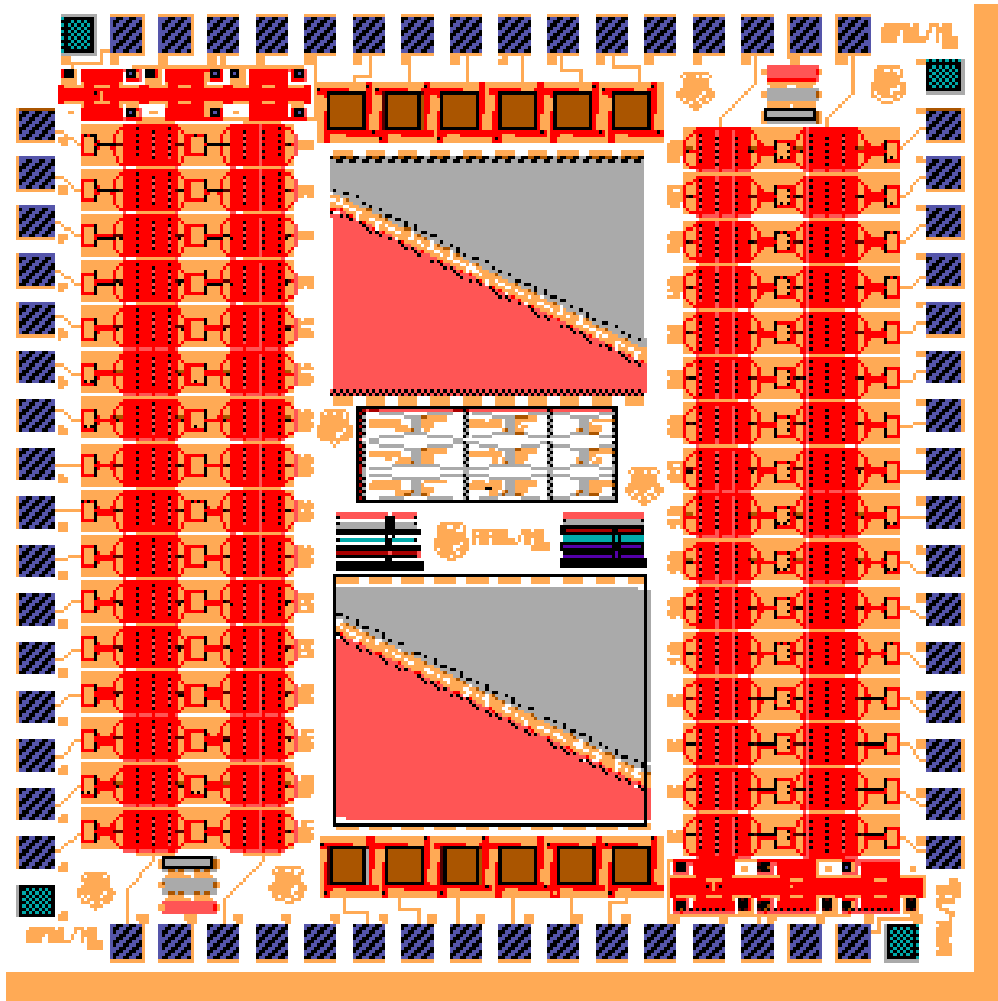
For additional design details beyond those described in the text, the reader is referred to my layout files shown on the next several pages. I accomplished all of my design layouts using L-edit. The top cell name required to open the CIF/GDS II files is listed for each design layout.

### *B.1 Test Chips*

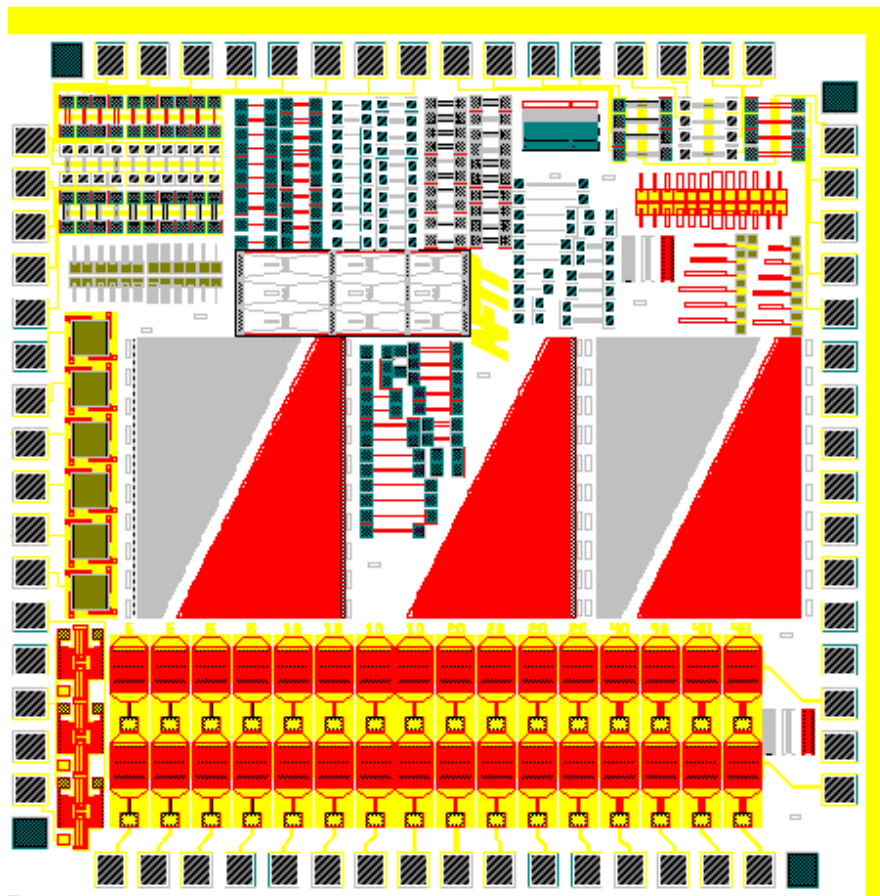
To characterize the material parameters to include the residual stress and Young's modulus, several different MEMS die were designed and fabricated. These identical die were used in the post-processing annealing, phosphorous diffusion, and ion implant doping experiments. In the following subsections, each MEMS test die I designed is briefly addressed indicating the primary test structures and there usage.



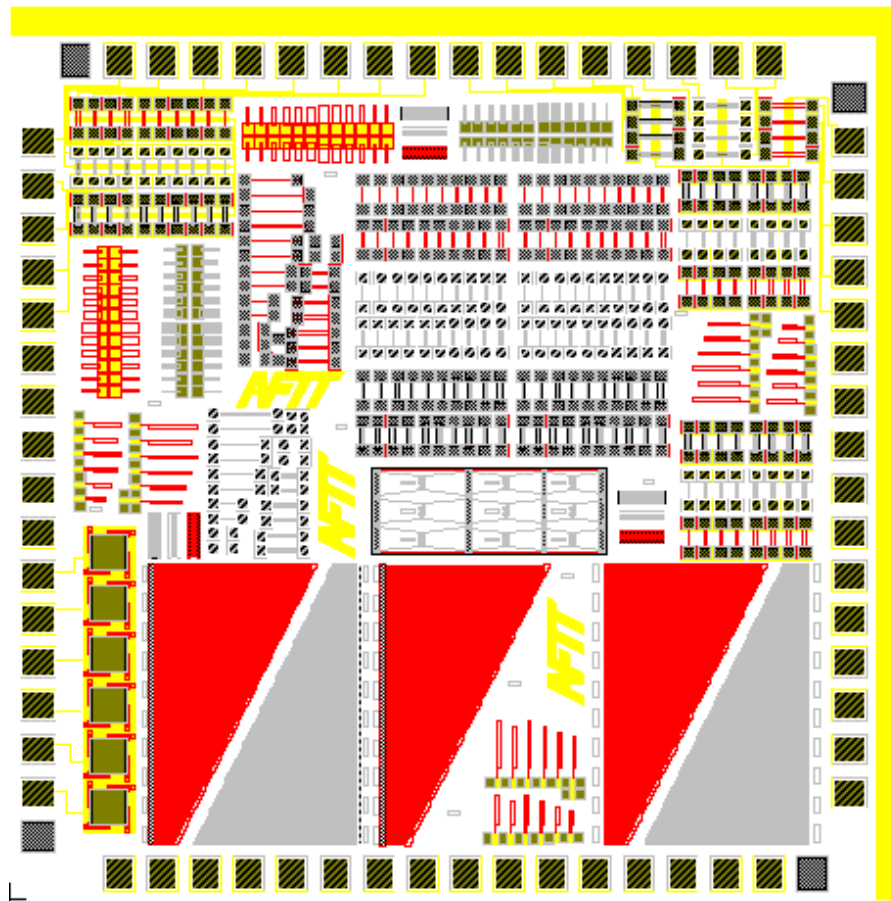
Top cell name:	mumps21_kladitis
MUMPs® Fabrication Run:	21
Chip Actuation:	electrostatic
Layout:	Raman residual stress test structures
Die Remaining:	0
Package:	68 LCC
Other Devices:	100 $\mu\text{m}$ Poly1 & Poly2 test bridges, micromirror array
Suggested Usage:	Diffusion doping, Raman spectroscopy analysis.
Comments:	No MUMPs® gold deposited, used to determine the effects of diffusion doping on the localized residual stress.



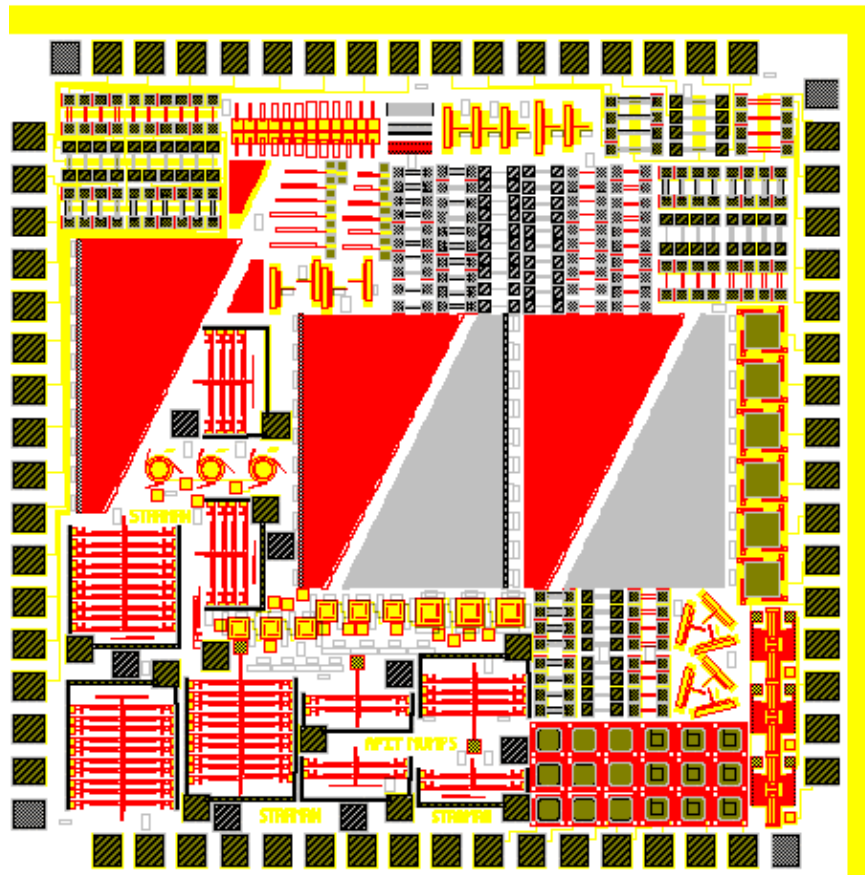
<b>Top cell name:</b>	Raman_Chip_1
<b>MUMPs® Fabrication Run:</b>	38
<b>RamanChip Actuation:</b>	electrostatic
<b>Layout:</b>	Uniaxial Stress test structures
<b>Die Remaining:</b>	1
<b>Package:</b>	68 LCC
<b>Other Devices:</b>	Poly1/Poly2 cantilevers, fixed-fixed beam arrays, comb drive resonators, micromirror array
<b>Suggested Usage:</b>	Determine the localized residual stress and Young's modulus, obtain PDP constants.
<b>Comments:</b>	MUMPs® gold deposited, used primarily to determine the localized residual stress and Young's modulus, and the PDP constants.



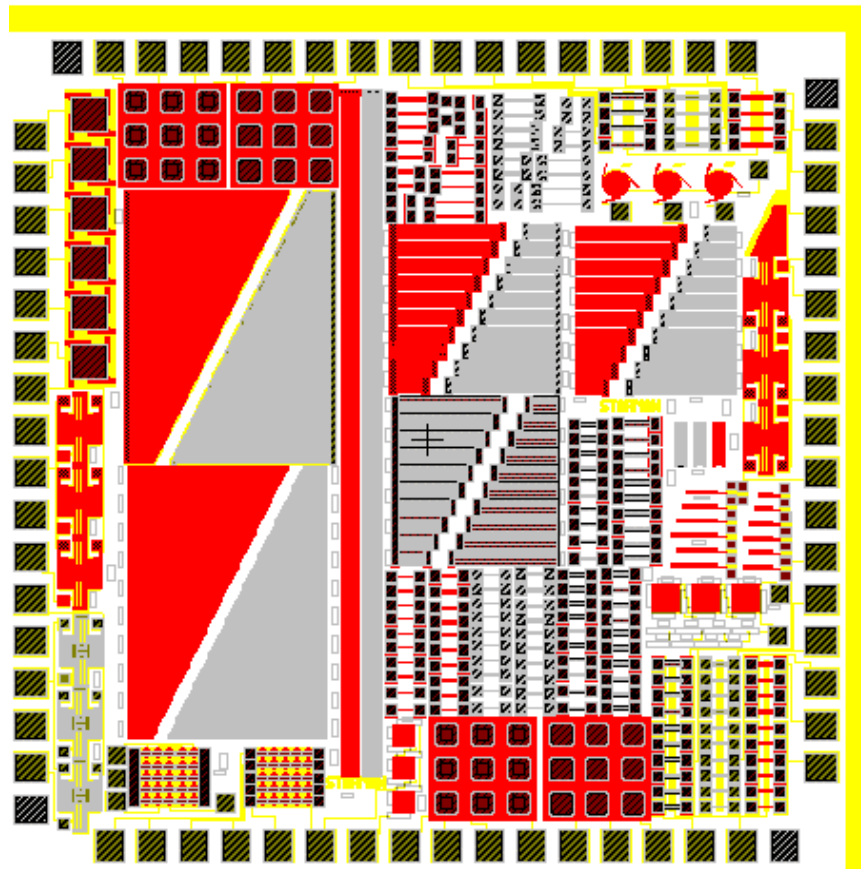
<b>Top cell name:</b>	Raman_Chip_G (designed by L. A. Starman)
<b>MUMPs® Fabrication Run:</b>	41
<b>RamanChip Actuation:</b>	electrostatic
<b>Layout:</b>	Uniaxial/residual Stress test structures
<b>Die Remaining:</b>	6
<b>Package:</b>	68 J-LDCC, 0.300 Sq cavity
<b>Other Devices:</b>	Poly1/Poly2 cantilevers, fixed-fixed beam arrays, comb drive resonators, micromirror array, 100 $\mu m$ and 200 $\mu m$ Poly1/Poly2 microbridge structures, electrostatic uniaxial structures, uniaxial pull test structures
<b>Suggested Usage:</b>	Localized residual stress and Young's modulus determination, determine phonon deformation potentials, initial Raman spectroscopy analysis
<b>Comments:</b>	MUMPs® gold deposited, used to determine the localized material parameters, Raman stress analysis.



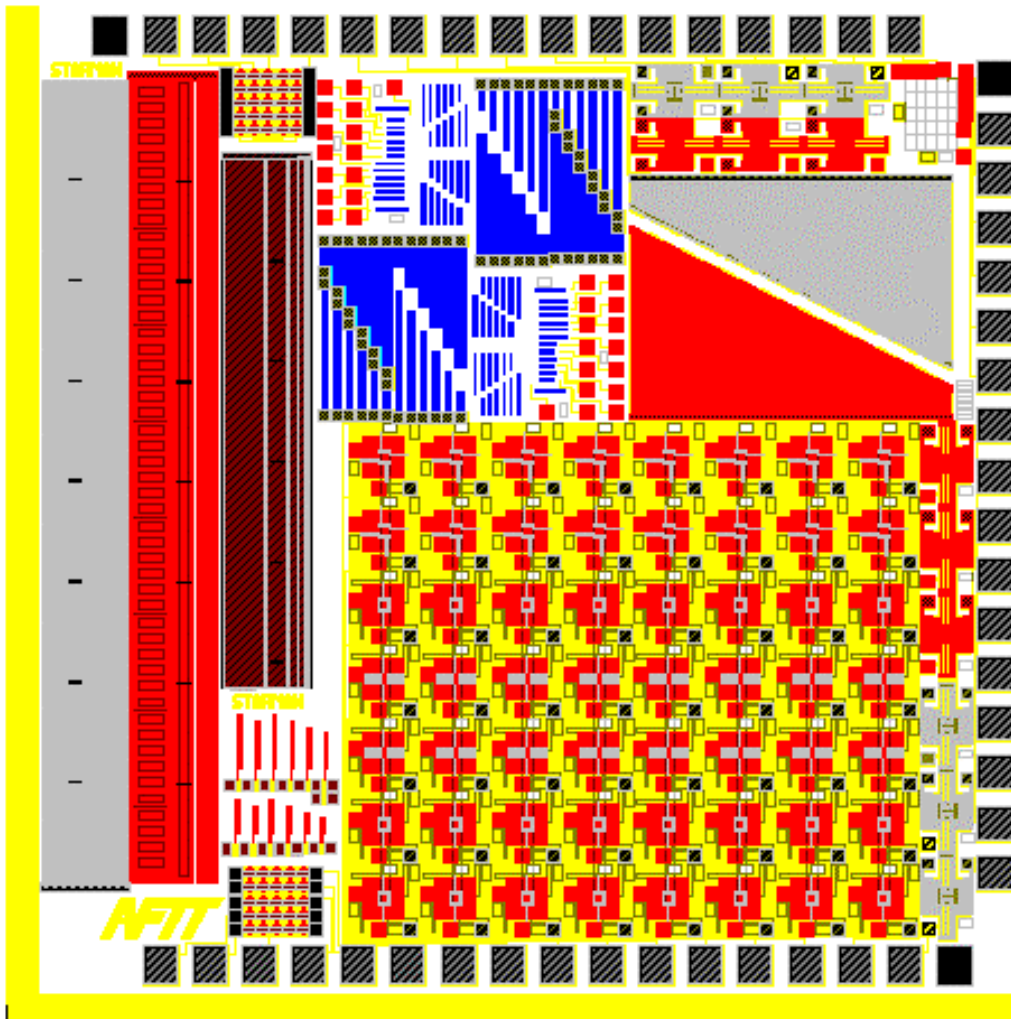
<b>Top cell name:</b>	Raman_Chip_NG (designed by L. A. Starman)
<b>MUMPs® Fabrication Run:</b>	41
<b>RamanChip Actuation:</b>	electrostatic
<b>Layout:</b>	Uniaxial/residual Stress test structures
<b>Die Remaining:</b>	7
<b>Package:</b>	68 J-LDCC, 0.300 Sq cavity
<b>Other Devices:</b>	Poly1/Poly2 cantilevers, fixed-fixed beam arrays, micromirror array, microbridge structures, electrostatic uniaxial structures, uniaxial pull test structures
<b>Suggested Usage:</b>	Post processing ion implantation doping studies, annealing experiments, localized residual stress and Young's modulus determination, Raman spectroscopy analysis.
<b>Comments:</b>	No gold deposited, used primarily to determine the influence of post processing annealing and doping on the localized residual stress.



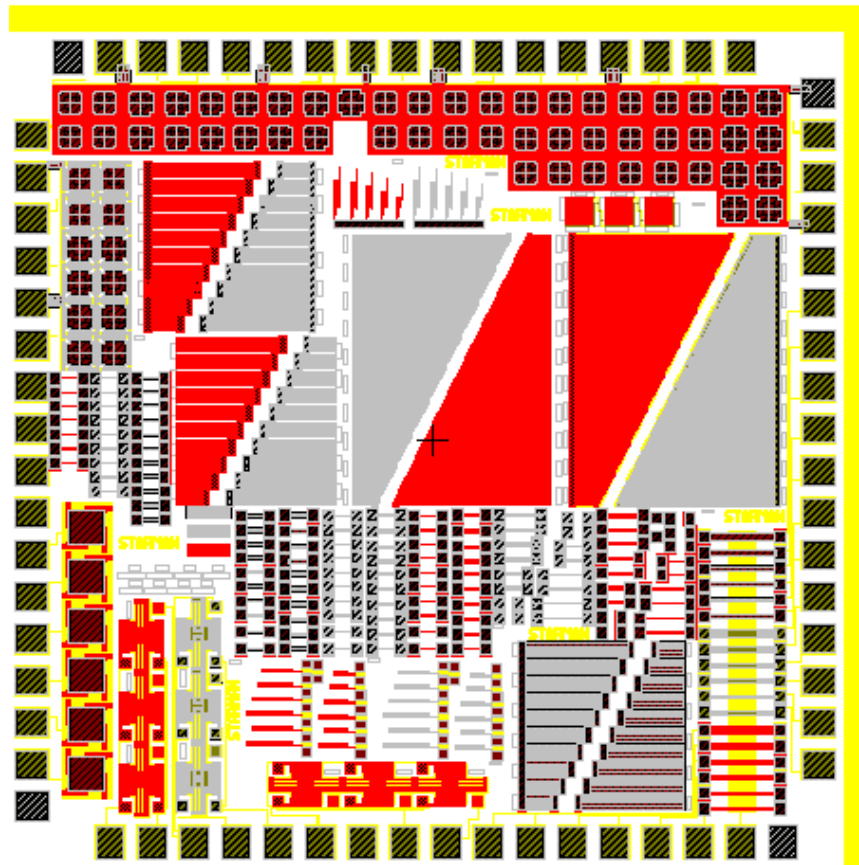
<b>Top cell name:</b>	Mumps_42 (designed by L. A. Starman)
<b>MUMPs® Fabrication Run:</b>	42
<b>RamanChip Actuation:</b>	electrostatic and thermal
<b>Layout:</b>	Uniaxial/residual stress test structures
<b>Die Remaining:</b>	3
<b>Package:</b>	68 J-LDCC, 0.300 Sq cavity
<b>Other Devices:</b>	Poly1/Poly2 cantilevers, fixed-fixed beam arrays, micromirror arrays, 100 $\mu\text{m}$ & 200 $\mu\text{m}$ Poly1/Poly2 microbridge structures, thermal uniaxial strain structures, thermal uniaxial pull test structures
<b>Suggested Usage:</b>	Post processing ion implantation doping studies, annealing experiments, localized residual stress and Young's modulus determination, Raman spectroscopy analysis
<b>Comments:</b>	No gold deposited, used primarily to determine the influence of post processing annealing and doping on the localized residual stress.



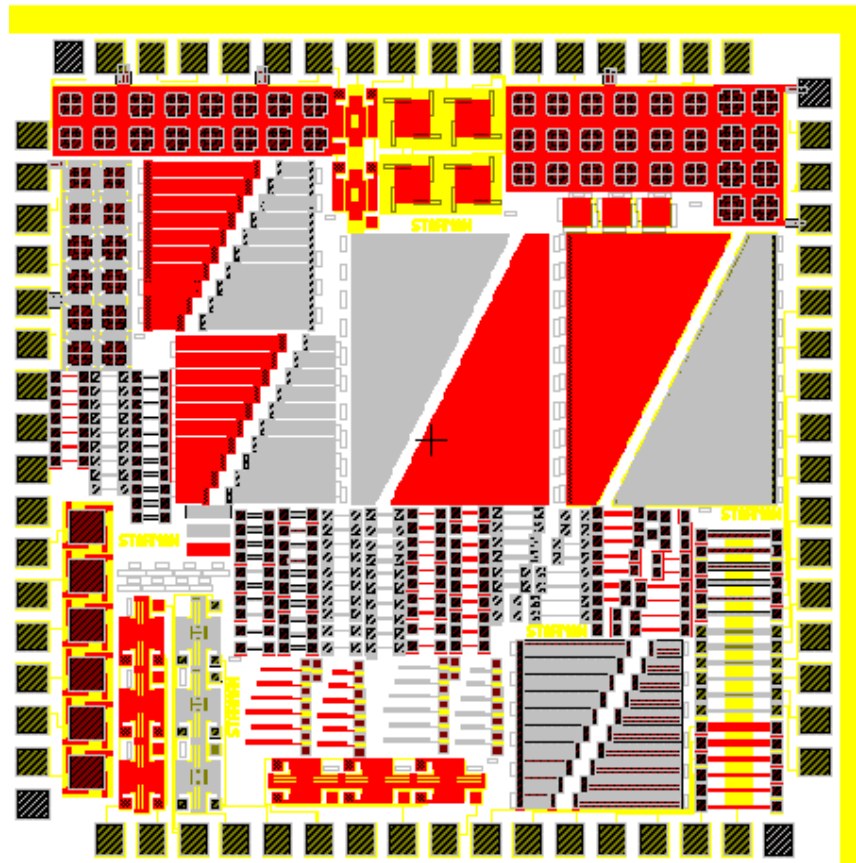
<b>Top cell name:</b>	Mumps_43 (designed by L. A. Starman)
<b>MUMPs® Fabrication Run:</b>	43
<b>RamanChip Actuation:</b>	electrostatic and thermal
<b>Layout:</b>	Uniaxial/residual stress test structures
<b>Die Remaining:</b>	2
<b>Package:</b>	68 J-LDCC, 0.300 Sq cavity
<b>Other Devices:</b>	Poly1/Poly2 cantilevers, fixed-fixed beam arrays, micromirror arrays, 100 $\mu m$ & 200 $\mu m$ Poly1/Poly2 microbridge structures, thermal test structures
<b>Suggested Usage:</b>	Post processing ion implantation doping studies, annealing experiments, localized residual stress and Young's modulus determination, Raman spectroscopy analysis.
<b>Comments:</b>	No gold deposited, used to determine the influence of post processing annealing and doping on the localized residual stress, determine the PDP constants.



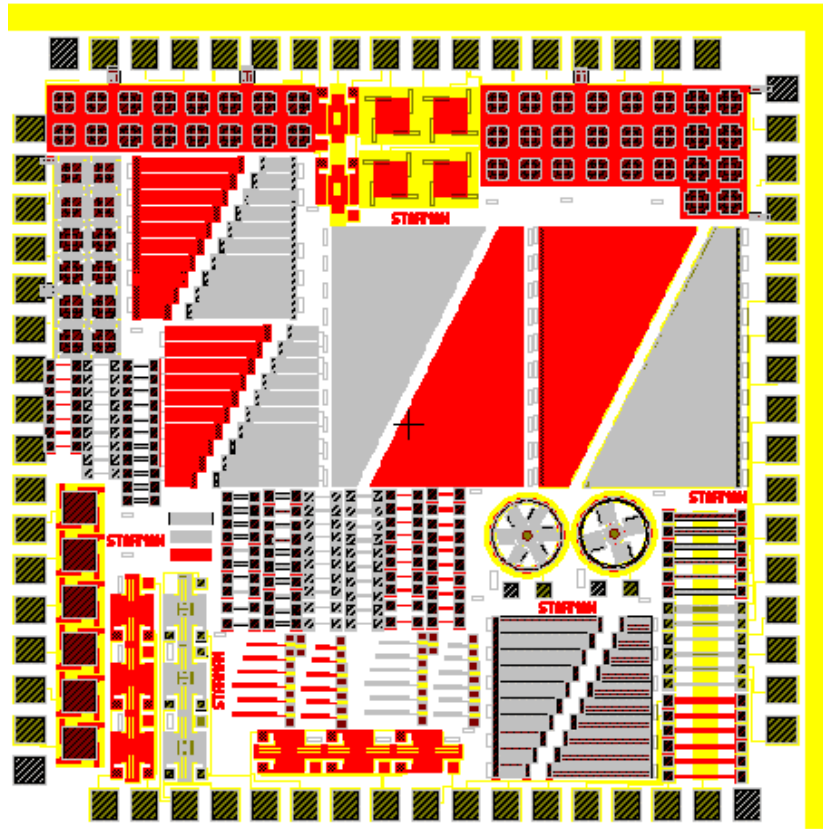
<b>Top cell name:</b>	Mumps.43q2 (designed by L. A. Starman)
<b>MUMPs® Fabrication Run:</b>	43
<b>RamanChip Actuation:</b>	electrostatic and thermal
<b>Layout:</b>	Uniaxial Stress cantilever structures
<b>Die Remaining:</b>	10
<b>Package:</b>	68 J-LDCC, 0.300 Sq cavity
<b>Other Devices:</b>	Poly1/Poly2 fixed-fixed beam arrays, flip-chip micromirrors, Gold cantilever and fixed-fixed beams, comb resonators, thermal test structures
<b>Suggested Usage:</b>	Localized residual stress and Young's modulus determination, PDP experimentation.
<b>Comments:</b>	MUMPs® gold deposited, long cantilevers used for strain tests to determine PDP constants.



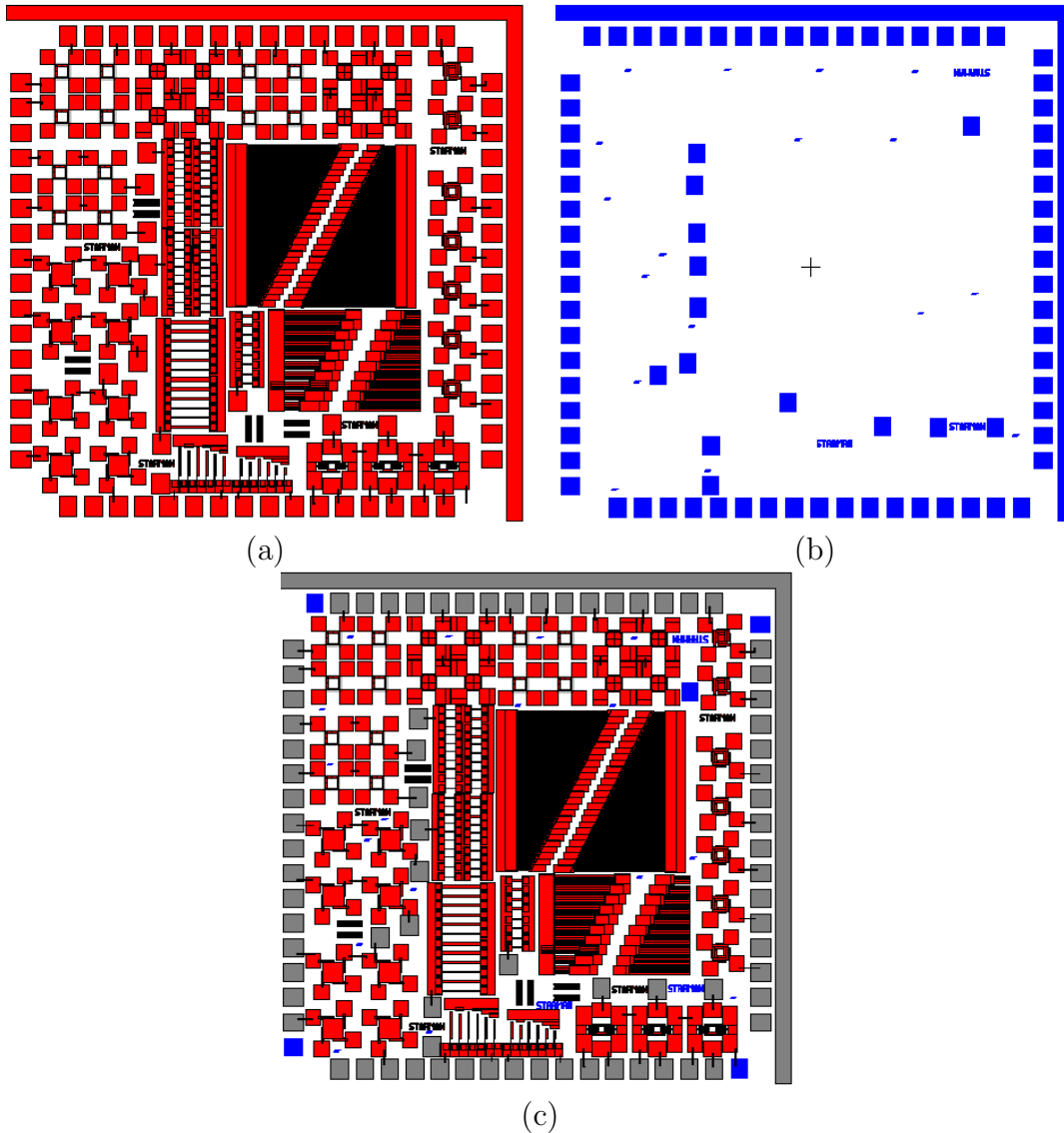
<b>Top cell name:</b>	Mumps_44a (designed by L. A. Starman)
<b>MUMPs® Fabrication Run:</b>	44
<b>RamanChip Actuation:</b>	electrostatic and thermal
<b>Layout:</b>	Uniaxial/residual Stress test structures
<b>Die Remaining:</b>	2
<b>Package:</b>	68 J-LDCC, 0.300 Sq cavity
<b>Other Devices:</b>	Poly1/Poly2 cantilevers, fixed-fixed beam arrays, micromirror arrays, 380 $\mu\text{m}$ Poly1/Poly2 microbridge structures, thermal test structures
<b>Suggested Usage:</b>	Post processing ion implantation doping studies, annealing experiments, localized residual stress and Young's modulus determination, Raman spectroscopy analysis
<b>Comments:</b>	No gold deposited, used to determine the influence of post processing annealing and doping on the localized residual stress, micromirror optical flatness measurements



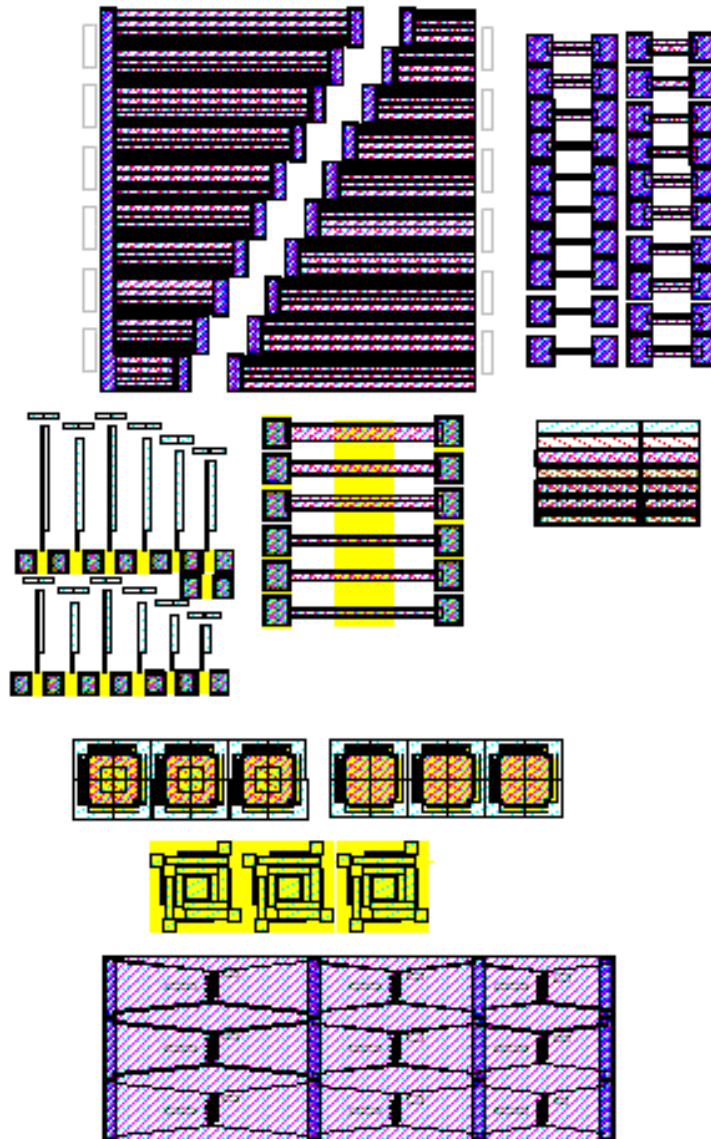
<b>Top cell name:</b>	Mumps_44b (designed by L. A. Starman)
<b>MUMPs® Fabrication Run:</b>	44
<b>RamanChip Actuation:</b>	electrostatic and thermal
<b>Layout:</b>	Uniaxial/residual Stress test structures
<b>Die Remaining:</b>	6
<b>Package:</b>	68 J-LDCC, 0.300 Sq cavity
<b>Other Devices:</b>	Poly1/Poly2 cantilevers, fixed-fixed beam arrays, micromirror arrays, 380 $\mu\text{m}$ Poly1/Poly2 microbridge structures, thermal test structures
<b>Suggested Usage:</b>	Post processing ion implantation doping studies, annealing experiments, localized residual stress and Young's modulus determination, Raman spectroscopy analysis.
<b>Comments:</b>	No gold deposited, used to determine the influence of post processing annealing and doping on the localized residual stress, micromirror optical curvature measurements



<b>Top cell name:</b>	Mumps_45 (designed by L. A. Starman)
<b>MUMPs® Fabrication Run:</b>	45
<b>RamanChip Actuation:</b>	electrostatic and thermal
<b>Layout:</b>	Residual Stress test structures
<b>Die Remaining:</b>	5
<b>Package:</b>	68 J-LDCC, 0.300 Sq cavity
<b>Other Devices:</b>	Poly1/Poly2 cantilevers, fixed-fixed beam arrays, micromirror arrays, 380 $\mu m$ Poly1/Poly2 microbridge structures, thermal test structures, scratch drive
<b>Suggested Usage:</b>	Post processing ion implantation doping studies, annealing experiments, residual stress and Young's modulus characterization, Raman spectroscopy analysis
<b>Comments:</b>	No gold deposited, used to determine the influence of post processing annealing and doping on the localized residual stress, micromirror actuation improvements



<b>Top cell name:</b>	GaAs_Mask_Structural (designed by L. A. Starman for GaAs)
<b>Chip Actuation:</b>	electrostatic and thermal
<b>Layout:</b>	Residual stress test structures
<b>Package:</b>	68 J-LDCC, 0.300 Sq cavity
<b>Other Devices:</b>	GaAs cantilevers, fixed-fixed beam arrays, micromirror arrays, thermal test structures.
<b>Suggested Usage:</b>	Residual stress characterization of III-V MEMS test structures, Raman spectroscopy analysis.
<b>Comments:</b>	(a)Mask to define the structural layer, (b) Gold contact mask (c) Final mask overlay.



**Top cell name:** Cell0 (designed by L. A. Starman for MUSiC)  
**Chip Actuation:** electrostatic and thermal  
**Layout:** Residual stress characterization structures  
**Package:** 68 J-LDCC, 0.300 Sq cavity  
**Other Devices:** Cantilevers, fixed-fixed beam arrays, various micromirrors , thermal test structures.  
**Suggested Usage:** Residual stress characterization of SiC MEMS structures.  
**Comments:** Test structures can be used for residual stress characterization using  $\mu$ Raman spectroscopy.

## *Appendix C. TSUPREM<sup>TM</sup> Simulation of MUMPs<sup>®</sup> Fabrication*

Appendix C contains an example input file for simulating the MUMPs<sup>®</sup> fabrication process in *TSUPREM<sup>TM</sup>*-4. This particular file was used for evaluating the dopant concentration levels of a MUMPs<sup>®</sup> Poly2 structure following a phosphorous implant and accompanying anneals as discussed in Chapter 7. The file describes the fabrication of a 12  $\mu m$ -wide Poly2 linestructure with no surrounding Poly0 or Poly1 structures. The commands for creating and patterning Poly0 and Poly1 are in the example but have been commented out so that they are not executed. Figure C.1 illustrates an example *TSUPREM<sup>TM</sup>* 3-D phosphorus doping profile for a 10  $\mu m$ -wide Poly2 linestructure.

### *C.1 TSUPREM<sup>TM</sup> Input File for MUMPs<sup>®</sup> Poly 1 Fabrication*

```

$ Capt LaVern Starman
$ MUMPs Poly2 Process
$ Implant Simulation for 12 um Wide Poly1 Linestructure

$ Set up the grid
LINE X LOC=0.0 SPAC=0.5
LINE X LOC=13.0 SPAC=0.5

LINE Y LOC=0.0 SPAC=0.5
LINE Y LOC=3.0 SPAC=0.5

$ (100) Si substrate with Phosphor doping concentration of 1E15
INITIALIZE <100> phosphor=1E15

$deposit nitride, poly0, and 1st oxide
deposition nitride thick=0.6
$deposit poly thick=0.5
deposition oxide thick=2.0 phosphor=4.2E20

SELECT Z=LOG10(phosphor) TITLE="Phosphor Doping before anneals"
PLOT.1D X.V=3.1 y.min=15

$ first anneal
diffusion time= 60 temp=1050 inert

SELECT Z=LOG10(phosphor) TITLE="Phosphor Doping after 1st Anneal"
PLOT.1D X.V=3.1 y.min=15

$deposit poly1
$deposition poly thick=2.0
deposition oxide thick=.2 phosphor=4.2E20

$ second anneal
diffusion time=60 temp=1050 inert

$ pattern poly
etch oxide old.dry thick=.2

$ etch poly all
ETCH poly left P1.X=3

STRUCTURE REFLECT RIGHT

SELECT Z=LOG10(phosphor) TITLE="Phosphor Doping after 2nd (Center)"
PLOT.1D X.V=9 y.min=15

SELECT Z=LOG10(phosphor) TITLE="Phosphor Doping after 2nd (Edge)"
PLOT.1D X.V=3.1 y.min=15

$ deposit 2nd oxide
deposition oxide thick=0.75 phosphor=4.2E20
$ phosphor initially 4.2E20

SELECT Z=LOG10(phosphor) TITLE="Phosphor Doping after 2nd ox (Center)"
PLOT.1D X.V=9 y.min=15

```

```

SELECT Z=LOG10(phosphor) TITLE="Phosphor Doping after 2nd ox (Edge)"
PLOT.1D X.V=3.1 y.min=15

$ Third anneal
diffusion time=60 temp=1050 inert

SELECT Z=LOG10(phosphor) TITLE="Phosphor Doping after 3rd (Center)"
PLOT.1D X.V=9 y.min=15

SELECT Z=LOG10(phosphor) TITLE="Phosphor Doping after 3rd (Edge)"
PLOT.1D X.V=3.1 y.min=15
etch oxide old.dry thick=.75
$ deposit poly2
deposition poly thick=1.5
deposition oxide thick=.2 phosphor=4.2E20

SELECT Z=LOG10(phosphor) TITLE="Phosphor Doping after 2nd cap (Center)"
PLOT.1D X.V=9 y.min=15

SELECT Z=LOG10(phosphor) TITLE="Phosphor Doping after 2nd cap (Edge)"
PLOT.1D X.V=3.1 y.min=15

$ Fourth anneal
diffusion time=60 temp=1050 inert

$ pattern poly
etch oxide old.dry thick=.2

$ etch poly all
ETCH poly left P1.X=3
ETCH poly right p1.x=23

SELECT Z=LOG10(phosphor) TITLE="Final Phosphor Doping (Center)"
PLOT.1D X.V=9 y.min=15

SELECT Z=LOG10(phosphor) TITLE="Final Phosphor Doping (Edge)"
PLOT.1D X.V=3.1 y.min=15

$ 2D contour plot of phosphor contours
SELECT Z=LOG10(phosphor) TITLE="2-D Phosphor Doping"
PLOT.2D y.max=2.0 y.min=-8.2

COLOR MIN.V=(LOG10(1E1)) MAX.V=(LOG10(1E17)) COLOR=12
COLOR MIN.V=(LOG10(1E17)) MAX.V=(LOG10(1E18)) COLOR=13
COLOR MIN.V=(LOG10(1E18)) MAX.V=(LOG10(1E19)) COLOR=14
COLOR MIN.V=(LOG10(1E19)) MAX.V=(LOG10(5E19)) COLOR=15
COLOR MIN.V=(LOG10(5E19)) MAX.V=(LOG10(1E20)) COLOR=16
COLOR MIN.V=(LOG10(1E20)) MAX.V=(LOG10(5E20)) COLOR=17
COLOR MIN.V=(LOG10(5E20)) MAX.V=(LOG10(1E21)) COLOR=18
COLOR MIN.V=(LOG10(1E21)) MAX.V=(LOG10(1E22)) COLOR=19

PLOT.2D ^AXIS ^CLEAR
LABEL X=.55 Y=-8.0 LABEL="Log10(Phosphor)" SIZE=0.3
LABEL X=2.15 Y=-7.8 LABEL="<1E17" SIZE=0.3 C.RECT=12 W.R=0.4 H.R=0.4
LABEL X=2.15 Y=-7.6 LABEL="1E17-1E18" SIZE=0.3 C.RECT=13 W.R=0.4 H.R=0.4
LABEL X=2.15 Y=-7.4 LABEL="1E18-1E19" SIZE=0.3 C.RECT=14 W.R=0.4 H.R=0.4
LABEL X=2.15 Y=-7.2 LABEL="1E19-5E19" SIZE=0.3 C.RECT=15 W.R=0.4 H.R=0.4

```

```

LABEL X=2.15 Y=-7.0 LABEL="5E19-1E20" SIZE=0.3 C.RECT=16 W.R=0.4 H.R=0.4
LABEL X=2.15 Y=-6.8 LABEL="1E20-5E20" SIZE=0.3 C.RECT=17 W.R=0.4 H.R=0.4
LABEL X=2.15 Y=-6.6 LABEL="5E20-1E21" SIZE=0.3 C.RECT=18 W.R=0.4 H.R=0.4
LABEL X=2.15 Y=-6.4 LABEL="1E21-1E22" SIZE=0.3 C.RECT=19 W.R=0.4 H.R=0.4

$ 2D contour plot of phosphor contours
SELECT Z=LOG10(phosphor) TITLE="2-D Phosphor Doping"
PLOT.2D y.max=2.0 y.min=-8.2

COLOR MIN.V=(LOG10(1E19)) MAX.V=(LOG10(2E19)) COLOR=13
COLOR MIN.V=(LOG10(2E19)) MAX.V=(LOG10(5E19)) COLOR=14
COLOR MIN.V=(LOG10(5E19)) MAX.V=(LOG10(9E19)) COLOR=15
COLOR MIN.V=(LOG10(9E19)) MAX.V=(LOG10(2E20)) COLOR=16
COLOR MIN.V=(LOG10(2E20)) MAX.V=(LOG10(5E20)) COLOR=17
COLOR MIN.V=(LOG10(5E20)) MAX.V=(LOG10(8E20)) COLOR=18
COLOR MIN.V=(LOG10(8E20)) MAX.V=(LOG10(1E21)) COLOR=10
COLOR MIN.V=(LOG10(1E21)) MAX.V=(LOG10(9E21)) COLOR=08

PLOT.2D ^AXIS ^CLEAR
LABEL X=2.15 Y=-7.7 LABEL="<1E18-2E19" SIZE=0.3 C.RECT=13 W.R=0.4 H.R=0.4
LABEL X=2.15 Y=-7.3 LABEL="<2E19-5E19" SIZE=0.3 C.RECT=14 W.R=0.4 H.R=0.4
LABEL X=2.15 Y=-6.9 LABEL="<5E19-9E19" SIZE=0.3 C.RECT=15 W.R=0.4 H.R=0.4
LABEL X=2.15 Y=-6.5 LABEL="<9E19-2E20" SIZE=0.3 C.RECT=16 W.R=0.4 H.R=0.4
LABEL X=2.15 Y=-6.1 LABEL="<2E20-5E20" SIZE=0.3 C.RECT=17 W.R=0.4 H.R=0.4
LABEL X=2.15 Y=-5.7 LABEL="<5E20-8E20" SIZE=0.3 C.RECT=18 W.R=0.4 H.R=0.4
LABEL X=2.15 Y=-5.3 LABEL="<8E20-1E21" SIZE=0.3 C.RECT=10 W.R=0.4 H.R=0.4
LABEL X=2.15 Y=-4.9 LABEL="<1E21-9E21" SIZE=0.3 C.RECT=08 W.R=0.4 H.R=0.4

$ 3D contour plot of phosphor contours
SELECT Z=LOG10(phosphor) TITLE="Final 3-D Phosphor Doping"
PLOT.3D theta=45 phi=45 y.max=1.0 num.cnt=30

$ End of Simulation

$Phosphorous implant at 200 KeV

IMPLANT PHOSPHORUS ENERGY=200 DOSE=1E16 MONTECAR TILT=7 N.ION=100

$ 2D contour plot of phosphor contours
SELECT Z=LOG10(phosphor) TITLE="2-D Phosphor Implant Doping"
PLOT.2D y.max=2.0 y.min=-8.2

COLOR MIN.V=(LOG10(1E19)) MAX.V=(LOG10(2E19)) COLOR=13
COLOR MIN.V=(LOG10(2E19)) MAX.V=(LOG10(5E19)) COLOR=14
COLOR MIN.V=(LOG10(5E19)) MAX.V=(LOG10(9E19)) COLOR=15
COLOR MIN.V=(LOG10(9E19)) MAX.V=(LOG10(2E20)) COLOR=16
COLOR MIN.V=(LOG10(2E20)) MAX.V=(LOG10(5E20)) COLOR=17
COLOR MIN.V=(LOG10(5E20)) MAX.V=(LOG10(8E20)) COLOR=18
COLOR MIN.V=(LOG10(8E20)) MAX.V=(LOG10(1E21)) COLOR=10
COLOR MIN.V=(LOG10(1E21)) MAX.V=(LOG10(9E21)) COLOR=08

PLOT.2D ^AXIS ^CLEAR
LABEL X=2.15 Y=-7.7 LABEL="<1E18-2E19" SIZE=0.3 C.RECT=13 W.R=0.4 H.R=0.4
LABEL X=2.15 Y=-7.3 LABEL="<2E19-5E19" SIZE=0.3 C.RECT=14 W.R=0.4 H.R=0.4
LABEL X=2.15 Y=-6.9 LABEL="<5E19-9E19" SIZE=0.3 C.RECT=15 W.R=0.4 H.R=0.4
LABEL X=2.15 Y=-6.5 LABEL="<9E19-2E20" SIZE=0.3 C.RECT=16 W.R=0.4 H.R=0.4
LABEL X=2.15 Y=-6.1 LABEL="<2E20-5E20" SIZE=0.3 C.RECT=17 W.R=0.4 H.R=0.4

```

```

LABEL X=2.15 Y=-5.7 LABEL="<5E20-8E20" SIZE=0.3 C.RECT=18 W.R=0.4 H.R=0.4
LABEL X=2.15 Y=-5.3 LABEL="<8E20-1E21" SIZE=0.3 C.RECT=10 W.R=0.4 H.R=0.4
LABEL X=2.15 Y=-4.9 LABEL="<1E21-9E21" SIZE=0.3 C.RECT=08 W.R=0.4 H.R=0.4

$Activation Anneal
$deposition oxide thick=.01
DIFFUSION TEMP=300 TIME=30 WETO2

$ 2D contour plot of phosphor contours
SELECT Z=LOG10(phosphor) TITLE="Wet02 oxide growth"
PLOT.2D y.max=2.0 y.min=-8.2

$COLOR MIN.V=(LOG10(1E17)) MAX.V=(LOG10(1E18)) COLOR=13
$COLOR MIN.V=(LOG10(1E18)) MAX.V=(LOG10(1E19)) COLOR=14
COLOR MIN.V=(LOG10(1E19)) MAX.V=(LOG10(2E19)) COLOR=13
COLOR MIN.V=(LOG10(2E19)) MAX.V=(LOG10(5E19)) COLOR=14
COLOR MIN.V=(LOG10(5E19)) MAX.V=(LOG10(9E19)) COLOR=15
COLOR MIN.V=(LOG10(9E19)) MAX.V=(LOG10(2E20)) COLOR=16
COLOR MIN.V=(LOG10(2E20)) MAX.V=(LOG10(5E20)) COLOR=17
COLOR MIN.V=(LOG10(5E20)) MAX.V=(LOG10(8E20)) COLOR=18
COLOR MIN.V=(LOG10(8E20)) MAX.V=(LOG10(1E21)) COLOR=10
COLOR MIN.V=(LOG10(1E21)) MAX.V=(LOG10(9E21)) COLOR=08

PLOT.2D ^AXIS ^CLEAR
$LABEL X=0.55 Y=-7.7 LABEL="Log10(Phosphor)" SIZE=0.3
$LABEL X=1.15 Y=-7.7 LABEL="<1E17-1E18" SIZE=0.3 C.RECT=13 W.R=0.4 H.R=0.4
LABEL X=2.15 Y=-7.7 LABEL="<1E18-2E19" SIZE=0.3 C.RECT=13 W.R=0.4 H.R=0.4
LABEL X=2.15 Y=-7.3 LABEL="<2E19-5E19" SIZE=0.3 C.RECT=14 W.R=0.4 H.R=0.4
LABEL X=2.15 Y=-6.9 LABEL="<5E19-9E19" SIZE=0.3 C.RECT=15 W.R=0.4 H.R=0.4
LABEL X=2.15 Y=-6.5 LABEL="<9E19-2E20" SIZE=0.3 C.RECT=16 W.R=0.4 H.R=0.4
LABEL X=2.15 Y=-6.1 LABEL="<2E20-5E20" SIZE=0.3 C.RECT=17 W.R=0.4 H.R=0.4
LABEL X=2.15 Y=-5.7 LABEL="<5E20-8E20" SIZE=0.3 C.RECT=18 W.R=0.4 H.R=0.4
LABEL X=2.15 Y=-5.3 LABEL="<8E20-1E21" SIZE=0.3 C.RECT=10 W.R=0.4 H.R=0.4
LABEL X=2.15 Y=-4.9 LABEL="<1E21-9E21" SIZE=0.3 C.RECT=08 W.R=0.4 H.R=0.4

DIFFUSION TEMP=900 TIME=30 NITROGEN

$ 2D contour plot of phosphor contours
SELECT Z=LOG10(phosphor) TITLE="Drive in Anneal 2-D Phosphor Doping"
PLOT.2D y.max=2.0 y.min=-8.2

COLOR MIN.V=(LOG10(1E19)) MAX.V=(LOG10(2E19)) COLOR=13
COLOR MIN.V=(LOG10(2E19)) MAX.V=(LOG10(5E19)) COLOR=14
COLOR MIN.V=(LOG10(5E19)) MAX.V=(LOG10(9E19)) COLOR=15
COLOR MIN.V=(LOG10(9E19)) MAX.V=(LOG10(2E20)) COLOR=16
COLOR MIN.V=(LOG10(2E20)) MAX.V=(LOG10(5E20)) COLOR=17
COLOR MIN.V=(LOG10(5E20)) MAX.V=(LOG10(8E20)) COLOR=18
COLOR MIN.V=(LOG10(8E20)) MAX.V=(LOG10(1E21)) COLOR=10
COLOR MIN.V=(LOG10(1E21)) MAX.V=(LOG10(9E21)) COLOR=08

PLOT.2D ^AXIS ^CLEAR
$LABEL X=0.55 Y=-7.7 LABEL="Log10(Phosphor)" SIZE=0.3
$LABEL X=1.15 Y=-7.7 LABEL="<1E17-1E18" SIZE=0.3 C.RECT=13 W.R=0.4 H.R=0.4
LABEL X=2.15 Y=-7.7 LABEL="<1E18-2E19" SIZE=0.3 C.RECT=13 W.R=0.4 H.R=0.4
LABEL X=2.15 Y=-7.3 LABEL="<2E19-5E19" SIZE=0.3 C.RECT=14 W.R=0.4 H.R=0.4
LABEL X=2.15 Y=-6.9 LABEL="<5E19-9E19" SIZE=0.3 C.RECT=15 W.R=0.4 H.R=0.4
LABEL X=2.15 Y=-6.5 LABEL="<9E19-2E20" SIZE=0.3 C.RECT=16 W.R=0.4 H.R=0.4

```

```

LABEL X=2.15 Y=-6.1 LABEL="<2E20-5E20" SIZE=0.3 C.RECT=17 W.R=0.4 H.R=0.4
LABEL X=2.15 Y=-5.7 LABEL="<5E20-8E20" SIZE=0.3 C.RECT=18 W.R=0.4 H.R=0.4
LABEL X=2.15 Y=-5.3 LABEL="<8E20-1E21" SIZE=0.3 C.RECT=10 W.R=0.4 H.R=0.4
LABEL X=2.15 Y=-4.9 LABEL="<1E21-9E21" SIZE=0.3 C.RECT=08 W.R=0.4 H.R=0.4

```

DIFFUSION TEMP=1100 Time=05 NITROGEN

```

$ 2D contour plot of phosphor contours
SELECT Z=LOG10(phosphor) TITLE="Poly2 2-D 5-min Anneal"
PLOT.2D y.max=2.0 y.min=-8.2

```

```

COLOR MIN.V=(LOG10(1E19)) MAX.V=(LOG10(2E19)) COLOR=13
COLOR MIN.V=(LOG10(2E19)) MAX.V=(LOG10(5E19)) COLOR=14
COLOR MIN.V=(LOG10(5E19)) MAX.V=(LOG10(9E19)) COLOR=15
COLOR MIN.V=(LOG10(9E19)) MAX.V=(LOG10(2E20)) COLOR=16
COLOR MIN.V=(LOG10(2E20)) MAX.V=(LOG10(5E20)) COLOR=17
COLOR MIN.V=(LOG10(5E20)) MAX.V=(LOG10(8E20)) COLOR=18
COLOR MIN.V=(LOG10(8E20)) MAX.V=(LOG10(1E21)) COLOR=10
COLOR MIN.V=(LOG10(1E21)) MAX.V=(LOG10(6E21)) COLOR=08

```

```

PLOT.2D ^AXIS ^CLEAR
$LABEL X=0.55 Y=-7.7 LABEL="Log10(Phosphor)" SIZE=0.3
$LABEL X=1.15 Y=-7.7 LABEL="<1E17-1E18" SIZE=0.3 C.RECT=13 W.R=0.4 H.R=0.4
LABEL X=2.15 Y=-7.7 LABEL="<1E18-2E19" SIZE=0.3 C.RECT=13 W.R=0.4 H.R=0.4
LABEL X=2.15 Y=-7.3 LABEL="<2E19-5E19" SIZE=0.3 C.RECT=14 W.R=0.4 H.R=0.4
LABEL X=2.15 Y=-6.9 LABEL="<5E19-9E19" SIZE=0.3 C.RECT=15 W.R=0.4 H.R=0.4
LABEL X=2.15 Y=-6.5 LABEL="<9E19-2E20" SIZE=0.3 C.RECT=16 W.R=0.4 H.R=0.4
LABEL X=2.15 Y=-6.1 LABEL="<2E20-5E20" SIZE=0.3 C.RECT=17 W.R=0.4 H.R=0.4
LABEL X=2.15 Y=-5.7 LABEL="<5E20-8E20" SIZE=0.3 C.RECT=18 W.R=0.4 H.R=0.4
LABEL X=2.15 Y=-5.3 LABEL="<8E20-1E21" SIZE=0.3 C.RECT=10 W.R=0.4 H.R=0.4
LABEL X=2.15 Y=-4.9 LABEL="<1E21-9E21" SIZE=0.3 C.RECT=08 W.R=0.4 H.R=0.4

```

DIFFUSION TEMP=1100 Time=05 NITROGEN

```

$ 2D contour plot of phosphor contours
SELECT Z=LOG10(phosphor) TITLE="Poly2 2-D 10-min Anneal"
PLOT.2D y.max=2.0 y.min=-8.2

```

```

COLOR MIN.V=(LOG10(1E19)) MAX.V=(LOG10(2E19)) COLOR=13
COLOR MIN.V=(LOG10(2E19)) MAX.V=(LOG10(5E19)) COLOR=14
COLOR MIN.V=(LOG10(5E19)) MAX.V=(LOG10(9E19)) COLOR=15
COLOR MIN.V=(LOG10(9E19)) MAX.V=(LOG10(2E20)) COLOR=16
COLOR MIN.V=(LOG10(2E20)) MAX.V=(LOG10(5E20)) COLOR=17
COLOR MIN.V=(LOG10(5E20)) MAX.V=(LOG10(8E20)) COLOR=18
COLOR MIN.V=(LOG10(8E20)) MAX.V=(LOG10(1E21)) COLOR=10
COLOR MIN.V=(LOG10(1E21)) MAX.V=(LOG10(6E21)) COLOR=08

```

```

PLOT.2D ^AXIS ^CLEAR
LABEL X=2.15 Y=-7.7 LABEL="<1E18-2E19" SIZE=0.3 C.RECT=13 W.R=0.4 H.R=0.4
LABEL X=2.15 Y=-7.3 LABEL="<2E19-5E19" SIZE=0.3 C.RECT=14 W.R=0.4 H.R=0.4
LABEL X=2.15 Y=-6.9 LABEL="<5E19-9E19" SIZE=0.3 C.RECT=15 W.R=0.4 H.R=0.4
LABEL X=2.15 Y=-6.5 LABEL="<9E19-2E20" SIZE=0.3 C.RECT=16 W.R=0.4 H.R=0.4
LABEL X=2.15 Y=-6.1 LABEL="<2E20-5E20" SIZE=0.3 C.RECT=17 W.R=0.4 H.R=0.4
LABEL X=2.15 Y=-5.7 LABEL="<5E20-8E20" SIZE=0.3 C.RECT=18 W.R=0.4 H.R=0.4
LABEL X=2.15 Y=-5.3 LABEL="<8E20-1E21" SIZE=0.3 C.RECT=10 W.R=0.4 H.R=0.4
LABEL X=2.15 Y=-4.9 LABEL="<1E21-9E21" SIZE=0.3 C.RECT=08 W.R=0.4 H.R=0.4

```

DIFFUSION TEMP=1100 Time=10 NITROGEN

\$ 2D contour plot of phosphor contours  
SELECT Z=LOG10(phosphor) TITLE="Poly2 2-D 20-min Anneal"  
PLOT.2D y.max=2.0 y.min=-8.2

COLOR MIN.V=(LOG10(1E19)) MAX.V=(LOG10(2E19)) COLOR=13  
COLOR MIN.V=(LOG10(2E19)) MAX.V=(LOG10(5E19)) COLOR=14  
COLOR MIN.V=(LOG10(5E19)) MAX.V=(LOG10(9E19)) COLOR=15  
COLOR MIN.V=(LOG10(9E19)) MAX.V=(LOG10(2E20)) COLOR=16  
COLOR MIN.V=(LOG10(2E20)) MAX.V=(LOG10(5E20)) COLOR=17  
COLOR MIN.V=(LOG10(5E20)) MAX.V=(LOG10(8E20)) COLOR=18  
COLOR MIN.V=(LOG10(8E20)) MAX.V=(LOG10(1E21)) COLOR=10  
COLOR MIN.V=(LOG10(1E21)) MAX.V=(LOG10(6E21)) COLOR=08

PLOT.2D ^AXIS ^CLEAR  
\$LABEL X=0.55 Y=-7.7 LABEL="Log10(Phosphor)" SIZE=0.3  
\$LABEL X=1.15 Y=-7.7 LABEL="<1E17-1E18" SIZE=0.3 C.RECT=13 W.R=0.4 H.R=0.4  
LABEL X=2.15 Y=-7.7 LABEL="<1E18-2E19" SIZE=0.3 C.RECT=13 W.R=0.4 H.R=0.4  
LABEL X=2.15 Y=-7.3 LABEL="<2E19-5E19" SIZE=0.3 C.RECT=14 W.R=0.4 H.R=0.4  
LABEL X=2.15 Y=-6.9 LABEL="<5E19-9E19" SIZE=0.3 C.RECT=15 W.R=0.4 H.R=0.4  
LABEL X=2.15 Y=-6.5 LABEL="<9E19-2E20" SIZE=0.3 C.RECT=16 W.R=0.4 H.R=0.4  
LABEL X=2.15 Y=-6.1 LABEL="<2E20-5E20" SIZE=0.3 C.RECT=17 W.R=0.4 H.R=0.4  
LABEL X=2.15 Y=-5.7 LABEL="<5E20-8E20" SIZE=0.3 C.RECT=18 W.R=0.4 H.R=0.4  
LABEL X=2.15 Y=-5.3 LABEL="<8E20-1E21" SIZE=0.3 C.RECT=10 W.R=0.4 H.R=0.4  
LABEL X=2.15 Y=-4.9 LABEL="<1E21-9E21" SIZE=0.3 C.RECT=08 W.R=0.4 H.R=0.4

DIFFUSION TEMP=1100 Time=10 NITROGEN

\$ 2D contour plot of phosphor contours  
SELECT Z=LOG10(phosphor) TITLE="Poly2 2-D 30-min Anneal"  
PLOT.2D y.max=2.0 y.min=-8.2

\$COLOR MIN.V=(LOG10(1E17)) MAX.V=(LOG10(1E18)) COLOR=13  
\$COLOR MIN.V=(LOG10(1E18)) MAX.V=(LOG10(1E19)) COLOR=14  
COLOR MIN.V=(LOG10(1E19)) MAX.V=(LOG10(2E19)) COLOR=13  
COLOR MIN.V=(LOG10(2E19)) MAX.V=(LOG10(5E19)) COLOR=14  
COLOR MIN.V=(LOG10(5E19)) MAX.V=(LOG10(9E19)) COLOR=15  
COLOR MIN.V=(LOG10(9E19)) MAX.V=(LOG10(2E20)) COLOR=16  
COLOR MIN.V=(LOG10(2E20)) MAX.V=(LOG10(5E20)) COLOR=17  
COLOR MIN.V=(LOG10(5E20)) MAX.V=(LOG10(8E20)) COLOR=18  
COLOR MIN.V=(LOG10(8E20)) MAX.V=(LOG10(1E21)) COLOR=10  
COLOR MIN.V=(LOG10(1E21)) MAX.V=(LOG10(6E21)) COLOR=08

PLOT.2D ^AXIS ^CLEAR  
\$LABEL X=0.55 Y=-7.7 LABEL="Log10(Phosphor)" SIZE=0.3  
\$LABEL X=1.15 Y=-7.7 LABEL="<1E17-1E18" SIZE=0.3 C.RECT=13 W.R=0.4 H.R=0.4  
LABEL X=2.15 Y=-7.7 LABEL="<1E18-2E19" SIZE=0.3 C.RECT=13 W.R=0.4 H.R=0.4  
LABEL X=2.15 Y=-7.3 LABEL="<2E19-5E19" SIZE=0.3 C.RECT=14 W.R=0.4 H.R=0.4  
LABEL X=2.15 Y=-6.9 LABEL="<5E19-9E19" SIZE=0.3 C.RECT=15 W.R=0.4 H.R=0.4  
LABEL X=2.15 Y=-6.5 LABEL="<9E19-2E20" SIZE=0.3 C.RECT=16 W.R=0.4 H.R=0.4  
LABEL X=2.15 Y=-6.1 LABEL="<2E20-5E20" SIZE=0.3 C.RECT=17 W.R=0.4 H.R=0.4  
LABEL X=2.15 Y=-5.7 LABEL="<5E20-8E20" SIZE=0.3 C.RECT=18 W.R=0.4 H.R=0.4  
LABEL X=2.15 Y=-5.3 LABEL="<8E20-1E21" SIZE=0.3 C.RECT=10 W.R=0.4 H.R=0.4  
LABEL X=2.15 Y=-4.9 LABEL="<1E21-9E21" SIZE=0.3 C.RECT=08 W.R=0.4 H.R=0.4

DIFFUSION TEMP=1100 Time=30 NITROGEN

\$ 2D contour plot of phosphor contours

SELECT Z=LOG10(phosphor) TITLE="Poly2 2-D 60-min Anneal"

PLOT.2D y.max=2.0 y.min=-8.2

\$COLOR MIN.V=(LOG10(1E17)) MAX.V=(LOG10(1E18)) COLOR=13

\$COLOR MIN.V=(LOG10(1E18)) MAX.V=(LOG10(1E19)) COLOR=14

COLOR MIN.V=(LOG10(1E19)) MAX.V=(LOG10(2E19)) COLOR=13

COLOR MIN.V=(LOG10(2E19)) MAX.V=(LOG10(5E19)) COLOR=14

COLOR MIN.V=(LOG10(5E19)) MAX.V=(LOG10(9E19)) COLOR=15

COLOR MIN.V=(LOG10(9E19)) MAX.V=(LOG10(2E20)) COLOR=16

COLOR MIN.V=(LOG10(2E20)) MAX.V=(LOG10(5E20)) COLOR=17

COLOR MIN.V=(LOG10(5E20)) MAX.V=(LOG10(8E20)) COLOR=18

COLOR MIN.V=(LOG10(8E20)) MAX.V=(LOG10(1E21)) COLOR=10

COLOR MIN.V=(LOG10(1E21)) MAX.V=(LOG10(6E21)) COLOR=08

PLOT.2D ^AXIS ^CLEAR

\$LABEL X=0.55 Y=-7.7 LABEL="Log10(Phosphor)" SIZE=0.3

\$LABEL X=1.15 Y=-7.7 LABEL="<1E17-1E18" SIZE=0.3 C.RECT=13 W.R=0.4 H.R=0.4

LABEL X=2.15 Y=-7.7 LABEL="<1E18-2E19" SIZE=0.3 C.RECT=13 W.R=0.4 H.R=0.4

LABEL X=2.15 Y=-7.3 LABEL="<2E19-5E19" SIZE=0.3 C.RECT=14 W.R=0.4 H.R=0.4

LABEL X=2.15 Y=-6.9 LABEL="<5E19-9E19" SIZE=0.3 C.RECT=15 W.R=0.4 H.R=0.4

LABEL X=2.15 Y=-6.5 LABEL="<9E19-2E20" SIZE=0.3 C.RECT=16 W.R=0.4 H.R=0.4

LABEL X=2.15 Y=-6.1 LABEL="<2E20-5E20" SIZE=0.3 C.RECT=17 W.R=0.4 H.R=0.4

LABEL X=2.15 Y=-5.7 LABEL="<5E20-8E20" SIZE=0.3 C.RECT=18 W.R=0.4 H.R=0.4

LABEL X=2.15 Y=-5.3 LABEL="<8E20-1E21" SIZE=0.3 C.RECT=10 W.R=0.4 H.R=0.4

LABEL X=2.15 Y=-4.9 LABEL="<1E21-9E21" SIZE=0.3 C.RECT=08 W.R=0.4 H.R=0.4

## Final 3-D Phosphor Doping

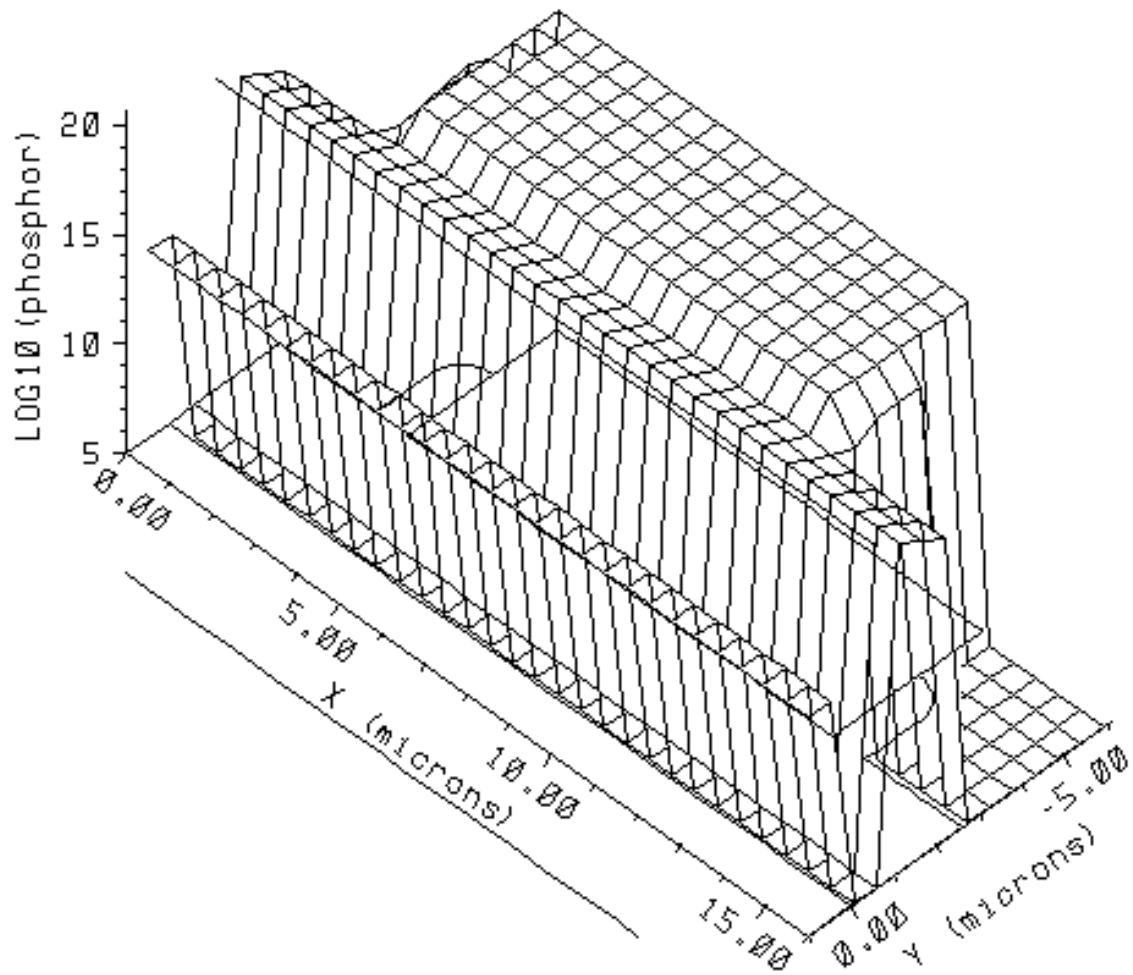


Figure C.1: TSUPREM 3-D phosphorus doping profile for a 10  $\mu\text{m}$ -wide Poly2 linestructure.

## *Appendix D. Vita*

LaVern A Starman, Captain, USAF

Captain LaVern A Starman Jr. was born in Tilden, Nebraska. He graduated from the University of Nebraska Lincoln with a Bachelor of Science degree in Electrical Engineering in 1994. He entered the United States Air Force through Officer Training School and was commissioned on 22 September 1995. He was immediately assigned to the Electronic Countermeasures Branch at the National Air Intelligence Center (NAIC) at Wright-Patterson AFB, OH. His work at NAIC included exploitation of electronic countermeasure systems such as radar warning receivers, jammers, and infrared detectors. While at NAIC, he pursued his Master of Science degree in Electrical Engineering from Wright State University, graduating in December 1997. Captain Starman also has over 10 years of experience in Air Force maintenance and testing facilities. Immediately following his assignment to NAIC, in January of 1999 Captain Starman was assigned to the Air Force Institute of Technology to pursue a Ph.D. in Electrical Engineering. He is a member of Tau Beta Pi and Eta Kappa Nu.

<b>REPORT DOCUMENTATION PAGE</b>				Form Approved OMB No. 074-0188	
<p>The public reporting burden for this collection of information is estimated to average 1 hour per response, including the time for reviewing instructions, searching existing data sources, gathering and maintaining the data needed, and completing and reviewing the collection of information. Send comments regarding this burden estimate or any other aspect of the collection of information, including suggestions for reducing this burden to Department of Defense, Washington Headquarters Services, Directorate for Information Operations and Reports (0704-0188), 1215 Jefferson Davis Highway, Suite 1204, Arlington, VA 22202-4302. Respondents should be aware that notwithstanding any other provision of law, no person shall be subject to a penalty for failing to comply with a collection of information if it does not display a currently valid OMB control number.</p> <p><b>PLEASE DO NOT RETURN YOUR FORM TO THE ABOVE ADDRESS.</b></p>					
<b>1. REPORT DATE (DD-MM-YYYY)</b> 26-03-2002		<b>2. REPORT TYPE</b> Doctoral Dissertation		<b>3. DATES COVERED (From – To)</b> Jun 2000 – Mar 2002	
<b>4. TITLE AND SUBTITLE</b>  CHARACTERIZATION OF RESIDUAL STRESS IN MICROELECTROMECHANICAL SYSTEMS (MEMS) DEVICES USING RAMAN SPECTROSCOPY				<b>5a. CONTRACT NUMBER</b>	
				<b>5b. GRANT NUMBER</b>	
				<b>5c. PROGRAM ELEMENT NUMBER</b>	
<b>6. AUTHOR(S)</b>  Starman, LaVern, A., Captain, USAF				<b>5d. PROJECT NUMBER</b>	
				<b>5e. TASK NUMBER</b>	
				<b>5f. WORK UNIT NUMBER</b>	
<b>7. PERFORMING ORGANIZATION NAMES(S) AND ADDRESS(S)</b> Air Force Institute of Technology Graduate School of Engineering and Management (AFIT/EN) 2950 P Street, Building 640 WPAFB OH 45433-7765				<b>8. PERFORMING ORGANIZATION REPORT NUMBER</b>  AFIT/DS/ENG/02-01	
<b>9. SPONSORING/MONITORING AGENCY NAME(S) AND ADDRESS(ES)</b> <div style="display: flex; justify-content: space-between;"> <div style="width: 45%;"> AFRL/MLMR Attn: Mr. John D. Busbee 2977 P Street Rm 215 WPAFB OH 45433-7746 DSN: 674-4323 e-mail: John.Busbee@wpafb.af.mil </div> <div style="width: 45%;"> AFRL/MLPJ Attn: Lt Col William D. Cowan 2977 P Street WPAFB OH 45433-7746 DSN: 785-2911 x4192 e-mail: William.Cowan@wpafb.af.mil </div> </div>				<b>10. SPONSOR/MONITOR'S ACRONYM(S)</b>	
				<b>11. SPONSOR/MONITOR'S REPORT NUMBER(S)</b>	
<b>12. DISTRIBUTION/AVAILABILITY STATEMENT</b>  APPROVED FOR PUBLIC RELEASE; DISTRIBUTION UNLIMITED.					
<b>13. SUPPLEMENTARY NOTES</b>					
<b>14. ABSTRACT</b> <p>Due to the small scale of MEMS devices, the inherent residual stresses during the deposition processes can affect the functionality and reliability of the fabricated devices. Residual stress often causes device failure due to curling, buckling, or fracture. Currently, few techniques are available to measure the residual stress in MEMS devices. In this dissertation, Raman spectroscopy is used to measure and monitor the residual and induced stresses in MUMPs polysilicon MEMS devices. Raman spectroscopy was selected since it is nondestructive, fast, and provides potential <i>in situ</i> stress monitoring. Raman spectroscopy scans on unreleased and released MEMS fixed-fixed beams, cantilevers, and micromirror flexures were performed to obtain residual stress profiles. The profiles are compared to analytical models to assess the accuracy of Raman spectroscopy.</p> <p>I performed post-processing thermal anneals, phosphorous diffusions and phosphorous ion implantations to characterize the residual stress changes within MEMS devices. From post-processing experiments, the Raman residual stress profiles on MUMPs structures indicate a stress reduction by over 90%, which is verified with on-chip test structures. The reduced residual stress levels can improve the performance, reliability, and yield of the MEMS devices as they become smaller. In addition, I present the first Raman stress measurements on III-V MEMS.</p>					
<b>15. SUBJECT TERMS</b> Residual Stress, Raman Spectroscopy, MUMPs, MEMS, Polysilicon					
<b>16. SECURITY CLASSIFICATION OF:</b>			<b>17. LIMITATION OF ABSTRACT</b>	<b>18. NUMBER OF PAGES</b>	<b>19a. NAME OF RESPONSIBLE PERSON</b>
a. REPORT	b. ABSTRACT	c. THIS PAGE			James A. Lott, Lt Col, USAF (ENG)
U	U	U	UU	297	<b>19b. TELEPHONE NUMBER (Include area code)</b> (937) 255-3636, ext 4527; e-mail: James.Lott@afit.edu